INFLUENCE OF NUCLEON-NUCLEON COLLISIONS ON MULTI-FRAGMENTATION AND NUCLEAR FLOW

A THESIS

submitted to the

THAPAR UNIVERSITY, PATIALA

for the degree of

DOCTOR OF PHILOSOPHY

IN THE FACULTY OF SCIENCE

By

Varinderjit Kaur

Regn. No. 900812006

SCHOOL OF PHYSICS AND MATERIALS SCIENCE

THAPAR UNIVERSITY

PATIALA-147004, PUNJAB,

(INDIA)

OCTOBER 2011

Dedicated to

My Beloved Husband

THAPAR UNIVERSITY, PATIALA

CANDIDATE'S DECLARATION

I hereby certify that the work which is being presented in the thesis entitled **"INFLUENCE OF NUCLEON NUCLEON COLLISIONS ON MULTI-FRAGMENTATION AND NUCLEAR FLOW"** in partial fulfillment of the requirement for the award of the Degree of Doctor of Philosophy and submitted in the School of Physics and Materials Science of Thapar University, Patiala is an authentic record of my own work carried out during a period from July 2008 to June 2011 under the supervision of **Dr. Suneel Kumar**, Assistant Professor, Thapar University and **Dr. Rajeev Kumar Puri**, Associate Professor, Department of Physics, Panjab University Chandigarh.

The matter presented in this thesis has not been submitted by me for the award of any other degree of this or any other Institute/University.

Varinder 14.10.2011

(VARINDERJIT KAUR)

This is to certify that the above statement made by the candidate is correct to the best of our knowledge.

S Kumar

Date: 14.10.2011 (Dr. Suneel Kumar) (Dr. Rajeev K. Puri)

Signature of HOD Signature of Dean R&SP Signature of Examiner

Acknowledgments

Upon attaining this goal of my doctorate degree, I must recall back what has brought me to this point. Therefore, I devote this space to acknowledge all those who helped me in this journey, however, these few words cannot convey the proper gratitude to all my dear ones. First of all, **GOD** has been kind enough to shower his blessings on me, for I find myself in most fortunate circumstances in this time span at Thapar University. During this period, I have gone through great successes and rare failures. The return from failure was due to the almighty.

My foremost thanks goes to my worthy supervisor **Dr. Suneel Kumar**, *Assistant Professor, Thapar University, Patiala* for guiding me in achieving this goal. I started my Ph.D in 2007 as a part time student with absolute no idea about research. It was his enthusiasm and faith in me that encouraged me to become a regular student. In spite of his busy and hectic schedule, he always made it a point to ensure that every bit of work was completed to its perfection. He is very hard working personality, who knows the value of time very well. His intuition and persistency are the key reasons I could successfully finish each of my research topics. He has always been present to support and encourage me in my professional life when times were tough.

Special thanks go to my second supervisor **Dr. Rajeev K. Puri**, *Associate Professor, Panjab University, Chandigarh* for fruitful discussions. **Dr. Puri** has continued to stand by us in all our problems we presented before him. His ideas were the seeds that became this document, and every page bears his imprint. I am truly grateful for his support and confidence his invaluable guidance, and his sense of humor. He has really contributed a lot to my research work while writing papers and revising my thesis. Dr. Puri gave me numerous advices about research, and the experiences I learned from him are invaluable.

I offer special thanks to **Prof. O.P. Pandey**, *Head, School of Physics and Materials*

Science, Thapar University, Patiala, for providing all the necessary facilities in the department. I wish to express thankfulness to all the faculty and staff of the School for their kind support. I am thankful to Prof. K.K. Raina, Deputy Director, for their encouragement and constant moral support to accomplish this task. I acknowledge the useful suggestions given by the members of my doctoral committee Drs. A. K. Lal and M. K. Sharma. Thanks also goes to Dr. P. K. Bajpai, Dean, research and sponsored projects for providing the possible research facilities here at Thapar University campus. Special thanks to Dr. Kulvir Singh who supported me very nicely in all presentations.

I am fortunate enough to have worked with my lab mates Dr. Sanjeev Kumar, Mrs. Rajni, Karan, Anupriya, Mrs. Shefali, Gudveen, Deepika and all other research scholars here at School of Physics and Materials Science. I am thankful to them for their sincere help and cooperation. I acknowledge the co-operation and encouragement extended by my colleagues in the Heavy-ion Reactions Theory Group at Panjab University, Chandigarh, particularly, Sakshi, Supriya, Rajkumari, Sukhjit, Yogesh, for their fruitful discussions and novel views. I would love to mention my close and ever cheerful friends Dr. Meenu Sachian, Kavita, Puja and Ruchika for moral support and all the fantastic moments we spent together.

Of course, goal could not have been achieved without the blessings and immense moral support of my parents **S. Balwinder Singh and Mrs. Paramjit Kaur**, my brother and bhabi, **Er. Tejinder Singh and Mrs. Geetinder Kaur** who have been my backbone in all the difficult phases of my life. Special thanks are due to my in-laws **S. Hakam Singh and Mrs. Charanjit Kaur**, my brother in-law **Harpreet Singh** for their unconditional love and support. It gives me immense pleasure to express special thanks to my Mama ji **S. Inderjit Singh** and Mr. Pawan Kumar who always took keen interest in guiding me regarding the DST project.

Everything will be meaningless, if I would not mention here about my sons **Jap Kunwar Singh** and **Simar Rajan Singh** for reminding me what really matters in the life. I think my sons suffered the most during my Ph.D. Their lovely and cute faces act as a strength that enabled me to work untiringly and continuously, be it a working day or holiday.

Last, but not the least, my husband **Mr. Mandeep Singh**, who provided smiling and untiring support towards this end. I would not be able to go through all the challenges in the Ph.D research without his support and understanding. He is the first person who motivated me towards research. Although there are number of sweet and sour moments we spent together during my research, yet I would mention here the day 17^{th} Feb. 2011, when my paper was selected in Phys. Lett. B. It was the most beautiful day of my research period.

The financial support from the **Department of Science and Technology (DST)**, New Delhi, Govt. of India, is greatly acknowledged. I am grateful to all the members of WOS-A committee, specially Dr. H. B. Singh for giving me the opportunity to interact with the eminent scientists in the field of physics.

Let some words of thanks to those people whom I couldn't mention............................

Varinder 14.10.11.

Varinderjit Kaur

Date: June 2011

Patiala

List of Publications :

A. Journals :

1. Systematic study of multi-fragmentation in asymmetric colliding nuclei.

   Varinderjit Kaur and Suneel Kumar,

   Physical Review C 81, 064610(6) (2010).

2. On the elliptical flow and mass asymmetry of the colliding nuclei.

   Varinderjit Kaur, Suneel Kumar, and Rajeev K. Puri,

   Physics Letter B 679, 512-516 (2011).

3. Rapidity distribution as a probe for elliptical flow at intermediate energies.

   Sanjeev Kumar, Varinderjit Kaur and Suneel Kumar,

   Central European Journal of Physics 9(4), 986-995 (2011).

4. On the nuclear stopping in asymmetric colliding nuclei.

   Varinderjit Kaur, Suneel Kumar, and Rajeev K. Puri,

   Nuclear Physics A 861, 37-46 (2011).

5. Mass independence and asymmetry of the reaction: Multi-fragmentation as an example.

   Varinderjit Kaur, Suneel Kumar, and Rajeev K. Puri,

   Journal of Physics Conference Series 312, 082028 (2011).

6. On the elliptical flow for nearly symmetric collisions and nuclear equation of state.

   Varinderjit Kaur and Suneel Kumar,

Pramana Journal of Physics (2011) (In press).

7. Energy of vanishing flow in heavy-ion collisions: Role of Coulomb interactions and asymmetry of a reaction.

   Varinderjit Kaur, Sanjeev Kumar and Suneel Kumar,

   Pramana Journal of Physics (2011) (In press).

8. Phase space analysis of fragmentation and role of mass asymmetry.

   Varinderjit Kaur and Suneel Kumar,

   Physical Review C (2011) (submitted).

9. Mass dependence of various fragments in multi-fragmentation.

   Varinderjit Kaur, Bhawna Sharma and Suneel Kumar,

   Pramana Journal of Physics (2011) (submitted).

10. Isospin dependence of balance energy in heavy-ion collisions.

    Varinderjit Kaur, Dolly Sood and Suneel Kumar,

    Physics of atomic nuclei (2011) (submitted).

11. Probing the effect of different cross-sections in asymmetric systems.

    Deepinder Kaur, Varinderjit Kaur and Suneel Kumar,

    Ukrain Journal of Physics (2011) (submitted).

12. Role of momentum dependent interactions in asymmetric collisions.

    Varinderjit Kaur and Suneel Kumar,

    Physical Review C (to be submitted).

13. Contribution of different interaction potentials in heavy-ion collisions.

    Varinderjit Kaur and Suneel Kumar,

    Physical Review C (to be submitted).

B. Symposia/Workshops/Conferences:

14. Review of Heavy-ion collisions and its equation of state.

    Varinderjit Kaur and Suneel Kumar,

    National Conference on Emerging Trends in Engineering Materials, Feb. 1-3, Thapar University, Patiala (India), pp. 33 (2007).

15. Study of nuclear flow at different energies.

    Varinderjit Kaur and Suneel Kumar,

    11^{th} Punjab Science Congress, Thapar University, Patiala (India), pp. 114 (2008).

16. Study of elliptic flow near balance energy for asymmetric reactions.

    Varinderjit Kaur, Suneel Kumar and Rajeev K. Puri,

    53^{rd} DAE symposium on Nuclear Physics, IIT, Roorkee (India) **Vol. 53**, pp. 575 (2008).

17. Transverse momentum dependence of elliptic flow at intermediate energies.

    Varinderjit Kaur, Suneel Kumar and Rajeev K. Puri,

    3^{rd} Chandigarh Science Congress, Chandigarh (India) (2009).

18. Isotopic effects in the production of different fragments for asymmetric systems.

    Varinderjit Kaur, Suneel Kumar and Rajeev K. Puri,

    Indian Nuclear Society seminar on Nuclear Technology for Sustainable Development, Oct. 10-11, Thapar University, Patiala (India) (2009).

19. Effect of system size asymmetry on multi-fragmentation in heavy-ion collisions.

    Varinderjit Kaur, Suneel Kumar and Rajeev K. Puri, International Symposium on Nuclear Physics, December 08-12, BARC, Mumbai (India) **Vol. 54**, 448 (2009).

20. Nuclear stopping in asymmetric colliding nuclei.

    Varinderjit Kaur and Suneel Kumar,

    DAE symposium on Nuclear Physics, December 20-24, Birla Institute of Technology and Science, Pilani, Rajasthan (India) **Vol. 55**, 518 (2010).

21. Influence of Coulomb interactions on directed transverse flow.

    Varinderjit Kaur, Suneel Kumar and Rajeev K. Puri,

    DAE symposium on Nuclear Physics, December 20-24, Birla Institute of Technology and Science, Pilani, Rajasthan (India) **Vol. 55**, 520 (2010).

Contents

List of Figures

List of Tables

ABSTRACT

The present work deals with the theoretical study of multi-fragmentation and its related phenomena like rapidity distribution, collective flow and nuclear stopping for asymmetric colliding nuclei at intermediate energy heavy-ion collisions. The theoretical investigations are carried out using microscopic *isospin-dependent quantum molecular* (IQMD) model. We aim to discuss the role of Coulomb interactions, nuclear equations of state (NEOS) and various rapidity bins by taking mass asymmetry into account. An attempt will also be made to understand the disappearance of directed transverse flow and elliptical flow and hence balance energy and transition energy, respectively. We shall also present the comparison of theoretical simulations with data produced by various experimental collaborations.

The present thesis is divided into following seven chapters.

Chapter 1 outlines the general introduction and background of the present work. The different phenomena, observables at intermediate energies i.e. NEOS, isospin physics, multi-fragmentation, collective Flow, as well as nuclear stopping are introduced. It also presents the status of the available experimental and theoretical attempts made to understand the above mentioned phenomena.

Chapter 2 gives the detail of primary and secondary models. The primary models include various theoretical models used in literature to study the phase space of nucleons in heavy-ion reactions and secondary models include the different clusterization algorithms. In the first part, the different theoretical models like Boltzman Uehling-Uhlenbeck (BUU) model, Classical Molecular Dynamics (CMD) model, Quantum Molecular Dynamics (QMD) model, Relativistic QMD (RQMD) model and Isospin-dependent QMD (IQMD) model are discussed to study heavy-ion reactions. The second part presents the different secondary models used to analyze the phase space of nucleons generated by the primary models. These secondary models include Minimum Spanning Tree (MST) method, MST with momentum cut (MSTP), MST with binding energy cut (MSTB), and Simulated Annealing Clusteriza-

tion Algorithm (SACA). Since our theoretical basis is the QMD and IQMD model, we shall discuss these two models in detail, while the detail of MST method is given where ever it is used.

In **Chapter 3**, we present a complete systematic theoretical study of multi-fragmentation for free nucleons and various fragments by simulating different asymmetric reactions at incident beam energies between 50 and 600 MeV/nucl. at semi-central impact parameter using soft and hard NEOS. While the total mass of the system stays constant, mass asymmetry varies between 0.2 and 0.7. We find that in the case of nearly symmetric reaction, spectator parts will come from both projectile and target, whereas in the case of highly asymmetric reaction, no spectator part will come from projectile i.e. only target will contribute to the spectators. Although nearly symmetric nuclei depict a well-known trend of rising and falling for intermediate mass fragment (IMF's) production with peak around E= 100 MeV/nucl., this trend, however, is completely missing for large asymmetric colliding nuclei. The measured distributions are also given as a function of the total charge of all projectile fragments, Z_{bound}. The highly asymmetric system produces largest Z_{bound}, while, maximum number of intermediate mass fragments (IMF's) are produced at $Z_{bound} = 20$. This observation may throw light on the formation mechanisms behind multi-fragmentation. Moreover, the brief study of the directed transverse flow shows that balance energy is affected by the Coulomb interactions as well as different NEOS. This balance energy is further parametrized in terms of mass power law.

In **Chapter 4**, within the semi-classical transport simulations of energetic semi-central collisions of the ${}_{79}Au^{197}+{}_{79}Au^{197}$ reaction, we present a new investigation of the interplay between the participant and spectator regions in terms of rapidity distributions. The maxima and minima in the incident energy dependence of elliptical flow are produced by different contributions of the passing time of the spectator and the expansion time of the participant. The shadowing of the spectator matter plays an important role up to later times due to the comparable magnitude of the passing and expansion times up to energies of 400 MeV/nucl. However, at high energies the shadowing effect is dominant only at earlier times due to the fact that the passing time is shorter than the expansion time. The transition from in-plane to out-of-plane emission is observed only when the mid-rapidity region is included into the rapidity bin. Otherwise, no transition is observed. The transition energy is found to be strongly dependent on the size of the rapidity bin, while only depends weakly on the type of the rapidity distributions. The transition energy is parameterized by a straight-line interpolation. A comparison with experimental bins reveals that a competition is observed between the rapidity bins of $|Y^{red}| \leq 0.1$ and $|Y^{red}| \leq 0.3$.

In **Chapter 5**, we present the systematic theoretical results on elliptical flow by analyzing nearly symmetric and asymmetric reactions at different incident energies. In the case of nearly symmetric reactions, general features of the elliptical flow are investigated with the help of theoretical simulations, particularly, the transverse momentum, impact parameter, system size and incident energy dependence. Special emphasis is put on the energy dependence of the elliptical flow. We also compare our theoretical calculations with 4π Array data. This comparison, performed for the reaction of ${}_{18}Ar^{40} +_{21} Sc^{45}$ shows that the hard NEOS explains the data nicely. In general, a reasonable agreement is obtained between the data and calculations. We also predict that elliptical flow for different kind of fragments follows power law dependence α C$(A_{tot})^{\tau}$.

Moreover, in the case of asymmetric reactions, elliptical flow is analyzed by varying the mass asymmetry of colliding nuclei while total mass is kept fixed. The mass asymmetry dependence of elliptical flow (in terms of transverse momentum dependence) for free nucleons and LMF's shows a weaker squeeze-out flow as compared to larger asymmetric reactions. Moreover, the elliptical flow is found to show a transition from in-plane to out-of-plane in the mid rapidity region with incident energy, while no such transition is observed when integrated over the entire rapidity region. The transition energy, at which elliptical flow $< V_2 >$ changes sign from positive to negative values, is different for different mass asymmetries, and is found to increase with the mass asymmetry for lighter fragments. The comparison with experimental data of INDRA@(GSI+GANIL) and MSU collaborations supports our findings.

In **Chapter 6**, we study the nuclear stopping in asymmetric colliding channels by keeping total mass fixed. The calculations are carried out by varying the mass asymmetry of the colliding pairs with different neutron-proton ratios at incident beam energy 250 MeV/nucl. The contribution of the neutrons and protons is checked in terms of anisotropy ratio $< R >$ and quadrupole moment $< Q_{zz} >$. The maximum stopping is obtained for nearly symmetric systems. Also a reasonable agreement is observed between theoretical results of anisotropy ratio $< R >$ and energy dependent anisotropy ratio $< R_E >$ with the experimental data of INDRA collaboration.

Finally, we will summarize our results in **Chapter 7**.

Chapter 1

Introduction

The science of nuclear physics concerns itself with the properties of "nuclear matter" that makes up the massive centers of the atoms accounting for 99.95% of the matter. The main properties of interest were/are the structure of nuclei, interaction among nucleons (i.e. protons and neutrons), nucleon-nucleon scattering, as well as the structure of nucleons. Nuclear physics apart from a subject of basic research also makes remarkable contributions to the needs of society, in terms of nuclear energy and nuclear medicine etc. It also explores the heavy nucleus-nucleus collisions which is of relevance not only for nuclear physics, but also for the astrophysical research [1]. The bulk properties of nuclear matter i.e. nuclear equation of state (NEOS) and possible co-existence of liquid-gas phases (LGP) of nuclear matter helps in understanding of the origin of the early universe, structure and formation of the compact heavenly bodies such as neutron stars, and supernova explosions etc. [1, 2].
The heavy-ion collisions at intermediate energies (10 MeV/nucleon $\leq$ E $\leq$ 2 GeV/nucleon) provide a unique way of exploring several interesting phenomenon such as multi-fragmentation, collective flow and nuclear stopping etc. Let us now review some of the features of heavy-ion physics.

1.1 Nuclear Matter and Phase Diagram

The normal nuclear matter is described by the physics at normal nuclear density and low temperature. One is interested to know what would happen if one compresses it strongly and/or if it is heated upto several billion degree Kelvin. Several physical effects might be happening which are illustrated in Fig. 1.1. This figure shows the schematic phase diagram of hot and dense nuclear matter. The X-axis represents the normal density, whereas temperature is shown on Y-axis. Nuclear matter can appear in different phases (i.e. Liquid, Hadron Gas and Quark-Gluon Plasma phases) depending upon temperature and density [3] The normal nuclear matter at ($\rho = \rho_0$, T = 0) represents the liquid phase. The liquid-

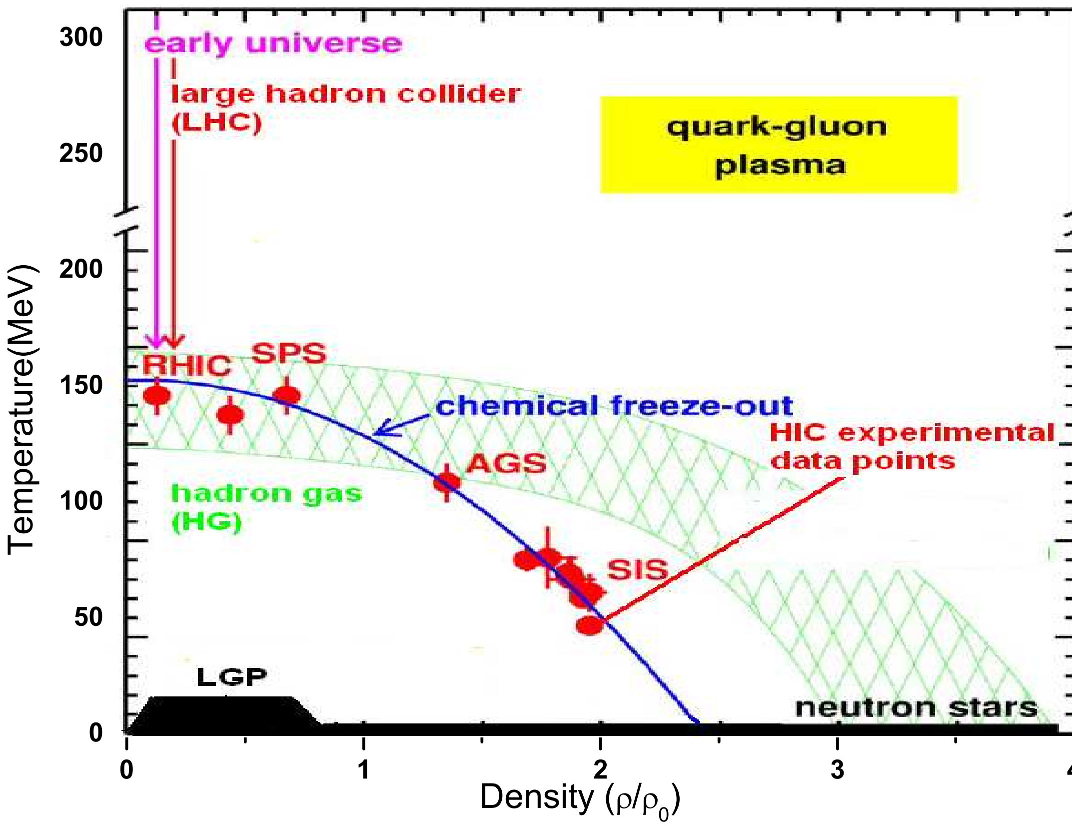

Figure 1.1: Phase diagram of nuclear matter in terms of temperature T and scaled density ρ/ρ_0 and its relation to heavy-ion collisions. The experimental data points are also displayed by solid red circles.

gas phase (LGP) transition region at the lower left corner of figure is characterized by the temperature below $\approx$ 15 MeV and densities ($\frac{\rho}{\rho_0} < 1$) [3]. A highly dense and hot region corresponds to the Quark-Gluon Plasma (QGP) phase [4, 5]. The hadron gas (HG) phase exists at intermediate temperature and density. The two lines separating the QGP phase from the HG phase is the phase co-existence and/or transition region [6]. The chemical freeze out points reached at SPS, RHIC, AGS, and SIS experiments [6] are shown here as solid red circles. These points are written as experimental data points. Generally one di-

Table 1.1: Different candidates at high densities and temperatures.

S. No	Candidates	Max. Density	Max. Temp.	Scope
1.	Finite Nucleus (Monopole)	$\frac{\rho}{\rho_0}$= 1	T = 0 MeV	Very small range of density is available
2.	Neutron Star	$\frac{\rho}{\rho_0}$= 6	T = 0 MeV	Rare in time and remote in space
3.	Supernova	$\frac{\rho}{\rho_0}$= 4	T = 10 MeV	
4.	HIC @ Intermediate energies	$\frac{\rho}{\rho_0}$= 2-3	T = 100 MeV	Give unique possibility to study the matter at high density and temperature

vide reaction dynamics into three regions comprises of low, intermediate and high energy reactions.

In the low energy reactions, basic interest is to look for the structure of nuclei. One can also study the phenomena of fusion-fission [7, 8], cluster radioactivity [9], as well as halo nuclei [10]. The high energy reactions on the other hand, could explore the QGP phase. The phase between these two limits, i.e. intermediate energy reactions provide unique possibility to study nucleon-nucleon collisions, multi-fragmentation, formation and flow of fragments etc. The study of nuclear matter under the extreme conditions of temperature and density can be handled by a number of possible candidates listed in table 1.1.

As seen from table 1.1, finite nuclei yield a small range of densities only. Other candidates like the neutron stars as well as supernova explosions are far in space and remote in time therefore, are of limited interest only. The best candidate that provides nuclear matter under the extreme conditions is the **heavy-ion collisions at intermediate energies** that offers excellent opportunities to study nucleon-nucleon collisions, multi-fragmentation, collective flow and nuclear stopping etc.

The specific region of the phase diagram and corresponding physics depends crucially on the incident energy. Reactions at intermediate energies are violent enough to excite the system to very high temperature leading to the break-up of initial correlations among nucleons, but not enough to break the internal structure of nucleons or hadrons.

1.2 Need to study nucleon-nucleon collisions

The study of nucleon-nucleon collisions is of broad scientific interest, that offers a unique possibility to investigate various microscopic features of complex nuclei at high densities and excitation energies [11]. These investigations include the study of compression of nuclear matter, production and properties of secondary particles, multi-fragmentation, and the quantitative description of collective effects like the directed transverse flow and elliptical flow etc. Following three points are important to note.

1. Heavy-ion collisions allow to test the effects originating from the collective motion of the nucleons inside a nucleus e.g. Giant dipole resonances, fragmentation etc.

2. The effects of excited nuclear matter e.g. formation of resonances can also be pindown.

3. The production of new particles e.g. pions, mesons and delta resonances etc. is essential of the outcome.

1.3 What happens in a nucleon-nucleon collision?

In a heavy-ion experiment, two nuclei collide and form a short-living hot high density region, which after wards expands as shown in Fig. 1.2. Finally, the particles emitted from the expanding system are detected, identified and their momenta are determined. In a high density hot region, many nuclear resonances are produced and finally the hot region starts expanding and cools down. With the passage of time, unstable resonances decay and particles are detected in the detector. The remnants of the projectile and target which did not belong the overlap region are scattered off from the compressed region in the transverse direction, which is known as transverse flow.

1.4 Need of a theoretical treatment

Since the study of neutron stars and supernova has its natural limitations, heavy-ion collisions provide an excellent tool to study the nuclear matter under the extreme conditions of temperature and density. The studies are performed in terms of theoretical models and

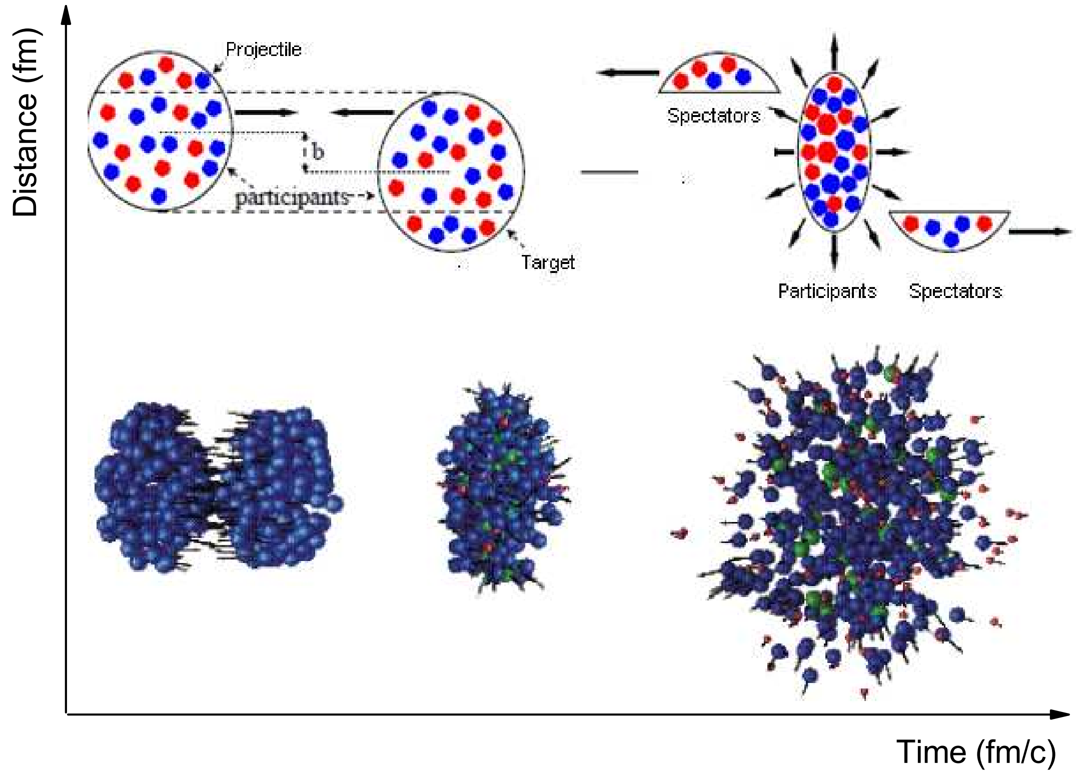

Figure 1.2: Schematic view of nucleus-nucleus collision (upper Panel) shows the definition of impact parameter (b) as well as participants which are nucleons in the overlap region, and spectators which are nucleons that do not directly participate in the reaction. In the lower panel, schematic illustration of collision of Au^{197} nuclei is shown. This figure is taken from Ref. [12]

compared with experimental data available. Since particles detected in experiments are cold, the phenomena of hot and dense nuclear matter cannot be seen in experiments, therefore, theoretical models are essential which may trace the full time evolution of the reaction. Thus, a mutual exchange between theory and experiments is necessary to understand what is going on in a heavy-ion collision.

Let us review briefly various phenomena, observables of heavy-ion collisions at intermediate energies.

1.5 The Nuclear Equation of State (NEOS)

If an equilibrium is reached during a heavy-ion collision, the system can be described by the nuclear equation of state (NEOS), i.e., a relation between three thermodynamical variables, namely, pressure, volume and temperature. For nuclear matter, these are replaced by internal energy E, temperature T and density ρ. The internal energy can be decomposed into a thermal (E_{th}) and a compressional part (E_c)

$$E(\rho, T) = E_{th}(\rho, T) + E_c(\rho, T = 0) + E_0 \tag{1.1}$$

where the compressional part is defined at zero temperature and E_0 is the ground state energy. There are two possible means to explore the dependence of the compressional energy per nucleon on the density ρ and temperature T, $E(\rho, T)$: astrophysical observations [13] and heavy-ion collisions. The $E(\rho, T)$ region explored by astrophysical observations is, however, quite different from that accessible in heavy-ion collisions. The astrophysical objects are usually cold, whereas in heavy-ion collisions compression goes along with excitation. Therefore, NEOS offers an insight into new phases of nuclear matter and conditions inside a supernova explosions, neutron stars, big-bang and heavy-ion collisions.
For an incompressibility ($K_\propto$) of approximately 200 MeV, the NEOS is 'soft'. At higher values of $K_\propto$ (= 380 MeV), the NEOS is called 'stiff'(hard).

1.5.1 Isospin Physics

The components of atomic nuclei, the neutron and the proton, form an isospin doublet since they differ only in the electric charge. The isospin dependence of the NEOS is often expressed in terms of symmetry energy. Considerable efforts are being made to experimentally extract symmetry energy and its dependence on nuclear density and temperature [14].
A binding energy formula expresses the energy E of a nucleus in terms of nucleon numbers, $E = E(A, Z)$. Here, A and Z are the net nuclear nucleon and proton numbers, respectively, and the neutron number is $N = A - Z$. The basic termed Bethe- Weizsacker [16, 17](BW), formula represents the energy as a sum of five terms only:

$$E = -a_V A \ + \ a_s A^{2/3} \ + \ \frac{a_c Z(Z-1)}{A^{1/3}} \ + \ \frac{a_A (N-Z)^2}{A} \ + \ \delta. \tag{1.2}$$

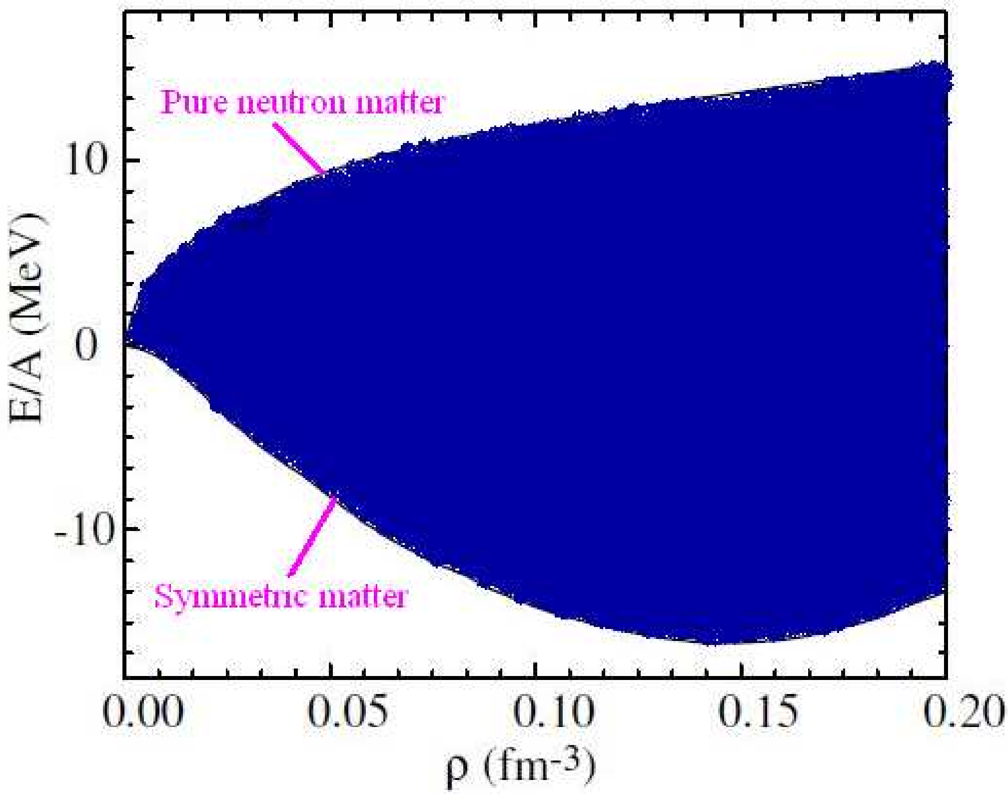

Figure 1.3: The concept of symmetry energy: The top line is the energy density for pure neutron matter and lower line is that for symmetric nuclear matter. The difference of two lines is the symmetry energy. This figure is taken from Ref. [15].

For the details of these terms the reader is referred to the Ref. [17]. The term of interest is the fourth term in the formula, $a_A(N-Z)^2/A$, with $a_A \approx 21$ MeV, is commonly called a symmetry energy term.

This symmetry energy in term of symmetry potential V_{Sym} can be written in three different forms [18].

$$V^1_{Sym} = cF_1(u)\delta\tau_z, \tag{1.3}$$

$$V^2_{Sym} = cF_2(u)\delta\tau_z + \frac{1}{2}cF_2(u)\delta^2, \tag{1.4}$$

$$V^3_{Sym} = cF_3(u)\left[\delta\tau_z - \frac{1}{4}\delta^2\right], \tag{1.5}$$

with $\tau_z = 1$ for neutrons, and -1 for protons.

where $F_1(u) = u$, $F_2(u) = u^2$ and $F_3(u) = u^{1/2}$ and, $u = \frac{\rho}{\rho_0}$; δ is the relative neutron excess $\delta = \frac{\rho_n-\rho_p}{\rho_n+\rho_p} = \frac{\rho_n-\rho_p}{\rho}$; ρ, ρ_0, ρ_n and ρ_p are the total, normal, neutron and proton densities respectively. The strength of c is of the order of 32 MeV to reproduce the 4^{th} term of the Bethe Weizsacker mass formula.

The IQMD code [19, 20] developed at Subatech, France by C. Hartnack and collaborators reduces the above symmetry potentials in the form as:

$$V_{Sym} = t_6 \frac{1}{\varrho_0} T_3^i T_3^j \delta(r_i{}' - r_j) \tag{1.6}$$

where, T_3^i, T_3^j are their respective T_3 components (i.e. 1/2 for protons and -1/2 for neutrons), $t_6 = 100$ MeV and $\delta(r_i{}' - r_j)$ represents the distance between the two nuclei. Here, again the strength of symmetry energy is found to be of the order of 32 MeV.

An elementary illustration of concept of symmetry energy is shown in Fig. 1.3. Symmetric matter is represented by the lower line, while pure neutron matter is represented by the upper line. The difference between the two lines is the symmetry energy, which express the effect of the isospin on nuclear matter energy density. The effect of isospin on Multi-fragmentation, directed transverse flow, elliptical flow, and nuclear stopping is studied in respective chapters in this thesis. In the following section, we shall introduce these phenomena's briefly.

1.6 Different phenomena's at intermediate energies

1.6.1 Multi-fragmentation

It is well known that when two nuclei collide, they break into several small and medium size pieces and lot of nucleons are also emitted. The produced particles include the free particles, light charged particles as well as very heavy clusters. This branch is termed as multi-fragmentation. The pictorial view of multi-fragmentation process is shown in Fig. 1.4. This process depends on the number of entrance channel parameters such as incident energy (E), collision Geometry (b), mass of colliding nuclei (M_P, M_T), and mass asymmetry ($\eta = (A_T - A_P)/(A_T + A_P)$) [21].

During last two decades, extensive efforts have been made both theoretically and experimentally to explore the questions like why do nuclei break into several fragments? How and

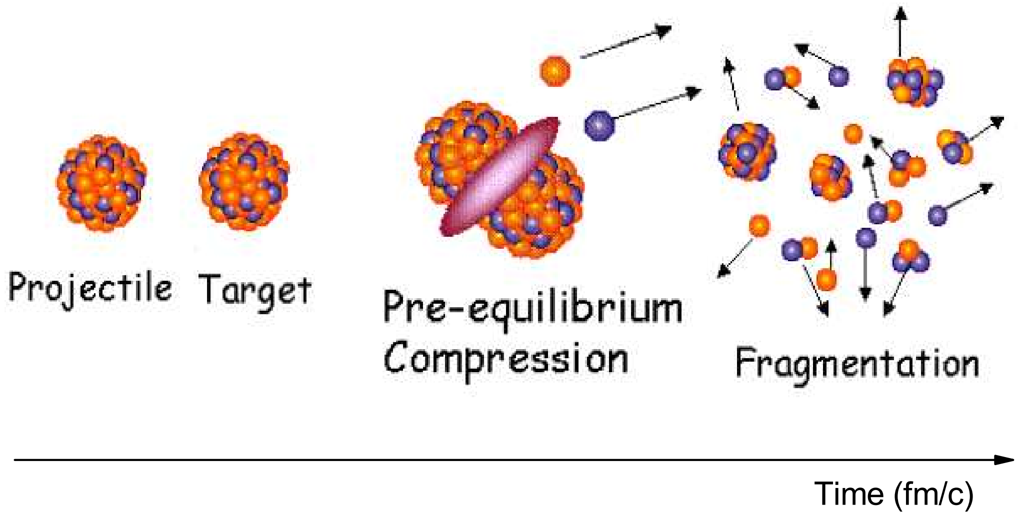

Figure 1.4: Schematic view of the multi-fragmentation process, clearly indicating the production of lighter and heavier fragments.

when are these fragments formed? What is the mechanism behind the multi-fragmentation? Why do nuclei shatter into several fragments if hit by a projectile? Is this a statistical or dynamical process or mixing of both? Can we relate this process to astrophysical happenings etc. etc.? The detailed analysis of multi-fragmentation by taking mass asymmetry into account [22] is discussed in chapter 3.

1.6.2 Collective Flow

The Collective flow is a measure of the transverse motion imparted to particles and fragments during the collision of two nuclei. The development of collective flow is closely related to the pressure build-up during the compression stage of the reaction, and gives us information about the pressure and particle density relation (that is, the NEOS). Generally, there are four type of flows, namely, longitudinal, radial, directed, and elliptical flows.

1. “Longitudinal flow” describes the collective motion of the particles along the beam di-

rection.

2. "Radial flow"describes the *azimuthal symmetric* flow, observed in central collisions in which the particles are emitted near $\theta_{c.m.} = 90^0$ relative to the beam axis.

3. "Directed flow", also called "in-plane" or "sidewards" flow refers to the *azimuthal asymmetric* emission of particles within the reaction plane.

4. "Elliptical flow" describes the *azimuthal asymmetric* emission pattern in which particles found to be preferentially emitted perpendicular to the reaction plane.

The pictorial view of directed and elliptical flow is shown in Fig. 1.5. Whereas, directed

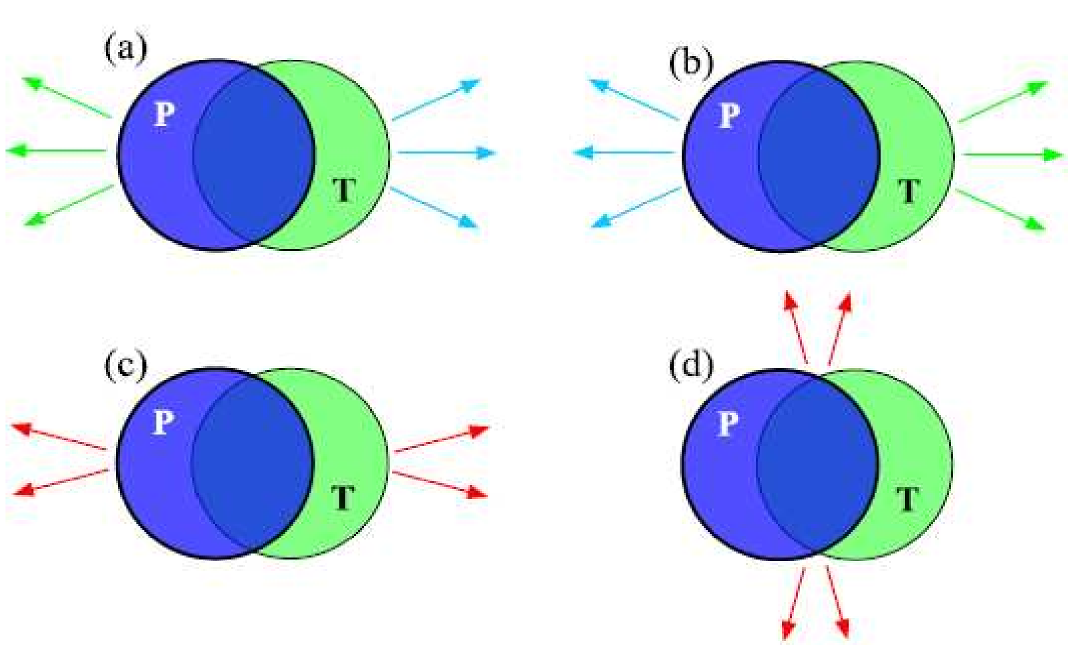

Figure 1.5: The four major types of azimuthal anisotropies, viewed in the transverse plane and looking in the direction of the beam. The target is denoted by T and the projectile by P, and blue (green) arrows indicate the preferred emission direction of projectile-like (target-like) fragments. (a) Negative directed flow; (b) positive directed flow; (c) in-plane elliptical flow; and (d) out-of-plane elliptical flow. This figure is taken from Ref. [23]

flow is anti-symmetric with respect to the ϕ distribution for forward rapidity ($y_{c.m.} > 0$) and backward rapidity ($y_{c.m.} < 0$) [23], elliptical flow has the same distribution in both rapidity regions, at least for symmetric reactions. These two observables together represent the anisotropic part of the transverse flow and appear only in the non-central heavy-ion collisions [24]. The detailed analysis of directed transverse flow including the mass asymmetry is discussed in chapter 3.

The elliptical flow refers to the anisotropy of the ϕ distribution at mid-rapidity and its value indicates whether the particle emission is in-plane or out-of-plane. Azimuthal distribution which are peaked at 0^0 and 180^0 exhibit predominantly in-plane emission, while ϕ distribution peaked at $\pm 90^0$ signify out-of-plane emission. The term elliptical flow has replaced the old naming such as "squeeze out", "rotational motion", or "anisotropic flow" because the shape of ϕ distribution at mid-rapidity resembles an ellipse with a major axis along the x-axis (in-plane emission) or y-axis (out-of-plane emission). A pictorial display of "in-plane" and "squeeze-out" is presented in Fig. 1.5. The systematic study of elliptical flow by using different rapidity bins [25] is discussed in chapter 4, while the detailed analysis of the same for nearly symmetric and asymmetric nuclei with and without isospin [26] is carried out in chapter 5.

1.6.3 Nuclear stopping

At intermediate energies, a mixture of attractive mean field and repulsive nucleon-nucleon scattering exists [19, 20, 27, 28]. Both these regimes together, lead the matter from a fused state to total disassembly. One is also interested to understand the mechanism behind this. Further, the origin of small pieces (fragments) is also of great interest. One is trying to correlate this origin with the nuclear stopping [29]. The pictorial view of nuclear stopping is shown in Fig. 1.6.

The degree of nuclear stopping in heavy-ion collisions is one of the essential observables which are necessary to understand the basic reaction dynamics. It is also closely related to the question of whether an equilibrium is reached or not for a colliding system in order to obtain correctly the information of NEOS and the reaction mechanism. This problem has been studied extensively both theoretically and experimentally [30]. Nuclear stopping in heavy-ion collisions in terms of mass asymmetry [31] has been studied with the help of different variables in chapter 6.

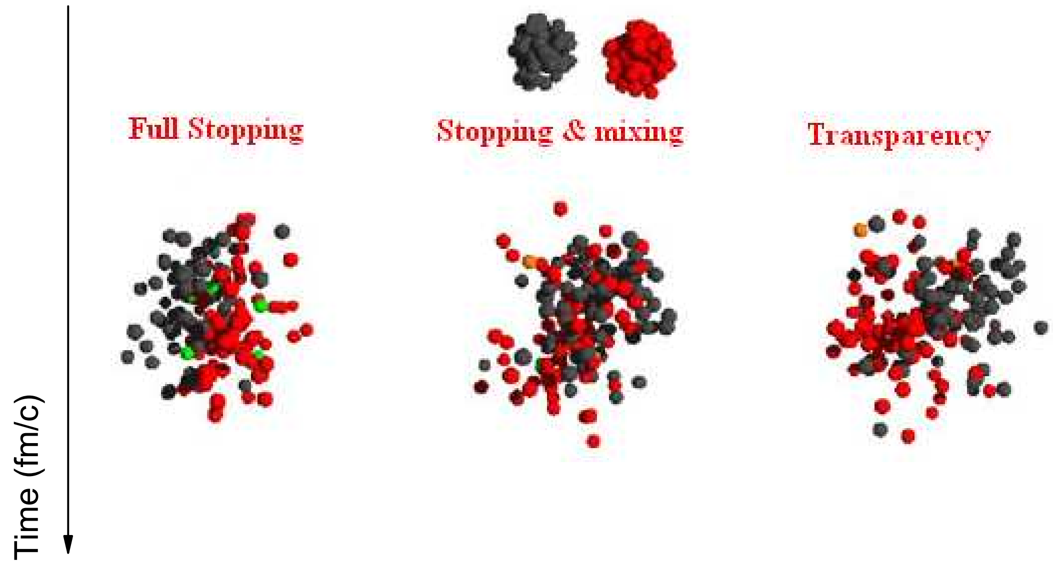

Figure 1.6: Three possible nuclear stopping scenarios representing the movement of projectile and target nucleons. The figure is representing (1) full stopping (2) stopping and mixing (3) transparency. This figure is taken from Ref. [12].

1.7 Review of experimental attempts

Many experimental efforts have been made in studying the process of multi-fragmentation, collective flow and nuclear stopping in heavy-ion collisions at intermediate energies. In the following, we shall present the review of these phenomena explained by different experimental collaborations.

Earlier natural accelerator available was cosmic rays. Cosmic rays are energetic particles originating from the outer space that impinge on earth's atmosphere. About 89% of all incoming cosmic ray particles are protons, nearly 10% are α nuclei. Slightly less than 1% consist of heavier nuclei e.g. C^{12}, O^{16} [32]. Since cosmic rays give inclusive spectra, need was felt to built accelerator or exclusive spectra in a controlled fashion.

Earlier, one could accelerate light ions only, therefore, field was dominated by shooting light particles on heavy targets. With the passage of time, new and larger accelerators were built which could accelerate heavy nuclei upto several hundreds of GeV that led to new unexplored world of nuclear physics. As such, it represents a rich and challenging world well worthy of intellectual pursuit and its study is important for a deep and a more complete understanding of nature. Nuclear fragmentation, discovered in cosmic rays, was a puzzling phenomena accompanying the collision of relativistic protons with a target and consisted of the emission of slow nuclear fragments. These fragments were in the range of $3 \leq Z \leq 30$, dubbed as intermediate mass fragments. Using radiochemical methods, a total cross-section of the fragmentation could not be determined and the process has been considered quite rare and exotic. In 1980's, Jakobsson *et.al.*, [33] observed multiple emission of IMF's in emulsion irradiated by the carbon beam of 250 MeV/nucl. This result created the interest in the nuclear community toward multi-fragmentation. Since then, the study of multi-fragmentation has been considered of such interest that a lot of detectors are designed to understand the each and every aspect in detail.

The first accelerator in this series was **BEVALAC accelerator** at Lawrence Berkeley Laboratory that served mainly to get the experimentalists and theoreticians aware of the problems and pitfalls of the way from medium energy heavy-ion collisions to the NEOS. Later on several accelerators were built. Some of them are: at Michigan state university (MSU)(USA), Grand Accelerateur National D'ions Lourds (GANIL)(France), Relativistic Heavy-Ion Collider (RHIC) (USA), Superconducting SuperCollider (SSC) at BNL (USA), Superconducting Cyclotron (SC) at Texas (USA), Superconducting Cyclotron (SC) and CHIMARA detector at Laboratori Nazionali del Sud in INFN, Catania (Italy), Heavy-ion Synchrotron (SIS) accelerator at GSI (Germany). These accelerators have contributed a lot in the field of heavy-ion collisions. All these setup focus on different aspects of reaction dynamics.

- The **Berkeley group** focuses mainly on the *asymmetric reactions* at incident energy between 50 and 110 MeV/nucl. [34]. The aim was to investigate the role of entrance-channel mass asymmetry on reaction dynamics. The emphasis was on the different parameters like excitation energy, angular distribution, cross-section as well as velocity distribution. The aim of the EOS collaboration at BEVALAC was to study the phase transition in nuclear matter. Various critical exponents like surface energy, volume energy, symmetry energy, entropy etc. [35] were extracted for the asymmetric reactions in the energy region of 1 GeV/nucl. In earlier studies, similar exponents were extracted for the symmetric reactions of $Au^{197} + Au^{197}$ [36].

- Like the Berkeley group, **National Superconducting Cyclotron Laboratory (NSCL)** of Michigan State University (MSU) focuses on the *asymmetric reactions* like $Xe^{129} + C^{12}$, Al^{27}, V^{51}, Cu^{64}, Y^{89} (50 MeV/nucl.), $Ar^{36} + Au^{197}$, $Xe^{129} + Au^{197}$ (50-110 MeV/nucl.), $Ar^{40} + Cu^{64}$, Ag^{108}, Au^{197} (at 17-115 MeV/nucl.) [37]. The average multiplicity as well as mass of the heaviest fragments are investigated. Apart from the asymmetric reactions, nearly symmetric channels such as $Ne^{20} + Al^{27}$, $Ar^{40} + Sc^{45}$, $Kr^{84} + Nb^{93}$, $Xe^{129} + La^{139}$ (15-135 MeV/nucl.) are also investigated [38]. The work on the isospin dependence of the nuclear matter is carried out by colliding Sn^{112} on Sn^{112} and Sn^{124} on Sn^{124} at 50 MeV/nucl. [39-43].

- On the other hand, *symmetric reactions* are studied by the **Superconducting Cyclotron of the Laboratori Nationali del Sud of INFN (Italy)**. The reactions of $Nb^{93} + Nb^{93}$ (at 17, 23, 30 and 38 MeV/nucl.) and $Sn^{116} + Sn^{116}$ (at 29.6, 38 MeV/nucl.) have been considered [44]. The multiplicity of light charged particles (LCP's) and intermediate mass fragments (IMF's) in the peripheral and semi-peripheral collisions as a function of excitation energy of emitting source, mass of the system and beam energy was presented [44]. Recently **Isospin collaboration** at INFN (Italy) studied the isospin effects for the neutron-rich and neutron-deficient reactions for non-central collisions at 35 MeV/nucl. [45].

- The **FOPI and ALADIN (A Large Acceptance DIpole magNet) groups at GSI** studied the multi-fragmentation process over a wide range of masses ranging from 12 to 208 units with wide range of incident energies between 100 to 1000 MeV/nucl. [47-49]. These groups studied particle evaporation, multi fragment emission as well as disassembly of the colliding nuclear matter. Rise and fall in the multiplicity of multi-fragments was one of the most exciting result obtained by ALADIN collaboration for

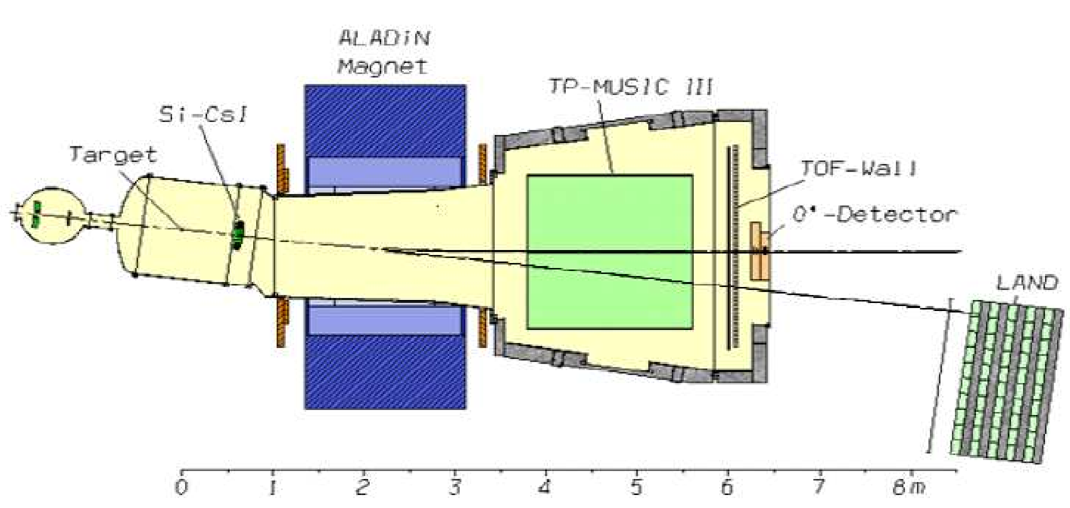

Figure 1.7: ALADIN detector. This figure is taken from Ref. [46].

Au^{197} + Au^{197} from 100 to 1000 MeV/nucl. [47]. Both detectors of ALADIN and FOPI are shown in Figs. 1.7 and 1.8 respectively.

- Similarly, **INDRA group at GANIL (France)** is also one of the leading group in this field. The system size effects, role of system size in entrance channel as well as Coulomb instabilities, kinetic energy spectra and fragment velocity correlation are studied in nearly *asymmetric reactions* of Ar^{36} + Ni^{58}, Gd^{155} + U^{238} and Xe^{129} + Sn^{nat} (at 30-95 MeV/nucl.), Ni^{58} + Ni^{58} (32-90 MeV/nucl.), Pb^{208} + Au^{197} (at 29 MeV/nucl.) and Ar^{36} + KCl [51] by this group. The entrance channel effects are also studied for different asymmetric reactions in the mass range 58 to 181 and beam energy between 24 to 90 MeV/nucl. [52]. The *symmetric reaction* of Au^{197} + Au^{197} was also studied between 40 and 150 MeV/nucl. [53]. It is also observed that fragmentation is responsible for fragment production around the excitation energy of 3 MeV/nucl. [54]. In a collaborative work of **ALADIN-INDRA**

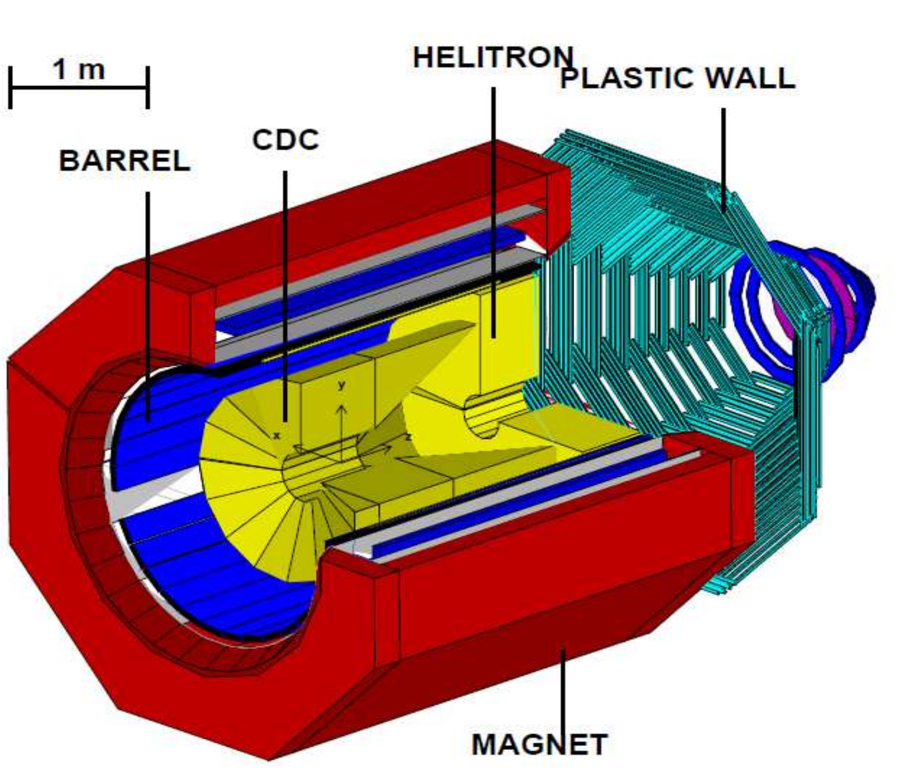

Figure 1.8: FOPI detector with various sub-detector components. This figure is taken from Ref. [50].

collaboration, bimodal behavior of heaviest fragment distribution in projectile fragmentation was found for the first time [55]. Recently, isospin effects are observed in semi-peripheral $Ni^{58}\ +\ Au^{197}$ collisions at intermediate energies [56].

- The **NIMROD collaboration at TAMU** focus on the reaction dynamics in the Fermi energy domain of heavy-ion collisions. The hot topic of recent years was the study of NEOS of isospin asymmetric nuclear matter [57] and a number of observables such as symmetry energy, isotopic and isobaric yield ratio, average N/P ratio for the reactions of $Sn^{124}\ +\ Sn^{124}$, $Xe^{124}\ +\ Sn^{124}$, $Sn^{112}\ +\ Sn^{112}$ at 28 MeV/nucl. have been explored [57, 58]. Recently, this group has studied the mass dependence of the nuclear caloric curve [59].

Many experimental efforts have also been made in studying the collective flow in heavy-ion collisions at intermediate energies. A lot of findings are presented in the literature on longitudinal, radial and directed flow [60-66], while an elliptical flow is yet to be fully explored. The review of experimental findings on elliptical flow by different collaborations is presented as follows:

Theoretically, the elliptical flow concept was originated in 1982 in terms of the mid rapidity emission perpendicular to the "reaction plane". This concept was given by Stocker *et al.*, [67] by calculating the angular distributions of the protons emitted from near-central collisions in a Fluid-dynamical model. They attributed the out-of-plane emission to the fact that compressed matter emitted perpendicular in the reaction plane is hindered or blocked by "spectator" matter. At the same time, Gyulassy, Frankel, and Stocker [68] put forward the kinetic energy tensor to analyze the flow patterns. Experimentally observed out-of-plane emission, termed as squeeze-out, was first observed in 1989 at nearly the same time by two competing collaborations. The **Diogene collaboration** at the Saturne synchrotron in Saclay observed slight peaks in the azimuthal distribution of particles at mid-rapidity in 800 MeV/nucl. Ne-induced reactions [69]. The **Plastic Ball group** at the Bevalac in Berkley observed out-of-plane emission in $Au^{197} + Au^{197}$ collisions at 400 MeV/nucl. [70, 71]. Furthermore, the transition from the in-plane to out-of-plane emission was first observed by the **NAUTILUS collaboration** at GANIL in 1994 [72].

In the past couple of years, the field of elliptical flow has expanded to include measurements at **NSCL, SIS, AGS, SPS, RHIC, BEVELAC**. Recently, the excitation function of elliptical flow parameters at energies from Fermi energy to relativistic energy regime for $Au^{197} + Au^{197}$ has been measured by various collaborations like **FOPI, INDRA, ALADIN** [61, 62].

- The **NSCL** at MSU (USA) focus on the disappearance of elliptical flow for *symmetric reactions* $Au^{197} + Au^{197}$ (at 500 MeV/nucl. to 11 GeV/nucl.) [73, 74]. The excitation function shows a transition from negative to positive elliptical flow at a beam energy $E \approx 4$ GeV/nucl. Later on, **NSCL** in collaboration with **STAR**, investigated the elliptical flow at $\sqrt{S_{NN}} = 130$ and 200 GeV [75]. They presented the pseudo rapidity, transverse momentum dependence and centrality dependence of elliptical flow. Moreover, the variation of elliptical flow with impact parameter and incident beam energy has also been shown for asymmetric reaction $Xe^{129} + Au^{197}$ [76].

- The other collaborations: **FOPI, ALADIN** at GSI, and the **INDRA** at GANIL emphasis on the transition of elliptical flow for different kind of fragments from in-plane to out-of-plane in intermediate energy heavy-ion collisions [61, 62, 63, 77]. Also, the **MINIBALL/ALADIN collaboration** observed the onset of out-of-plane emission in $Au^{197} + Au^{197}$ collisions at 100 MeV/nucl. [60], where out-of-plane emission is seen for central collisions, while peripheral collisions clearly show in-plane emission. The **FOPI collaboration** also got success in correlating the global stopping with flow [78] as well as with cluster formation during expansion [79]. On the other hand, the **INDRA and ALADIN collaborations** presented new results of flow analysis for set of reactions $Xe^{124,129}$ and $Sn^{112,124}$ (at 100 and 150 MeV/nucl.) [76]. The ratio of elliptical flow parameter of neutrons with respect to hydrogen isotopes measured for $Au^{197} + Au^{197}$ collisions at 400 MeV/nucl. in FOPI/LAND experiment has been used to determine the strength of symmetry term in NEOS [26]. Moreover, the new results of elliptical flow parameter for mid-peripheral $Au^{197} + Au^{197}$ collisions are presented as a function of transverse momentum per nucleon by ALADIN collaboration [80]. The recent study in the field of elliptical flow in intermediate energy heavy-ion collisions is by J.Y. Ollitrault and his co-workers [81]. They discussed how the different estimates of elliptical flow are influenced by flow fluctuations and non-flow effects.

In case of nuclear stopping, the latest study is by G. Lehaut [82] in central collisions at intermediate energies by analyzing kinematically complete events recorded with the help of the 4π multi-detector INDRA for a large variety of symmetric and asymmetric reactions such as $Au^{197} + Au^{197}$, $Xe^{129} + Sn^{118}$, $Ni^{58} + Ni^{58}$ etc. It is found that the behavior of isotropy ratio shows a rapid decrease as a function of the incident energy up to 400 MeV/nucl. Here the results are given for both momentum dependent and energy dependent anisotropy ratio. From the above experimental findings, one can notice that two different varieties of symmetric and asymmetric reactions merge. The symmetric reaction will generate high compression, whereas, asymmetric reaction will lead to heat or thermal energies. The aim of heavy target against light projectile is to look for the target-fragmentation, whereas, a heavy projectile on light target gives projectile-fragmentation. Naturally, the physics at central collisions follows the fire-ball dynamics, whereas at peripheral collisions the spectator physics dominates.

1.8 Review of theoretical models

Let us now review theoretical attempts developed to study the process of multi-fragmentation and various flows observed in heavy-ion collisions at intermediate energies. Different theoretical models have been proposed over the last two decades to study heavy-ion collisions at intermediate energies. These models can be divided into two categories: Primary models and Secondary models. "Primary models" generate the phase-space of nucleons while "secondary models" are needed to define clusters, if one is looking for cluster physics such as multi-fragmentation.

1.8.1 Primary Models

- Among various theoretical models developed to study different phenomena, one can group them into (i) static and statistical models and (ii) dynamical models as shown in Fig. 1.9. Statistical models [83], rely on the final break-up, neglecting the dynamics of the a reaction. On the other hand, dynamical models [84, 85] follow the reaction from two well separated nuclei to the final state where the matter is separated, fragmented and cold. Some of the statistical models are based on the droplet description of a nucleus, while the other ones are based on the percolation theory. Example of statistical models include multi-particle phase space models, such as the **Statistical Multi-fragmentation Model (SMM)** [83, 86] and the **Berlin Multi-fragmentation Model (BMM)** [87]. Additional static models include **Percolation** [88], **Lattice Gas (LG) Approach** [89] and **Expanding Emitting Source (EES) model** [90]. These statistical models have been extensively used to study the phe-

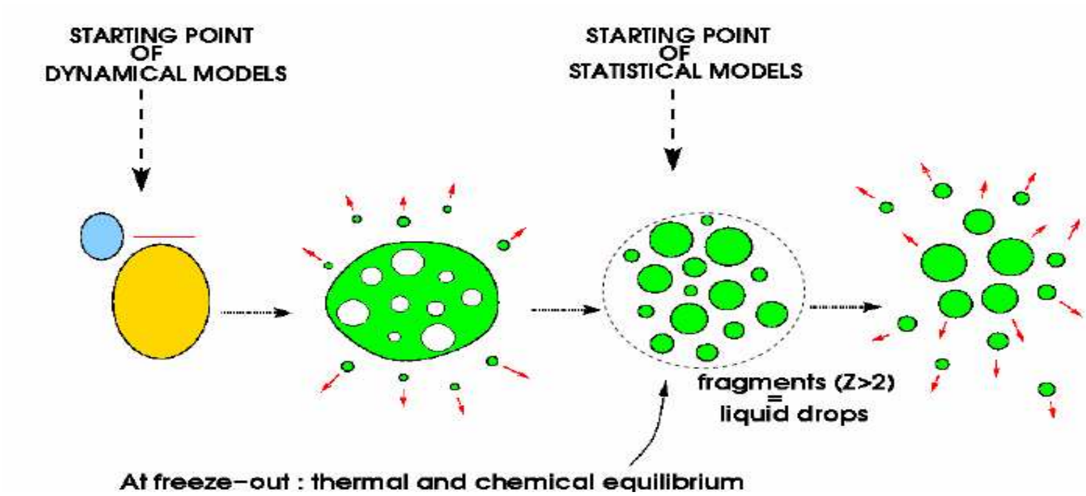

Figure 1.9: Schematic view of various statistical and dynamical models.

nomena of multi-fragmentation. The limitation of the statistical models are: (i) The situation at the start of a reaction is based on some assumption accounting for the degree of thermalization [83] and (ii) The statistical models give better description only of the final stage of a reaction. Since no dynamical information is possible, these models provide limited information. The study of dynamics of a reaction including correlations and fluctuations is possible by using the dynamical models.

Before looking for the different dynamical models at intermediate energies, we have to keep in the mind the dynamics involved at different incident energies. The key point to remember is that heavy-ion collisions involve very complicated non-equilibrium physics, therefore, its numerical modelling is not straight forward. Due to the lack of free phase space at low incident energy, about 98% of the attempted collisions are blocked. The whole dynamics at low energies is governed by the mean field or by the mutual two and three body interactions. On the contrary, the availability of large phase space at relativistic energies ($\geq$ GeV/nucl.) makes the Pauli-blocking [91] quite small (roughly 4% collisions are blocked) and hence the dynamics of a reaction is governed by the **Cascade picture**. On the other hand, both cascade and mean field pictures emerges at intermediate energies. Here one starts from two well defined nuclei and follow the dynamics within a dynamical model. These dynamical models, therefore, are capable of studying the detailed reaction phenomena with many-body features. Moreover, isospin picture also comes into existence in this energy range. Isospin is a factor that differentiate neutrons(n) from protons(p) inside a nucleus on the basis of the charges and makes possible interactions between the n-n, p-p and n-p. The isospin degree of freedom enters in term of symmetry potential, isospin-dependent in-medium nucleon-nucleon cross-section and Pauli blocking.

The dynamical approaches such as the **Time Dependent Hartree Fock (TDHF)** [19, 92] or its semi-classical version called *Vlasov equation* (in phase space) [93, 94] are suitable at low incident energies where nucleon-nucleon collisions are negligible. However, a suitable and reasonable approach for the intermediate energy heavy-ion physics should treat the nucleon-nucleon scattering and mean field on equal footing. Some attempts were made in the literature to extend the **TDHF** theory to take care of the residual NN interactions, which are responsible for the two-body collisions. This was dubbed as **Extended Time dependent Hartree-Fock (ETDHF)** theory [95]. However its numerical implementation prohibited its use for large scale investigations of heavy-ion collisions.

In the first attempt, the semi-classical version of **ETDHF** theory i.e. *Vlasov equation* [93] was coupled with nucleon-nucleon collisions and thus, a new realization named as, **Boltzmann -Uehling - Uhlenbeck equation (BUU)**, was developed to study the large deviation problems of low, intermediate and relativistic heavy-ion collisions. The **BUU** equation was solved by test particle method. The one body distribution function is described as a collection of NA test particles, where A is the mass number and N is event number. All possible collisions between the test particles are considered, i.e., there is no division of test particles. In other words, N parallel runs communicate with each other, therefore, event by event correlation can not be analyzed.

Keeping in mind the requirement of intermediate energy region, one would like to have those methods where correlations and fluctuations among nucleon can be preserved. Based on this, these dynamical models are further categorized into Classical Molecular Dynamics and Quantum Molecular Dynamics Models.

- The **Classical Molecular Dynamics (CMD)** [96] approach, in principle, is capable of predicting the fragments production. It also incorporate complete classical N-body dynamics which is necessary to describe the formation of the fragments. The simple Classical Molecular Dynamics, however, needs major refinements (including quantum features) which play a very important role at low incident energies.

- The Classical Molecular Dynamics (CMD) approach was later extended to incorporate the quantum features by Aichelin and Stocker [19, 27, 97]. This new approach, which explicitly incorporates the N-body correlations as well as nuclear matter equation of state and important quantum features (like the Pauli blocking, symmetry potential, nucleon-nucleon cross-section and particle production), was dubbed as **Quantum Molecular Dynamics (QMD)** model [19, 28, 97].

To extract the information of the NEOS of neutron-rich matter, especially the density dependence of the nuclear symmetry energy from heavy-ion reactions induced by neutron rich (stable and/or radioactive) beams, one needs reliable theoretical tools. For this purpose, one must have transport models that include explicitly the isospin degree of freedom and thus the isospin-dependent physical quantities such as the iso-vector (symmetry) potential and isospin-dependent in-medium nucleon-nucleon (NN) cross-sections and Pauli-blocking. As discussed above, the semi-classical models include mainly the two types: the BUU and the QMD model. With the development of radioactive ion-beam physics, several rather comprehensive isospin-dependent, but mostly semi-classical transport model such as IBUU [18], SMF [98] and IQMD [99] have been successfully developed in recent years to describe nuclear reactions induced by neutron-rich nuclei at intermediate energies.

The **isospin-dependent Boltzmann-Uehling-Uhlenbeck (IBUU)** transport model has successfully explained several isospin dependent phenomena in heavy-ion collisions at intermediate energies [18]. In this model, the isospin dependence was included in the dynamics through nucleon-nucleon collisions by using isospin-dependent cross-sections and Pauli blocking factors, the symmetry potential $V_{sym}(\rho, \delta)$, and the Coulomb potential. This model was used to calculate the ratio of yield of neutron and protons in pre-equilibrium emission [100]. The density fluctuations that lead to the fragment production are suppressed in the **BUU** equation, so the calculation of fragment yield directly via **BUU** model is not feasible. Therefore, alternate model such as, **Stochastic Mean Field (SMF)** model [98] and **Isospin Quantum Molecular Dynamics (IQMD)** model [20, 99] have been developed to address the density fluctuations.

The **IQMD** model [99] treats different charged states of nucleons, deltas and pions explicitly [101], as inherited from the *VUU* model [94]. The isospin degree of freedom enters into the calculations via symmetry potential and cross-sections [94]. This model is proven successful to study the isospin effects in intermediate energy heavy-ion collisions. The model incorporate the N-body correlations, reduces the fluctuations to minimum extent, explains the NEOS and includes the many quantum features like Pauli blocking, Stochastic scattering, particle production and isospin.

In recent years, several refinements and improvements were made over original QMD model. The new versions were named as **MQMD** [102], **HQMD** [20, 99], **PQMD** [103], **BQMD** [20, 99], **RQMD** [104], **ImQMD** [105], **UrQMD** [106], **IQMD** [20], **G-Matrix QMD** [107], **Glauber plus QMD** [108] etc.

All the single particle properties like density, collision number, collective/elliptical flow, nuclear stopping etc. are possible with either type of models. One simulates the reaction and the phase space is obtained that can be subjected to various variables. On the other hand, when one wants to understand the cluster physics including fragmentation of the nuclear matter, then one has to identify the fragments. Since phase space does not carry such information, one has to subject phase space to secondary algorithms.

1.8.2 Secondary Models

Secondary models include different "clusterization algorithms" used to construct fragments. In a very simple picture, nucleons are connected to a cluster using space correlation method. This method identifies the two nucleons in the same fragment if their centroids are less than some distance [109]. This method is known as **Minimum Spanning Tree (MST)** method [109]. Till today, it is one of the most extensively used methods. Several refinements to this method have been proposed including momentum cut and binding energy cut [110]. One more and newly developed secondary model is **"Simulated Annealing Clusterization Algorithm"**, developed by Puri, Hartnack and Aichelin [111], which is based on the minimization of energy of the system.

As discussed in the above paragraphs, we have several theoretical models that are available to study the heavy-ion collisions at intermediate energies. We shall study multi-fragmentation and and its related phenomena using primary model **IQMD** and then analyze by secondary model **MST**.

The thesis is organized as follows:

In **Chapter 2**, we will describe various theoretical models in brief. The primary models, Quantum Molecular Dynamics *(QMD)* and Isospin-dependent Quantum Molecular Dynamics *(IQMD)* will be discussed in detail. In addition, the secondary approach or algorithms such as Minimum Spanning Tree *(MST)*, Minimum Spanning Tree with momentum cut *(MSTM)* and Minimum Spanning Tree with binding energy cut *(MSTB)* will also be discussed in brief.

In **Chapter 3**, we present a complete systematic theoretical study of multi-fragmentation for different fragments i.e. free nucleons ($A = 1$), light mass fragments(LMF's) [$2 \leq A \leq 4$], and intermediate mass fragments(IMF's) [$5 \leq A \leq A_{tot}/6$] by simulating various asymmetric reactions of ${}_{26}Fe^{56}+{}_{44}Ru^{96}$ ($\eta = 0.2$), ${}_{24}Cr^{50}+{}_{44}Ru^{102}$ ($\eta = 0.3$), ${}_{20}Ca^{40}+{}_{50}Sn^{112}$ ($\eta = 0.4$), ${}_{16}S^{32}+{}_{50}Sn^{120}$ ($\eta = 0.5$), ${}_{14}Si^{28}+{}_{54}Xe^{124}$ ($\eta = 0.6$); ${}_{8}O^{16}+{}_{54}Xe^{136}$ ($\eta = 0.7$). First of all, the phase space of participant and spectator matter is shown for the reaction of ${}_{26}Fe^{56} +_{44} Ru^{96}$ ($\eta = 0.2$) having least mass asymmetry and ${}_{8}O^{16} +_{54} Xe^{136}$ ($\eta = 0.7$) having highest mass asymmetry respectively. After this, we have analyzed the effect of mass asymmetry on relative multiplicity of different fragments at E = 150 MeV/nucl. Also various parameters i.e multiplicity of different fragments (FN's, LMF's, IMF's), density distribution, mass and charge distributions, energy distribution etc. are studied in the energy range between 50 and 600 MeV/nucl. by using soft and hard NEOS. Also the Z_{bound} dependence of mean multiplicity of IMF's (N_{IMF}) is explained on the basis of time evolution and impact parameter dependence. N_{IMF} as a function of mass asymmetry is explained at different Z_{bound} values. At last, we have briefly discussed the directed transverse flow at various mass asymmetries and have shown the power law dependence of balance energy by taking mass asymmetry into account.

In **Chapter 4**, we study the interplay between the participant and spectator matter in terms of rapidity distribution of light charged particles (LCP's) using the reaction of ${}_{79}Au^{197} + {}_{79}Au^{197}$. The rapidity distribution for the light charged particles is explained at different incident energies. Rapidity distribution is divided into five different zones of which three are including participant zone, while, other two are excluding this region. Further, the incident energy dependence of elliptical flow for LCP's (i) collectively for projectile as well as target matter and

(ii) independently for projectile and target matter by including and excluding mid-rapidity regions is discussed in detail. At last, the results are compared with the experimental data of various collaborations.

In **Chapter 5**, we discuss elliptical flow in nearly symmetric and asymmetric reactions respectively. In nearly symmetric reactions ${}_{10}Ne^{20} + {}_{13}Al^{27}$, ${}_{18}Ar^{40} + {}_{21}Sc^{45}$, ${}_{30}Zn^{64} + {}_{28}Ni^{58}$ and ${}_{36}Kr^{86} + {}_{41}Nb^{93}$ we have analyzed the transverse momentum dependence of elliptical flow for different fragments i.e. free nucleons ($A = 1$), light mass fragments ($2 \leq A \leq 4$), and intermediate mass fragments ($5 \leq A \leq A_{tot}/6$) using static (soft, hard) NEOS at E = 95 MeV/nucl. The impact parameter and system size dependence of elliptical flow of different fragments is also explained at the same energy using soft NEOS. Moreover, to observe the transition from in-plane to out-of-plane emission, energy dependence of elliptical flow is shown for ${}_{18}Ar^{40} + {}_{21}Sc^{45}$ system using both the NEOS for light mass fragments (LMF's) and the results obtained are compared with the experimental findings of 4π collaboration [23]. In asymmetric reactions, we study the elliptical flow in terms of mass asymmetry parameter. For this, in the first instance, we analyz the detailed transverse momentum dependence of elliptical flow for different fragments (FN's, LMF's and IMF's) for the reactions of ${}_{24}Cr^{50} +_{44} Ru^{102}$ ($\eta = 0.3$), ${}_{16}S^{32} +_{50} Sn^{120}$ ($\eta = 0.5$), and ${}_{8}O^{16} +_{54} Xe^{136}$ ($\eta = 0.7$). To see the isospin effect due to symmetry energy, we discuss the transverse momentum dependence of elliptical flow for the reaction of ${}_{24}Cr^{50} +_{44} Ru^{102}$ ($\eta = 0.3$) in mid-rapidity region. Moreover, to observe the transition from in-plane to out-of-plane emission, excitation function of the elliptical flow is elaborated for the reactions mentioned above and the results are also compared with the experimental findings of INDRA@(GSI+GANIL) and MSU collaborations.

In Chapter 6, we have tried to correlate the mass asymmetry of colliding pairs with nuclear stopping and hence the equilibrium reached in a reaction (colliding pairs are same as used in Chapter 3). For this, first of all we discuss the origin of different fragments (FN's, LMF's, IMF's). To further elaborate, we have discussed the impact parameter dependence of LMF's and nuclear stopping parameters (R and Q_{zz}) at incident energy E = 250 MeV/nucl. Getting the reasonable agreement in the impact parameter variation of LMF's and nuclear stopping, we show the variation of stopping parameters (R and Q_{zz}) and transverse, longitudinal momentum with mass asymmetry. Also, N/Z (neutron/proton) dependence of the multiplicity of LMF's and nuclear stopping parameters $< R >$ and $< Q_{zz} >$ are parametrized in terms of power law. The results obtained are compared with the experimental findings of INDRA collaboration.

Our results will be summarized in **Chapter 7**, which will also contain an outlook of the work.

Chapter 2

Methodology

2.1 Introduction

As discussed in Chapter 1, dynamical study of heavy-ion collisions at intermediate energy requires equal weightage to both nucleon-nucleon/binary collisions and mean field. This demands exact information about the real (trajectory of nucleons) and imaginary (nucleon-nucleon collisions) parts of the nuclear potential. Furthermore, to extract the information of the nuclear equation of state (NEOS) from heavy-ion reactions, one must include explicitly the isospin degree of freedom. This isospin degree of freedom enters into real and imaginary parts in term of iso-vector (symmetry) potential, isospin-dependent in-medium nucleon-nucleon cross-sections, and Pauli-blocking, respectively. In addition, one has also to start from the initial state (where matter is non-equilibrated) to the final state (where matter is cold and fragmented). The dynamical transport models employed at intermediate energies are supposed to include essential collision physics. We shall discuss some of the models in brief whereas QMD and IQMD models in detail.

2.2 Boltzman Uehling-Uhlenbeck (BUU) model

The microscopic transport models for the one-body Wigner phase space density distribution obtained different names although they solve the same equation. They differ in the technical realization, i.e. the computer program, and are known as **Vlasov Uehling-Uhlenbeck (VUU) model** [94] (or **BUU** [93]). The following transport equation is solved for the one-body Wigner density $f(r, p, t)$ in the limit $\hbar \rightarrow 0$:

$$\frac{\partial f}{\partial t} \; + \; v \cdot \nabla_r f - \nabla_r U \cdot \nabla_p f \;\; = \;\; -\frac{4\pi^3(\hbar c)^4}{\hbar(mc^2)^2} \int \frac{d^3\acute{p}_1}{(2\pi\hbar)^3} \, \frac{d^3\acute{p}_2}{(2\pi\hbar)^3} \, d^3p_2 \, \frac{d\sigma}{d\Omega}$$

$$\times \left[f\ f_2(1-f_1')(1-f_2') \ - \ f_1' f_2'(1-f)(1-f_2) \right]$$
$$\times \delta^4(p\ + p_2\ - p_1' - p_2'). \tag{2.1}$$

The l.h.s. of this equation is the total differential of f with respect to the time assuming a momentum independent potential U. This potential corresponds to the real part of the Brückner G-matrix. Usually a Skyrme-parametrization

$$U \ = \ \alpha \left(\frac{\rho}{\rho_0}\right) \ + \ \beta \left(\frac{\rho}{\rho_0}\right)^{\gamma} \tag{2.2}$$

of the real part of the G-matrix is employed, where ρ is the nuclear density which is frequently measured in units of the saturation density ρ_0 of cold nuclear matter.

The r.h.s. of Eqn. 2.1 contains a Boltzmann collision integral, which is identified with the imaginary part of the G-matrix. This part describes the influence of binary hardcore collisions, where the term with ff_2 describes the loss of particles (in a phase space region) and the terms with $f_1 f_2$ describes the gain term. The δ-functions assure the conservation of the four momentum. The cross section σ is normally adjusted to the free nucleon-nucleon scattering. For the detailed derivation of this Eqn. see Ref. [112].

The **BUU equation** describes the time evolution of the one body distribution function in a 6 dimensional phase space. It is a non-linear differential integral equation. This equation is solved by test particle method. Here the phase-space of each nucleon is represented by a large number of pseudo-particles (test particles). In its numerical implementation, the above equation reduces to a set of $6 \times (A_T + A_P) \times N$ coupled first order differential equations in time. Here, N represents the number of test particles per nucleon and A_T and A_P are, respectively, the mass of the target and projectile. The test particle method replaces the expectation value of a single particle observable

$$\langle O(t) \rangle \ = \ \int f(r,p,t)\ O(r,p)\ d^3r\ d^3p, \tag{2.3}$$

by a Monte Carlo integration

$$\langle O(t) \rangle \ = \ \frac{1}{n(A_T\ + A_P)} \ \sum_{i=1}^{n(A_T+A_P)} \ O(r_i(t),\ p_i(t)), \tag{2.4}$$

Where the $r_i(t)$ and $p_i(t)$ are point in phase space which are distributed according to $f(r, p, t)$, i.e.,

$$f(r,\ p, t)\ =\ \lim_{n\rightarrow\infty}\frac{1}{n(A_T\ +\ A_P)}\ \sum_{i=1}^{n(A_T\ +\ A_P)}\ \delta(r\ -\ r_i(t))\delta(p\ -\ p_i(t)). \tag{2.5}$$

Obviously, large number of test particles (n) will be needed to avoid the numerical noise. In practice, the number n lies in the range between 15 and 500. In earlier attempts, test particles were represented by classical point particles. The recent calculations, however, use Gaussian wave packet for test particles [113]. The time evolution of these test particles is governed by the classical Hamilton's equations of motion

$$\dot{p_i}\ =\ -\ \frac{\delta\langle\ H\ \rangle}{\delta r_i};\ \ \dot{r_i}\ =\ \frac{\delta\langle\ H\ \rangle}{\delta p_i}, \tag{2.6}$$

For a solution of (Eqn. 2.1) proper boundary conditions have to be specified. In the case of heavy ion reactions, the test particles are distributed according to the density- and Fermi-momentum distribution of ground state nuclei. The later are then boosted toward each other with proper relative momentum. Initially the test particles are randomly distributed in a coordinate space sphere of the radius $R = 1.12A^{1/3}$ fm (where A is the atomic number of the nucleus) and in a momentum space sphere of the radius of the corresponding Fermi momentum.

One should keep in the mind that the forces acting on the test particles are calculated from the entire distribution including test particles from all events, hence the n parallel events are not independent and event-by-event correlations cannot be analyzed within these one-body transport models.

Any one-body observable can be calculated by averaging the values weighted with the distribution function. In brief, the **BUU** model is able to explain the one-body observables like the collective flow, stopping as well as particle spectra [113]. But fluctuations and correlations, such as the formation of fragments or the description of two-particle correlations in relativistic heavy ion collisions, are beyond the scope of a transport model based on a one-body distribution function [114]. The recent developments in the $\mathbf{BUU-type}$ model incorporate the momentum dependent potential [115], isospin dependent potential as well as isospin dependent nucleon-nucleon scattering cross section [18, 116]. In the following, we will first discuss **Classical Molecular Dynamics (CMD)** model [117] in brief and then will explain **Quantum Molecular Dynamics (QMD)** model [27, 118], which is N-body model.

2.3 Classical Molecular Dynamics (CMD) Model

When correlations and fluctuations become important in the dynamical evolution of a many-body system and mean-field approximations are not sufficient, molecular dynamics methods are frequently invoked. Molecular dynamics means the constituents (molecules) of the many-body system are represented by a few classical degrees of freedom (center-of-mass position and momentum) and interact through various potentials [117]. The equations of motion (Newtonian or Hamiltonian) are solved numerically. The major advantage of molecular dynamics simulations is that they do not rely on the quasi-particle approximations but include both the mean-field effects and many-body correlations. Therefore, they can provide insight into complex systems with correlations on different scales.

During the past decade, an increasing interest has developed in the dynamics of many-fermion systems in which correlations are important. In nuclear as well as in atomic physics, collisions of composite fermion systems like nuclei or atomic clusters demand many-body models that can account for a large variety of phenomena. Depending on the incident energy, one may observe various phenomena including fusion, fragmentation or even multi-fragmentation, vaporization, evaporation, and ionization of colliding matter.

One should keep in mind that classical molecular dynamics is applicable if de-Broglie wave-length of molecules is small compared to the length scale of typical variations of the interactions. If molecules are identical fermions of bosons, the de-Broglie wavelength should also be small compared to the mean inter-particle distance in phase space; otherwise Pauli or Bose principle is violated and the model will have the wrong statistical properties.

For nucleons bound in a nucleus, these conditions are not fulfilled. The same holds true for electrons in bound states or at high densities and low temperatures. Nevertheless, one would like to utilize the merits of a molecular-dynamics model for indistinguishable particles in the quantum regime. The closest quantum analog to a point in single-particle phase space representing a classical particle is a wave packet well localized in phase space. The analog to a point in many-body phase space representing several classical particles is a many-body state which is a product of localized single-particle packets.

When energetic collisions between heavy nuclei became available, classical molecular dynamics models were developed to describe various phenomena. To simulate the effect of anti-symmetrization on the classical trajectories, a two-body "Pauli potential" (which is supposed to keep fermions apart from each other in phase space) was added to the Hamiltonian.

In nuclear physics, nucleons cannot be treated as classical particles on trajectories. Their phase-space density is too large to ignore the Pauli principle. Therefore, various molecular-dynamics models that incorporate the Pauli principle on different levels are proposed in the literature. These models include Quantum Molecular Dynamics (QMD) model, Relativistic Quantum Molecular Dynamics (RQMD) model, Improved Quantum Molecular Dynamics (ImQMD) model, Ultrarelativistic Quantum Molecular Dynamics (UrQMD) model, and Isospin-dependent Quantum Molecular Dynamics (IQMD) model. In the following, we shall discuss **QMD** model [27, 97, 118], **RQMD** model [104] and **IQMD** model [20] in detail.

2.4 Quantum Molecular Dynamics (QMD) Model

The classical molecular dynamics (CMD) approach [117], which is a true N-body theory, is capable of treating both the compression and fragments formation, but on a completely classical level: the Hamilton's equation of motion are integrated for N classical point particles, with finite range nucleon-nucleon potential. Based on the CMD approach, Aichelin and Stocker [97], designed a novel model known as Quantum Molecular Dynamics (QMD) model, that incorporates N-body correlations, NEOS and many important quantum features, namely, the Pauli-principle, Stochastic scattering as well as particle production. The **QMD** model is a n-body theory that simulates heavy-ion reactions at intermediate energies on an event by event basis. Taking into account all fluctuations and correlations, it has basically two advantages:

(1) Many body processes, in particular, the formation of complex fragments are explicitly treated.

(2) The model allows for an event-by-event analysis of heavy-ion reactions.

Every such semi-classical model [27, 118] has three step evolution:

(1) Projectile and target are initialized. For each of these nuclei, nucleons are initialized according to a distribution function f(r,p,t = 0). This distribution is essentially constrained by the requirement to reproduce the ground state properties of the two nuclei, i.e., radii, binding energies etc. This procedure is called as **initialization**.

(2) The nucleons of projectile/target are propagated under the influence of surrounding mean field using Hamilton's equations of motion with a given Hamiltonian $\langle H \rangle$. This is termed as **propagation**.

(3) Finally, nucleons are bound to collide if they come too close to each other in coordinate space. The nucleons change their momenta respecting the Pauli principle. This part is dubbed as **nucleon-nucleon collisions**.

One has to keep in mind that the reaction dynamics depend on the various parameters which can be termed as entrance channel and technical parameters. Entrance channel parameters include projectile and target masses (and charges), bombarding energy, impact parameter, symmetry energy etc. These parameters define the whole kinematics of a single event. On the other hand, technical parameters may be Gaussian width, minimum collision distance, NEOS, rapidity distribution, and cut-off parameters etc.

Initialization

In **QMD model**, the nucleons are represented by Gaussian wave packets which interact by mutual two- and three-body forces. The model simulates the heavy ion collisions on an event by event basis and as a consequence, preserve the correlations and fluctuations. Each nucleon is represented by a coherent state of the form

$$\psi_i(r,\ p_i(t),\ r_i(t)) \ = \ \frac{1}{(2\pi L)^{3/4}} exp\left[\frac{i}{\hbar}\ p_i(t)\cdot r \ - \ \frac{(r\ -\ r_i(t))^2}{4L}\right]. \tag{2.7}$$

where r and p are the vector quantities. The parameter L is related to the extension of the wave packet in phase-space. For more details related to the L value, the reader is refered to Ref.[99]. The total N-body function is assumed to be the direct product of coherent states

(Eqn. 2.1)

$$\Phi = \prod_i \psi_i(r,\ r_i, p_i, t). \tag{2.8}$$

By doing this, one neglects the anti-symmetrization. First successful attempts to simulate the heavy ion reactions with anti-symmetrized states have been performed for smaller systems [119, 120]. As the model is semi-classical, so, in order to transit from quantum mechanical wave function to classical distribution function in phase space, the Wigner distribution function is used. The Wigner transform of the coherent states are Gaussian in momentum and coordinate space. The Wigner density reads as:

$$\begin{aligned} f_i(r,\ p, r_i(t),\ p_i(t)) &= \frac{1}{(2\pi\hbar)^3} \int e^{-\frac{i}{\hbar}p\cdot r_{12}} \psi_i(r + \frac{r_{12}}{2},\ t)\ \psi_i^*(r - \frac{r_{12}}{2},\ t) d^3r_{12} \\ &= \frac{1}{(\pi\hbar)^3} e^{-(r\ - r_i(t))^2/2L}\ e^{-(p\ - p_i(t))^2 2L/\hbar^2}, \end{aligned} \tag{2.9}$$

where $r_i(t),\ p_i(t)$ define the classical orbit or the center of the Gaussian wave packet in phase-space, whereas the squared width L is assumed to be independent of the time. The density of i^{th} particle is

$$\begin{aligned} \rho_i(r) &= \int f_i(r, p, r_i(t), p_i(t))\ d^3p \\ &= \frac{1}{(2\pi L)^{3/2}}\ e^{-[r\ -\ r_i(t)]^2/2L}. \end{aligned} \tag{2.10}$$

To build a nucleus, one has to first assign the coordinates and momenta to all the nucleons. In three dimensional space [inside a sphere of radius $R = 1.14\ A^{1/3}$, where A is the mass number of the nucleus under consideration], the centers of Gaussian wave packet r_i are uniformly distributed in polar coordinate by:

$$\begin{aligned} r &= R\ x_1^{1/3}, \\ cos\theta &= 1\ -\ 2x_2, \\ \phi &= 2\pi\ x_3, \end{aligned} \tag{2.11}$$

where $x_1,\ x_2,\ x_3$ are the random numbers. The coordinates of nucleons are rejected if the distance between them is less than 1.5 fm. The local Fermi momentum is determined by the relation

$$p_F(r_i) = \sqrt{-2mU(r_i)}, \tag{2.12}$$

where $U(r_i)$ is the local potential. The center of each Gaussian wave packet p_i are uniformly distributed in polar coordinate

$$
\begin{aligned}
p_i &= p_F(r_i)x_4^{1/3}, \\
cos\theta &= 1 - 2x_5, \\
\phi &= 2\pi x_6.
\end{aligned} \tag{2.13}
$$

where x_4, x_5 and x_6 are again random numbers. We reject those distributions where two particles are closer than some distance d_{min}. In other words, we demand

$$
(r_i - r_j)^2 \ (p_i - p_j)^2 \geq d_{min}. \tag{2.14}
$$

Typically 1 out of 50,000 initializations is accepted under the present criteria.

Numerical tests for the stability of nuclei

A large number of tests were conducted by Aichelin and co-workers to check the stability of nuclei [27, 97]. The nucleons inside a nucleus move under the influence of the mean field of their neighbours. During the motion, whenever a nucleon comes close to the surface of the nucleus, it is pulled back by other nucleons. Thus, every nucleon remains confined in a sphere as shown in Ref. [27, 104]. Due to the local density approximation used here, the light nuclei are unstable compared to heavier one. The Frankfurt group [103] showed that the inclusion of the Pauli-potential in the mean field keeps the nucleon stable for several thousand fm/c. The Nantes Group [27] checked the stability in terms of time evolution of the root mean square radius ($R_{r.m.s}$) as well as the binding energy. We have also carried out various checks by calculating the binding energy and $R_{r.m.s}$ of different nuclei as well as the propagation of the heaviest fragment. Fig. 2.1 shows the time evolution of the root mean square radii of Ca^{40} and Xe^{131} nuclei in coordinate space. The nuclei are found to be stable for a couple of hundred fm/c, which is long enough to study the reaction dynamics. Once the target and projectile are generated with proper initialization, we boost them with proper center of mass velocity. In the following, we shall first discuss the propagation and then shall discuss the nucleon-nucleon scattering/collision with Pauli-blocking effects.

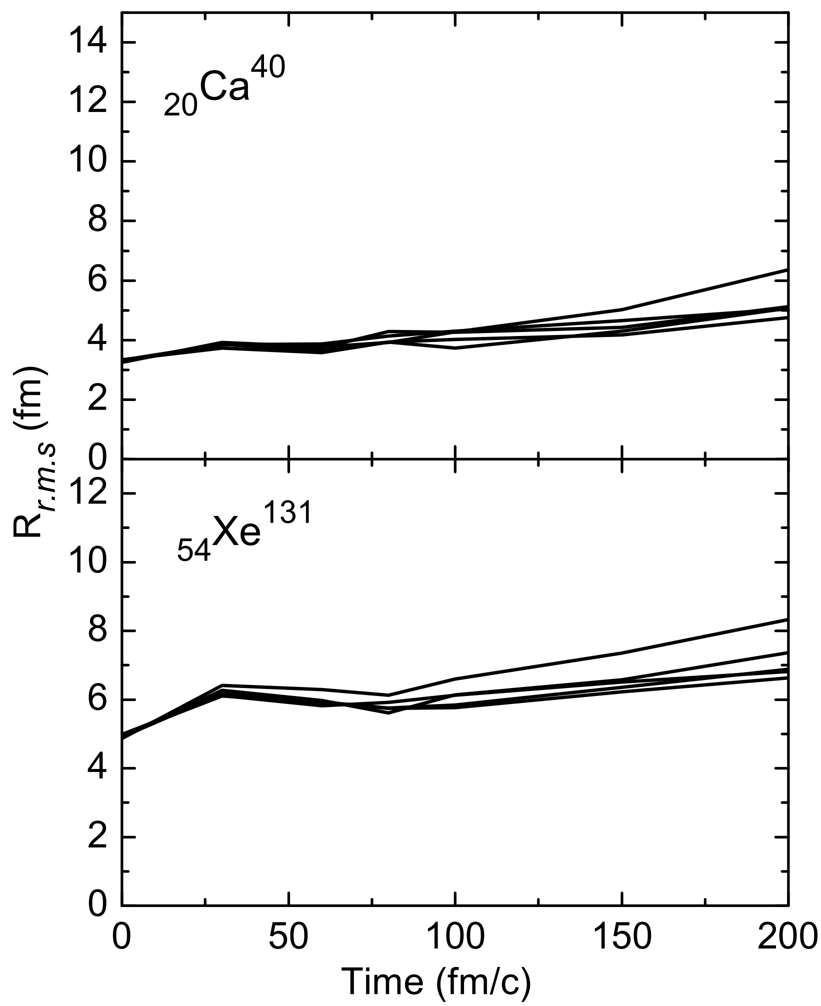

Figure 2.1: Time evolution of root mean square radii for Ca^{40} and Xe^{131} nuclei. Different lines correspond to number of events.

Propagation

The successfully initialized nuclei are then boosted towards each other with proper center of mass velocity using relativistic kinematics. The center of each distribution moves along the Coulomb trajectories. This distribution is kept fixed until the distance between surfaces of the nuclei is 2.5 fm. The equation of motion of many-body system is, then, calculated by means of a generalized variational principle. We start from the action

$$S = \int_{t_1}^{t_2} \mathcal{L}[\Phi, \Phi^*] d\tau, \tag{2.15}$$

with the Lagrange functional

$$\mathcal{L} = \langle\Phi|i\hbar\frac{d}{dt} - H|\Phi\rangle, \tag{2.16}$$

Where the total time derivative includes the derivation with respect to the parameters. The time evolution is obtained by the requirement that the action is stationary under the allowed variation of the wave function

$$\delta S = \delta \int_{t_1}^{t_2} \mathcal{L}[\Phi, \Phi^*]dt = 0. \tag{2.17}$$

The time evolution of the parameters is obtained by the requirement that the action is stationary under allowed variations of the wave function. This yields an Euler-Lagrange equation for each parameter. We obtain for each parameter λ an Euler-Lagrange equation:

$$\frac{d}{dt}\frac{\partial\mathcal{L}}{\partial\dot{\lambda}} - \frac{\partial\mathcal{L}}{\partial\lambda} = 0. \tag{2.18}$$

If the true solution of the Schrödinger equation is contained in the restricted set of wave function $\psi_i(r,\ p_i(t),\ r_i(t))$, this variation of the action gives the exact solution of the Schrödinger equation. If the parameter space is too restricted, we obtain that wave function in the restricted parameter space which comes closest to the solution of the Schrödinger equation. Note that the set of wave functions which can be covered with special parameterizations is not necessarily a subspace of Hilbert-space, thus the superposition principle does not hold.

For the coherent states and a Hamiltonian of the form $H = \sum_i T_i + \frac{1}{2}\sum_{ij} V_{ij}$ ($T_i =$ kinetic energy, $V_{ij} =$ potential energy), the Lagrangian and the variation can easily be calculated and we obtain:

$$\mathcal{L} = \sum_i \dot{r}_i p_i - \sum_{j\neq i} < V_{ij} > -\frac{3}{2Lm}, \tag{2.19}$$

$$\dot{r}_i = \frac{p_i}{m} + \nabla_{p_i}\sum_j < V_{ij} > \ = \ \nabla_{p_i} < H >, \tag{2.20}$$

$$\dot{p}_i = -\nabla_{r_i}\sum_{j\neq i} < V_{ij} >= -\nabla_{r_i} < H >, \tag{2.21}$$

with $r_i = r_i + \frac{p_i}{m}t$ and $\langle V_{ij}\rangle = \int d^3r_1 d^3p_2 \langle\psi_i^*\psi_j^*|V(r_1,r_2)|\psi_i\psi_j\rangle$.

These equations represent the time evolution and can be solved numerically. Thus, the variational principle reduces the time evolution of the n-body Schrödinger equation to the time evolution equations $6 \cdot (A_P + A_T)$. The equations of motion now show a similar structure like classical Hamiltonian equations.

$$\dot{r}_i = \frac{d\langle H \rangle}{dp_i} \quad ; \quad \dot{p}_i = -\frac{d\langle H \rangle}{dr_i}, \tag{2.22}$$

The numerical solution can be achieved in the spirit of the classical molecular dynamics [121]. The expectation value of total Hamiltonian reads as:

$$\begin{aligned} \langle H \rangle &= \langle T \rangle + \langle V \rangle \\ &= \sum_i \frac{p_i^2}{2m_i} + V_{Skyrme} + V_{Yukawa} + V_{Coulomb} + V_{MDI}. \end{aligned} \tag{2.23}$$

where V_{Skyrme}, V_{Yukawa}, $V_{Coulomb}$ and V_{MDI} are, respectively, the local (two and three body) Skyrme, Yukawa, Coulomb and momentum dependent potentials. The effect of Coulomb interactions will be discussed in chapter 3. The local Skyrme interaction is written as:

$$V_{Skyrme} = \frac{1}{2!}\sum_{j;i\neq j} V_{ij}^{(2)} + \frac{1}{3!}\sum_{j,k;i\neq j\neq k} V_{ijk}^{(3)}, \tag{2.24}$$

Here, $V_{ij}^{(2)}$ and $V_{ijk}^{(3)}$ are the two and three-body interactions. The two-body interactions $V_{ij}^{(2)}$ is obtained by folding the two-body interactions with the densities of both particles.

$$\sum_{j;i\neq j} V_{ij}^{(2)} = \sum_{j;i\neq j} \int f_i(r_i, p_i, t)\ f_j(r_j, p_j, t)\ V(r_i, r_j) \times d^3r_i\ d^3r_j\ d^3p_i\ d^3p_j, \tag{2.25}$$

$$\begin{aligned} &= \sum_{j;i\neq j} \int f_i(r_i, p_i, t)\ f_j(r_j, p_j, t)\ t_1 \\ &\quad \times \delta(r_i - r_j) d^3r_i\ d^3r_j\ d^3p_i\ d^3p_j, \\ &= \sum_{j;i\neq j} t_1 \int f_i(r_i, p_i, t)\ f_j(r_j, p_j, t) \\ &\quad \times d^3r_i\ d^3p_i\ d^3p_j, \\ &= \sum_{j;i\neq j} t_1 \int \frac{1}{(\pi\hbar)^3} e^{-(r-r_i(t))^2/2L} e^{-(p-p_i(t))^2 2L/\hbar^2} \\ &\quad \times \frac{1}{(\pi\hbar)^3} e^{-(r-r_j(t))^2/2L}\ e^{-(p-p_j(t))^2 2L/\hbar^2}\ d^3r_i\ d^3p_i\ d^3p_j, \\ &= \sum_j t_1 \frac{1}{(4\pi L)^{3/2}} e^{-(r_i - r_j)^2/4L}, \\ &= t_1 \sum_{j;i\neq j} \rho_{ij}. \end{aligned} \tag{2.26}$$

where

$$\rho_{ij} = \int d^3r\ \rho_i(r)\ \rho_j(r) = \frac{1}{(4\pi L)^{3/4}} e^{-(r_i - r_j)^2/4L}. \tag{2.27}$$

The three-body interaction can be calculated as follows

$$
\begin{aligned}
\sum_{j,k;i\neq j\neq k} V_{ijk}^{(3)} &= \sum_{j,k;i\neq j\neq k} \int f_i(r_i,p_i,t)\ f_j(r_j,p_j,t)\ f_k(r_k,p_k,t)\ V(r_i,r_j,r_k) \\
&\quad \times d^3r_i\ d^3r_j\ d^3r_k\ d^3p_i\ d^3p_j\ d^3p_k, \\
&= \sum_{j,k;i\neq j\neq k} \int f_i(r_i,p_i,t)\ f_j(r_j,p_j,t)\ f_k(r_k,p_k,t)\ t_2 \\
&\quad \times\delta(r_i-r_j)\ \delta(r_i-r_k)d^3r_i\ d^3r_j\ d^3r_k\ d^3p_i\ d^3p_j\ d^3p_k, \\
&= \frac{t_2}{(2\pi L)^3\cdot 3^{3/2}} \sum_{j,k;i\neq j\neq k} e^{-\left[(r_i-r_j)^2+(r_i-r_k)^2+(r_k-r_j)^2\right]/6L}, \\
&= \frac{t_2}{(2\pi L)^3 3^{3/2}} \sum_{j,k;i\neq j\neq k} e^{-\left[(r_i-r_j)^2+(r_i-r_k)^2\right]/6L\times\frac{3}{2}}, \\
&= \frac{t_2\ (4\pi L)^{3/2\times 2}}{(2\pi L)^3\cdot 3^{3/2}} \left[\sum_{j\neq i} \frac{1}{(4\pi L)^{3/2}} e^{-(r_i-r_j)^2/4L}\right]^2, \\
&= \frac{t_2\ 2^3}{3^{3/2}} \left[\sum_{j\neq i} \rho_{ij}\right]^2. \qquad (2.28)
\end{aligned}
$$

From above derivation, we see that the three-body term reduces to a two body term. The finite range Yukawa term (V_{Yuk}) and an effective Coulomb potential (V_{Coul}) can be read as:

$$V_{Yukawa} = t_3 \frac{exp\{-|r_i-r_j|\}/\mu}{|r_i-r_j|/\mu}. \qquad (2.29)$$

$$V_{Coulomb} = \frac{Z_{eff}^2\ e^2}{|r_i-r_j|}. \qquad (2.30)$$

The Yukawa term (with t_3= -6.66 MeV and μ=1.5 fm) has been added to improve the surface properties of the interaction which are very important for multi-fragmentation. The two body part $V_{local}^{(2)}$ is directly proportional to ($\frac{\rho}{\rho_o}$), whereas, the three-body part $V_{local}^{(3)}$ of the interaction is proportional to $(\frac{\rho}{\rho_o})^2$. In nuclear matter, the local potential energy has the form

$$V_{local} = \frac{\alpha}{2}\left(\frac{\rho}{\rho_o}\right) + \frac{\beta}{\gamma+1}\left(\frac{\rho}{\rho_o}\right)^2. \qquad (2.31)$$

The above potential has two free (α and β) parameters, which can be fixed by the requirement that at normal nuclear matter density the average binding energy should be -16 MeV/nucleon and the total energy should have a minimum at ρ_o. In order to investigate the influence of different compressibilities, one can generalize the above potential energy to

$$V_{local} = \frac{\alpha}{2}\left(\frac{\rho}{\rho_o}\right) + \frac{\beta}{\gamma+1}\left(\frac{\rho}{\rho_o}\right)^\gamma. \qquad (2.32)$$

This equation leads to the nuclear matter equation of state which connects the pressure and energy [27]. By varying the parameter γ, one can study different NEOS. In the study of heavy-ion collisions one usually uses the so-called Skyrme parameterization of NEOS, which contains two different incompressibilities K. One corresponds to soft NEOS with $K = 200$ MeV (at smaller value of γ), another corresponds to hard NEOS with $K = 380$ MeV (at larger value of γ). The density dependence of the compressional energy per nucleon is shown in Fig. 2.2 for the soft and hard interactions.

When the momentum dependence is introduced, we have to re-adjust the parameters

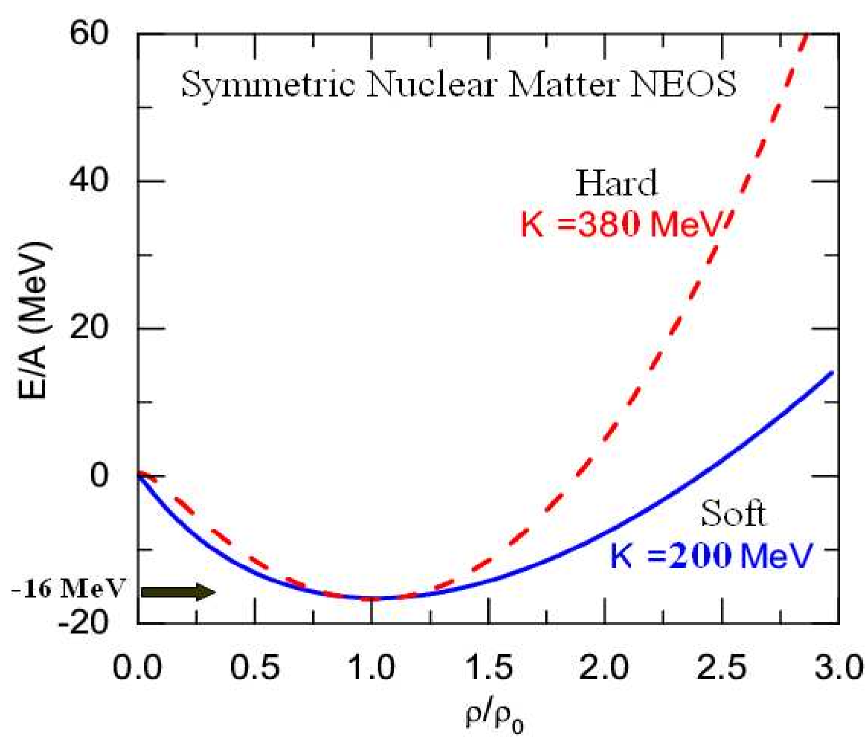

Figure 2.2: The density dependence of compression energy per nucleon. The soft and hard interactions are shown by dash and solid lines, respectively. The figure is taken from Ref. [27].

of Skyrme force to have correct saturation properties for normal nuclear matter and the same incompressibilities as those of the soft and hard NEOS. The new parameter sets with the momentum dependence are called SMD and HMD, respectively. These four sets of parameters are listed in table 2.1 together with the incompressibilities.

Table 2.1: Parameters of static and momentum dependent potentials [27]

K(MeV)	$\alpha(MeV)$	$\beta(MeV)$	γ	NEOS
200	-356	303	1.17	Soft(S)
380	-124	70.5	2	Hard(H)
200	-390	320	1.14	SMD
380	-130	59	2.09	HMD

Nucleon-Nucleon(NN) Collisions

During the propagation, two nucleons can collide if they come close to each other. The effect of N-body collision is found to be rather small, therefore, we neglect the N-body collisions [122]. The collisions in QMD are treated in the same way as in the BUU model. Two particles undergo scattering if they are closer than a distance $\sqrt{\frac{\sigma^{tot}(\sqrt{s})}{\pi}}$. This scattering is further subjected to the fulfillment of Pauli-principle. If the final state of scattered nucleons violate the Pauli-principle, the collision is neglected. Here the $\sigma^{tot}(\sqrt{s})$ represents the total NN cross section and '$\sqrt{s}$' is the center-of-mass energy. In most of the parameterizations of NN cross-section, the following processes are always there.

$$\begin{aligned}
&N+N \rightarrow \ N+N \quad (a),\\
&N+N \rightarrow \ N+\Delta \quad (b),\\
&N+N \rightarrow \ \Delta+\Delta \quad (c),\\
&N+\Delta \rightarrow \ N+N \quad (d),\\
&\Delta \rightarrow \ N+\pi\\
&N+\Delta \rightarrow \ N+\Delta \quad (e),\\
&\Delta+\Delta \rightarrow \ \Delta+\Delta \quad (f).
\end{aligned} \tag{2.33}$$

The cross-sections which are used in the QMD analysis are energy dependent cross-section (Cugnon cross-section) [123], in-medium cross-section (G-Matrix cross-section) [107], and constant cross-sections (30, 40 and 55mb) [110]. Out of these three, the G-Matrix cross-section depends on the medium in which the interaction is taking place and takes a lot of time for simulations. Also it gives values quite close to the experimental data.

Pauli-blocking

The Pauli-blocking is very important quantum feature of any dynamical model, to understand the exact reaction mechanism. Whenever a collision occurs, the phase space around the scattering partners is checked. For simplicity, we assume that each nucleon occupies a sphere in coordinate and momentum space [27]. We calculate the fractions P_1 and P_2 of final phase spaces for each of the two scattering partners that is already occupied by other nucleons. The collision is blocked with a probability

$$P_{block} = 1 - (1 - P_1)(1 - P_2), \tag{2.34}$$

and, correspondingly, is allowed with probability $1 - P_{block}$. For a nucleus in its ground state, we obtain an averaged blocking probability $< P_{block} >$ of 0.96. For absolute blocking, this factor should be one. From above description, it is clear that the Pauli factor will be zero

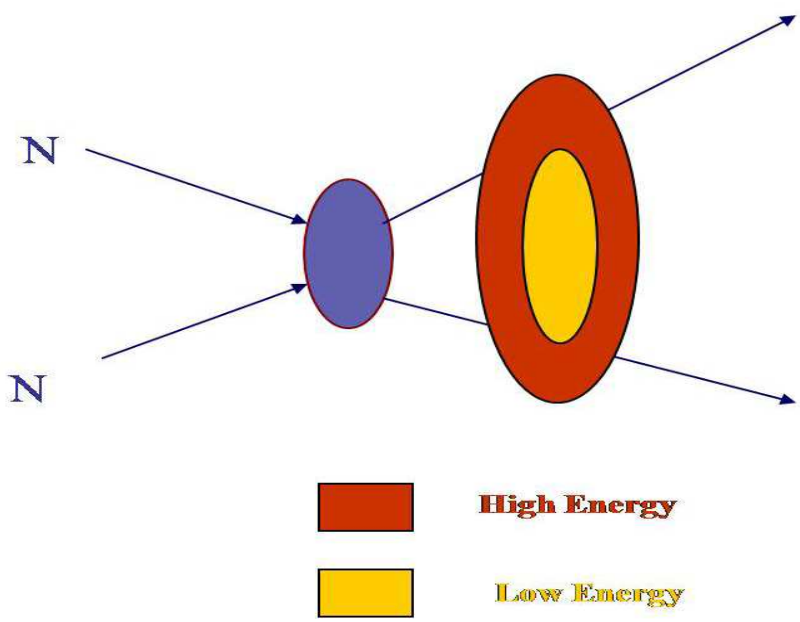

Figure 2.3: Pictorial view of Pauli-blocking at low and high incident energies.

or one depending whether the final phase-space is occupied or not. This sharp occupancy is valid for the cold nuclear matter only. The pictorial view of Pauli-blocking is shown in

Fig. 2.3, indicating the more Pauli-blocking effect at low incident energies as compared to high incident energies. On the other hand, with an increase in the bombarding energy, the velocity of particles becomes comparable to the velocity of light, therefore, the relativistic effects become very important.

As discussed earlier in Chapter 1, several refinement and improvements were made over the original QMD model. Apart from the QMD type models and its modified versions, there are other dynamical models, which can also be used for studying the heavy-ion collisions at intermediate energies. The crucial quantum features like the antisymmetrization were implemented in approaches like **FMD** [119] and **AMD** [120], which were further modified by including the stochastic incorporation of the diffusion and the deformation of wave packet [124]. Recently the improved version of AMD [125] was used to show the cluster-shell competition of these nuclei. However, the use of AMD and FMD models are restricted to light systems only. To study the fermionic nature of the N-body system, a new microscopic model, dubbed as **Constrained Molecular Dynamics (CoMD)**, was also proposed in Ref. [126]. To study hadrons and quarks, a new formalism **quark Molecular Dynamics (qMD)** was put forward by Hoffmann *et al.* [127].

2.5 Relativistic Quantum Molecular Dynamics (RQMD) model

The detailed formulation of Relativistic Quantum Molecular Dynamics (RQMD) model is given in Ref. [104, 128, 129, 130]. The RQMD model is an extension of the QMD approach successfully developed to study heavy-ion collisions upto their relativistic energies (AGS and CERN/SPS domain). Like the non-relativistic QMD, RQMD incorporates the classical propagation of the hadrons (molecular dynamics) with some quantum effects such as stochastic scattering, particle decay and Pauli blocking in collisions. The Hamiltonian for an N-particle system is expressed in terms of 8N variables (4N position coordinates $q_{i\mu}$ and 4N momentum coordinates $p_{i\mu}$). This means that here each particle carries its own energy and time. Since the physical events are described as world lines in a 6N dimensional phase-space, the extra (2N-1) degrees of freedom have to be eliminated and a global evolution parameter τ has to be defined. This can be achieved with the help of 2N constraints. In this approach, the first N constraints are chosen as Poincaré invariant mass-on shell constraints [104].

$$\xi_i = p_i^\mu p_{i\mu} - m_i^2 - \tilde{V}_i = 0 \qquad ; \qquad i = 1, ..., N. \tag{2.35}$$

This choice of Poincaré invariant constraints requires that the potential part $\tilde{V}_i$ should be a function of the Lorentz scalars only. Since in RQMD, a system with mutual two- and three-body interactions (like in QMD) has to be defined, $\tilde{V}_i$ should be given by the sum of these two-body interactions. Further, as we want to look for the relativistic effects in the dynamics, we have to generalize the non-relativistic Skyrme force in such a way that the force is covariant and reduces also to the usual Skyrme force in non-relativistic limit. This can be done as [104]

$$\tilde{V}_i = \sum_{j \neq i}^{N} \tilde{V}_{ij}(q_{Tij}^2). \tag{2.36}$$

This shows that the two-body interactions depend only on the Lorentz invariant squared transverse distance

$$q_{Tij}^2 = q_{ij}^2 - \frac{(q_{ij}^\mu p_{ij\mu})^2}{p_{ij}^2}, \tag{2.37}$$

with $q_{ij}^\mu = q_i^\mu - q_j^\mu$ being the simple four dimensional distance and $p_{ij}^\mu = p_i^\mu + p_j^\mu$ the sum of the momenta of the two interacting particles i and j.

The next set of the constraints (which fix the relative times of all particles) should be chosen in such a way that these constraints must respect the principle of causality and (N-1) of these constraints should be Poincaré invariant so that the world line invariance can also be fulfilled. Another feature which these constraints has to fulfill is the cluster separability. This means that the system can be divided into single particles or clusters as soon as their Minkowski distances are space-like. Furthermore, a global evolution parameter should also be defined. These features can be fulfilled by choosing the following set of time constraints:

$$\chi_i = \sum_{j(\neq i)} \frac{1}{q_{ij}^2/L_C} \exp(q_{ij}^2/L_C) \;\; p_{ij}^\mu q_{ij\mu} = 0 \qquad ; \qquad i = 1, ..., N-1, \tag{2.38}$$

$$\chi_{2N} = \hat{P}^\mu Q_\mu - \tau = 0. \tag{2.39}$$

with $\hat{P}^\mu = P^\mu/\sqrt{P^2}$, $P^\mu = \sum_i p_i^\mu$, $Q^\mu = \frac{1}{N}\sum_i q_i^\mu$.

These time fixations take care that the time coordinates of the interacting particles should not be much dispersed in the center-of-mass system of two particles. The Hamiltonian is a linear combination of the Poincaré invariant constraints:

$$H = \sum_{i=1}^{2N-1} \lambda_i \Psi_i, \tag{2.40}$$

with

$$\Psi_i = \begin{cases} \xi_i & ; \quad i \leq N \\ \chi_{i-N} & ; \quad N < i \leq 2N-1. \end{cases} \tag{2.41}$$

This Hamiltonian then generates the equations of motion

$$\frac{dq_i^\mu}{d\tau} = [H, q_i^\mu], \tag{2.42}$$

$$\frac{dp_i^\mu}{d\tau} = [H, p_i^\mu]. \tag{2.43}$$

Here square brackets represent the Poisson brackets. The unknown Lagrange multipliers λ_i in Eqn. 2.40 are determined by the condition that all constraints must be fulfilled for all times during the simulations. These equations of motion are used to propagate the baryon during the reaction.

The propagation and the "soft interaction" between baryons is combined with the quantum effects like stochastic scattering and the Pauli-blocking etc.. In RQMD, the collision part is treated in a covariant fashion. Therefore, all quantities which determine the collision must be Lorentz invariant. In RQMD, two baryons are allowed to collide if their distance $\sqrt{-q_{Tij}^2} \leq \sqrt{\sigma(\sqrt{s})/\pi}$, where q_{Tij}^2 is the Lorentz-invariant squared transversal distance and $\sigma(\sqrt{s})$ is the cross section depending on the available invariant mass $\sqrt{s}$.

2.6 Isospin-dependent Quantum Molecular Dynamics (IQMD) Model

The most widely used microscopic models for the description of heavy-ion collisions were based on the **Vlasov-Uehling-Uhlenbeck (VUU)** theory [94], which explicitly treats non-equilibrium and (stochastic) quantum effects in the framework of one particle quantities, as well as nuclear potential/equation of state (NEOS). However, certain fluctuations and correlations, such as the formation of fragments in heavy-ion collisions, can not be studied with a transport model based on a single particles distribution function. This was one of the motivations for the development of the Quantum Molecular Dynamics (QMD) model [27, 118].

Isospin is treated explicitly (in the so called QMD version), a symmetry potential (to achieve corrected distributions of protons and neutrons in the nucleus) and explicit Coulomb forces between the Z_P and Z_T protons are included. The **isospin-dependent quantum molecular dynamics (IQMD)** [99] model treats different charge states of nucleons, deltas and pions explicitly [101], as inherited from the VUU model [94]. The IQMD model has been used successfully for the analysis of large number of observables from low to relativistic energies [99, 131]. The isospin degree of freedom enters into the calculations via both cross-sections and mean field [94]. This model also includes three important steps:

1. First, one has to generate the nuclei. This procedure is called **initialization**.
2. In the second step, nuclei propagate under the influence of surrounding mean field. This is termed as **propagation**.
3. Finally, nucleons are bound to collide if they come too close to each other. This part is dubbed as **collisions**.

The elastic and inelastic cross-sections for proton-proton, neutron-neutron as well as proton-neutron are supposed to be affected in the presence of isospin. The details for these cross-sections will also be discussed in the last step. In the following, we shall discuss all of these parts in detail.

Initialization

In this model, baryons are represented by Gaussian-shaped density distributions

$$f_i(r,p,t) = \frac{1}{\pi^2\hbar^2}\ e^{-(r-r_i(t))^2\frac{1}{2L}}\ e^{-(p-p_i(t))^2\frac{2L}{\hbar^2}}. \tag{2.44}$$

Here Gaussian width L is regarded as a description of the interaction range of particle. The system dependence of L has been introduced in IQMD in order to obtain maximum stability of the nucleonic density profiles. For the heavier system (e.g. Au + Au), its value is chosen 8.66 fm^2, while for lighter one (i.e. Ca + Ca), the value is 4.33 fm^2.

Nucleons are initialized in a sphere with radius $R = 1.12A^{1/3}$ fm, in accordance with the liquid drop model. Each nucleon occupies a volume of h^3, so that phase space is uniformly filled. The initial momenta are randomly chosen between 0 and Fermi momentum(p_F), without any further local constraints.. The Fermi momentum p_F depends on the ground state density. For $\rho_0 = 0.17\ fm^{-3}$, it has a value of about 268 MeV/c. Moreover, the IQMD model performs a Lorentz contraction of the nucleus coordinate distribution, which becomes important at the higher energies.

Propagation

The successfully initialized nuclei are then boosted towards each other with proper center of mass velocity using relativistic kinematics. The nucleons of target and projectile interact via two and three-body Skyrme forces, a Yukawa potential and momentum dependent interactions. The isospin degree of freedom is treated explicitly by employing a symmetry potential and explicit Coulomb forces between protons of colliding target and projectile. This helps in achieving correct distribution of protons and neutrons within nucleus.
The hadrons propagate using Hamilton equations of motion:

$$\frac{dr_i}{dt} = \frac{d\langle\ H\ \rangle}{dp_i} \quad ; \quad \frac{dp_i}{dt} = -\frac{d\langle\ H\ \rangle}{dr_i}, \tag{2.45}$$

with

$$\begin{aligned} \langle\ H\ \rangle &= \langle\ T\ \rangle + \langle\ V\ \rangle \\ &= \sum_i \frac{p_i^2}{2m_i} + \sum_i \sum_{j>i} \int f_i(r,p,t) V^{ij}(\vec{r}', r) \\ &\quad \times f_j(r',p',t)\, dr\, dr'\, dp\, dp'. \end{aligned} \tag{2.46}$$

The baryon-baryon potential V^{ij}, in the above relation, reads as:

$$\begin{aligned} V^{ij}(r'-r) &= V^{ij}_{Skyrme} + V^{ij}_{Yukawa} + V^{ij}_{Coulomb} + V^{ij}_{MDI} + V^{ij}_{Sym} \\ &= \left(t_1\delta(r'-r) + t_2\delta(r'-r)\rho^{\gamma-1}\left(\frac{r'+r}{2}\right)\right) \\ &\quad + t_3\frac{exp(|r'-r|/\mu)}{(|r'-r|/\mu)} + \frac{Z_iZ_je^2}{|r'-r|} \\ &\quad + t_4\ln^2[t_5(p_i'-p)^2+1]\delta(r'-r) \\ &\quad + t_6\frac{1}{\varrho_0}T_3^iT_3^j\delta(r_i'-r_j). \end{aligned} \tag{2.47}$$

Here Z_i and Z_j denote the charges of i^{th} and j^{th} baryon, and T_3^i, T_3^j are their respective T_3 components (i.e. 1/2 for protons and -1/2 for neutrons). The finite range Yukawa potential with t_3 = -6.7 MeV is important to stabilize the surface of a finite nucleus. Meson potential consists of Coulomb interaction only. The parameters μ and $t_1, ..., t_6$ are adjusted to the real part of the nucleonic optical potential. Other baryonic potentials like V_{Skyrme}^{ij} and V_{MDI} are isospin-independent. For the density dependence of nucleon optical potential, standard Skyrme-type parameterization is employed as displayed in Eqn. 2.32.
Two different NEOS have been implemented (as discussed in QMD also): A hard NEOS with a compressibility of 380 MeV and a soft NEOS with a compressibility of 200 MeV [27]. The Yukawa potential in IQMD V_{Yukawa}^{ij} is very short ranged (μ = 0.4 fm in contrast to μ = 1.5 fm in QMD) and weak. Yukawa forces also stabilize the nuclei because of the increase of the interaction range as compared to a δ-like Skyrme potentials. This results in the reduction of fluctuations.

Nucleon-Nucleon (NN) Collisions

The binary nucleon-nucleon collisions are included by employing the collision term of well known VUU-BUU equation [94]. The binary collisions are done stochastically, in a similar way as are done in all CASCADE models [132]. During the propagation, two nucleons are supposed to suffer a binary collision if the distance between their centroids

$$|r_i - r_j| \leq \sqrt{\frac{\sigma_{tot}}{\pi}}, \sigma_{tot} = \sigma(\sqrt{s}, type), \tag{2.48}$$

"type" denotes the ingoing collision partners (N-N, N-Δ, N-π,..). In addition, Pauli blocking (of the final state) of baryons is taken into account by checking the phase space densities in the final states. The final phase space fractions P_1 and P_2 which are already occupied by other nucleons are determined for each of the scattering baryons. The collision is then blocked with probability

$$P_{block} \ = \ 1 - (1 - P_1)(1 - P_2). \tag{2.49}$$

Furthermore, parametrized free *pn* and *pp* cross-sections are used instead of an averaged nucleon-nucleon cross-sections. The respective strength of different cross-sections in shown in Fig. 2.4. The total cross-section is the sum of the elastic and all inelastic cross-sections.

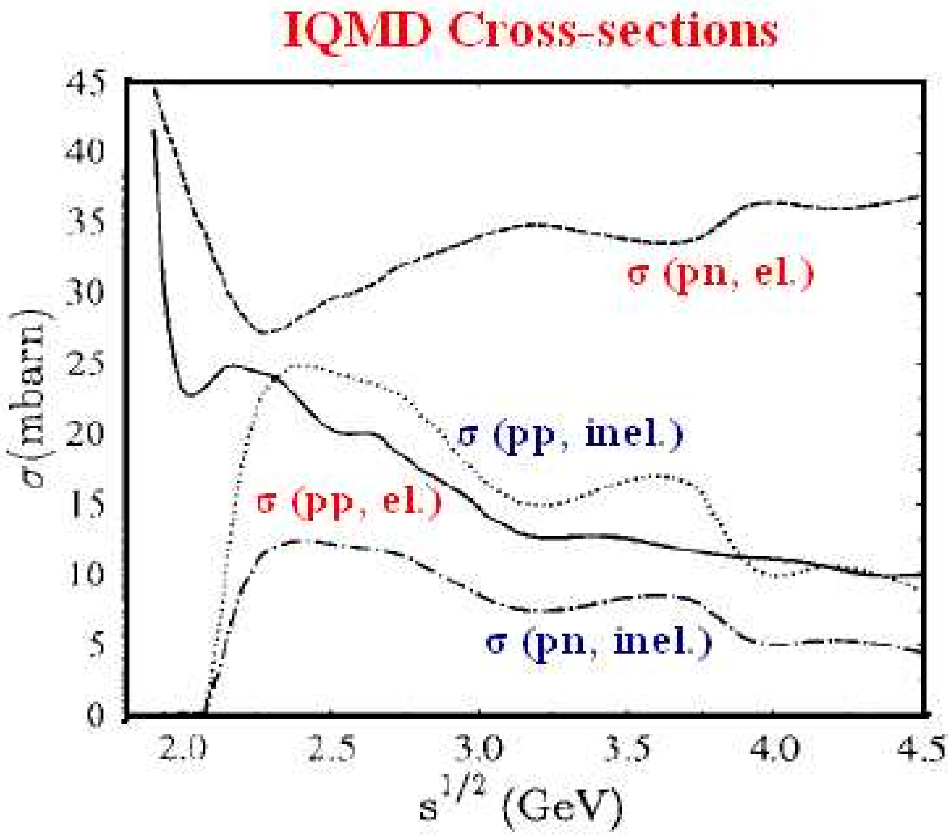

Figure 2.4: The elastic and inelastic cross-sections for proton-proton (pp) and proton-neutron (nn) used in IQMD. The neutron-neutron (nn) cross-section is assumed to be equal to pp. The total cross-section is equal to sum of elastic and inelastic cross-section. This figure is taken from Ref. [99].

$$\sigma_{tot} \;=\; \sigma el \;+\; \sigma_{inel} \;=\; \sigma_{el} \;+\; \Sigma_{channels}\sigma_i \tag{2.50}$$

The following inelastic reactions might influence the dynamics of the collision and are explicitly taken into account:

$$\begin{aligned}
&N + N \rightarrow\; \Delta + N \;(hard - delta\ production) && (a),\\
&\Delta \rightarrow\; N + \pi \;(delta\ decay) && (b),\\
&\Delta + N \rightarrow\; N + N \;(delta\ absorption) && (c),\\
&N + \pi \rightarrow\; \Delta \;(soft - delta\ production) && (d).
\end{aligned} \tag{2.51}$$

Table 2.2: a(s) and b(s) as a function of the c.m. energy

$x = \sqrt{s}$ (GeV)	a (fm)	b
2.104 - 2.12	$294.6(x-2.014)^{2.578}$	$19.71(x-2.014)^{1.551}$
2.12 - 2.43	$\frac{0.01224}{(x-2.225)^2 + 0.004112}$	$19.71(x-2.014)^{1.551}$
2.43 - 4.50	$\left(\frac{2.343}{x}\right)^{43.17}$	$33.14\ arctan(0.5404(x-2.146)^{0.9784})$

Experimental cross-sections are used for processes (a) and (d) [133], as well as for the elastic NN collisions. Inaccessible reactions like ΔN→ NN are calculated from their reverse reactions(here $NN \rightarrow \Delta N$) using modified detailed balance formula [134]. The conventional detailed balance formula is only correct for particles with infinite lifetimes (zero width). The elastic nucleon-nucleon scattering angular distribution is taken to be [123]

$$\frac{d\sigma_{el}}{d\Omega} \approx exp\left[A(s)t\right], \tag{2.52}$$

where t is $-q^2$, the transverse momentum transfer and

$$A(s) = 6\frac{\left[3.65\left(\sqrt{s}-1.8766\right)\right]^6}{1+\left[3.65\left(\sqrt{s}-1.8766\right)\right]^6}. \tag{2.53}$$

$\sqrt{s}$ is the c.m energy in GeV and A is given in $(GeV/c)^{-2}$.

The isospin degree of freedom play an important role especially for the particle production. The employed inelastic channels $NN \rightarrow NN^*,\ N\Delta\ and\ \Delta\Delta$ are treated in an analogous fashion. The parameterization suggested by Huber and Aichelin [135] is used: fitted differential cross-sections are extracted from one-boson- exchange (OBE) calculations:

$$\frac{d\sigma_{in}}{d\Omega} \approx a(s)exp\left[b(s)cos\theta\right]. \tag{2.54}$$

The $a(s)$ and $b(s)$ are functions of $\sqrt{s}$ and vary in their definition for different intervals of $\sqrt{s}$ (see table 2.2). θ is the polar angle.

These isospin effects in the IQMD are found to vary the results, one obtained with QMD model.

2.7 Secondary models: methods of clusterization

The **Minimum Spanning Tree (MST)** method is the most extensively used to clusterize the nucleons [27, 29, 109]. In **MST** method, two nucleons share the same fragment if their centroids are closer than a certain distance. The method is discussed in detail in chapter 3. An improvement over the **MST** algorithm, is to put additional cut in momentum space [64]. This method is dubbed as **MSTM**. It will help to get rid of fragments that although close in spatial space are far in momentum space. As mentioned in the above clusterization methods, it is fairly straightforward to determine the cluster structure of a system, i.e. the particle number and velocity of each product. In practice, however, the additional running time required to reach this stage limits the practical utility of the model. It has been, therefore, of interest to devise methods for recognizing the clusters as early as possible. It is worth mentioning that it may also help to elucidate the mechanism of fragment production. A novel algorithm, namely, **Simulated Annealing Clusterization Algorithm (SACA)**, developed by Puri *et al.* [111] was based on the fact that at any given moment of the reaction, the configuration corresponding to largest binding energy is realized in nature.

In summary, we discussed the details of various models in this chapter. In the following chapters, we shall present the detailed analysis of multi-fragmentation using MST method. Apart from this, effect of mass asymmetry, within **IQMD** model, on the directed transverse flow, elliptical flow, and nuclear stopping will be discussed. Our results are also compared with the experimental data of INDRA@(GSI+GANIL), FOPI, MSU, Plastic ball collaborations.

Chapter 3

Systematic study of multi-fragmentation in asymmetric collisions

3.1 Introduction

The shattering/fragmentation of colliding nuclei into several pieces of different sizes is a complex phenomena. It appears as an intermediate mechanism bringing the low energy decay modes dominated by evaporation (fission, for heavier systems) and the high energy decay modes characterized by the complete vaporization of the system. The ability to understand the properties of nuclear matter at the extreme conditions of temperature and density is one of the challenges in present-day nuclear-physics research. Such extreme conditions can be generated in a heavy-ion-induced reaction at intermediate incident energies [27, 97, 136]. The outcome of a reaction depends on the incident energy, the impact parameter, as well as on the mass asymmetry of the colliding partners [19, 20, 47, 64, 136, 137]. For symmetric heavy colliding nuclei at central impact parameters, two primary fragments are formed: one that is the projectile-like fragment and the other that is the target-like fragment. These excited fragments deexcite through various exit channels: evaporation of light particles and emission of intermediate- mass fragments (IMF's) [47, 64, 136, 137]. The excitation energy deposited in the system at low incident energies is too small to allow the break up of the nuclei into fragments. With an increase in the incident energy, colliding nuclei may break into dozens of fragments consisting of light, medium, and heavy fragments. The size of the fragments and physics behind their formation differs in different physical conditions. No such fragments will survive at extremely high incident energies.

There has been considerable progress during recent years in the experimental studies of multi-fragmentation. Experimental evidence for the statistical property of nuclear fragmentation has been verified and various new quantities have been measured [47]. These quantities include the mean multiplicity of intermediate mass fragments $< N_{IMF} >$ $(5 \leq A \leq A_{tot}/6)$, the average charge of the largest fragment (Z_{max}), the sum of all charges with $Z \geq 2$, directed transverse flow associated with the particles etc. The quantity which is intimately related to the multi-fragmentation process is the multiplicity of intermediate mass fragments. The correlations between the mean multiplicity of IMF's, $< N_{IMF} >$, and the mass of the fragmenting system, whose measure is so called bound-charge Z_{bound} is an important aspect of multi-fragmentation that has been studied thoroughly by a number of groups [47, 138]. In a recent communication [139], Liu studied the isospin effects on the process of multi-fragmentation and dissipation by considering the two pairs of colliding systems $Zn^{76} + Ar^{40}$ and $Kr^{76} + Ca^{40}$, $Cd^{120} + Ar^{40}$ and $Xe^{120} + Ca^{40}$ for central collisions. In recent years, it has become possible to carry out exclusive measurements of multi-fragmentation process. This has been done with streamer chamber detectors, electronic detectors, and 4π detectors. The ALADIN [47, 138] group has reported that the mean multiplicity of IMF's $< N_{IMF} >$ remains same for all targets ranging from Beryllium to Lead at incident energies between 400 and 1000 MeV/nucl. De Souza *et al.*, [37] observed a linear increase in the multi-fragmentation of IMF's for central collisions with incident energies upto 110 MeV/nucl. In 1993, Tsang *et al.*, [140] reported a rise and fall in the production of IMF's. The maximal value of the IMF's shifts from nearly central to peripheral collisions as one goes for higher incident energies. A careful analysis of experimental efforts reveals that either one has studied the collision of symmetric nuclei (e.g., $_{79}Au^{197} +_{79} Au^{197}$) [47] or that one has studied asymmetric colliding nuclei (e.g., $_{20}Ar^{40} +_{21} Sc^{45}$, $_{20}Ar^{40} +_{79} Au^{197}$ $_{6}C^{12} +_{79} Au^{197}$, $_{20}Ca^{40} +_{79} Au^{197}$) [47].

Although the dynamics for symmetrically heavy nuclei is prominently exposed in experimental and theoretical studies, little attention is paid to the collision of asymmetric nuclei. We, at the same time, know that the symmetry and the isospin play decisive roles in a reaction. We want to discover the fragmentation of asymmetrically colliding pairs in the following different ways. (i) In the first case, we will perform a systematic study of the emission of various fragments as a function of the mass asymmetry η of a reaction. The mass asymmetry of a reaction can be defined by the asymmetry parameter $\eta = (A_T - A_P)/(A_T + A_P)$ [141, 142]; A_T and A_P are, respectively, the masses of the target and the projectile. The $\eta = 0$ corresponds to the symmetric reaction, whereas nonzero values of η define different mass asymmetries of the reaction. It is worth mentioning that the outcome and the physical mechanism behind the symmetric and asymmetric reactions are entirely different. This is due to the deposition of the excitation energy in the form of compressional energy and thermal energy in symmetric and asymmetric reactions, respectively. Here, for the systematic analysis, we start from the symmetrically colliding partners ($\eta = 0$), and then, mass asymmetry parameter η is varied gradually (η = -0.8 to 0.8) by keeping the total mass of the system fixed to demonstrate that mass asymmetry parameter plays an important role for the understanding of multi-fragmentation. Such an experiment was performed by Betts [143] in 1981, where fusion probabilities were measured for different colliding pairs, which lead to the same compound nucleus. (ii) In the second case, the projectile mass is varied from 16 to 56 units, while the total mass of the system is kept fixed. The targets are chosen to be the stable isotopes.

In the following section, we shall start with the phase-space simulations of projectile and target nucleons and hence participants and spectators and then shall present our detailed analysis of the effect of mass asymmetry on multi-fragmentation and directed transverse flow.

In the present study, isospin-dependent quantum molecular (IQMD) model is used to generate the phase space of nucleons and clusterization is done with minimum spanning tree (MST) method. Here, we shall discuss MST Method before coming to the results.

3.2 Method of analysis

3.2.1 Minimum Spanning Tree (MST) method

The *MST* method is the most extensively used to clusterize the nucleons [27, 109, 144, 145]. In *MST* method, two nucleons share the same fragment if their centroids are closer than a

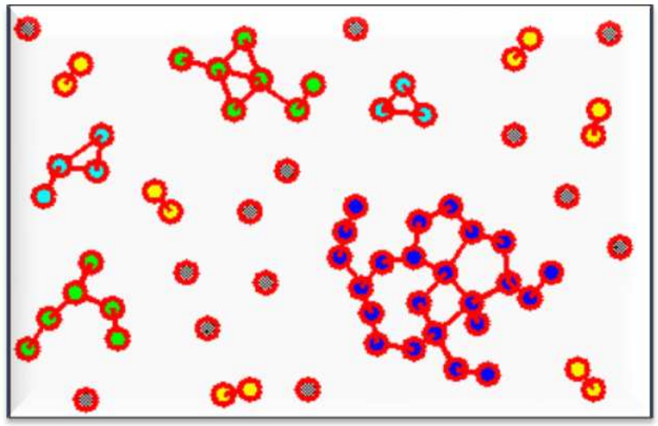

Figure 3.1: This figure is representing the fragments production with MST method where the distance between the nucleons is $\leq d_{min}$, here, $d_{min} = 4$ fm.

distance d_{min},

$$|\vec{r_i} - \vec{r_j}| \ \leq \ d_{min} \tag{3.1}$$

where $\vec{r_i}$ and $\vec{r_j}$ are the spatial positions of both nucleons. The value of d_{min} can vary between 2-4 fm. As reported, it has small effect on multi-fragmentation [145]. However, this method cannot address the question of time scale as it will give a big fragment during the early stage of the reaction where the density is quite high and the interactions among the nucleons are still active. It is worth mentioning that this method can only be used to analyze asymptotic configurations in which the fragmenting system can be viewed as a very dilute mixture of free particles and almost equilibrated fragments. To study the time of fragment formation, one needs to device a method which should be able to detect the overlapping fragments.

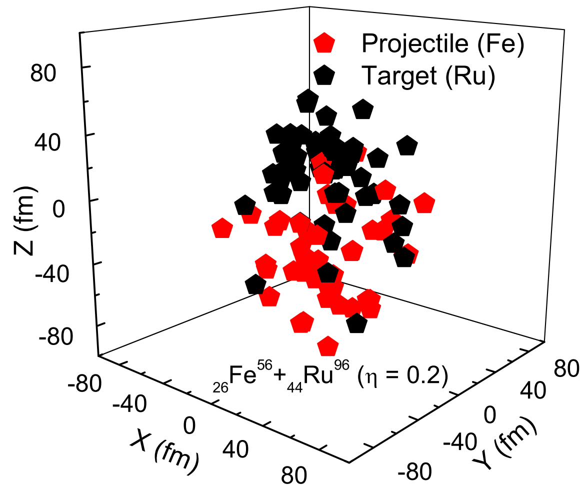

Figure 3.2: The 3-D phase space distribution of the projectile and target nucleons for the reaction of $_{26}Fe^{56} +_{44} Ru^{96}$ having η = 0.2 at incident energy E = 200 MeV/nucl. for semi-central geometry. The red (black) colour represent projectile (target) nucleons.

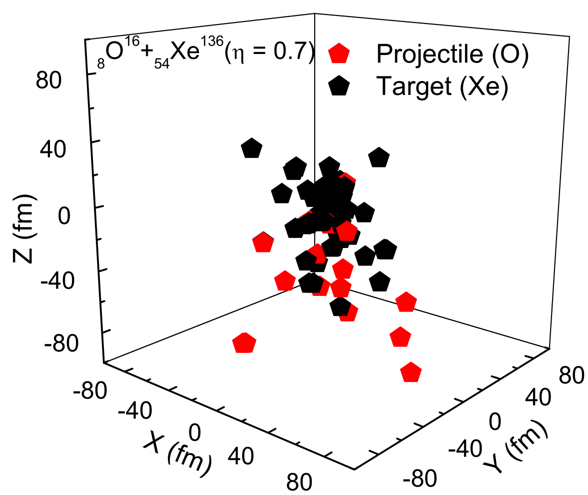

Figure 3.3: Same as Fig. 3.2 but for $_{8}O^{16} +_{54} Xe^{136}$ reaction having $\eta = 0.7$.

3.3 Snap-shots of Phase-Space

3.3.1 Analysis of projectile and target nucleons

We start by examining how the projectile and target interact in different asymmetric reactions. In Figs. 3.2 and 3.3, we display the three-dimensional (3-D) coordinate phase space (XYZ) of the nucleons of projectile and target for the reactions of $_{26}Fe^{56} +_{44} Ru^{96}$ having least mass asymmetry η= 0.2 and $_{8}O^{16} +_{54} Xe^{136}$ having highest mass asymmetry η= 0.7 respectively. After overlapping, repulsion is observed in the projectile as well as target nucleons. While the projectile nucleons travel through the target, they experience strong transverse forces due to strong density gradient at the surface of the projectile [27]. Therefore, these nucleons pick up transverse velocity and are deflected at finite angles. We note that the nearly symmetric collisions having η= 0.2 lead to a spherical distribution, whereas the asymmetric collisions having η= 0.7 lead to non-spherical distribution. This is due to the reason that number of nucleons in projectile and target are different in both cases although total number of nucleons are same. Therefore the contribution of the participant and spectator matter will also be different and hence the contribution of mean-field and NN collisions will get change. In the following, we shall calculate the number of projectile and target nucleons in participant and spectator matter.

3.3.2 Analysis of participant and spectator matter

The participant-spectator matter demonstration is based on the definition reported in Ref. [65]. Here, participant-spectator matter is defined in two different ways. (1) In the first definition, all the nucleons experiencing at least one collision are labelled as participant matter. The remaining nucleons are the part of spectator matter. (2) The second definition is based on the experimental method, where one uses different rapidity cuts to define the participant and spectator matter. The rapidity of i^{th} particle is defined as:

$$Y(i) = \frac{1}{2} ln \frac{E(i) + P_z(i)}{E(i) - P_z(i)}, \tag{3.2}$$

where E(i) and $P_z(i)$ are, respectively, the total energy and longitudinal momentum of the i^{th} particle. One can impose different rapidity cuts to study the different participant-spectator matter. However, both these definitions have been reported to give the same results [65].

In Figs. 3.4 and 3.5, we display the phase space of projectile and target nucleons for X-Z plane for the reaction of $_{26}Fe^{56} +_{44} Ru^{96}$ (η= 0.2) and $_{8}O^{16} +_{54} Xe^{136}$ (η= 0.7) respectively at semi-central geometry. The panels from the top to bottom are representing the position of nucleons of projectile and target at different times, while left and right panels are for participant and spectator matter, respectively. Here, we have also calculated the number of projectile and target nucleons contributing as participants and spectators. As we know, during the initial stages of the reaction, whole of the matter is in the form of spectator matter only. As the nuclei overlap, the density increases, that leads to more and more nucleon-nucleon binary collisions. This changes the matter from spectator to participants. With the evolution of the reaction, participant matter increases, leading to only a few spectator nucleons.

In case of $_{26}Fe^{56} +_{44} Ru^{96}$ (nearly symmetric) reaction, the spectator parts will come from both projectile and target, whereas in case of $_{8}O^{16}+_{54}Xe^{136}$ (highly asymmetric) reaction, no spectator part will come from projectile i.e. only target will contribute to the spectators. In the proceeding section, we shall study how these different contributions effect the phenomena of fragmentation if we vary the mass asymmetry systematically from 0.2 to 0.7 by the difference of 0.1.

3.4 Results and Discussions

Here 1000 events involving the asymmetric reactions of $_{26}Fe^{56} +_{44} Ru^{96}$ ($\eta = 0.2$), $_{24}Cr^{50} +_{44} Ru^{102}$ ($\eta = 0.3$), $_{20}Ca^{40} +_{50} Sn^{112}$ ($\eta = 0.4$), $_{16}S^{32} +_{50} Sn^{120}$ ($\eta = 0.5$), $_{14}Si^{28} +_{54} Xe^{124}$ ($\eta = 0.6$), $_{8}O^{16} +_{54} Xe^{136}$ ($\eta = 0.7$) at different center-of -mass energies between 50 and 600 MeV/nucl. for scaled impact parameter $\hat{b} = 0.3$ (semi-central collisions) have been simulated. Scaled impact parameter is defined as $\hat{b} = \frac{b}{b_{max}}$, (where b is particular impact parameter in Fermi (fm) and $b_{max} = 1.12({A_T}^{1/3} + {A_P}^{1/3})$). Since b_{max} is different for different systems, hence the value of impact parameter (b) will obviously be different. The mass asymmetry of the reaction is varied by changing the projectile masses between 16 and 56 units. For the present analysis, soft (S) as well as hard (H) nuclear equations of state (NEOS) with compressibility K = 200 MeV and K = 380 MeV respectively are used. By using the asymmetric (colliding) nuclei, the effect of mass asymmetry can be analyzed without

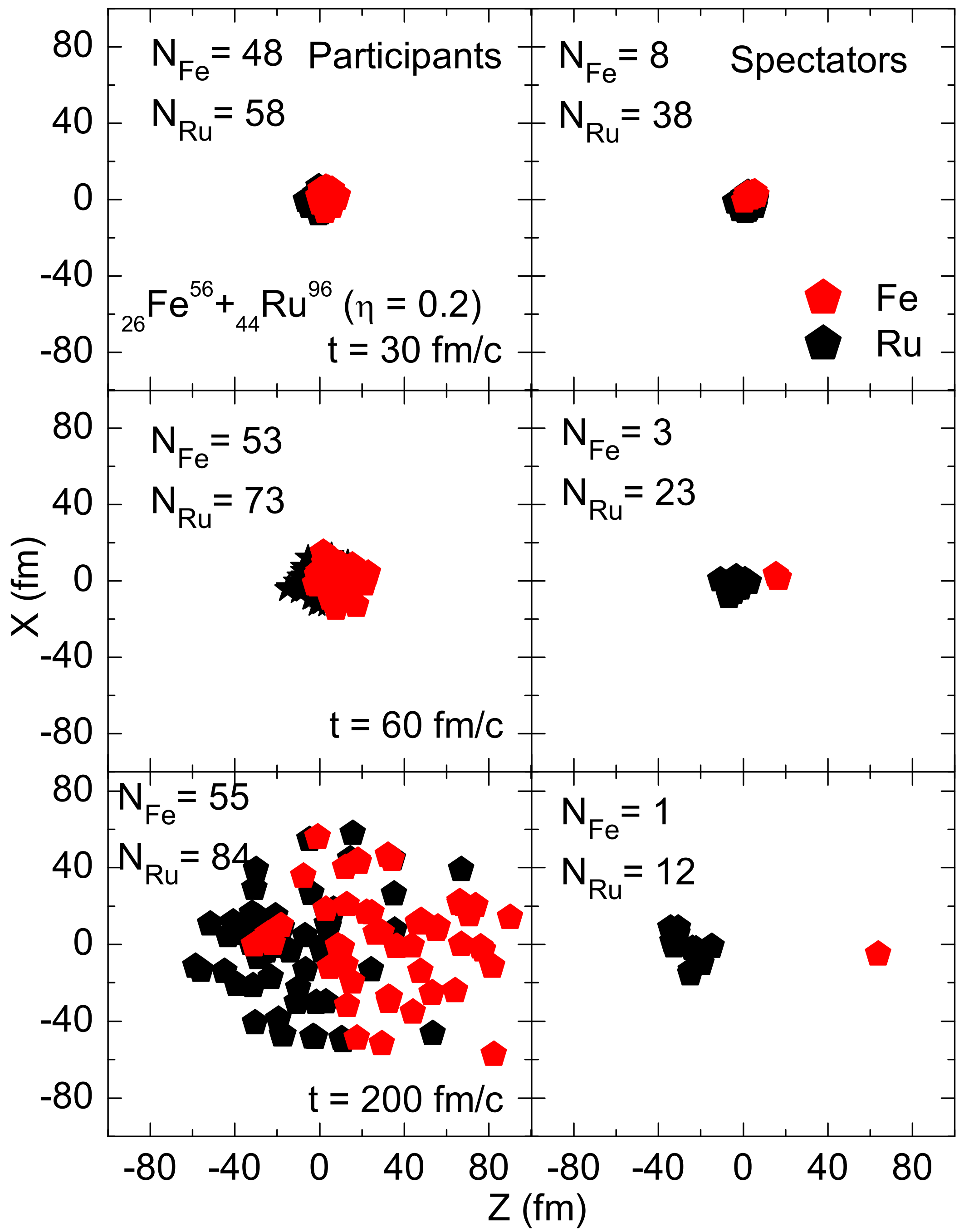

Figure 3.4: The time evolution of a single event of $_{26}Fe^{56} +_{44} Ru^{96}$ reaction having $\eta = 0.2$ at incident energy 200 MeV/nucl. for semi-central geometry in coordinate space. The red (black) colour represent projectile (target) nucleons. The left side is for participants, whereas the spectators are displayed on right side.

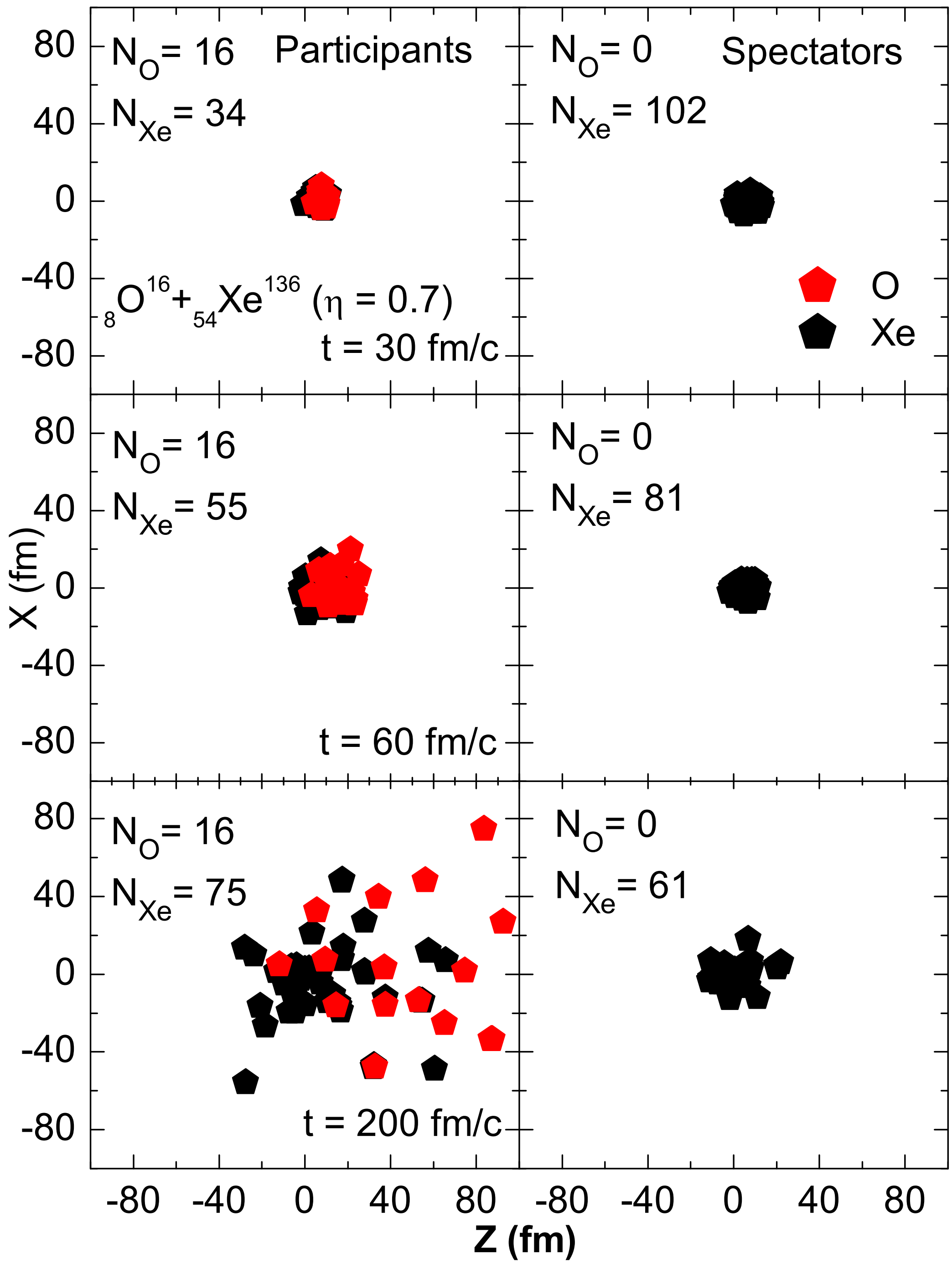

Figure 3.5: Same as Fig. 3.4, but for the reaction of $_8O^{16} +_{54} Xe^{136}$ having $\eta = 0.7$

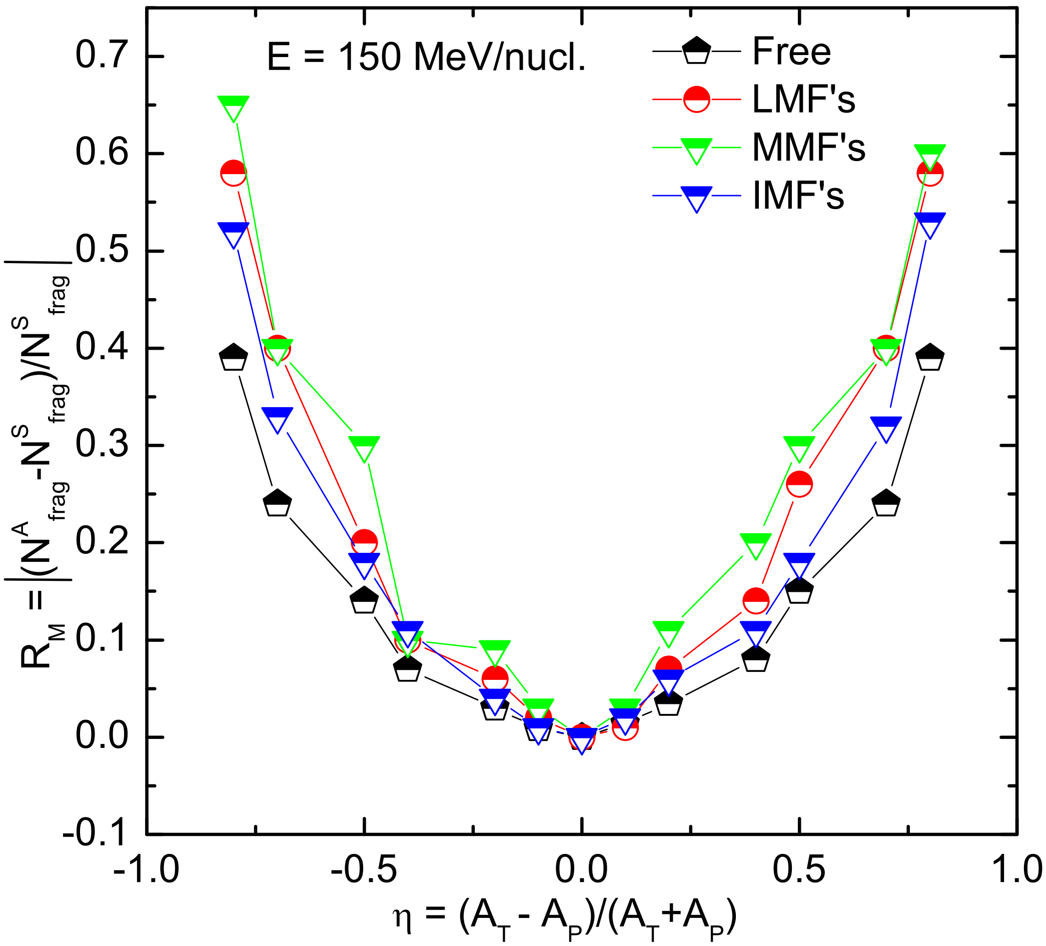

Figure 3.6: The relative multiplicity of different fragments as a function of mass asymmetry η at E = 150 MeV/nucl. and scaled impact parameter $\hat{b} = 0.3$.

varying the total mass of the system. It is worth mentioning that the experimental studies by the Michigan State University, Miniball and ALADIN [146] groups varied the mass asymmetry of the reaction, whereas the plastic ball and FOPI experiments [61, 62, 147] are performed only for symmetric reactions. In the following, we shall address the question of effect of mass asymmetry on multi-fragmentation.

3.4.1 Effect of mass asymmetry on relative multiplicity of fragments

We start from the symmetrically colliding partners ($\eta = 0$), and then, mass asymmetry parameter η (as defined in section 3.1) is varied gradually (η = -0.8 to 0.8) by keeping the total mass of the system fixed. The effect of mass asymmetry on fragmentation at an incident beam energy E = 150 MeV/nucl. and at $\hat{b} = 0.3$ is demonstrated in Fig. 3.6. Here, relative multiplicity R_N is defined as $= \mid \frac{(N^A_{frag} - N^S_{frag}}{N^S_{frag}} \mid$ where N^A_{frag} and N^S_{frag} are the multiplicities of various fragments obtained in the asymmetric and symmetric colliding nuclei, respectively. The relative multiplicity of free nucleons (A = 1), light mass fragments (LMF's) ($2 \leq A \leq 4$), medium mass fragments (MMF's) ($3 \leq A \leq 8$), and intermediate mass fragments (IMF's) ($5 \leq A \leq A_{tot}/6$) follows hyperbolic behavior. Here, the total mass is kept fixed at 140 units, and the mass of the target and the projectile is varied in steps of 10 units (e.g., $A_P = 130,\ A_T = 10,\ A_P = 120,\ A_T = 20$ etc). As mass asymmetry η shifts toward the positive side, the target fragmentation takes place since $A_T >> A_P$. In contrast, at η = -0.8, the projectile fragmentation takes place since $A_P >> A_T$. While going from η = -0.8 to η = 0.8, a zero effect can be seen in the relative multiplicity of various fragments. Since the emission of the nucleons (protons and neutrons) is maximum in the participant zone, one sees lesser nucleon emission compared to the emission of lighter fragments such as LMF's and MMF's. In this study, all reactions are performed in the laboratory frame. Note that the mirror reactions are also studied by the FOPI collaboration [148]. In the following section, effect of Coulomb interactions on the multiplicity of various fragments has been displayed by taking mass asymmetry into account.

3.4.2 Effect of Coulomb interactions on the multiplicity of fragments

To see the effect of the Coulomb interactions, in Fig. 3.7, we display the final phase space of a single event of $_{26}Fe^{56} +_{44} Ru^{96}$ (η= 0.2) (upper panel) and $_{14}Si^{28} +_{54} Xe^{124}$ (η=0.6) (lower panel) at a fixed center-of-mass energy of 250 MeV/nucl. with and without the Coulomb interaction. Here, the phase space of LMF's [($2 \leq A \leq 4$)], and IMF's [($5 \leq A \leq A_{tot}/6$)] is displayed. Irrespective of the Coulomb interaction, the reaction with η = 0.2 leads to

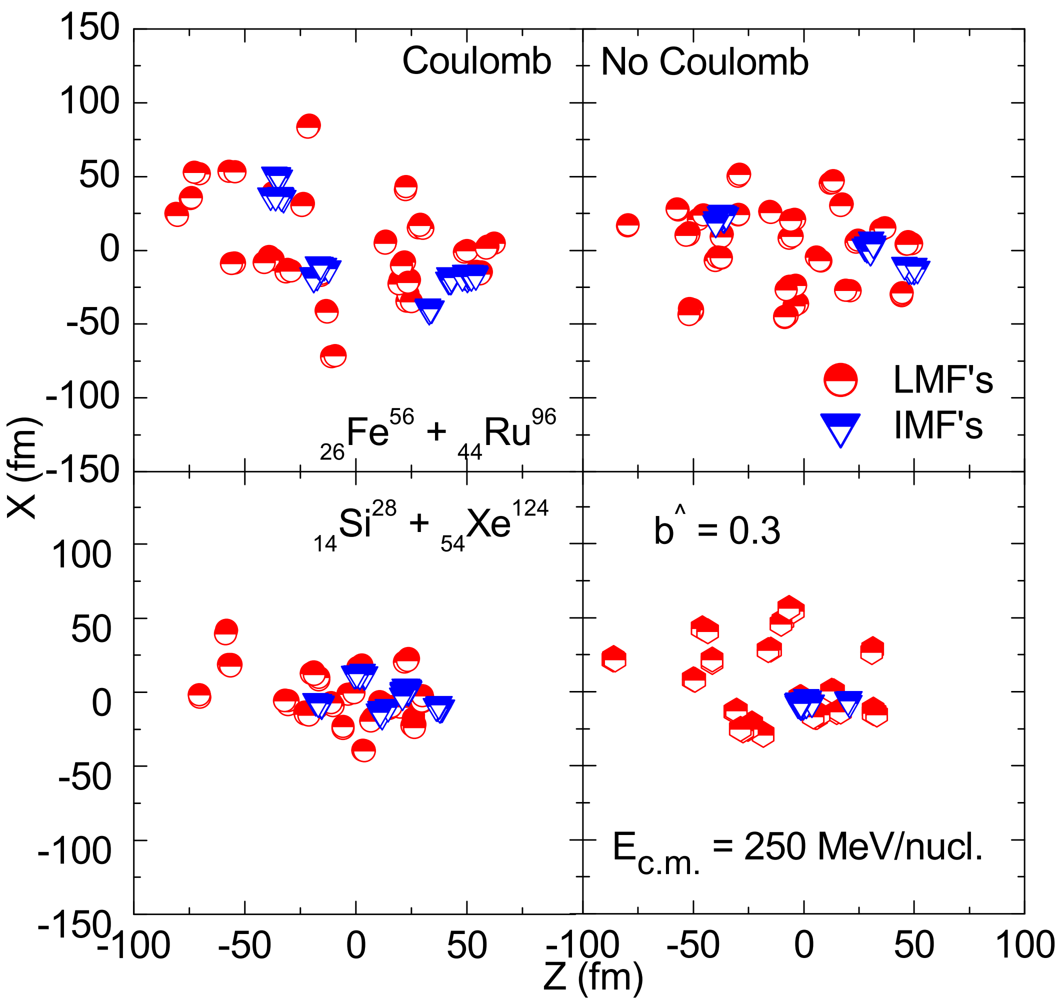

Figure 3.7: The final-state phase space of a single event for the reaction of $_{26}Fe^{56} +_{44} Ru^{96}$ with and without the Coulomb effects. Here, center-of-mass energy is $E_{c.m.} = 250$ MeV/nucl. and scaled impact parameter is $\hat{b} = 0.3$. Different symbols denote LMF's and IMF's.

isotropic emission compared to the reaction with η = 0.6 that projects a nearly binary character. Since LMF's originate from the mid-rapidity region, they are better suited for studying the effect of mass asymmetry on the reaction dynamics.

In Fig. 3.8, we compare the effect of the Coulomb forces on the multiplicities of various fragments at $E_{c.m.}$= 50 MeV/nucl. and $E_{c.m.}$= 250 MeV/nucl. For this we choose the reacting partners in such a way that mass asymmetry η varies between 0.2 and 0.7. One can see a clear effect of Coulomb forces. As expected, it is maximum for the low incident energies, and this effect diminishes as one move toward higher incident energies. An enhanced effect emerges for larger asymmetric reactions. The production of the heaviest fragment A^{max}, the free nucleons (A = 1), the LMF's ($2 \leq A \leq 4$), and the IMF's ($5 \leq A \leq A_{tot}/6$) shows expected behavior. The heavier mass continues to grow, and it is close to the mass of the reacting partners for larger mass asymmetries. In contrast, the production of free nucleons, LMF's, and IMF's shows a reverse trend with the mass asymmetry of the reaction. This happens because of decrease in the participant zone. Although, the role of Coulomb interaction decreases with energy, its effect, however, remains constant (20%) with the mass asymmetry of the reaction. Because of the presence of the Coulomb forces, the nuclear matter breaks into smaller pieces/free nucleons.

Generally, obvious effects associated with the mass asymmetry of a reaction are caused by the Coulomb interaction. To understand the role of mass asymmetry beyond the Coulomb effects, we switch off the Coulomb force in further analysis. We keep the center-of-mass energy fixed throughout the analysis.

3.4.3 Time evolution of various fragments

In Fig. 3.9, we display the time evolution of different fragments in the above cited reactions at $E_{c.m.}$= 250 MeV/nucl. using soft NEOS. We display the largest fragment A^{max}, the free nucleons (A = 1), the LMF's (($2 \leq A \leq 4$)), and the MMF's (($3 \leq A \leq 8$). It has been discussed by many authors [109, 32] that A^{max} has a peak around 50-100 fm/c. With the passage of time, A^{max} decreases followed by the increase in the multiplicity of free nucleons and fragments. Studying carefully the heavier fragment, we notice that the heaviest fragment is formed with larger mass asymmetry. On the other hand, free nucleons continue

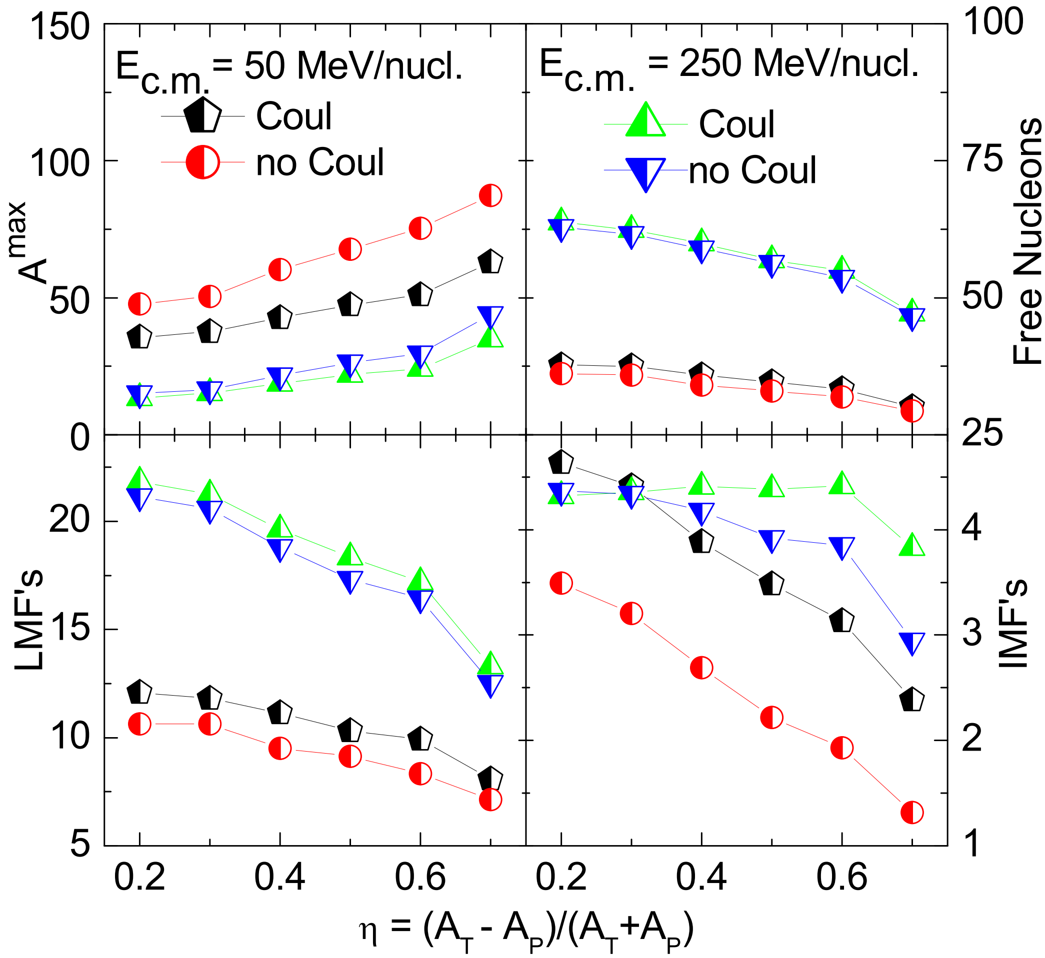

Figure 3.8: The variation of the production of A^{max}, free nucleons, LMF's and IMF's with and without the Coulomb effect at two different energies of $E_{c.m.}$ = 50 MeV/nucl. (left panels), 250 MeV/nucl. (right panels) and at scaled impact parameter $\hat{b} = 0.3$ for different mass asymmetries.

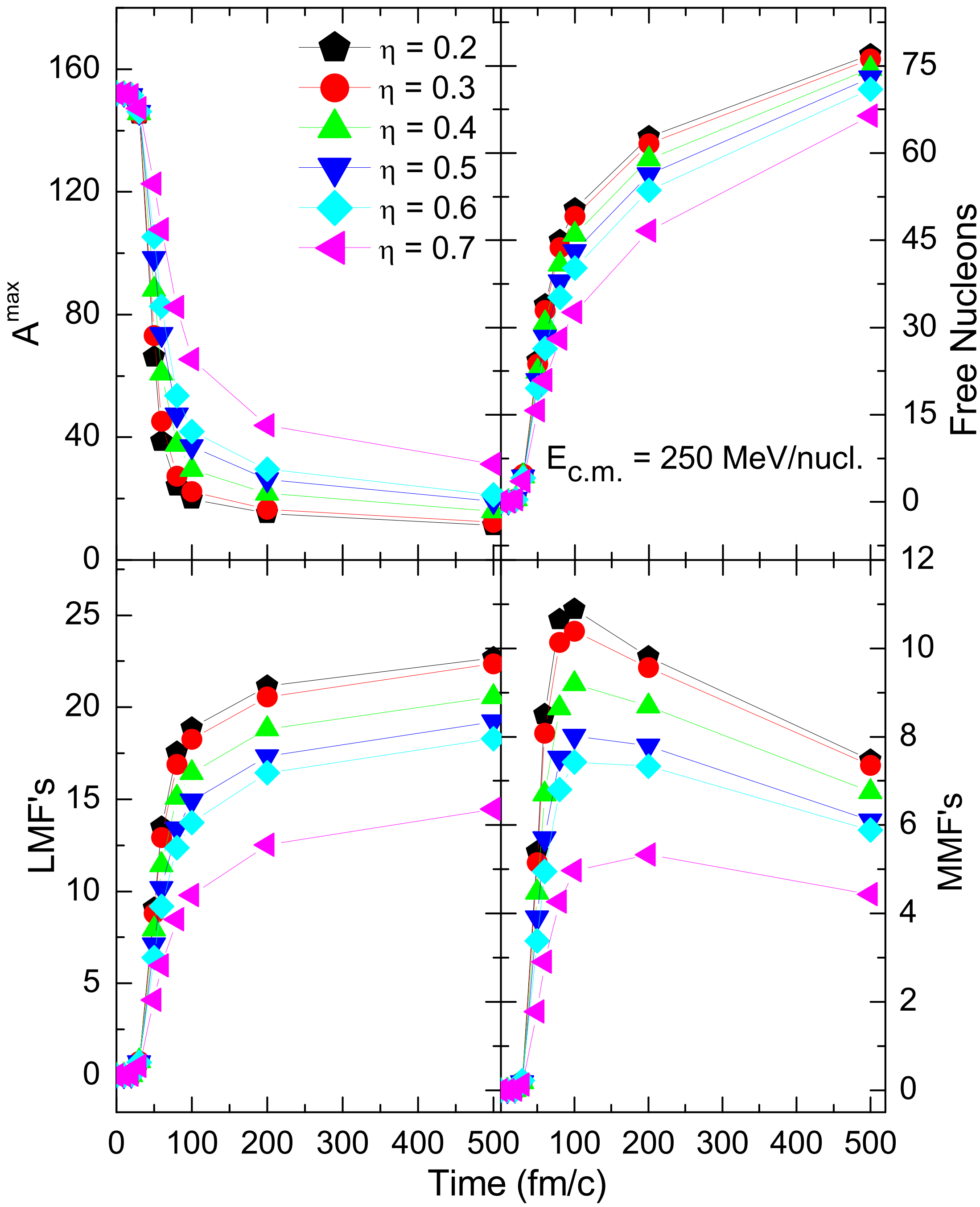

Figure 3.9: The time evolution of the largest fragment A^{max}, the free nucleons (A = 1), the LMF's ($2 \leq A \leq 4$), and the IMF's ($5 \leq A \leq A_{tot}/6$) for different mass asymmetries varying from 0.2 to 0.7 at $E_{c.m.} = 250$ MeV/nucl. for $\hat{b} = 0.3$ using Soft NEOS.

to be emitted suggesting the hot fragments getting cool down. The LMF's also depicts the well known trend of rise in their multiplicity, while, the MMF's decay after some time. It is also evident that the colliding nuclei having smaller mass asymmetries saturate much faster than the colliding nuclei having larger mass asymmetry i.e. since the participant zone decreases with the mass asymmetry, it takes longer time for larger asymmetric nuclei to saturate.

3.4.4 Density Distribution

To understand this aspect further, we display in Fig. 3.10, the saturation density of the reaction obtained at 200 fm/c. This density remains quite high for larger mass asymmetries. This is caused by the least amount of destruction of nuclear matter at larger mass asymmetries, which leads to higher nucleonic densities. As a result, one sees a heavier A^{max} compared to the smaller η values. which is also supported by Fig. 3.9.

3.4.5 Charge and Mass distribution

In Fig. 3.11, the charge distribution is displayed as a function of the fragment charge using soft (upper panel) and hard NEOS (lower panel). The symmetric reactions (η=0) lead to enhanced emission of nucleons and LMF's compared to asymmetric reactions, where incomplete fusion events or deep inelastic events are dominant. We can also say that a large asymmetric reaction leads to few nucleonic-transfer processes. One also notices that the slope of the distribution becomes steeper with hard NEOS compared to soft NEOS. Clear systematics can be seen in the production of fragments with the mass asymmetry of the reaction. Similarly, we show the mass yield at different mass asymmetries at the same incident beam energy and for same NEOS in Fig. 3.12. We see that the trend is quite similar for all the above mentioned mass asymmetries.

3.4.6 Energy Dependence

In Fig. 3.13, the variation of the multiplicity of LMF's is displayed as a function of the center-of-mass energy for various asymmetric reactions using hard and soft NEOS. Because

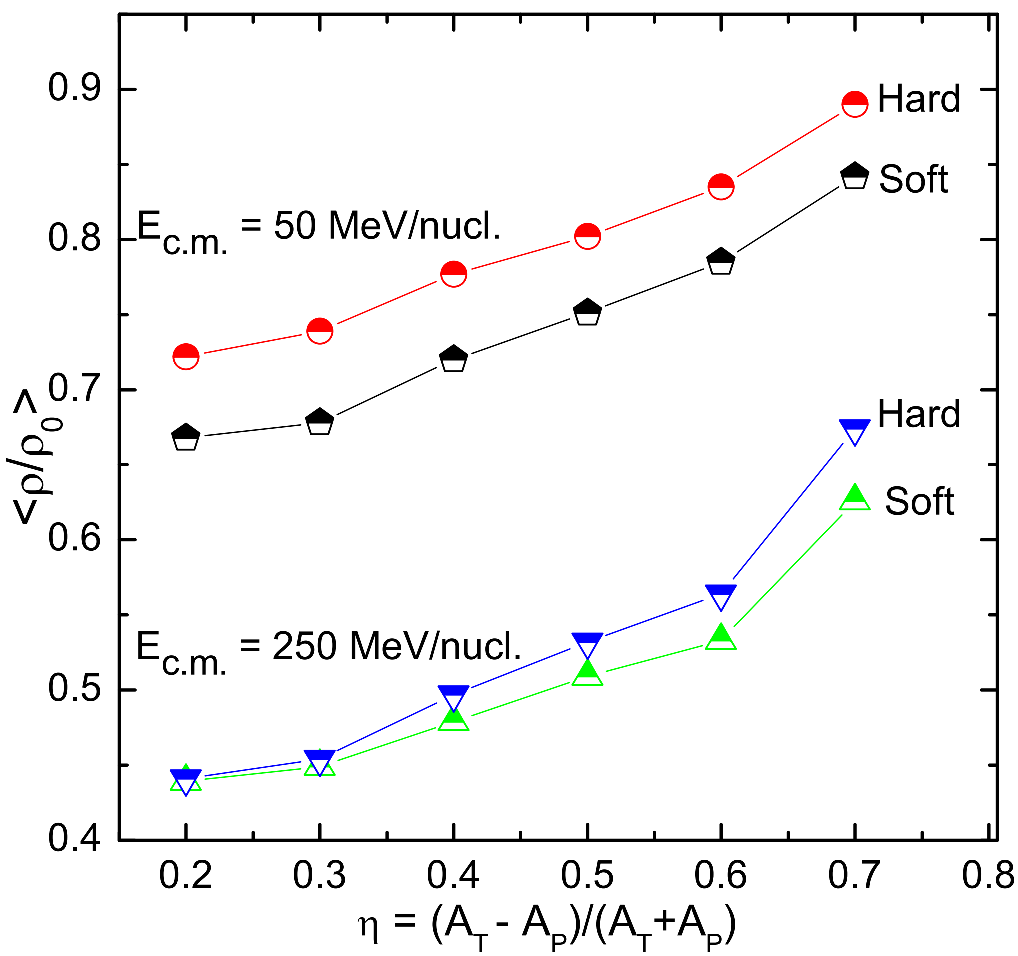

Figure 3.10: The variation of density with mass asymmetry at an impact parameter $\hat{b}$ = 0.3. The different symbols are at $E_{c.m.}$ = 50 MeV/nucl. and $E_{c.m.}$ = 250 MeV/nucl. with soft and hard NEOS.

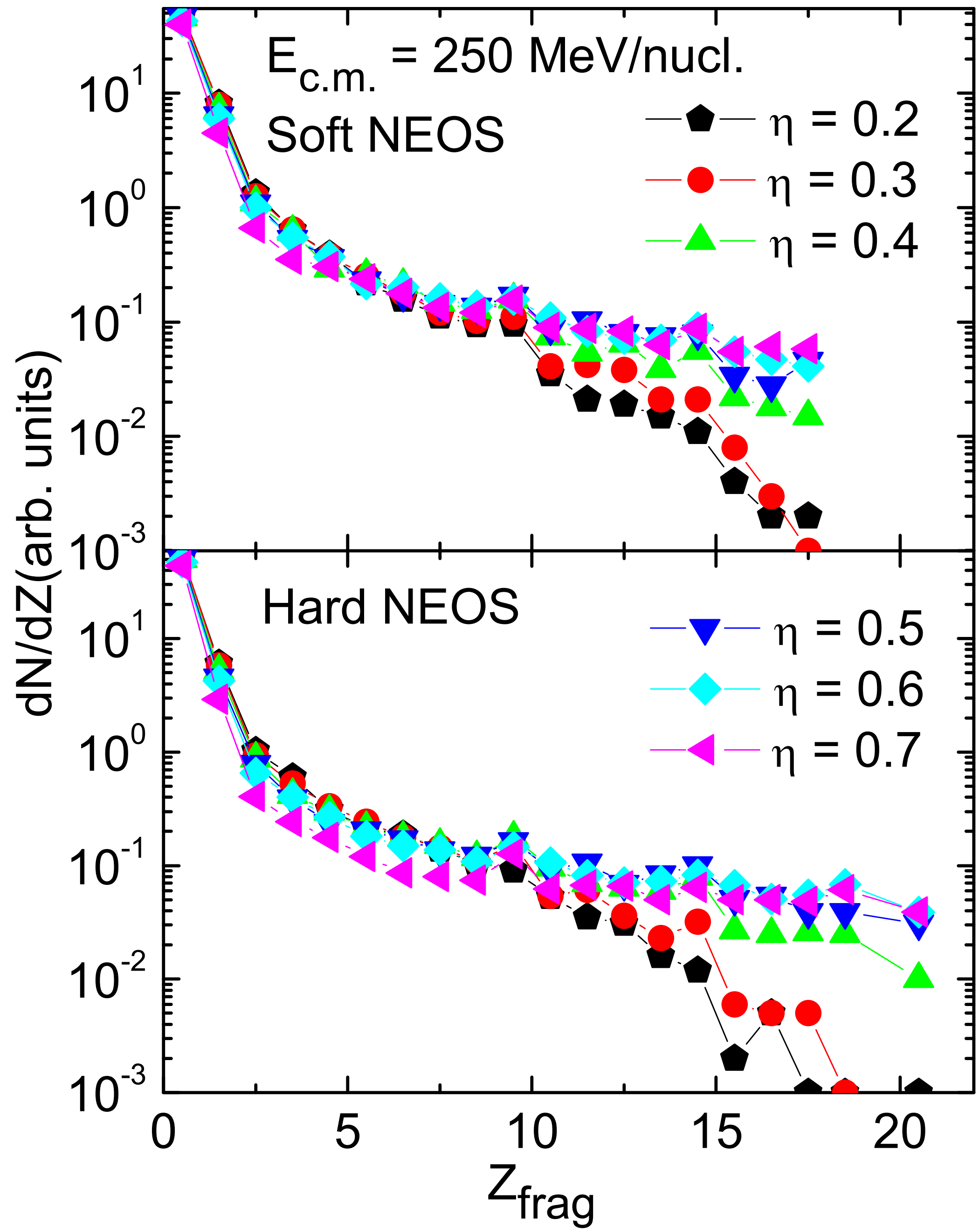

Figure 3.11: The charge distribution for different mass asymmetries between $\eta = 0.2$ to 0.7 at $E_{c.m.} = 250$ MeV/nucl. and scaled impact parameter $\hat{b} = 0.3$. The upper and lower panels are shown with soft and hard NEOS, respectively.

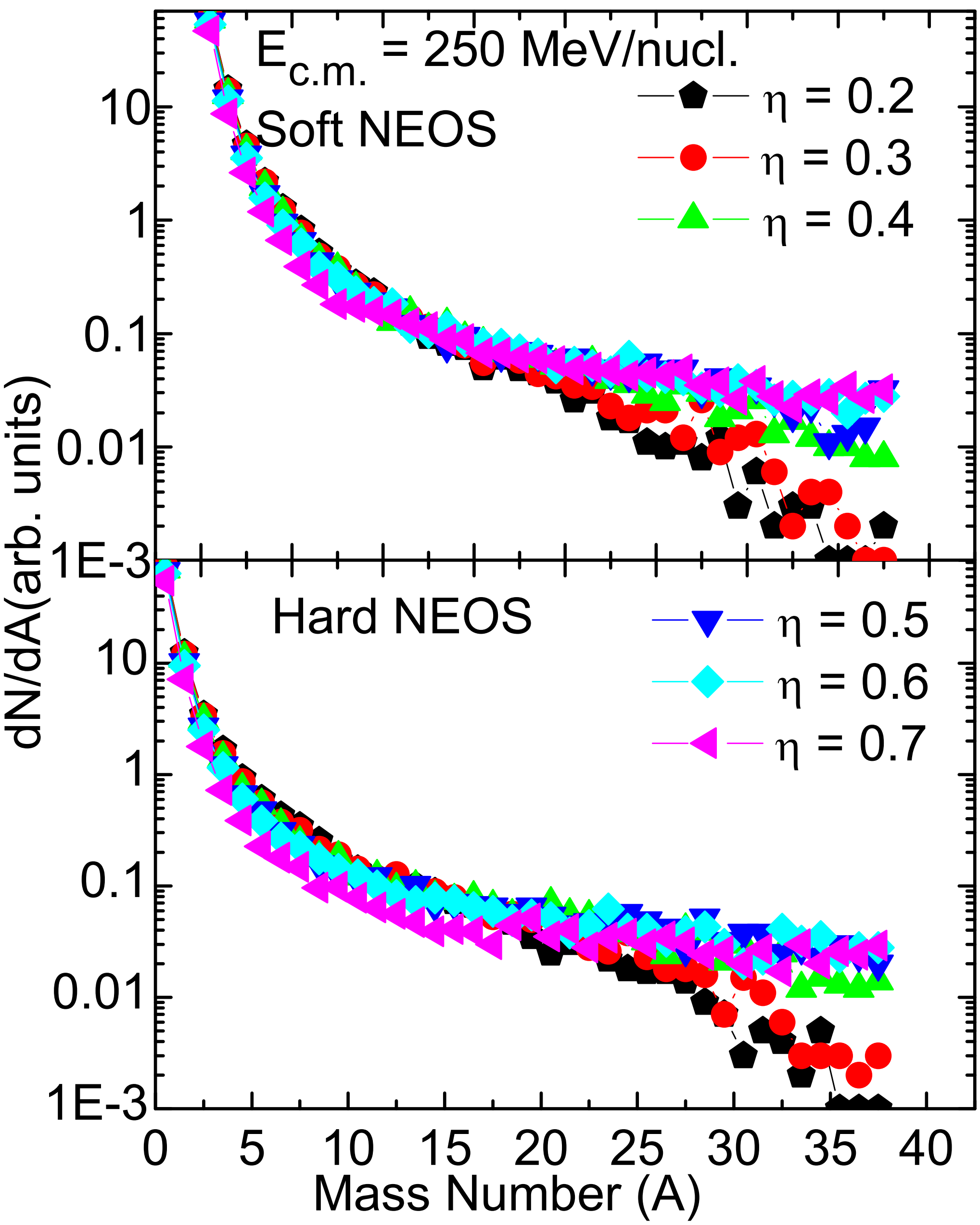

Figure 3.12: Same as Fig. 3.11, but showing the mass distribution.

of more compression, the nearly symmetric reaction drives matter into the participant zone and, as a result, more lighter fragments are emitted. In Fig. 3.14, the variation of the multiplicity of IMF's is displayed as a function of the center-of-mass energy $E_{c.m.}$. The multiplicity of IMF's first increases with the incident energy and then attains an equilibrium at later times. The trend at E = 50 MeV/nucl. is opposite to the trend at E = 600 MeV/nucl. Actually E = 50 MeV/nucl. is so less that it is not able to break the correlations between the particles and hence the fragment emitted is too large and is going out of the range of IMF's. At E = 600 MeV/nucl., trend is coming actually. Here, for $\eta = 0.2$ (nearly symmetric), compression is more and hence less number of IMF's are produced while the reverse is true for $\eta = 0.7$. One notices several interesting points: The nearly symmetric collision leads to a well-known trend (i.e., the maximum emission occurs around 100 MeV/nucl.). This trend, however is not shown by the large asymmetric reactions where we do not see any sharp rise or fall; and, furthermore, a flat plateau is obtained at much higher incident energies compared to nearly symmetric nuclei.

3.4.7 Correlation between N_{IMF} and Z_{bound}

It is worth mentioning that experimentalists studied many times the Z_{bound} dependence of N_{IMF} for symmetric [138] as well as asymmetric systems. In following attempts, a detailed analysis with mass asymmetry of the reaction is performed in two different ways:

Time evolution of N_{IMF} and Z_{bound}

In order to study the Z_{bound} dependence of N_{IMF} in terms of mass asymmetry, this study is performed in three steps.

In the first step, the time evolution of the intermediate mass fragments as well as Z_{bound} is shown in Fig. 3.15. One learns from this figure that the mean multiplicity of IMF's increases very fast and attains an equilibrium at later times. The system having least mass asymmetry gives rise to more IMF's as compared to system having large mass asymmetry. This might be due to the reason that as one moves toward the large mass asymmetries, the size of the fragments becomes larger than the size of IMF's and hence decrease in the multiplicity of IMF's is observed. On the other hand, one can also see that there is a continues

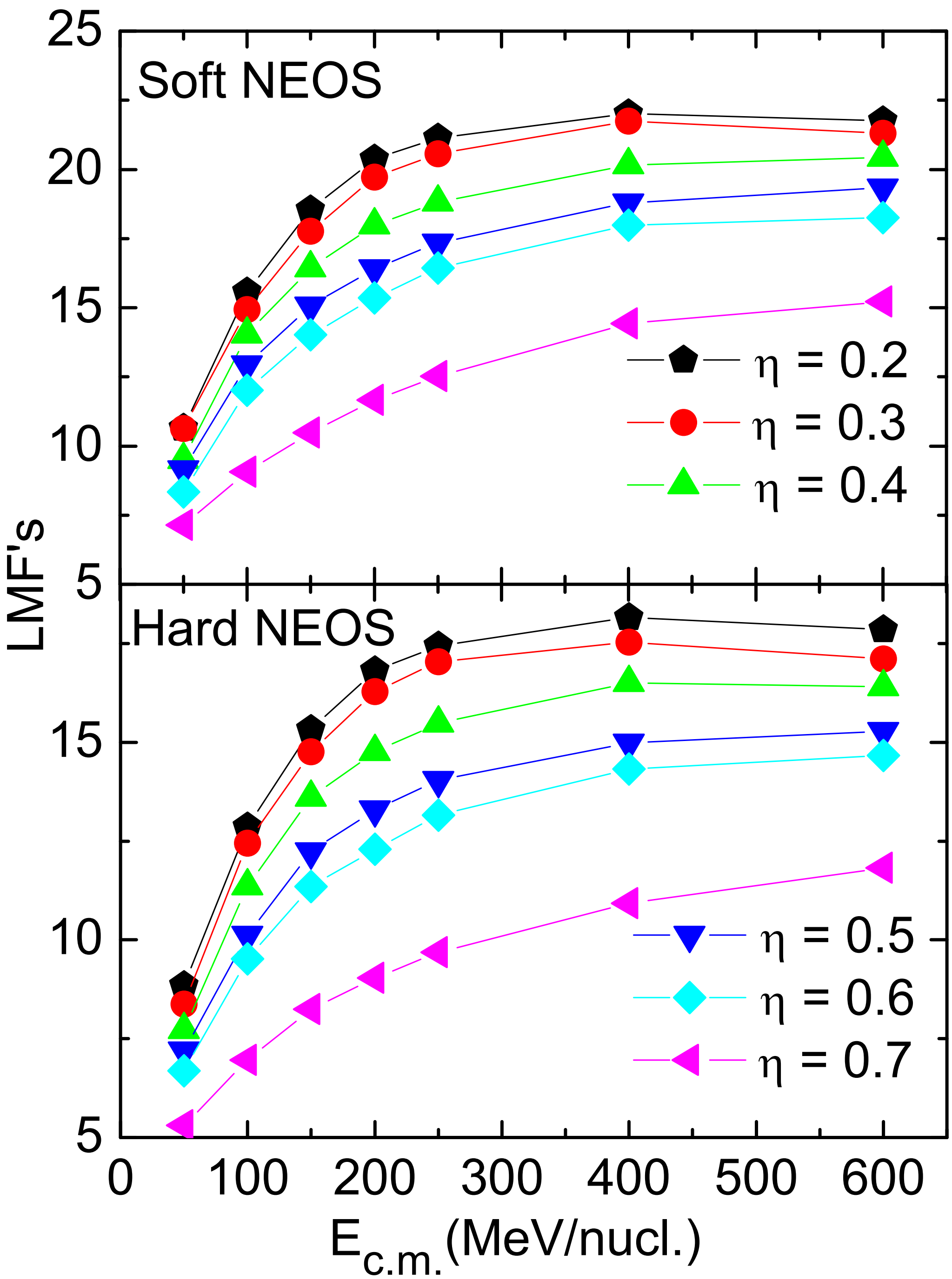

Figure 3.13: The variation of LMF's with center-of-mass energy using soft and hard NEOS at scaled impact parameter $\hat{b} = 0.3$. The different symbols show the results, which involve different mass asymmetries.

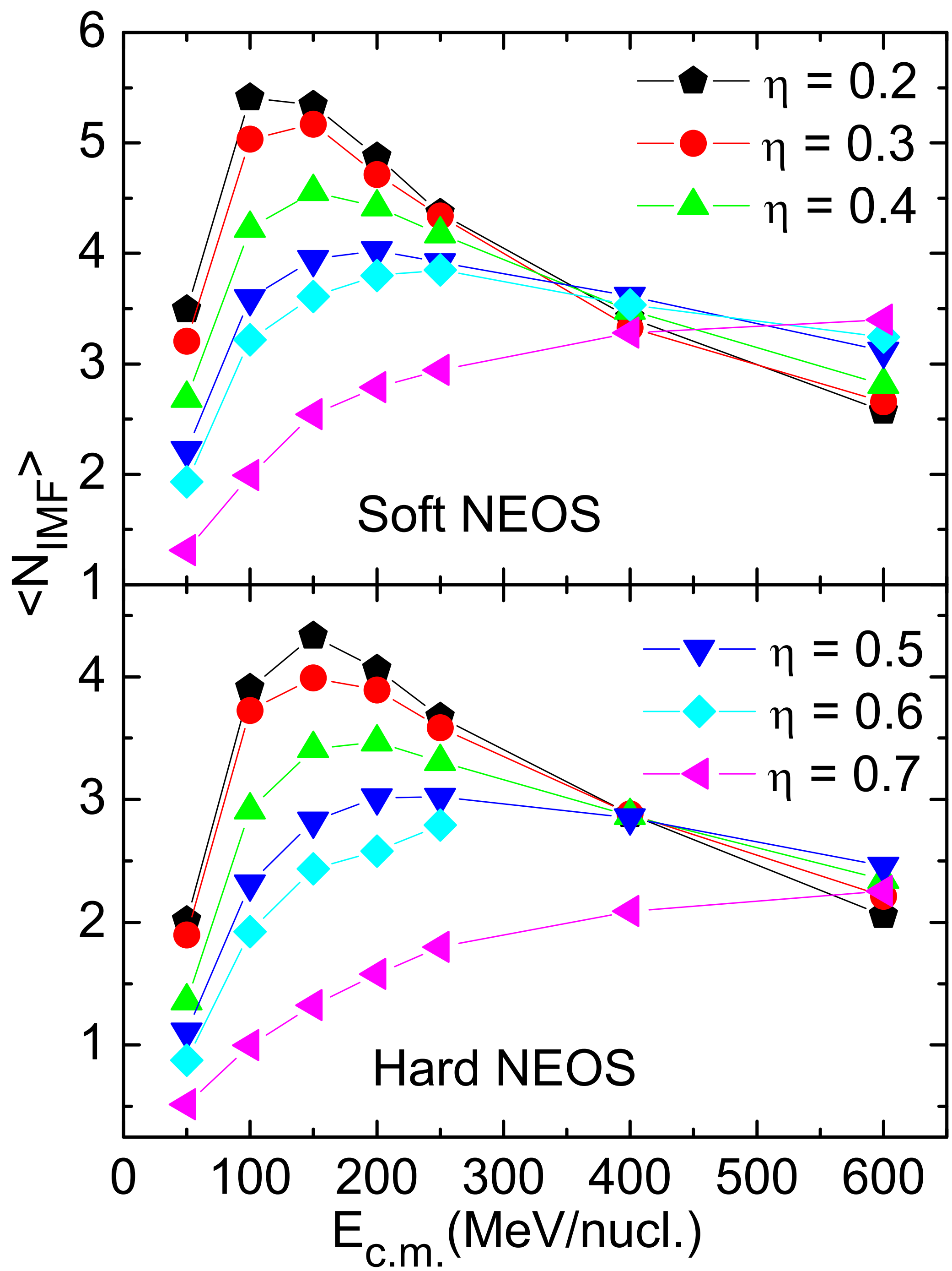

Figure 3.14: Same as Fig. 3.13, but for IMF's.

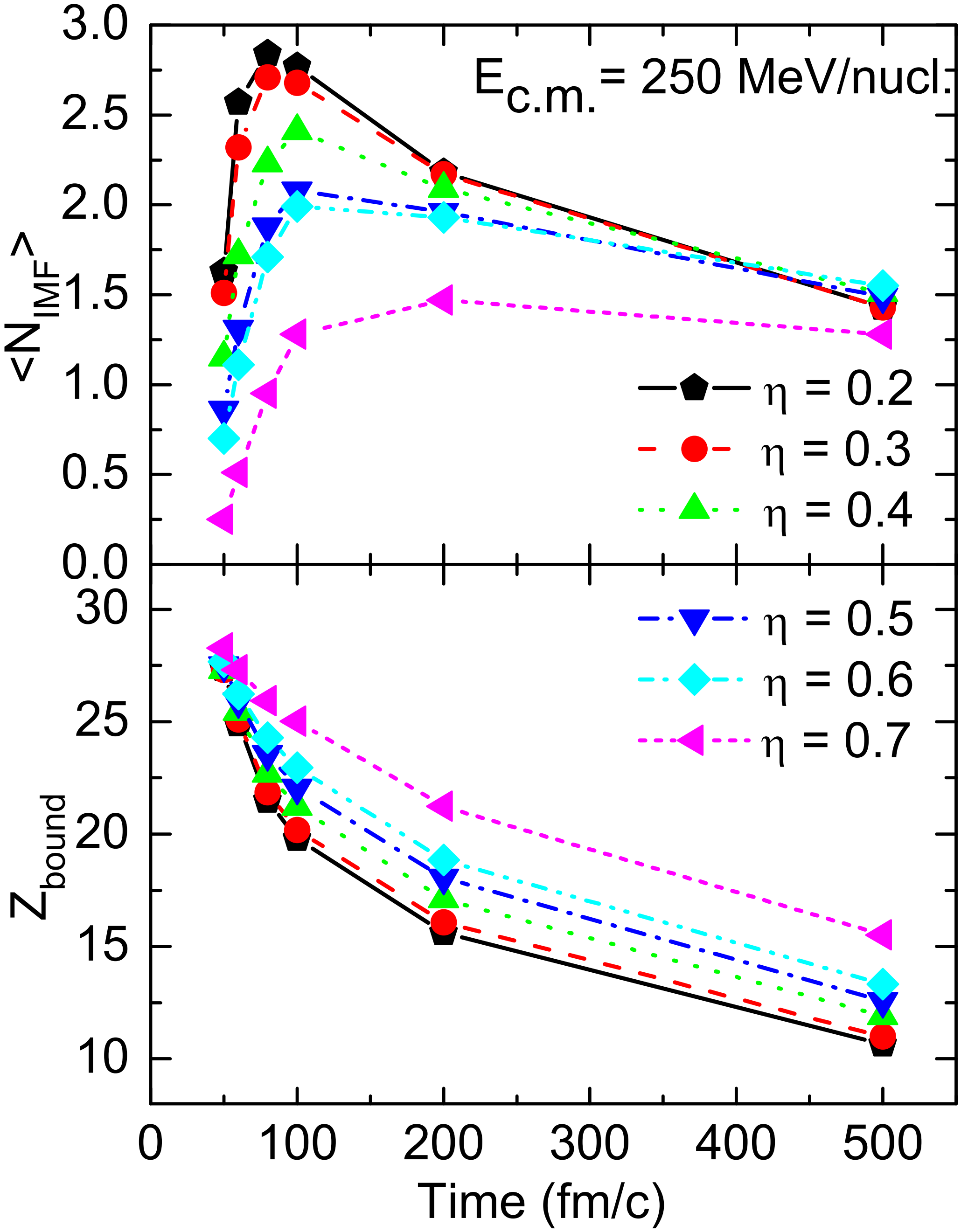

Figure 3.15: The mean multiplicity of intermediate mass fragments $< N_{IMF} >$ and Z_{bound} as a function of time at $E_{c.m.} = 250$ MeV/nucl. for soft NEOS using scaled impact parameter $\hat{b} = 0.3$. Different lines represent the different mass asymmetries varying from 0.2 to 0.7.

decrease in the value of Z_{bound} with time. This is due to the decay of compound nucleus into lighter particles (i.e free nucleons as well as LMF's etc.). It means that the system is still in non-equilibrium state. Moreover, the highly asymmetric system produces largest Z_{bound} because in such a case most of the part goes uninteracted.

In the second step, we show the variation of mean multiplicity of intermediate mass fragments $< N_{IMF} >$ with Z_{bound} in Fig. 3.16. Here the values of Z_{bound} are recorded at different time steps. The lowest value of Z_{bound} correspond to highest time step. With decrease in Z_{bound}, $< N_{IMF} >$ first increases, reaches a maxima, and then decreases again. Since in the present study, the range of IMF's is 5 to 25, therefore at $Z_{bound} = 20$, maximum number of $< N_{IMF} >$ are produced. After this, the IMF's start decaying on both sides of $Z_{bound} = 20$. For different mass asymmetries, a given value of Z_{bound} corresponds to different number of intermediate mass fragments. The system having least mass asymmetry give rise to more IMF's as compared to system having largest mass asymmetry. This might be due to the reason that system having largest mass asymmetry suffers less compression; and, hence, less numbers of IMF's are produced. These findings are supported by Fig. 3.14.

In the last step, we show the variation of mean multiplicity of IMF's with the mass asymmetry of the system at different values of Z_{bound} in Fig. 3.17. The $< N_{IMF} >$ decreases with the increase in the mass asymmetry of the system. This is true for smaller as well as for larger values of Z_{bound}. The lines are fitted with equation y = mx + c where, y = N_{IMF}, x = η, and m is the slope of the line. The slope values are -1.7, -2.7. -2.6 corresponding to Z_{bound} = 16, 20, 27, respectively. This indicates that for heavier Z_{bound}, the production of the $< N_{IMF} >$ is more sensitive with the mass asymmetry of the system compared to the lighter Z_{bound}. Moreover, the maximum IMF's are produced at $Z_{bound} = 20$, indicating the limit of IMF's for the present system.

Impact parameter dependence of N_{IMF} and Z_{bound}

Fig. 3.18, shows the impact parameter dependence of N_{IMF} (upper panel) and Z_{bound} (lower panel). Fig. 3.18 (upper panel) shows that due to the low center of mass energy $E_{c.m.}$ = 250 MeV/nucl., central collisions generate repulsion in a manner so that the colliding nuclei breakup into IMF's, whereas for the peripheral collisions, the size of the fragment is close to

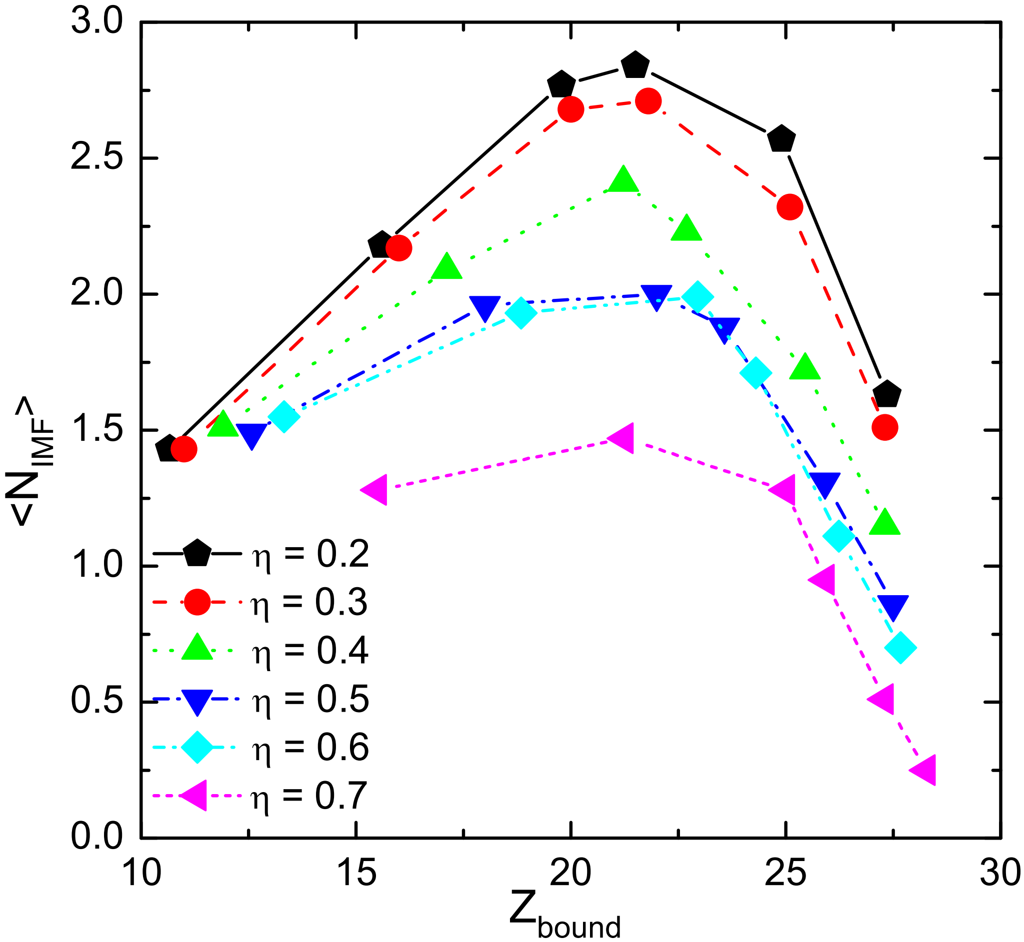

Figure 3.16: The mean multiplicity of intermediate mass fragments $< N_{IMF} >$ as a function of Z_{bound} at $E_{c.m.}$ = 250 MeV/nucl. for soft NEOS at scaled impact parameter $\hat{b}$ = 0.3. Different lines represent the different mass asymmetries varying from 0.2 to 0.7. Here, the values of Z_{bound} are recorded at different time steps.

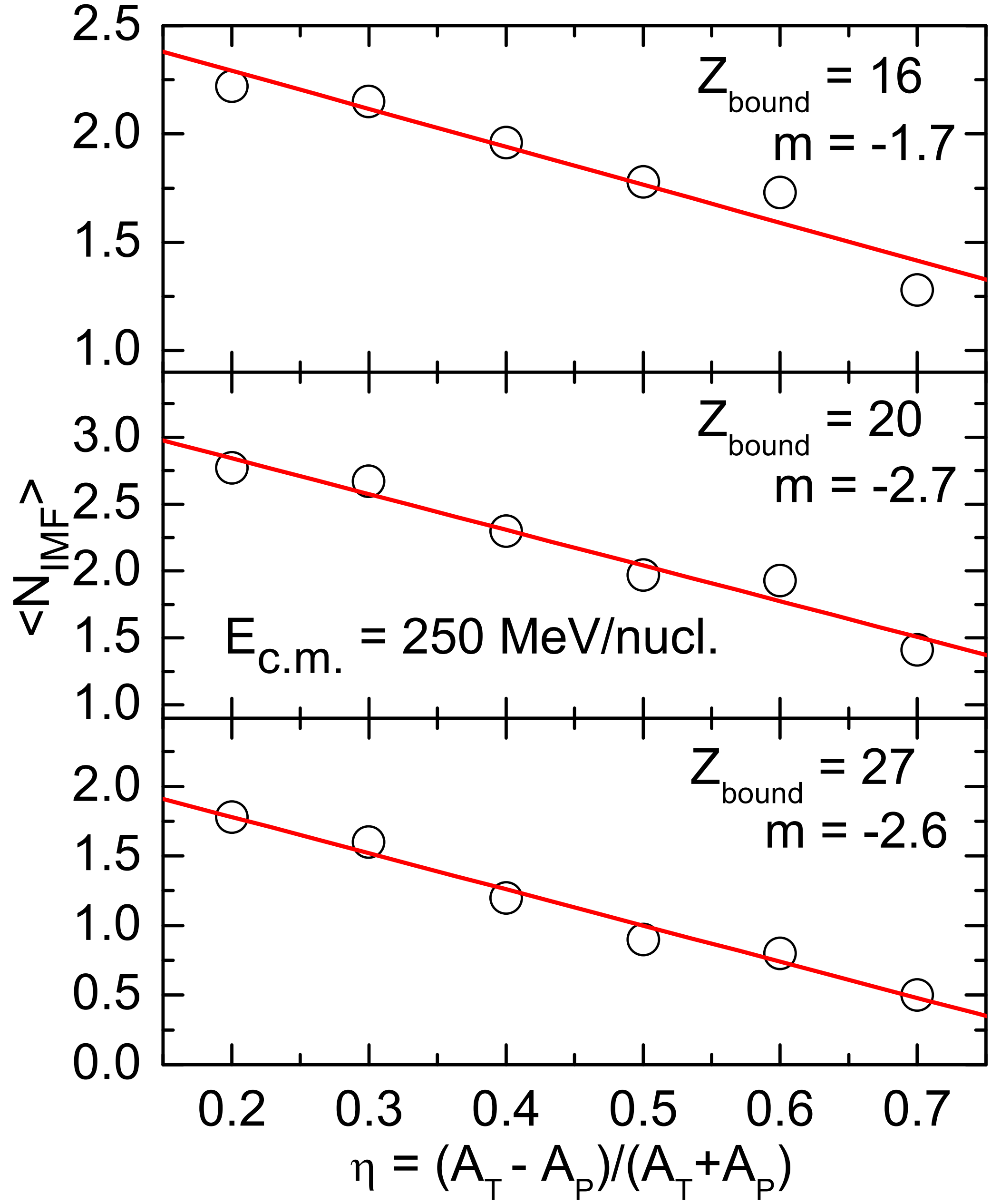

Figure 3.17: Mean multiplicity of intermediate mass fragments as a function of mass asymmetry parameter η for different Z_{bound} values at $E_{c.m.}$ = 250 MeV/nucl. for soft NEOS. The lines are fitted with an equation y = mx + c, where, m represents the slope of line.

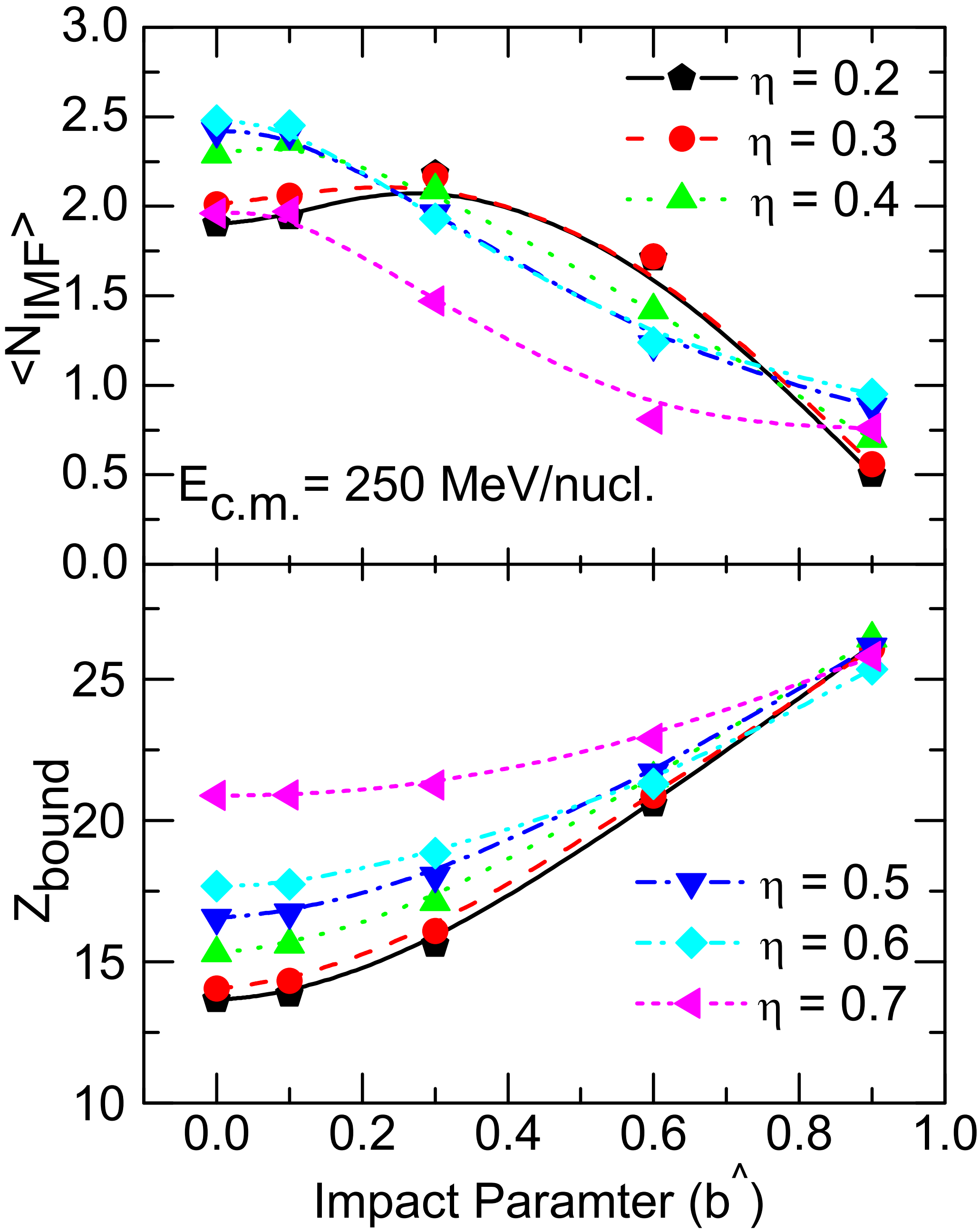

Figure 3.18: Variation of N_{IMF} and Z_{bound} with scaled impact parameter at $E_{c.m.}$ = 250 MeV/nucl. Different lines represent the different mass asymmetries varying from 0.2 to 0.7.

the size of the reacting nuclei, and therefore, one sees a very few IMF's. Interestingly, a rise and fall can also be seen for nearly symmetric systems, which indicates the possible existence of various decay modes from the evaporation (fission) mode to the multi-fragmentation mode and then to the vaporization mode [149]. Moreover, this behavior disappears with increase in the mass asymmetry of the reaction. On the other hand, in Fig. 3.18 (lower panel), the Z_{bound} is found to increase with impact parameter of the reaction. As impact parameter increases, participant zone decreases and spectator zone increases, that will lead to the further increase in the production of heavier fragments and hence increase in the value of Z_{bound} with impact parameter. The symmetric systems are more sensitive with the impact parameter dependence of Z_{bound} as compared to the asymmetric systems. The maximum mass asymmetry means that from projectile or target, one is heaviest one and other is lightest one. This leads to the possibility of IMF's production even at central collisions. The change in the geometry does not alter too much the production of IMF's in asymmetric systems compared to symmetric systems. This is further elaborated in Fig. 3.19, which shows correlation between the N_{IMF} and Z_{bound} by taking into account the mass asymmetry of the reaction ($\eta = 0.2$ to 0.7). Here, the values of Z_{bound} are recorded at different impact parameters varying from central to peripheral one. It was shown [47] that Z_{bound} allows a very good determination of the impact parameter and hence different reaction geometries. The smaller values of Z_{bound} correspond to central collisions. Since the IMF's are produced due to the target breakup into pieces, therefore, as we vary the mass asymmetry parameter from $\eta = 0.2$ to 0.7, the target fragmentation increases. The maximum number of IMF's are observed in the Z_{bound} range from 15 to 20. This is in agreement with the findings shown in Fig. 3.17. At lowest mass asymmetry, we get a rise and fall in the production of IMF's with Z_{bound}. But as the mass asymmetry increases, the curve shows a steep variation. These findings are supported by the findings of Fig. 3.18 (upper panel). From this, one can see that at highest mass asymmetry, the size of bounded fragment becomes largest. Therefore, reaction dynamics changes drastically as one moves from low mass asymmetry to high mass asymmetry. In the next section, we shall discuss directed transverse flow and hence balance energy for various mass asymmetries varying from 0.2 to 0.7.

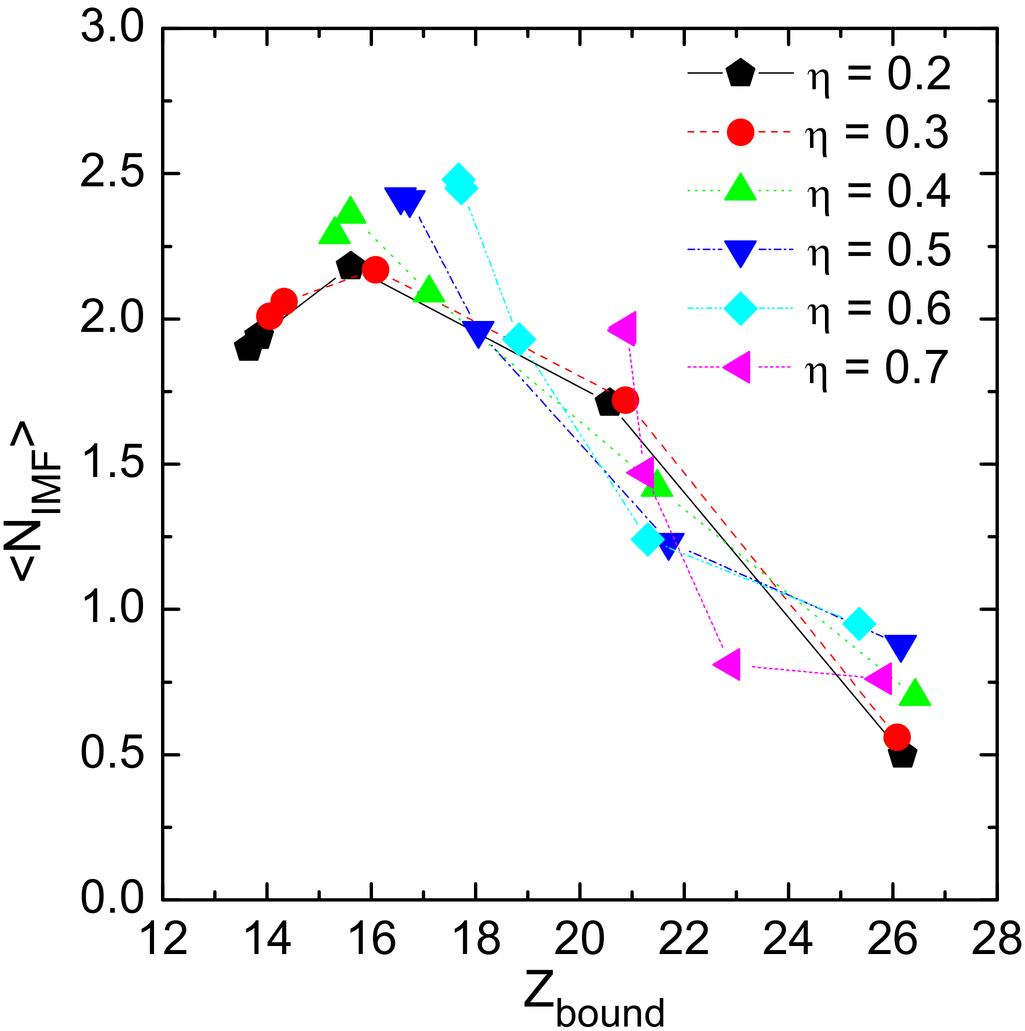

Figure 3.19: Same as Fig. 3.16. Here, the values of Z_{bound} are recorded at different scaled impact parameters varying from central to peripheral one.

3.4.8 Mass asymmetry and directed transverse flow

The directed transverse in-plane flow, $< P_x^{dir} >$ is defined as [29, 65, 150]:

$$< P_x^{dir} >= \frac{1}{A}\sum_i sgn\{Y(i)\}P_x(i), \tag{3.3}$$

where Y(i) and $P_x(i)$ are, respectively, the rapidity distribution and transverse momentum of the i^{th} particle. The study of transverse flow gives insight into the reaction dynamics as well into the hot and dense nuclear matter formed in a reaction. This quantity vanishes at a certain incident energy. This energy is dubbed as balance energy (E_{bal}) or the energy of vanishing flow (EVF) [65, 151]. This is due to the counterbalancing of attractive mean-field at low incident energies and repulsive nucleon-nucleon (NN) collisions at higher incident energies. Here, we shall understand the effect of NEOS and Coulomb interactions on the energy of vanishing flow or alternatively, on the balance energy by taking into account the mass asymmetry of a reaction at scaled impact parameter $\hat{b} = 0.3$.

Asymmetry dependence of directed transverse flow

We display in Fig. 3.20, variation of the mass asymmetry η on directed flow $< P_x^{dir} >$ at incident energy of E = 50 MeV/nucl. The upper panel represents the directed transverse flow, while the bottom panel is for the relative Coulomb effect with respect to the mass asymmetry of the reaction. This relative effect is calculated as:

$$< \Delta P_x^{dir} |_{Coul}>=< P_x^{dir} >_{Coul+Sym} - < P_x^{dir} >_{NoCoul+Sym} \tag{3.4}$$

As is evident from the figure, directed flow is found to increase in a systematic manner at E = 50 MeV/nucl. with mass asymmetry of the reaction. The inclusion of Coulomb interactions does not alter the conclusions. Note that the mass asymmetry of a reaction increases with N/Z, except for $\eta = 0.4$ and $\eta = 0.6$. Moreover, the increase in the mass asymmetry is governed by the increase in $(A_T - A_P)$, $(Z_T - Z_P)$ and $(N_T - N_P)$. The percentage increase of the neutron excess $(N_T - N_P)$ is increasing over the rest of two factors. Because the symmetry potential for the neutron rich systems is stronger compared to the neutron poor systems due to large relative neutron strength. Furthermore, the symmetry potential

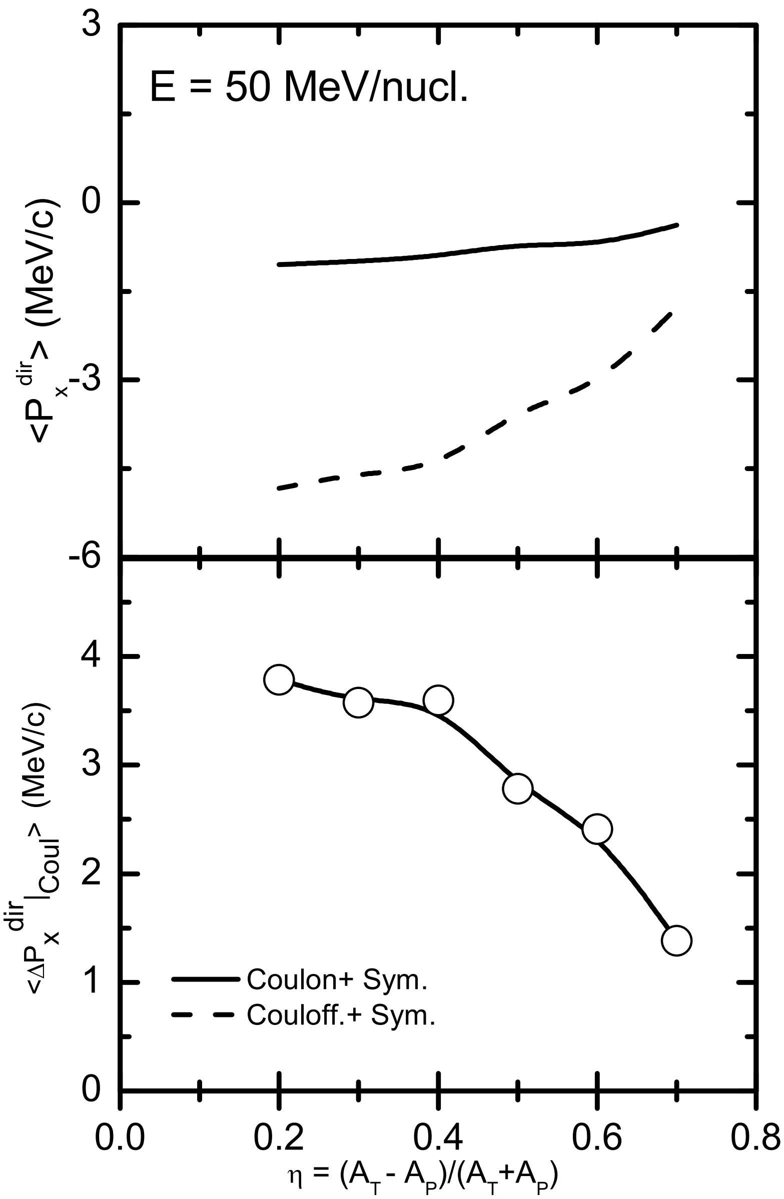

Figure 3.20: Asymmetry dependence of directed flow at scaled impact parameter $\hat{b} = 0.3$ in center of mass frame in upper panel, while, lower panel shows the relative effect of Coulomb interactions. The different lines in the figure are representing the effect of symmetry energy and Coulomb interactions.

is repulsive for neutrons and attractive for protons. On the other hand, more negative value of directed flow (dominating the mean field) is observed in the absence of Coulomb interactions. This is due to the enhancement of the chemical and mechanical instability domains in the absence of Coulomb interactions [152]. Similar type of study and conclusion was also performed for nuclear stopping in ref. [153].

To further strengthen our interpretation of the results, the relative effect of Coulomb interactions $< \Delta P_x^{dir} |_{Coul}>$ is studied. The relative effect of the Coulomb interactions is found to decrease with increase in the mass asymmetry of a reaction. For the further study, we have performed the simulations using different NEOS as well as different options of Coulomb (Coul-on and Coul-off) because we want to see the shift in the balance energy due to both these factors.

Energy dependence of directed transverse flow

In Figs. 3.21 and 3.22, we display the excitation function of directed flow at different mass asymmetries from $\eta = 0.2$ to 0.7. The value of abscissa at zero value of $< P_x^{dir} >$ corresponds to the energy of vanishing flow (EVF) or alternatively, the balance energy (E_{bal}). The Fig. 3.21 shows the shift in the balance energy due to Coulomb interactions, while, Fig. 3.22 is representing the shift in the balance energy due to different NEOS. In Fig. 3.21, one sees a linear enhancement in the nuclear flow with increase in the incident energy. This increase in the transverse flow is sharp at smaller incident energies (upto 200 MeV/nucl.). If one goes to higher incident energies, the value gets saturated as discussed in Ref. [65]. We have displayed here the results upto 250 MeV/nucl., since we are interested in and around balance energy. In the presence of Coulomb interactions, more positive value of the flow is obtained. This is due to the well known repulsive nature of Coulomb interactions. At higher energies, the repulsion due to Coulomb interactions is stronger during the early phase of the reaction and transverse momentum increases sharply. The overall effect depends on the mass asymmetry of the reaction. If one looks at the balance energy, the shift in the incident energy towards the higher value is obtained at $< P_x^{dir} >= 0$ with the mass asymmetry of the reaction. This is showing that with increase in mass asymmetry of the reaction and in the absence of Coulomb interactions, attractive mean-field is dominating the large region of

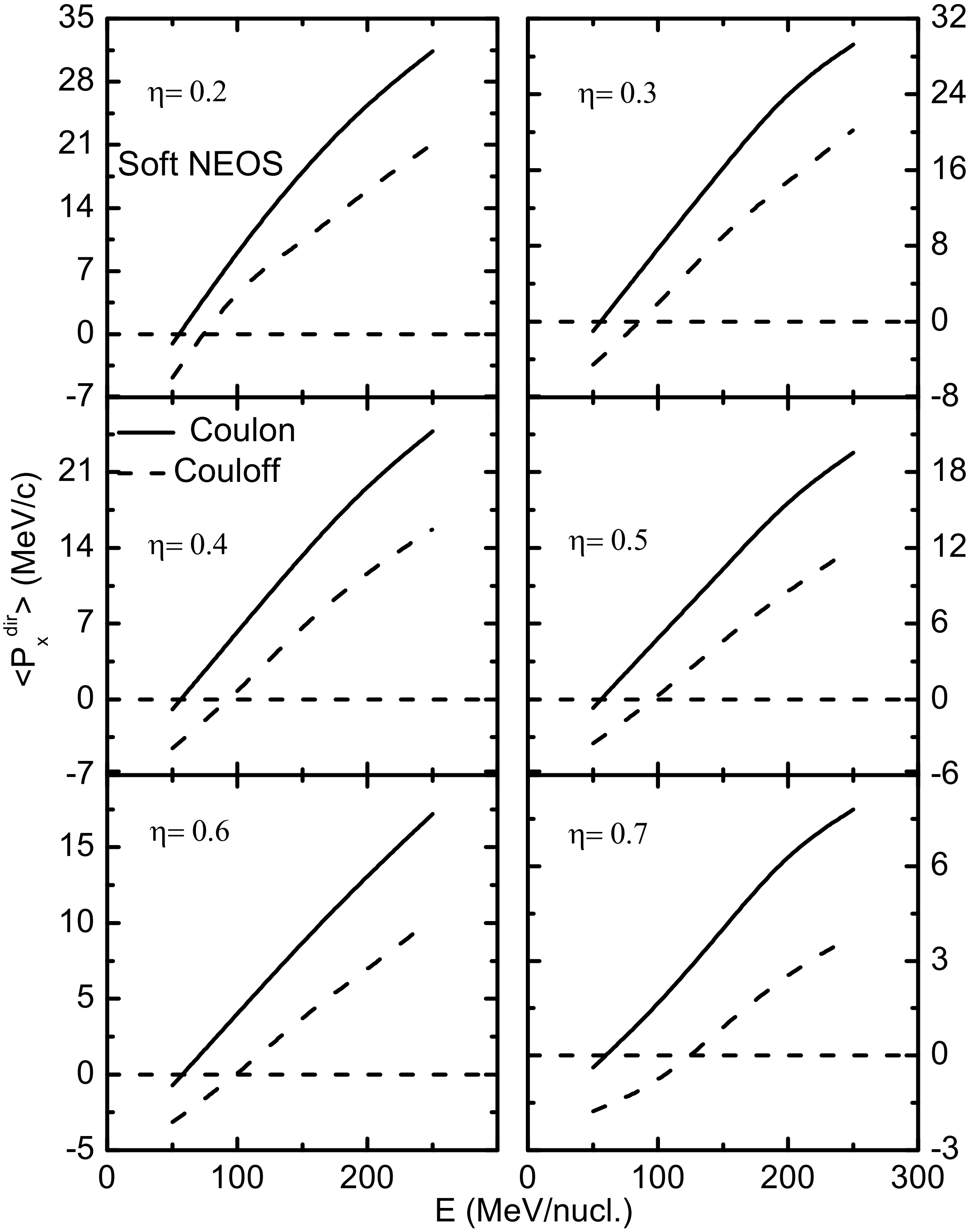

Figure 3.21: Excitation function of directed flow at different mass asymmetries with and without Coulomb interactions at semi-central geometry.

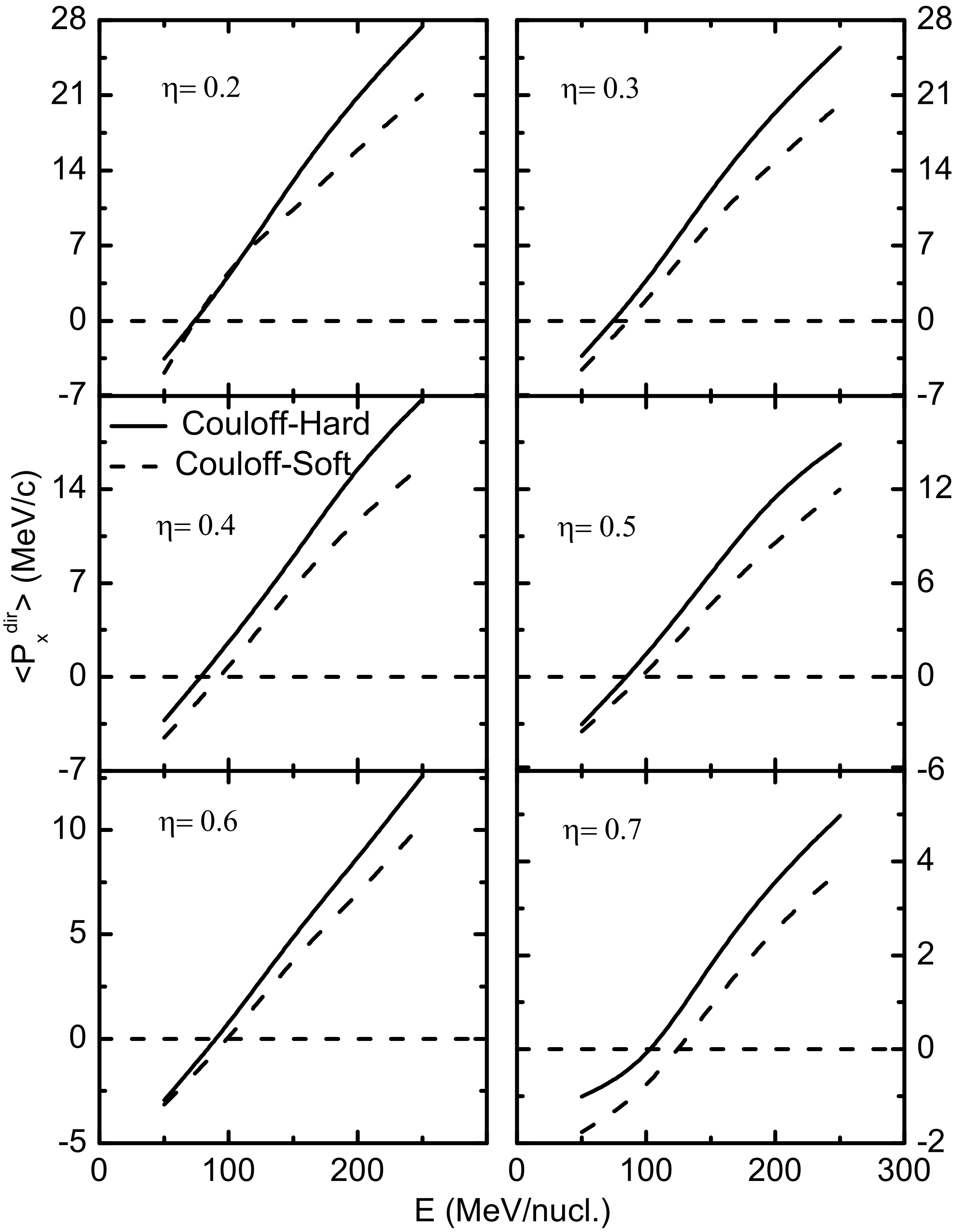

Figure 3.22: Excitation function of directed flow with hard and soft NEOS in the absence of Coulomb interactions for different mass asymmetries at semi-central geometry.

incident energy. The systematics of the balance energy with mass asymmetry of the reaction is discussed in Fig. 3.23.

The detailed analysis with soft (S) and hard (H) NEOS is displayed in Fig. 3.22. The excitation function of directed flow follows similar trend as explained in Fig. 3.21. For nearly symmetric systems ($\eta = 0.2$), the balance energy is found to be independent of the NEOS, however, reasonable differences are observed at higher incident energies. More positive values of directed flow are obtained with hard NEOS compared to soft NEOS. This is true at all mass asymmetries from ($\eta = 0.3$ to 0.7). This is due to different compressibilities of hard (380 MeV) and soft (200 MeV) NEOS. With an increase in the mass asymmetry of a reaction, the shift in the balance energy towards the higher value of incident energy takes place with soft NEOS compared to hard one. This is consistent with the findings in the literature [154].

Power law dependence of balance energy

To sum up, in Fig. 3.23, we have displayed the mass asymmetry dependence of balance energy. We displayed the results for hard and soft NEOS by switching off the Coulomb interactions. In addition, for a comparative study, the results in the presence of Coulomb interactions with soft NEOS are also shown. All the lines are fitted with power law of the form $E_{bal} = C(\eta)^{\tau}$, where C and τ are the constants. The values of τ in the absence of Coulomb interactions for soft and hard NEOS are 0.375 and 0.282, respectively, while in the presence of Coulomb interactions for soft NEOS is $\tau = 0.06$.

If we compare the mass asymmetry dependence of balance energy with mass dependence, the trend is opposite [65]. It is also clear from the figure, that shift in the balance energy is observed due to Coulomb interactions as well as due to different NEOS with mass asymmetry of the reaction. The shift is more due to Coulomb interactions in comparison to NEOS, indicating the importance of Coulomb interactions in intermediate energy heavy-ion collisions. The higher balance energy is obtained with Coulomb-off + soft NEOS followed by Coulomb-off + hard NEOS and finally Coulomb-on + soft NEOS.

For the further understanding, the relative percentage difference in the balance energy is plotted in the lower panel denoted by the quantity $\Delta E_{bal}^{Coul}\%$ given by

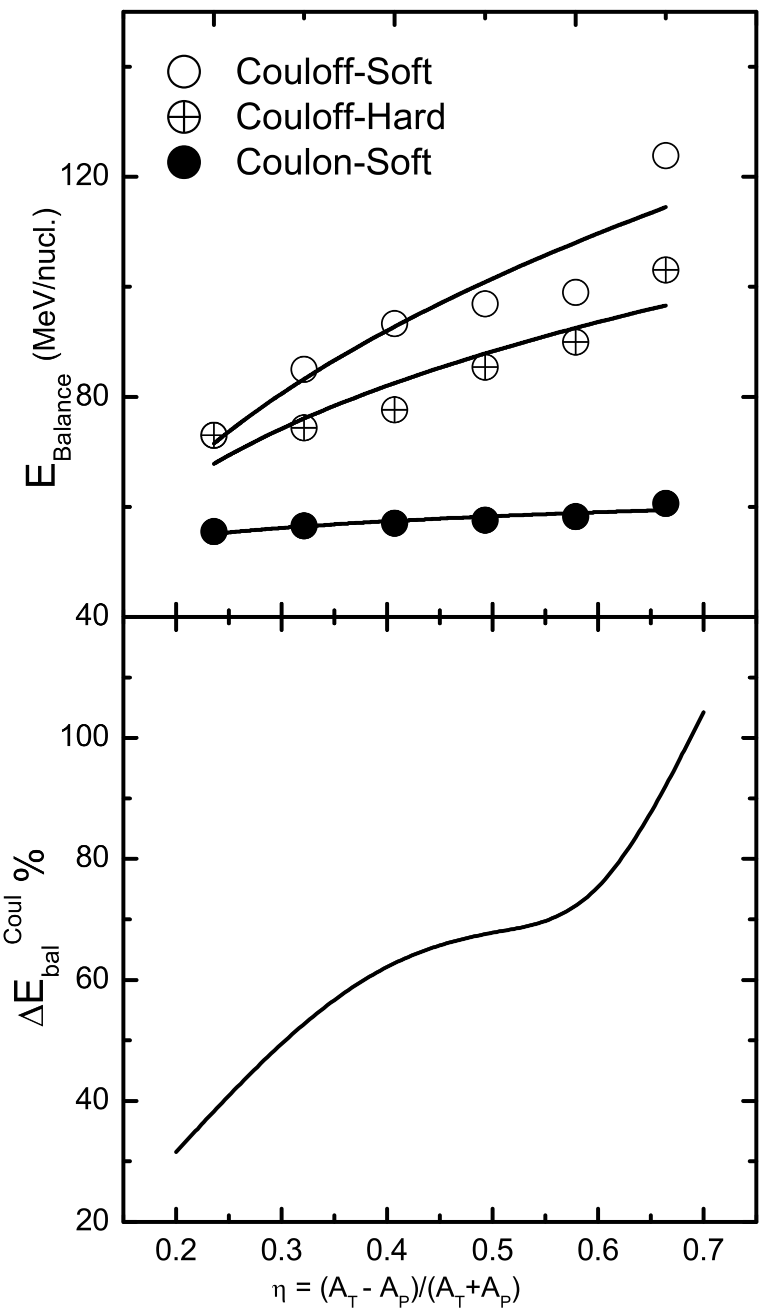

Figure 3.23: Power law dependence of balance energy with mass asymmetry of the reaction. The lower panel is representing the relative % effect of Coulomb interactions on the balance energy.

$$\Delta E_{bal}^{Coul}\% = \left[\frac{E_{bal}^{Couoff+soft} - E_{bal}^{Couon+soft}}{E_{bal}^{Couon+soft}}\right] \times 100 \tag{3.5}$$

The $\Delta E_{bal}^{Coul}\%$ is found to increase with the increase in the mass asymmetry of a reaction. This indicates shift of the nuclear matter towards the attractive mean-field region in the absence of Coulomb interactions with the mass asymmetry of the reaction. This difference $\Delta E_{bal}^{Coul} = 30$ at $\eta = 0.2$, while it is 115 at $\eta = 0.7$. The difference of 90 in the shift of balance energy with mass asymmetry cannot be ignored. This study shows that the balance energy is affected by the Coulomb interactions as well as different NEOS.

3.5 Summary

Using the isospin-dependent quantum molecular dynamics (IQMD) model, coupled with MST method of clusterization, we presented the recent results of multi-fragmentation and directed transverse flow in asymmetric colliding nuclei leading to same compound nucleus, which use a variety of reactions that employ different NEOS as well as incident energies. We envision an interesting outcome for large asymmetric colliding nuclei. In case of nearly symmetric reaction, the spectator parts will be mixture of both projectile and target, whereas in the case of highly asymmetric reaction, no spectator part will come from projectile i.e. only target will contribute to the spectators. Although nearly symmetric nuclei depict a well-known trend of rising and falling with peak around E= 100 MeV/nucl., this trend, however, is completely missing for large asymmetric nuclei. The measured distributions are also given as a function of the total charge of all projectile fragments, Z_{bound}. The highly asymmetric system produces largest Z_{bound}, while, maximum number of intermediate mass fragments (IMF's) are produced at $Z_{bound} = 20$. These observations may throw light on the formation mechanisms behind multi-fragmentation. Moreover, in the case of directed transverse flow, the balance energy is found to increase with the increase in the mass asymmetry of the reaction. The balance energy is affected by the Coulomb interactions as well as different NEOS. This balance energy is further parametrized in terms of mass power law.

Chapter 4

Rapidity distribution as a probe for elliptical flow at intermediate energies

4.1 Introduction

In recent years, investigations of the nuclear equation of state (NEOS) at extreme conditions of density and temperature has been one of the primary driving forces in heavy-ion studies at intermediate energies. The interest at low energies, however, is for isospin effects in fusion processes [27, 28, 64]. These investigations have been performed with the help of rare phenomena, such as multi-fragmentation, collective flow, particle production as well as nuclear stopping [60, 61, 62, 63, 68, 155, 156, 157]. The relation between the NEOS and flow phenomena has been explored extensively in simulations.

Recently, the analysis of the transverse-momentum dependence of elliptical flow has also been put forwarded [61, 62, 158]. The elliptical flow is shaped by the interplay between the geometry and the mean field and, when gated by the transverse momentum, reveals the momentum dependence of the mean field at supra-normal densities. The elliptical flow describes the eccentricity of an ellipse like distribution. Quantitatively, it is the difference between the major and minor axis. The orientation of the major axis is confined to azimuthal angle ϕ or $\phi+\frac{\pi}{2}$ for ellipse like distribution. The major axis lies within the reaction plane for ϕ; while $\phi+\frac{\pi}{2}$ indicates that the orientation of the ellipse is perpendicular to the reaction plane, which is the case for squeeze out flow and may be expected at mid rapidity [24]. The elliptical flow is quantified by the second-order Fourier coefficient [24]

$$V_2 \;=\; \langle \cos 2\phi \rangle = \left\langle \frac{p_x^2 - p_y^2}{p_x^2 + p_y^2} \right\rangle, \tag{4.1}$$

from the azimuthal distribution of the detected particles at mid rapidity as:

$$\frac{dN}{d\phi} = a_0(1 + 2V_1 \cos\phi + 2V_2 \cos 2\phi + \ldots), \tag{4.2}$$

where p_x and p_y are the x and y components of the momentum. The p_x is in the reaction plane, while p_y is perpendicular to the reaction plane, and ϕ is the azimuthal angle of the emitted particle's momentum relative to the x-axis. The positive values of $\langle\cos 2\phi\rangle$ reflect preferential in-plane emission, while negative values reflect preferential out-of-plane emission. The pulsating sign observed recently at intermediate energies has received particular attention, as it reflects the increased pressure build-up in the non-isotropic collision zone [159]. The reason for the anisotropic flow is orthogonal asymmetry in the configuration space (non-central collisions) and re-scattering. In the case of elliptical flow, the initial "ellipticity" of the overlap zone is usually characterized by a quantity $\epsilon = \frac{(<y^2-x^2>)}{(<y^2+x^2>)}$, assuming the reaction plane being xz. As the system expands, spatial anisotropy decreases.

A careful analysis of various experimental collaborations reveals that elliptical flow is very sensitive to the choice of the rapidity cut, that determines the difference between spectator and participant matter. The elliptical-flow pattern of the participant matter is affected by the presence of cold spectators [158]. When nucleons are de-accelerated in the participant region, the longitudinal kinetic energy associated with the initial colliding nuclei is converted into thermal and potential compressional energy. In a subsequent rapid expansion (or explosion), collective transverse energy develops [158], and many particles from the participant region get emitted into the transverse directions. The particles emitted towards the reaction plane can encounter cold spectator pieces, and hence they get redirected. In contrast, the particles emitted essentially perpendicular to the reaction plane are largely unhindered by the spectators. Thus, for the beam energies leading to rapid expansion in the vicinity of the spectators, elliptical flow directed out of the reaction plane (squeeze-out) is expected. This squeeze-out is related to the pace at which the expansion develops and is, therefore, related to the NEOS. This contribution of the participant and spectator matter [158] in the intermediate-energy heavy-ion collisions has motivated us to perform a detailed analysis of the excitation function of elliptical flow over different regions of the participant and the spectator matter. If the excitation function is found to be affected by the different contributions, it will definitely also affect the in-plane to out-of-plane emission, i.e., the transition energy.

The rapidity distribution is an important parameter for the study of the participant–spectator contribution in intermediate-energy heavy-ion collisions [160]. A careful analysis reveals that elliptical flow is very sensitive to the choice of the rapidity cut, which determines the difference between spectator and participant matter.

In this chapter, we shall start with the origin of elliptical flow and then will investigate the effects of the participant and spectator matter on the excitation function of elliptical flow in terms of different rapidity distributions. Attempts shall also be made to parameterize the transition energy in terms of different rapidity bins.

The transition energy for $_{79}Au^{197}$ + $_{79}Au^{197}$ is one of the topics in chapter 4. The transition energy is also measured for light charged particles. This energy is further compared with the findings of INDRA, FOPI and PLASTIC BALL collaborations for $_{79}Au^{197}$ + $_{79}Au^{197}$ for protons and $Z \leq 2$ particles. In the following sections, we shall first discuss the origin of elliptical flow and its disappearance and then present the results.

4.2 Elliptical flow

4.2.1 Origin of Elliptical Flow

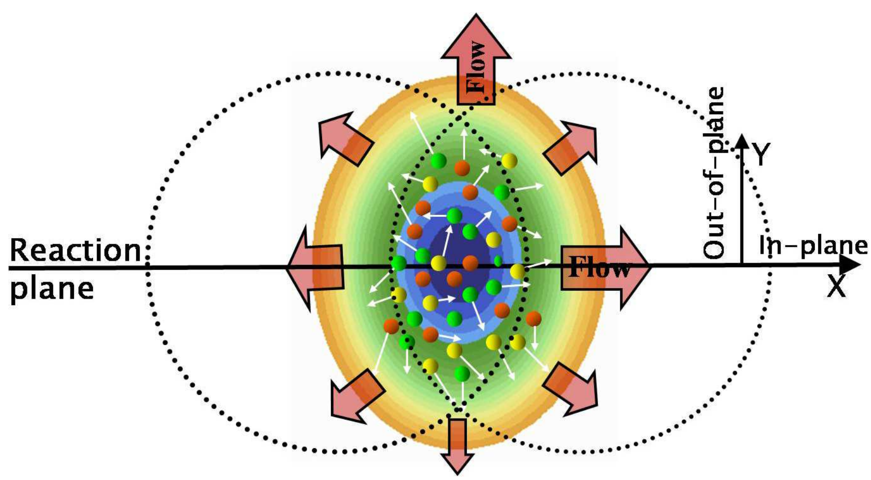

Figure 4.1: Pictorial view of the possible movement of the nucleons in the compressed zone. The directions of in-plane and out-of-plane emission is shown in the figure.

The term “elliptical flow” was introduced in 1997 by H. Sorge [161], a theoretician at SUNY-Stony Brook. Elliptical flow refers to the anisotropy of the ϕ distribution at mid rapidity and its value indicates whether the particle emission is in-plane or out-of-plane. The pictorial view of the in-plane emission and out-of-plane emission is shown in Figs. 4.1 and 4.2. Fig. 4.1 is collectively representing the in-plane as well as out-of-plane directions, while Fig. 4.2 is indicating separately both in-plane [left side] and out-of-plane [right side]) emission. Azimuthal distributions which are peaked at 0^o and 180^o exhibit predominantly in-plane emission, while ϕ distributions peaked at $\pm 90^o$ signify out-of-plane emission. The term elliptical, initially, was known with the names like “Squeeze-out”, “rotational motion”, or “anisotropic flow”, because the shapes of ϕ distributions at mid rapidity resemble ellipse with a major axis along the x-axis (in-plane emission) or y-axis (out-of-plane emission).

Out-of-plane elliptical flow, which occurs in non-central collisions, is an interesting phe-

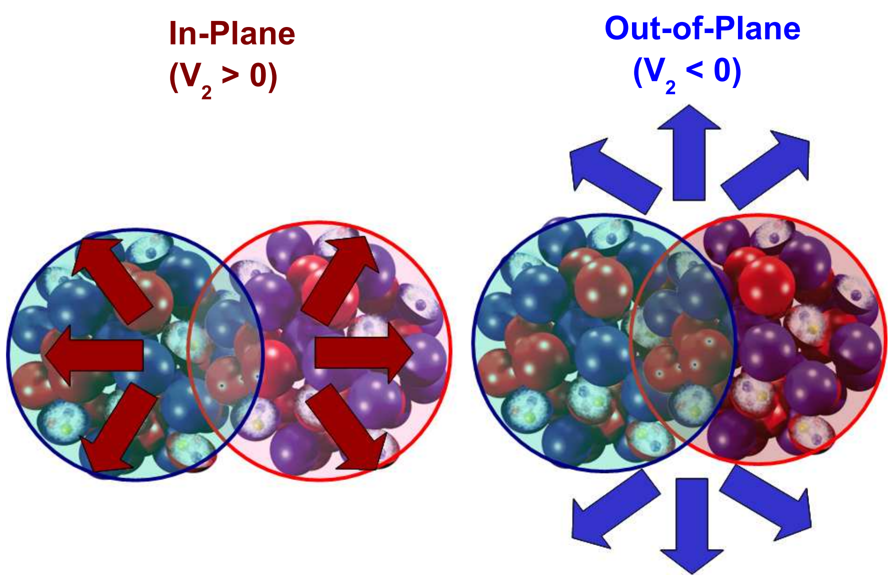

Figure 4.2: In-plane (left side) and out-of-plane (right side) emission of nucleons in the reaction plane and perpendicular to reaction-plane, respectively, is represented. This concept will give rise to transition energy at certain incident energy.

nomena which has been observed at incident energies ranging from 100 MeV/nucl. to ≈ 4 GeV/nucl. The following two factors are responsible for out-of-plane emission at mid rapidity: (1) The pressure build up in the compression stage compared to the energy density, and (2) The passage time for the removal of the projectile- and target-like spectator of the Fireball model. If the participant zone emits particles at an early stage of the collision, the spectator pieces may still be close enough to cause pressure gradients in the out-of-plane direction.

4.2.2 Fourier expansion's second harmonic as elliptical flow

The elliptical flow is a measure that quantifies the azimuthal anisotropy of the momentum distribution. Specifically, we fit the azimuthal distribution of nucleons about the reaction plane with a Fourier expansion of the form:

$$\frac{dN}{d\phi} = a_0 \left[1 + a_1 cos(\phi) + a_2 cos(2\phi)\right], \tag{4.3}$$

The elliptical flow is quantified in term of a_2 coefficient. The ratio of the out-of-plane to in-plane emission, called the number squeeze-out ratio by Gutbroad *et al.* [71], is defined by the particles emitted perpendicular to the reaction plane divided by the number of the particles emitted in the reaction plane at mid rapidity and is given by

$$R_N = \frac{N(90^o) + N(-90^o)}{N(0^o) + N(180^o)}, \tag{4.4}$$

where N(ϕ) represents the summed number of particles in a 90^o wedge centered at ϕ. More explicitly, it can be written as:

$$R_N = \frac{\int_{45^o}^{135^o} \frac{dN}{d\phi} d\phi \; + \; \int_{-135^o}^{-45^o} \frac{dN}{d\phi} d\phi}{\int_{-45^o}^{45^o} \frac{dN}{d\phi} d\phi \; + \; \int_{135^o}^{225^o} \frac{dN}{d\phi} d\phi} \tag{4.5}$$

According to this definition, $R_N < 1$ and > 1 are related to a preferential emission of the matter in the reaction plane and out-of-plane, respectively, while $R_N = 1$ corresponds to a perfect azimuthally isotropic distribution.

Interestingly, R_N can be expressed in term of a_2 coefficient from the Fourier expansion taking into account that directed flow coefficient a_1 should be zero at mid rapidity ($y_{c.m.} = 0$). Therefore, inserting Eqn. 4.3 into 4.5:

$$R_N = \left(\frac{[1 + a_2 Cos(180^o)] \; + \; [1 + a_2 Cos(-180^o)]}{[1 + a_2 Cos(0^o)] \; + \; [1 + a_2 Cos(360^o)]} \right)_{y_{c.m.}=0}, \tag{4.6}$$

which further reduces to

$$R_N = \frac{1 - a_2}{1 + a_2} \tag{4.7}$$

Further for the elliptical flow, in term of particle momentum, it is determined from the average difference between the square of the x and y components of particle transverse momentum provided the beam direction along z axis and the reaction plane on the x-z plane as usual:

$$V_2 = \langle \frac{p_x^2 - p_y^2}{p_x^2 + p_y^2} \rangle, \tag{4.8}$$

where p_x is in the reaction plane, while p_y is perpendicular to the reaction plane. This V_2 is a measure of the aspect ratio of the flow ellipsoid. A positive value of V_2 describes the in-plane enhancement of the particle emission i.e. a rotational behavior. On the other hand, a negative value of V_2 shows the squeeze-out effects perpendicular to reaction plane.

V_2 can be related to the Fourier coefficient a_2 by recognizing that

$$\langle \frac{p_x^2 - p_y^2}{p_x^2 + p_y^2} \rangle = \langle cos(2\phi) \rangle \tag{4.9}$$

and since $\langle cos(2\phi) \rangle$ corresponds to $a_2/2$ in the Fourier expansion of Eqn. 4.3,

$$V_2 = \frac{a_2}{2}. \tag{4.10}$$

On the basis of this, R_N can be expressed in term of V_2 as:

$$R_N = \frac{1 - 2V_2}{1 + 2V_2} \tag{4.11}$$

Eqns. 4.7, 4.10 and 4.11 give the expressions for relating the Fourier coefficient a_2 to other methods for measuring anisotropy. In the present analysis, V_2 is the chosen elliptical flow representation.

4.2.3 Disappearance of elliptical flow

A promising and useful feature of the elliptical flow is the existence of transitions between two forms of the observable. These transitions amount to measuring "zeros" in the flow excitation functions, or the energy dependence of the flow variables.

Fig. 4.3 is a schematic representation of the elliptical flow excitation functions for nucleons over a wide range of beam energies. Dashed area of the curve at higher incident energies represent studies that are currently underway and the dashed area in the NSCL energy regime represents the energy range studied in this chapter. The following transitions are believed to be present in the excitation functions, indicated by stars($\star$):

1.The transition from the in-plane to out-of-plane elliptical flow in the NSCL and near SIS

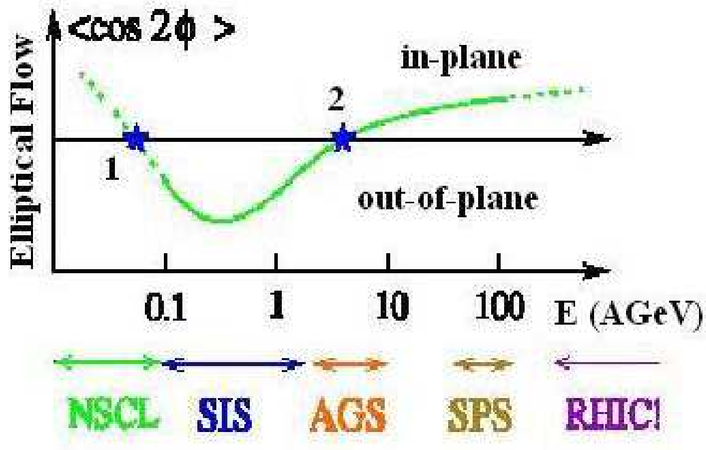

Figure 4.3: Schematic behavior of the elliptical flow as a function of the beam energy. The figure is taken from the Ref. [162].

energy region;

2.The transition from the out-of-plane to in-plane elliptical flow at AGS beam energies.

The first one is the object of study in this thesis and will be explained in detail in the results and discussion section.

Transition region **1** in Fig. 4.3 corresponds to the change in the direction of preferred fragment emission from the compressed participant region. The energy in this energy region at which elliptical flow reduces to zero is known as transition energy. At energies below the transition energy, emission is primarily in the reaction plane (ϕ distribution is peaked at $0^o, 180^o$). Above the transition energy, a maximum emission appears in the direction perpendicular to the reaction plane on both sides (known as squeeze-out) In other words, one can say that the azimuthal emission pattern is primarily out-of-plane, signified by peaks at $\pm 90^o$.

Transition **2** in the Fig. 4.3 has been studied extensively in the past couple of years by experimental groups at the AGS energy. The most interesting results are from the E895 collaborations, which measured the proton elliptical flow in ${}_{79}Au^{197}$ + ${}_{79}Au^{197}$ collisions for beam energies of 2-8 GeV/nucl. [74]. They observed the elliptical flow excitation exhibits a cross-over at $\approx$ 4 GeV/nucl.

4.3 Results and Discussion

For the present analysis, simulations are carried out for thousands of events for the reaction of ${}_{79}Au^{197}$+${}_{79}Au^{197}$ at a semi-central geometry using a hard NEOS. The entire analysis in this chapter is performed for light charged particles (LCP's) [1$\leq$ A $\leq$ 4]. The reaction conditions and fragments are chosen on the basis of the availability of experimental data [61, 62, 63]. As noted in Ref. [104], the relativistic effects do not play a significant role at these incident energies, and the intensity of sub-threshold particle production is very small. In recent years, more sophisticated and complicated algorithms have also become available in the literature [111]. All calculations are performed at t = 200 fm/c using semi-central impact parameter $\hat{b} = 0.3$. This time is chosen as the saturation of the collective flow [64, 65].

4.3.1 Rapidity distribution

As our purpose in the present study is to understand the effects of participant–spectator matter on the excitation function of elliptical flow, we will concentrate on the rapidity distribution only [160]. The important concept of spectators and participants in collisions was first introduced by Bowman *et al.* [163] and later employed for the description of wide-angle energetic particle emission by Westfall *et al.* [164]. The two nuclei slamming against each other can be viewed as producing cylindrical cuts through each other. The swept-out nucleons or participants (from the projectile and the target) undergo a violent collision process. In the meantime, the remnants of the projectile and the target continue with largely undisturbed velocities and are much less affected by the collision process than the participant nucleons. On one hand, this picture is supported by features of the data [62] and on the other hand by dynamic simulations [69]. During the violent stage of a reaction, the spectators can influence the behavior of the participant matter. Following the same reasoning, we are

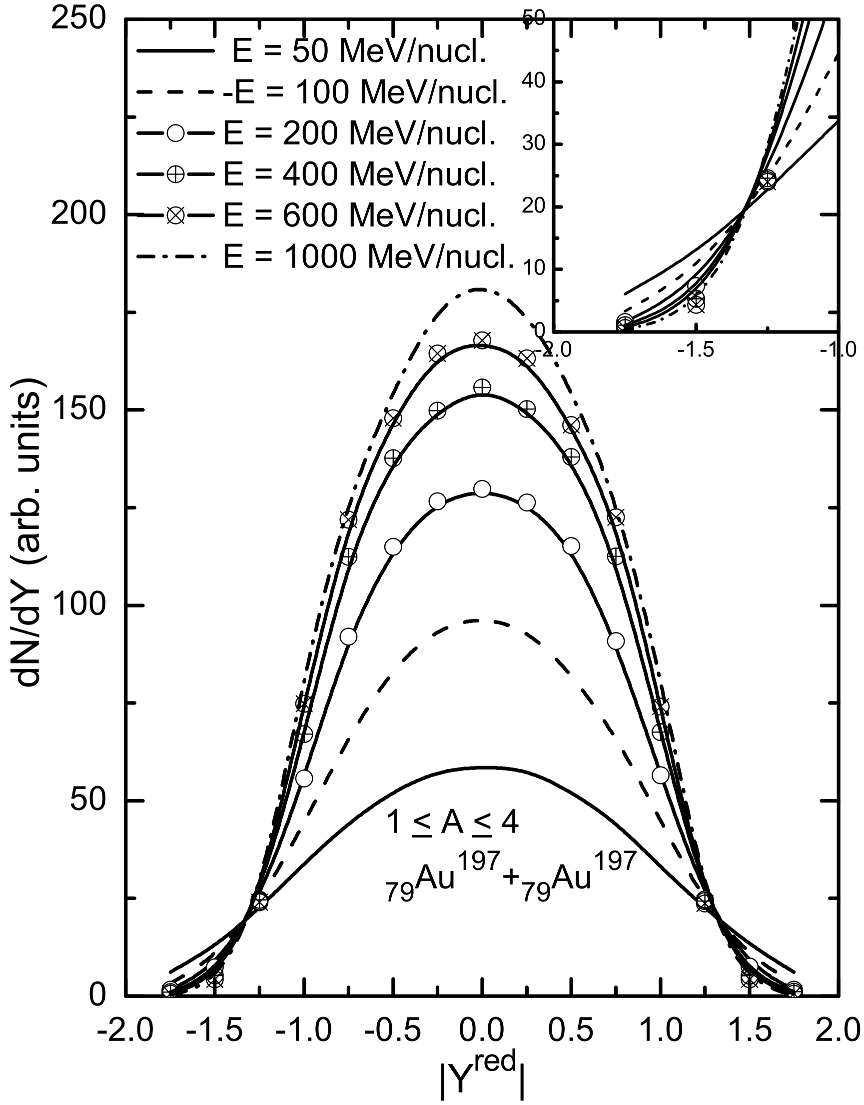

Figure 4.4: Rapidity distribution dN/dY as a function of $Y_{c.m.}/Y_{beam}$ at different incident energies ranging from 50 to 1000 MeV/nucl. for LCP's using $\hat{b} = 0.3$. The inset shows only one side of the rapidity distribution.

dividing the rapidity distribution into different cuts in terms of the parameter $Y_{c.m.}/Y_{beam}$, which is given as:

$$Y(i) = \frac{1}{2}\ln\frac{E(i)+P_z(i)}{E(i)-P_z(i)}, \tag{4.12}$$

where $E(i)$ and $P_z(i)$ are, respectively, the total energy and the longitudinal momentum of i^{th} particle.

As we are interested in studying the effect of the rapidity distribution on the incident-energy dependence of elliptical flow, one has to understand dN/dY as a function of $Y_{c.m.}/Y_{beam} = Y^{red}$ at different energies. To this end, we display in Fig. 4.4 the rapidity distribution for LCP's at different incident energies. The rapidity distribution is found to vary drastically throughout the range of $|Y^{red}| \leq 1.75$.

This indicates a compressed or participant zone around zero value and the decay into the spectator zone towards both sides of the zero value. However around the zero value, the region between -0.1 and 0.1 is specified as the mid-rapidity region in the literature [62, 156]. The decay from -0.1 towards the negative side approaches a target-like spectator, while the other side is known as a projectile-like spectator. Interestingly, these regions are found to be affected drastically by the incident energy. With increasing incident energy, the number of particles is increasing in the region from -1.25 to 1.25, while it is decreasing away from this region on both sides. The inset in the figure clearly shows the change in behavior around -1.25, which is also true for the other side. The rapidity distribution is also often used as the thermalization source in the literature [64]. On this basis, we have divided the rapidity distribution into five different zones, of which three include $|Y^{red}| < 0.1$ (participant zone), while other two exclude this region (target and projectile spectator). These zones are as follows:

(i) From $-0.1 \leq Y^{red} \leq 0.1$ with increments of 0.2 on both sides up to $-1.5 \leq Y^{red} \leq 1.5$.

(ii) From $0 \leq Y^{red} \leq 0.1$ with increments of 0.2 on the latter side up to $0 \leq Y^{red} \leq 1.5$.

(iii) From $-0.1 \leq Y^{red} \leq 0$ with decrements of 0.2 the on the former side up to $-1.5 \leq Y^{red} \leq 0$.

(iv) From $Y^{red} \geq 0.1$ with increments of 0.2 up to $Y^{red} \geq 1.5$.

(v) from $Y^{red} < -0.1$ with decrements of 0.2 up to $Y^{red} < -1.5$.

4.3.2 Incident energy dependence of elliptical flow on the basis of various rapidity distributions

Let us now understand the effect of these rapidity cuts on the excitation function of elliptical flow. In Fig. 4.5, we present the excitation function of elliptical flow for the first condition. This condition is a mixture of the participant and the spectator zone from projectile as well as target matter. There are two points to discuss here. One is the change in the elliptical flow with the incident energy, and the other is the effect of the bin size on the elliptical flow. The elliptical flow evolves from a positive value, rotational-like emission to a negative value, collective expansion with increasing incident energy. In other words, a transition from in-plane to out-of-plane behavior takes place. The energy at which this transition takes place is known as the transition energy. This transition is due to the competition between the mean field at low incident energies and NN collisions at high incident energies. The incident-energy dependence of the directed flow also shows a type of transitions from negative to positive values, which is known as the balance energy [64, 65]. After this transition, the strength of the collective expansion overcomes the rotational-like motion [165]. This leads to an increase in out-of-plane emission to a maximum around 400 MeV/nucl. This maximum is further supported by the nuclear stopping at 400 MeV/nucl. [78].

Beyond this energy, the elliptical flow decreases indicating a transition to preferentially in-plane emission [74]. This rise-and-fall behavior of the elliptical flow in the expansion region is due to the variation in the passing time t_{pass} of the spectator and the expansion time of the participant zone [62]. In a simple participant–spectator model, $t_{pass} = 2R/(\gamma_s v_s)$, where R is the radius of the nucleus at rest, v_s is the spectator velocity in the center-of-mass frame, and γ_s the corresponding Lorentz factor. Due to the comparable values of the passing time and the expansion time in the collective expansion region up to 400 MeV/nucl., the elliptical flow results in an interplay between fireball expansion and spectator shadowing. In other words, due to the comparable duration of the two times (the fireball expansion and spectator shadowing), the participant particles that are responsible for spectator shadowing are deflected out of the plane and are thus more squeezed out.

However, in the energy range from 400 MeV/nucl. to 1.49 GeV/nucl., t_{pass} decreases from 30 to 16 fm/c (not shown here), implying that overall the expansion gets about two times

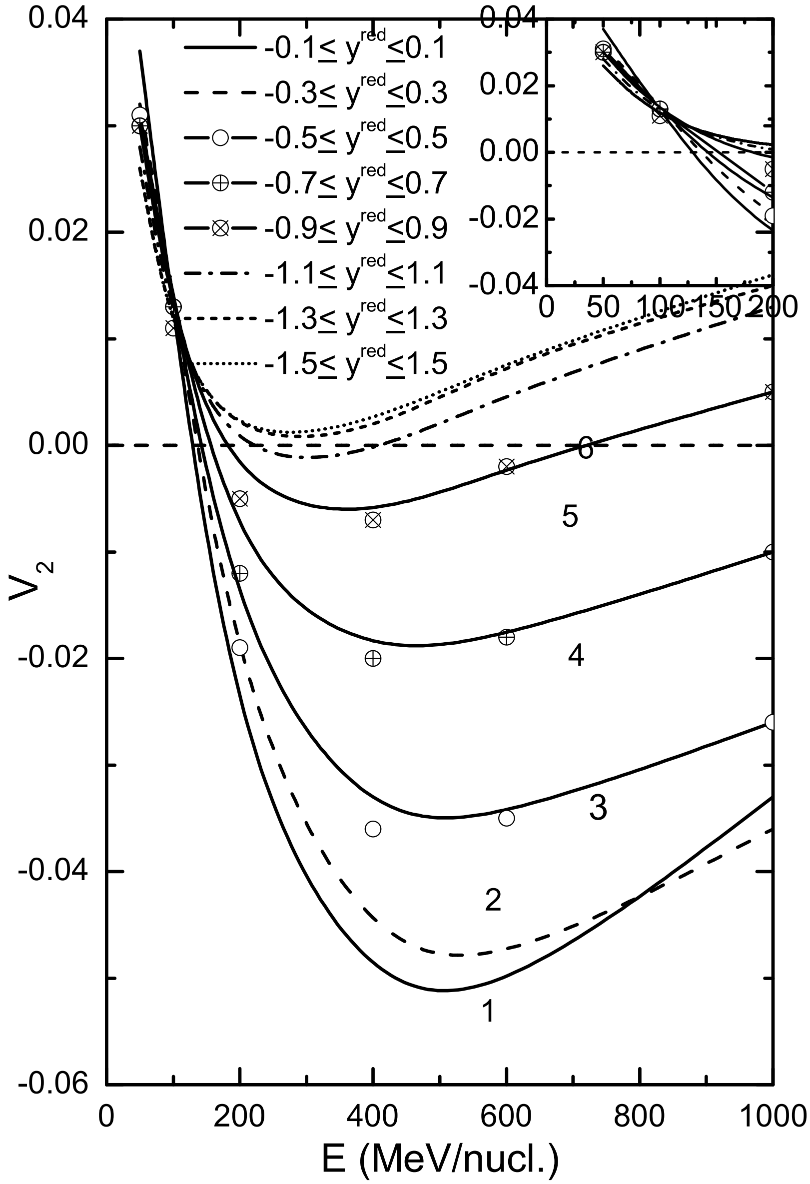

Figure 4.5: Incident-energy dependence of elliptical flow for LCP's for projectile as well as target matter in the mid-rapidity region. The different lines correspond to different sizes of the rapidity bin, which includes participant as well as spectator matter.

faster in this energy region [62]. This is supported by the average expansion velocities extracted from particle spectra [165]. In this case, which corresponds to a passing time much shorter than the expansion time, the participant zone is affected by the shadowing of the spectator at very early times. However, no shadowing effect is observed at later times when the expansion of the participant matter is still in progress. In other words, the participant particles at later times are not blocked by the shadowing of the spectator and hence a decrease is observed in the out-of-plane emission above 400 MeV/nucl.

On the other hand, with the increase in the rapidity region, the transition energy is found to be affected significantly. Using directed flow, the balance energy has also been calculated in the literature (but over the entire rapidity distribution) [65]. The rapidity distribution affects many phenomena in the intermediate-energy region, such as particle production, nuclear stopping [64], and now the elliptical flow. The transition energy increases in the rapidity region between $|Y^{red}| \leq 0.1$ and $|Y^{red}| \leq 1.5$. With this increase in the rapidity region, the projectile- and the target-spectator matter dominates, which will further result in the dominance of the mean field up to higher energies. After the transition energy, the collective expansion is found to have less squeeze-out with increasing rapidity region. In this region, the spectator-zone contribution along with the participant zone starts to come into play. As we know, the passing time for the spectator is significantly less than the expansion time of the participant zone, leading to a decreasing effect of the spectator shadowing on the participant zone. The chances of the participant to move in the plane increases with an increase in the rapidity bin, and hence less squeeze-out is observed with increasing sizes of the rapidity bin. A careful inspection reveals that no transition is observed after $|Y^{red}| \leq 1.1$. This is due to negligible effects of the participant zone when compared to the spectator zone. The inset in the figure shows interesting results: the intersection of all rapidity bins occurs at a particular incident energy. Below and above this energy, the incident-energy dependence of elliptical flow is changing its behavior with the rapidity distribution. It is possible to study the elliptical flow below and above this particular incident energy with a variation in the rapidity distribution.

In Fig. 4.5, we had displayed the effect on the participant as well as the spectator matter from the projectile and the target collectively including the distribution at $|Y^{red}| < 0.1$. It

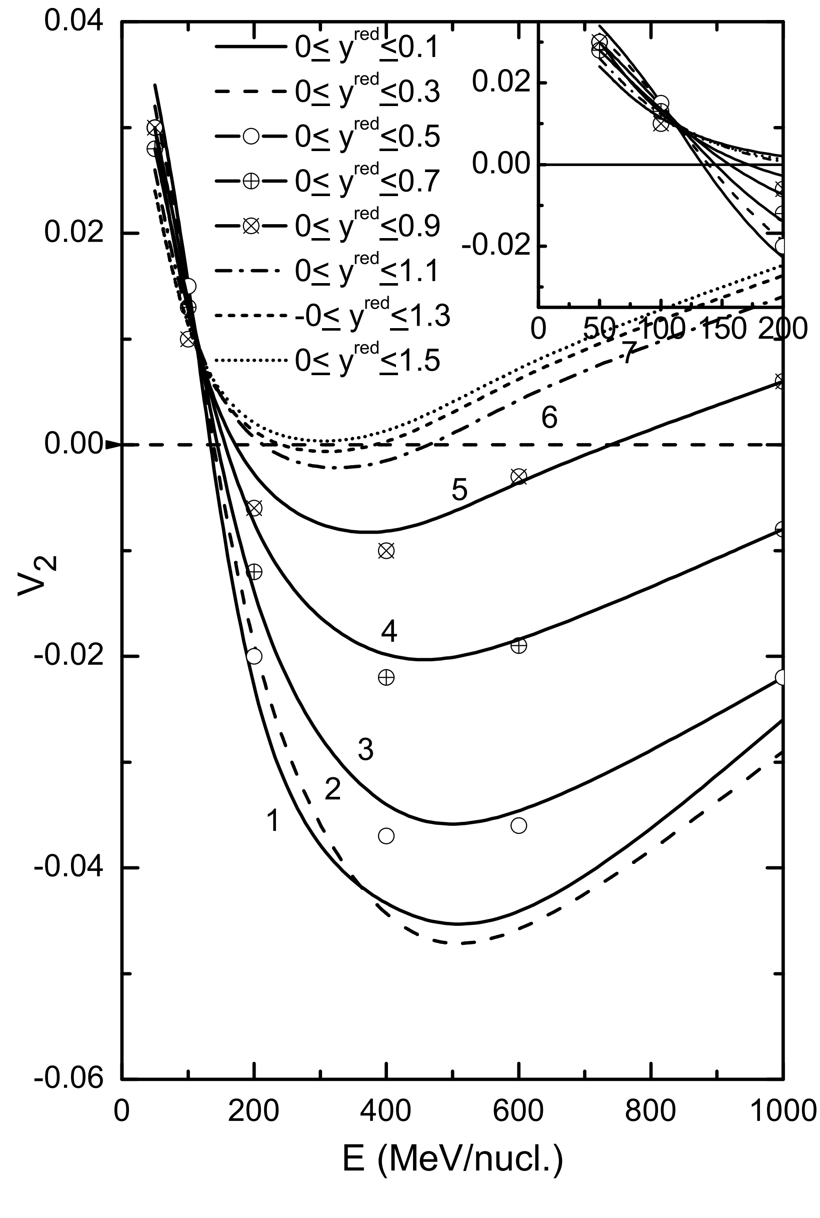

Figure 4.6: Same as Fig. 4.5, but the contribution for fragments arises from the projectile-like matter only. All bins include the mid-rapidity region.

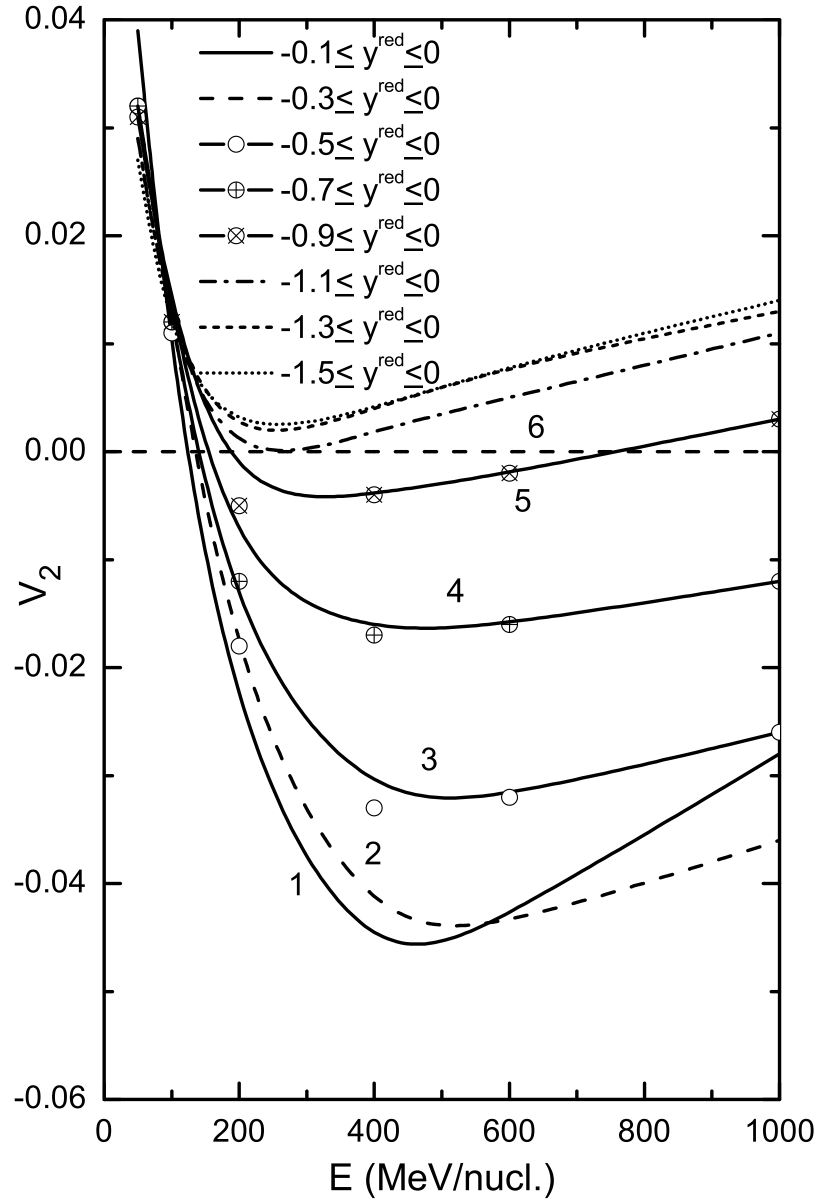

Figure 4.7: Same as Fig. 4.5, but the contribution for fragments arises from the target-like matter only. All bins include the mid-rapidity region.

becomes also quite interesting to study the participant- and spectator-matter contribution to the incident-energy dependence of elliptical flow for projectile as well as target matter separately. To this end, we have displayed in Figs. 4.6 and 4.7 the incident-energy dependence of the elliptical flow from the mid-rapidity to the spectator zone for projectile and target matter. Both of these plots follow the universal behavior of the in-plane to the out-of-plane emission with increasing incident energy, as was apparent in Fig. 4.5. On the other hand, the effect of the rapidity bins is also quite similar to that shown in Fig. 4.5.

If one inspects the maximum squeeze-out values in Figs. 4.5-4.7 around 400 MeV/nucl., one finds that less squeeze-out is observed for projectile matter and spectator matter separately, as compared to projectile and target matter collectively. However, it is almost same for the projectile or target matter separately. This is obvious because when a rapidity bin extends from 0 to 0.1 or -0.1 to 0, then the participant zone is less in comparison to the region from -0.1 to 0.1. This is further supported by Fig. 4.7, in which the rapidity distribution for different bins is displayed. This is true for all the bins under investigation. The effect of the rapidity distribution on the transition energy will be discussed later under different conditions.

One notices from the above figures that major contributions to the elliptical flow come from the mid-rapidity region. One can further infer a fall of the elliptical flow if the mid-rapidity region is excluded. To see this, we have excluded the $|Y^{red}| < 0.1$ region and plotted the incident-energy dependence for projectile and target matter from the participant to the purely projectile- or target-spectator matter in Figs. 4.8 and 4.9, respectively. The noted behavior is entirely different from that shown in the previous three figures. We now proceed to discuss these differences.

(a) The behavior of rise and fall in the elliptical flow at a particular incident energy is present as in the previous figures, but no transition from in-plane to out-of-plane emission is observed. For all incident energies, value of the elliptical flow remains positive. However, some competition is observed at low incident energies around 150 MeV/nucl. This is due to the dominance of the attractive mean field over the spectator matter, which restricts the effects of the participant zone.

(b) A higher value of the in-plane flow is observed at incident energies high compared

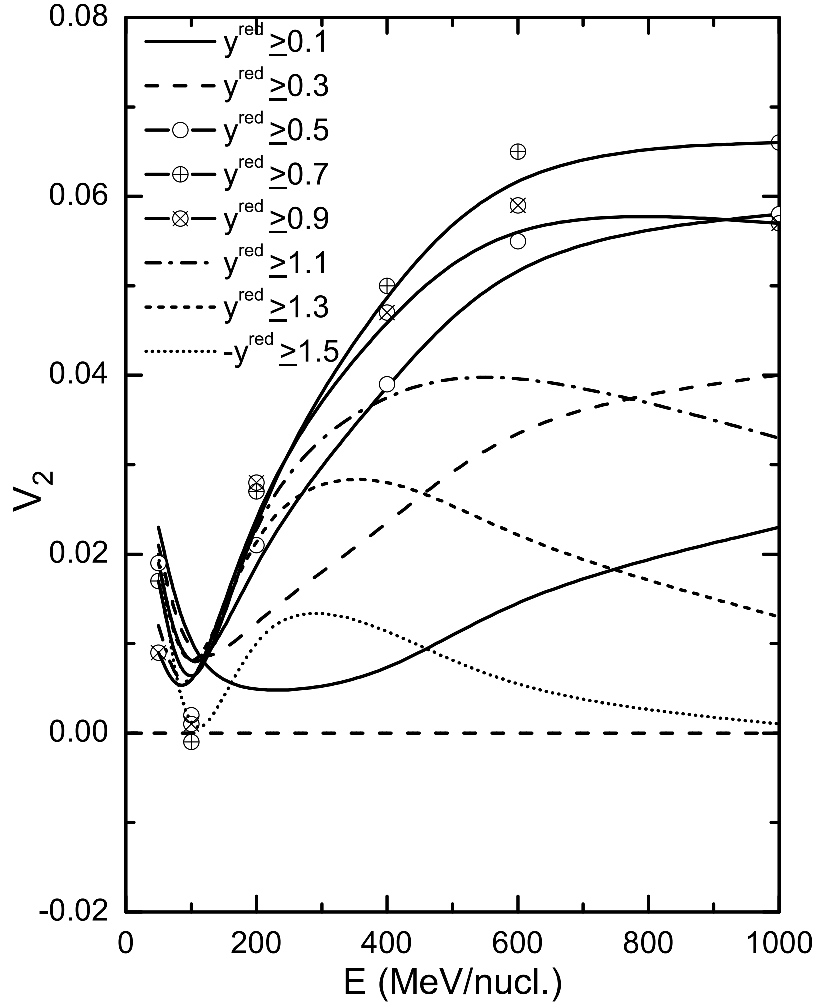

Figure 4.8: Same as Fig. 4.5, but the contribution for the fragments is from the projectile-like matter only. All the bins exclude the mid-rapidity region. In this case, we move from the participant and spectator contribution towards the spectator contribution.

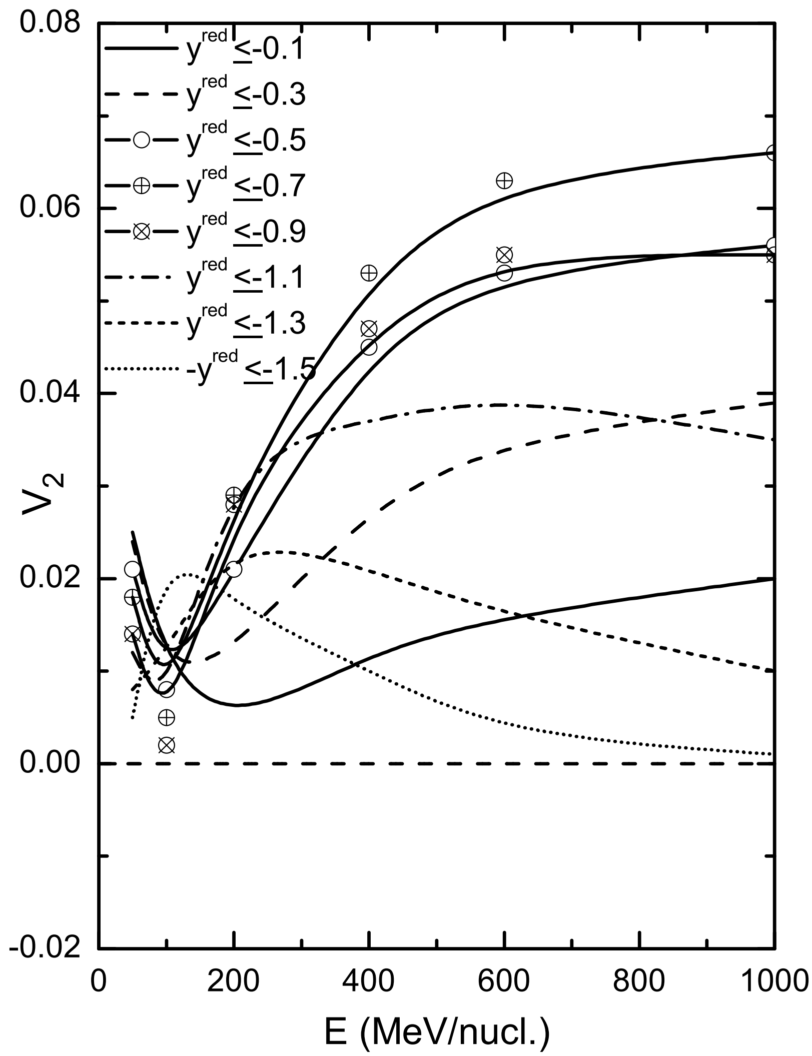

Figure 4.9: Same as Fig. 4.5, but the contribution for fragments is from the target-like matter only. All the bins exclude the mid-rapidity region. In this case, we move from the participant and spectator contribution towards the spectator contribution.

to the low incident energies up to $Y^{red} \geq 0.7$ in Fig. 4.8 for the projectile matter and $Y^{red} \leq -0.7$ for the target matter, which is in contrast to the previous figures. This is due to the fact that at low incident energies, the passing time of the spectator and the expansion time of the participant are comparable, while with increasing incident energies, the passing time is found to decrease relative to the expansion time. This will reduce the shadowing effect at higher incident energies on the particles of the participant zone, and it results in an enhanced plane flow. Moreover, higher values of the in-plane flow at higher incident energies are due to the absence of the most compressible region from the region $|Y^{red}| \leq -0.1$, which competes with the mean field of the spectator to a great extent.

(c) With an increase in the rapidity region from the participant and the spectator ($Y^{red} \geq 0.1$) to the purely spectator matter ($Y^{red} \geq 1.5$), the dominance of the in-plane flow occurs up to $Y^{red} \geq 0.7$. Past this region, a sudden decrease of the in-plane flow up to $Y^{red} \geq 1.5$ is apparent in Fig. 4.8, which is also true for Fig. 4.9. The decrease of the in-plane flow at $Y^{red} \geq 0.7$ can be explained with the help of Fig. 4.4. After this region, contribution of the participant is almost negligible, and the size of the spectator also decreases. Due to the decreasing size of the spectator matter, violence of the incident energy, and short passing time of the spectator, particles (which were previously staying in the plane due to their heavier size) now start to leave the plane. Hence, minimum in-plane flow is observed for $Y^{red} \geq 1.5$ where only 5–7 particles exist, as is apparent from Fig. 4.4. The same behavior is observed in Fig. 4.9.

From the above findings, we conclude that mid-rapidity region is responsible for the collective flow associated with light charged particles. Hence, in the coming section, we compare our theoretical results with various experimental collaborations.

4.3.3 Comparison with experimental findings

Going through all the aspects of the rapidity distribution, it is important to include the mid-rapidity region $|Y^{red}| < 0.1$ in the study of elliptical flow in heavy-ion collisions. In order to compare the findings with experimental results, one must have the transition from in-plane to out-of-plane emission, which is shown in Figs. 4.5–4.7. Moreover, more negative values are observed in Fig. 4.5 than in the other two figures. This discussion suggests to compare the findings of Fig. 4.5 with the experimental results obtained by different collaborations.

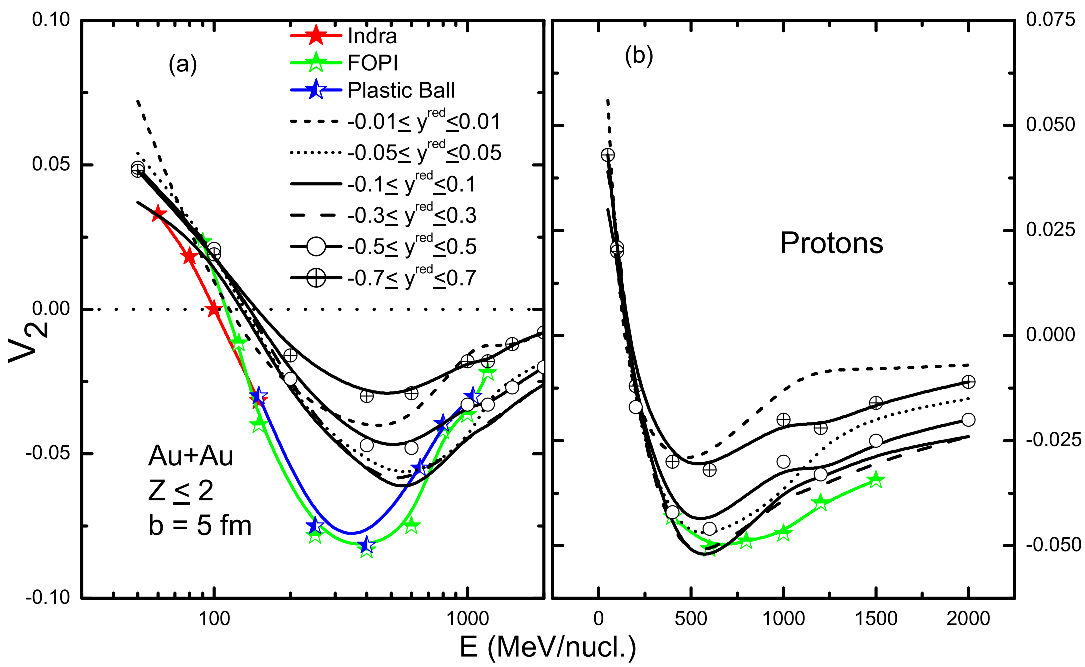

Figure 4.10: (Color online) Comparison of the results for the incident-energy dependence of the elliptical flow including different rapidity bins with experimental results from different collaborations [61, 62]. The left-hand side is for $Z \leq 2$ particles, while the right-hand side pertains to protons.

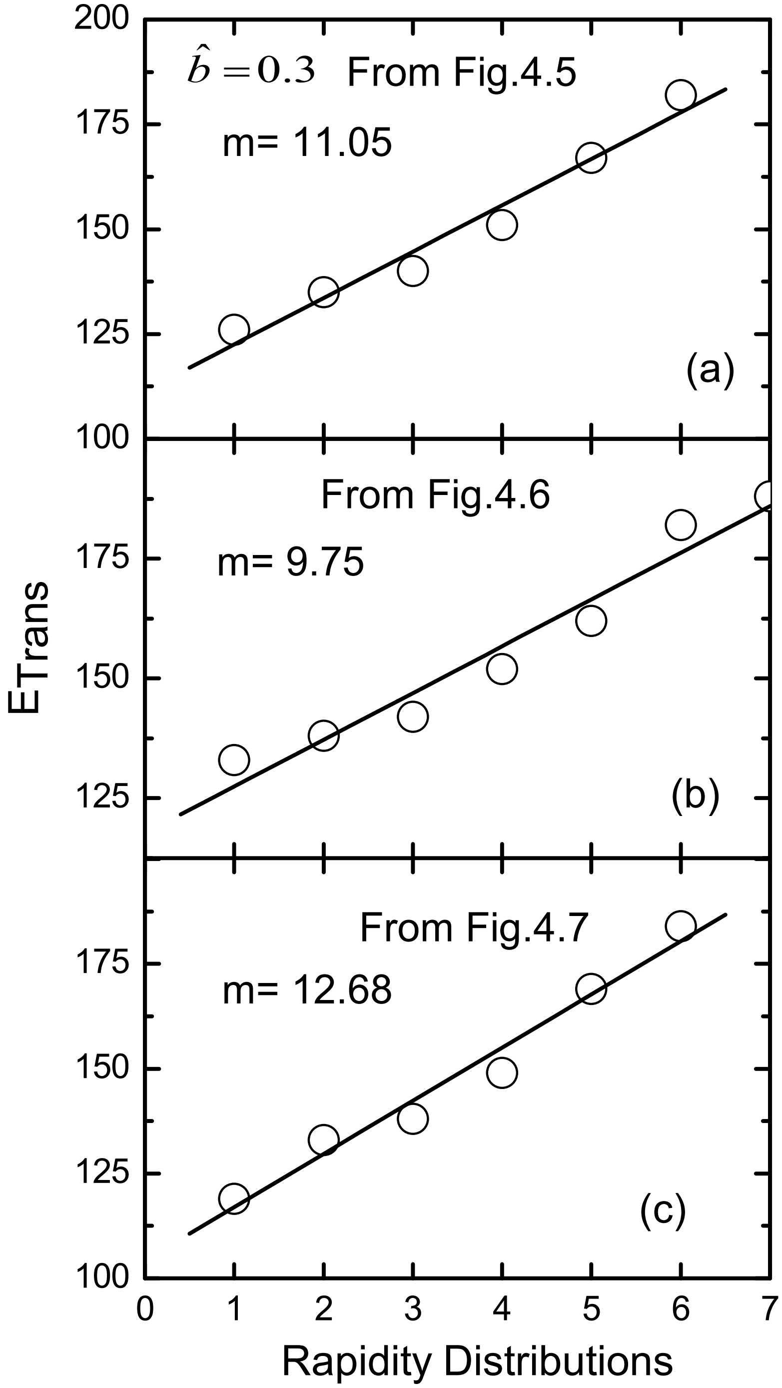

Figure 4.11: Dependence of the rapidity distributions on the transition energy. The transition energies are extracted from Figs. 4.5, 4.6, and 4.7 for the top, middle, and bottom panels, respectively. The numbering from 1 to 7 represents the different rapidity bins from the respective figures mentioned above. All panels are parameterized with the straight-line interpolation y = mx+c, where m is the slope displayed in the respective panels.

Such a comparison is displayed in Fig. 4.10 for LCP's ($Z \leq 2$) and for protons. The curves have a trend similar to that displayed in Fig. 4.5. Interestingly, it is apparent that there is a competition in the rapidity bins $|Y^{red}| \leq 0.1$ and $|Y^{red}| \leq 0.3$. After this competition, a systematic deviation is observed in the elliptical-flow values from the data values with an increase in the rapidity bin. There are some deviations in the middle region for LCP's between theory and data, while the data is well explained for the protons. From this, it is concluded that one can vary the mid-rapidity region from $|Y^{red}| \leq 0.1$ to $|Y^{red}| \leq 0.3$ to get a better agreement with the experimental data. However, the discrepancy with the data for LCP's can be reduced by varying the isospin-dependent cross-sections.

4.3.4 Power law dependence of transition energy

Last, but not least, the rapidity-distribution dependence of the transition energy is displayed in Fig. 4.11. The top, middle, and bottom panels represent the transition energies extracted from Figs. 4.5–4.7, respectively. The numbering from 1 to 7 in the figure refers to the bin size in the respective figure. All curves are fitted to a straight-line equation y=mx+c, where m is the slope of the line, and c is a constant. The transition energy is found to be sensitive to the different bins of rapidity distributions. It is observed that the transition energy increases with the size of the rapidity bin for LCP's. The necessary condition for the transition energy is that the mid-rapidity region must be included in the rapidity-distribution bin. It is also observed that no transition energy is obtained when the rapidity-distribution region extends away from $|Y_{red}| \leq 1.1$. This is due to the dominance of the spectator matter, which lies in the plane instead of out of the plane. The transition energy is found to be weakly sensitive to the choice of the different types of rapidity distributions (projectile–target, or projectile, or target), where we have included the mid-rapidity region. However, the transition energy is found to disappear when the mid-rapidity region is excluded. The system-size dependence of the transition energy is also studied in the present work and by other authors for different kinds of fragments [156]. Recently, we have investigated the fragment-size dependence of the transition energy under the influence of different NEOS, nucleon–nucleon cross-sections, etc. [64, 65]. These studies were made at a fixed rapidity bin. A detailed analysis of the transition energy with rapidity distributions has revealed many interesting aspects for the first time.

4.4 Summary

Within the semi-classical transport simulations of energetic semi-central collisions of the ${}_{79}Au^{197} + {}_{79}Au^{197}$ reaction, we have carried out a new investigation of the interplay between the participant and spectator regions in terms of rapidity distributions. The maxima and minima in the incident energy dependence of elliptical flow are produced by different contributions of the passing time of the spectator and the expansion time of the participant. The shadowing of the spectator matter plays an important role up to later times due to the comparable magnitude of the passing and expansion times up to energies of 400 MeV/nucl. However, at high energies the shadowing effect is dominant only at earlier times due to the fact that the passing time is shorter than the expansion time. The transition from in-plane to out-of-plane emission is observed only when the mid-rapidity region is included into the rapidity bin. Otherwise, no transition is observed. The transition energy is found to be strongly dependent on the size of the rapidity bin, while only weakly dependent on the type of the rapidity distributions. The transition energy is parameterized by a straight-line interpolation. From our preliminary results, we can conclude that the isospin content of the colliding partners ($N/Z = 1.49$) plays an appreciable role in the analysis of elliptical flow in intermediate-energy heavy-ion collisions in terms of (i) the agreement of the results with experimental findings of different collaborations, and (ii) the effect on the elliptical flow by changes in the rapidity bins. A comparison with experimental bins reveals that a competition is observed between the rapidity bins of $|Y^{red}| \leq 0.1$ and $|Y^{red}| \leq 0.3$. To remove this discrepancy in the middle region for LCP's, one has to reduce the strength of nucleon–nucleon cross-section.

Chapter 5

Elliptical flow in nearly symmetric and asymmetric collisions

5.1 Introduction

The study of elliptical flow performed in Chapter 4 is further extended for nearly symmetric and asymmetric colliding nuclei. In the following chapter, we shall deal with the physics interpretation of elliptical flow of different fragments. As stated earlier, Pauli principle blocks majority of the scattering at low incident energies. Therefore, attractive mean field dominates the physics in this energy regime. At intermediate energies, however, an interplay of attractive mean field and repulsive nucleon-nucleon scattering decides the fate of a reaction. Both these regimes together, lead the matter from a fused state to total disassembly. One is also interested to understand the mechanism behind this. Further, the flow of small pieces (fragments) is also of great interest. One is trying to correlate this flow with the nuclear equation of state (NEOS) as well as mass asymmetry of the colliding partners.

In this chapter, we shall present the results of elliptical flow for nearly symmetric and asymmetric reacting nuclei. First of all, we have studied the effect of transverse momentum dependence, impact parameter dependence, system size dependence as well as energy dependence on the elliptical flow in nearly symmetric collisions and then further study has been extended for asymmetric collisions. Moreover, the theoretical results are compared with the experimental data available.

5.2 Results and discussion

5.2.1 Elliptical flow in nearly symmetric collisions

In this study, the free nucleons and different fragments i.e., light mass fragments (LMF's)(2 $\leq$ A $\leq$ 4) and intermediate mass fragments (IMF's)($5 \leq A \leq A_{tot}/6$) are selected to study the elliptical flow analysis. We perform a complete systematic study using the nearly symmetric reactions $_{10}Ne^{20}+_{13}Al^{27}$, $_{18}Ar^{40}+_{21}Sc^{45}$, $_{30}Zn^{64}+_{28}Ni^{58}$, $_{36}Kr^{86}+_{41}Nb^{93}$ at incident energies between 45 and 105 MeV/nucl. We have simulated these reactions over the full collision geometry starting from the central to peripheral one. The fragments are constructed within minimum spanning tree (MST) method [27] as presented in detail in Chapter 3.

Transverse momentum dependence

In Fig. 5.1, the final state elliptical flow is displayed for the free particles (upper panel), LMF's (middle panel), and IMF's (lower panel) at the scaled impact parameter $\hat{b}$ = 0.5. One can see a Gaussian type behavior quite similar to the one reported by Colona and Toro *et al.*, [166]. This Gaussian type behavior is integrated over the entire rapidity range. There is a linear increase in the elliptical flow with transverse momentum upto certain P_t. Obviously particles with larger momentum will escape the reaction zone earlier. After certain transverse momentum, it starts decreasing due to decrease of number of particles in that particular P_t range. In the starting, number of particles increases and the momentum of the corresponding particles average out to a large value and hence large positive value of elliptical flow is obtained. But when the number of particles decreases, then the average value of the momentum of corresponding particles also decreases and hence decrease in positive value of elliptical value. One also sees from the figure, that the elliptical flow of nucleons/LMF's/IMF's is positive in the whole range of P_t which signifies an in-plane emission. Moreover, collective rotation is one of the main mechanisms for inducing the positive elliptical flow in the whole range of P_t. It is also evident from the figure that the peaks of Gaussian shifts toward the lower value of P_t for heavier fragments. The reason is that the emitted free and light charged particles can feel the role of mean-field directly, while the heavier fragments have weak sensitivity [167]. It is also evident from the figure that the

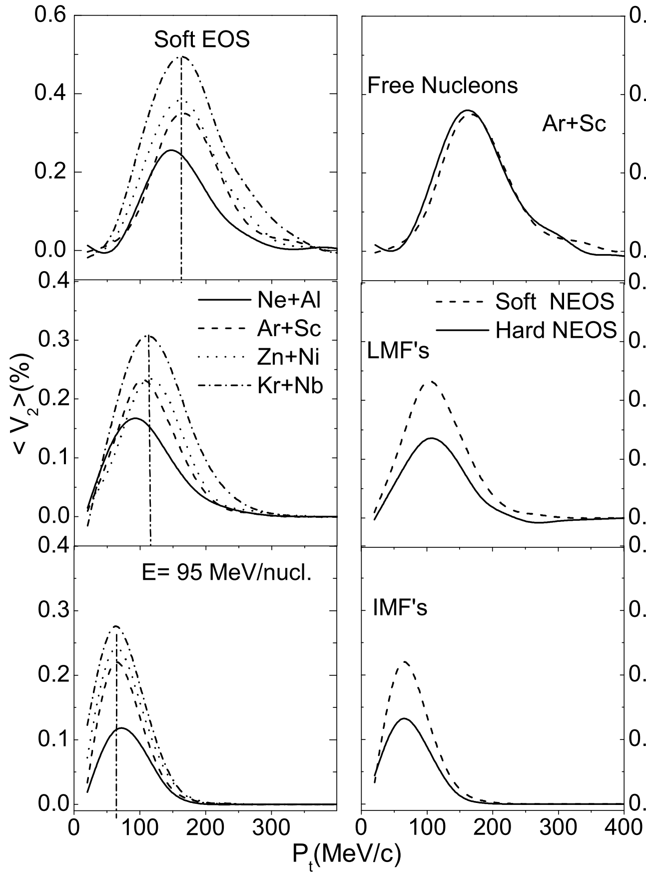

Figure 5.1: The elliptical flow as a function of the transverse momentum at incident energy 95 MeV/nucl. for free particles, LMF's and IMF's in top, middle and bottom panels respectively using $\hat{b} = 0.5$. On the right hand side, elliptical flow for soft and hard NEOS for Ar+Sc system has been displayed.

reactions under consideration have different system mass dependence as well as N/Z ratios. Moreover, the results are found to vary drastically with the change of NEOS. To make this point more clear, we have displayed on the right hand side of the Fig. 5.1, the transverse momentum dependence of elliptical flow using soft and hard NEOS. For this analysis, we choose the reaction of $_{18}Ar^{40} +_{21} Sc^{45}$ at $\hat{b} = 0.5$ and E = 95 MeV/nucl. We can see clear effect of the hard and soft NEOS in the production of light mass fragments (LMF's) and intermediate mass fragments (IMF's). In contrary, very little change is observed in the case of free particles. This is due to the different compressibility values for hard NEOS (K= 380 MeV), and soft NEOS (K= 200 MeV).

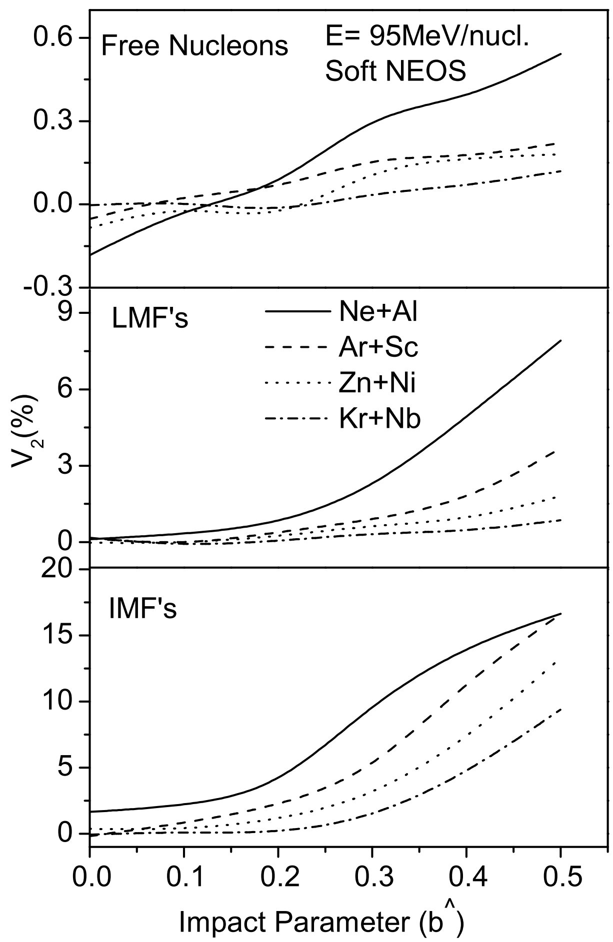

Figure 5.2: The elliptical flow as a function of scaled impact parameter for different systems at incident energy E = 95 MeV/nucl. for free particles, LMF's and IMF's in top, middle and bottom panels respectively.

The investigation of the elliptical flow with scaled impact parameter for the above mentioned systems is displayed in Fig. 5.2. The simulations have been carried out at 95 MeV/nucl. for the scaled impact parameter range between $\hat{b}$ = 0.0 and 0.5. The results for the free nucleons (upper panel), LMF's (middle panel) and IMF's (lower panel) have been shown for all four systems considered in this analysis. The value of the elliptical flow V_2 becomes more positive (in-plane) with the impact parameter. There is an obvious difference among the elliptical flow associated with the free particles (upper panel), LMF's (middle panel), and IMF's (lower panel). This is true at higher impact parameters. One can see the isotropic distribution of the fragments at small impact parameters which turns into anisotropic distribution as we move away towards semi-central zone. For lighter systems, the value of V_2 increases more rapidly with impact parameter. This is due to the azimuthal anisotropy, that becomes larger with the impact parameter and reduces with the beam energy. For semi- central collisions, less number of nucleons participate in the collision process and hence lead to more elliptical flow. Since the production of the intermediate mass fragments is due to the spectator part, the elliptical flow is stronger for the heavier fragments compared to the lighter colliding nuclei.

System size dependence

We further carry out the study of the system size dependence of the elliptical flow of free particles (upper panel), LMF's (middle panel), and IMF's (lower panel) in Fig. 5.3 for different reactions, namely ${}_{10}Ne^{20} +_{13} Al^{27}$, ${}_{18}Ar^{40} +_{21} Sc^{45}$, ${}_{30}Zn^{64} +_{28} Ni^{58}$, ${}_{36}Kr^{86} +_{41} Nb^{93}$ at two different impact parameters $\hat{b} = 0.3$ and $\hat{b} = 0.5$. The elliptical flow varies with the mass number. It has been shown that there is a linear relationship between the system size and particle emission [71, 99]. One can see that elliptical flow starts to approach negative value (i.e. squeeze-out) with composite mass of the system. This is due to the reason that the pressure produced by the Coulomb interactions increases with the system size i.e. heavier systems have much larger Coulomb repulsion. This repulsion will force the fragments to go out-of-plane and hence the elliptical flow starts to approach negative value as one goes from lighter to heavier systems. On the other hand, elliptical flow is observed to be in-plane compared to out-of-plane at higher impact parameters. With the increase in the impact parameter, the participant zone decreases, resulting in an increase in the spectator region, which will lead the fragments to enjoy in-plane as compared to out-of-plane. All the curves are fitted using the function α $\mathrm{C}(A_{tot})^{\tau}$, where C and τ are the fitting parameters.

Energy dependence

In Fig. 5.4, we show the elliptical flow V_2 for the mid-rapidity region $(-0.3 \leq Y \leq 0.3)$ for LMF's $(2 \leq A \leq 4)$ as a function of the incident energy. The rapidity cut is in accordance with the experimental findings. The theoretical results are compared with the experimental

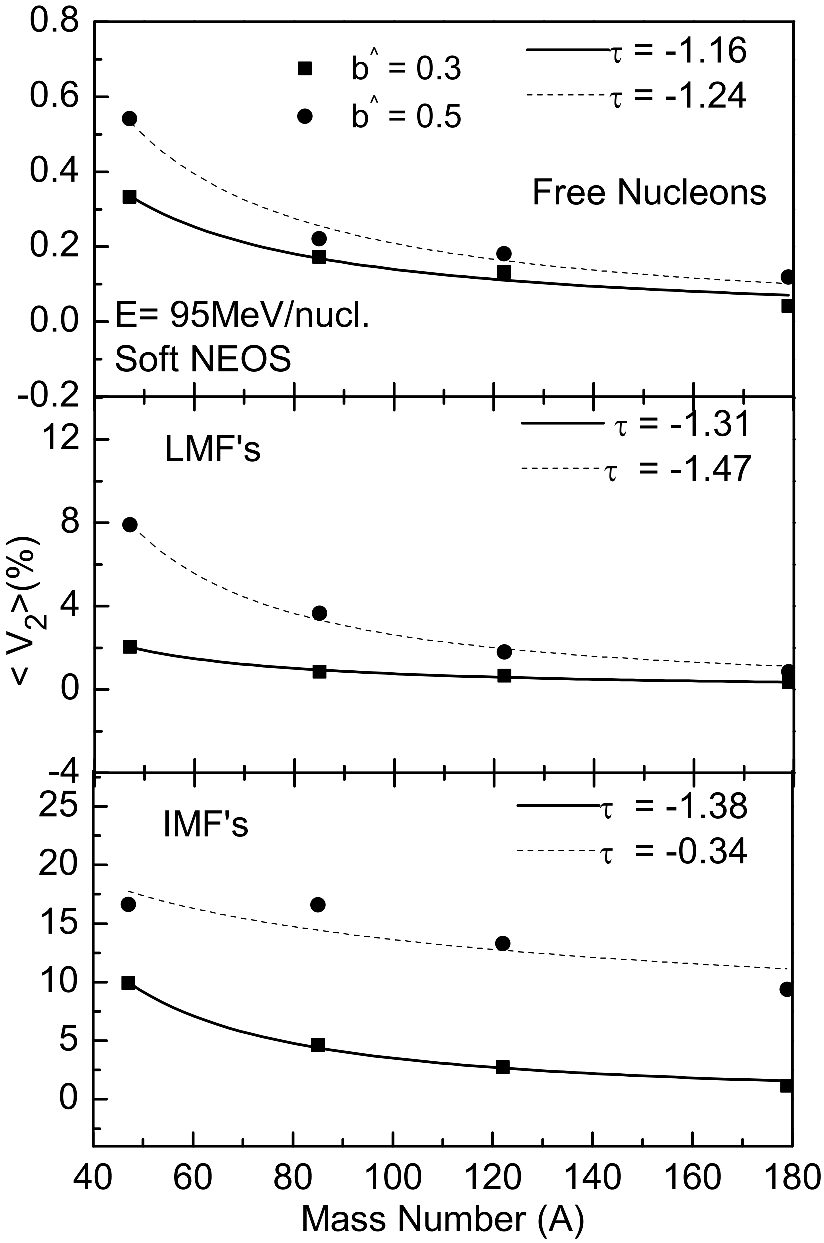

Figure 5.3: The dependence of elliptical flow on the composite mass of the systems for free nucleons, LMF's and IMF's in top, middle and bottom panels, respectively. The curves are fitted using an equation α C$(A_{tot})^{\tau}$.

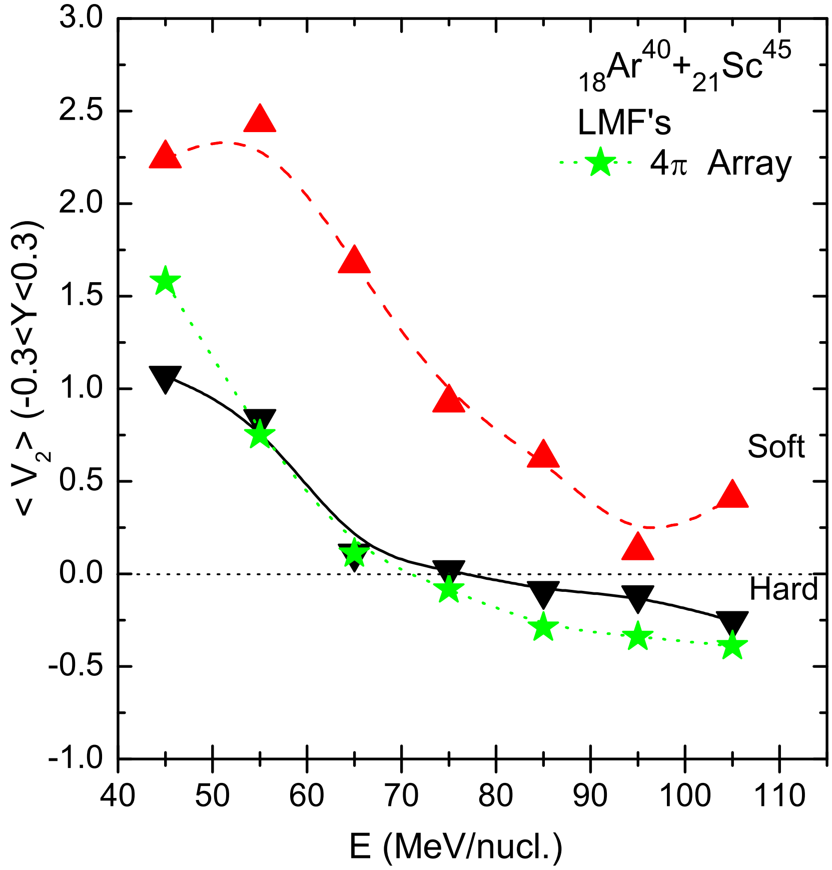

Figure 5.4: The variation of the elliptical flow with beam energy for the reaction of $_{18}Ar^{40}+_{21}Sc^{45}$, using hard and soft NEOS. Here comparison is shown with experimental findings of the 4π Array.

data extracted by the 4π Array group [162]. For the comparison of calculations with experimental findings, we have performed the detailed analysis by taking into account static NEOS. The comparison has been done at the same impact parameter as suggested by Magestro [60, 154, 162] after correction. The general behavior of the elliptical flow calculated with different NEOS's resembles. The elliptical flow evolves from a preferential in-plane (rotational like) emission ($V_2 > 0$), to the out-of-plane (squeeze-out) emission ($V_2 < 0$), with an increase of the incident energies. The elliptical flow decreases with the incident energy. The decrease in elliptical flow is sharp at smaller incident energies (upto 65 MeV/nucl.). This starts saturating at higher incident energies. In other words, the elliptical shape of nuclear flow dominates the physics at low incident energies. One can see from the figure that the transition energies at which the elliptical flow parameter V_2 changes sign from positive to negative are different for different NEOS. The transition from the in-plane emission to out-of plane occurs because the mean-field that contributes to the formation of the compound nucleus becomes less important. At the same time, the collective expansion process (based on the nucleon-nucleon scattering) starts dominating. The competition between the mean-field and the nucleon-nucleon collisions strongly depends on the effective interactions, which leads to the divergence of the transition energies calculated with hard and soft NEOS. Clearly the hard NEOS provides stronger pressure that leads to a stronger out-of plane emission and thus to the smaller transition energy. The difference of elliptical flow between hard and soft NEOS decreases as we move towards the higher incident energies. The elliptical flow calculated with hard NEOS agrees with the 4π Array experimental data. From our analysis, we find that hard NEOS explains the data closely.

5.2.2 Elliptical flow in asymmetric collisions

For the controlled study of the role of mass asymmetry of a reaction, we simulated several thousands events of various reactions by keeping the total reacting mass (= 152 units). While the total mass stays constant, mass asymmetry parameter η is varied by choosing different combinations of projectiles-targets. We shall perform exclusive studies by simulating the reactions of $_{24}Cr^{50} +_{44} Ru^{102}$ ($\eta = 0.3$), $_{16}S^{32} +_{50} Sn^{120}$ ($\eta = 0.5$), and $_{8}O^{16} +_{54} Xe^{136}$ ($\eta = 0.7$) at incident energies between 50 and 250 MeV/nucl. for semi-central impact parameter using a soft NEOS.

Transverse Momentum dependence

In Fig. 5.5, the final-state elliptical flow is displayed for the free particles (A = 1)(upper panel) and light mass fragments (LMF's) [$(2 \leq A \leq 4)$] (lower panel) as a function of transverse momentum (P_t) at an incident beam energy E = 50 MeV/nucl. (left) and 100 MeV/nucl. (right). The different curves in each panel correspond to different mass asymmetries. Here, elliptical flow is summed over all rapidity bins. The figure reveals the following points:

(i) A Gaussian shape is observed for $< V_2 >$ at all mass asymmetries. This Gaussian shaped behavior is quite similar to the one reported by Colona and Toro *et al.*, [166]. Note that these results are integrated over entire rapidity range and

(ii) The neutron-rich system ($_{8}O^{16}+_{54}Xe^{136}$ with N/Z = 1.4) exhibits a weaker squeeze-out flow compared to other reactions and prominent peaks of Gaussian diminishes especially for LMF's. This indicates significant dependence of $< V_2 >$ on the mass asymmetry of colliding pairs. These findings are in agreement with the one reported by Zhang *et al.*, [156]. Moreover, the N/Z effect is more pronounced at E = 50 MeV/nucl.

In Fig. 5.6, we divide the total elliptical flow into contributions from target-like(TL) (left panels), mid-rapidity (middle panels), and projectile-like(PL) (right panels) particles at an incident beam energy E = 50 MeV/nucl. The upper and lower panels represent the free nucleons and LMF's. From the figure, we see that the projectile-like (PL) nucleons and LMF's feel more squeeze out compared to target-like (TL) nucleons/LMF's. At the larger mass asymmetry, only small fraction of nucleons/LMF's experience squeeze out compared to symmetric reactions. This decrease of squeeze out with mass asymmetry happens due to decreasing participant zone. This is in agreement with earlier calculations where fragments were found to exhibit similar trends.

Energy dependence

In Fig. 5.7, we display the variation of excitation function $< V_2 >$ for LMF's as a function of incident energy for entire rapidity region (upper panel) and for mid rapidity region $[-0.1 \leq Y^{red} \leq 0.1]$ (lower panel) only. The general behavior of excitation function of elliptical flow for various mass asymmetries is quite similar. The microscopic behavior, however, depends on the mass asymmetry of the reaction. Interestingly, we find that no transition in the elliptical flow occurs when entire rapidity region is considered. In contrast, a transition from the preferential in-plane (rotational like) emission ($V_2 > 0$) to out-of-plane (squeeze-out) emission ($V_2 < 0$) occurs at mid rapidity zone. This happens due to the fact that the contribution of spectator matter increases with rapidity region, leading to less squeeze-out of the particles in entire rapidity region. On the other hand, the contribution of the participant zone dominates the reaction in mid-rapidity region leading to the transition from in-plane to out-of-plane. This happens because the mean field which contributes to the formation of a rotating compound system becomes less important and collective expansion

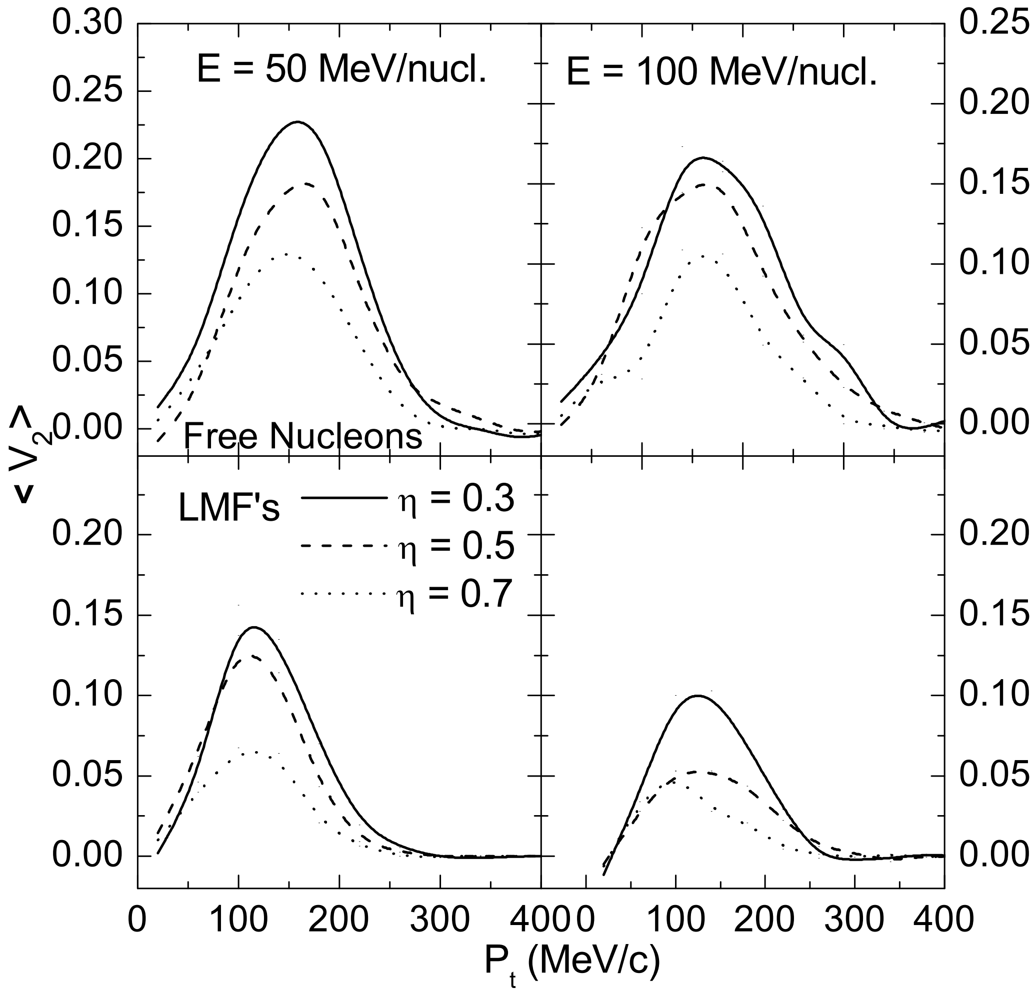

Figure 5.5: The transverse momentum dependence of elliptical flow, summed over all rapidity bins at $\hat{b} = 0.3$ for different mass asymmetries at 50 MeV/nucl. (left) and 100 MeV/nucl. (right) The upper and lower panels represent the free nucleons and light mass fragments (LMF's), respectively.

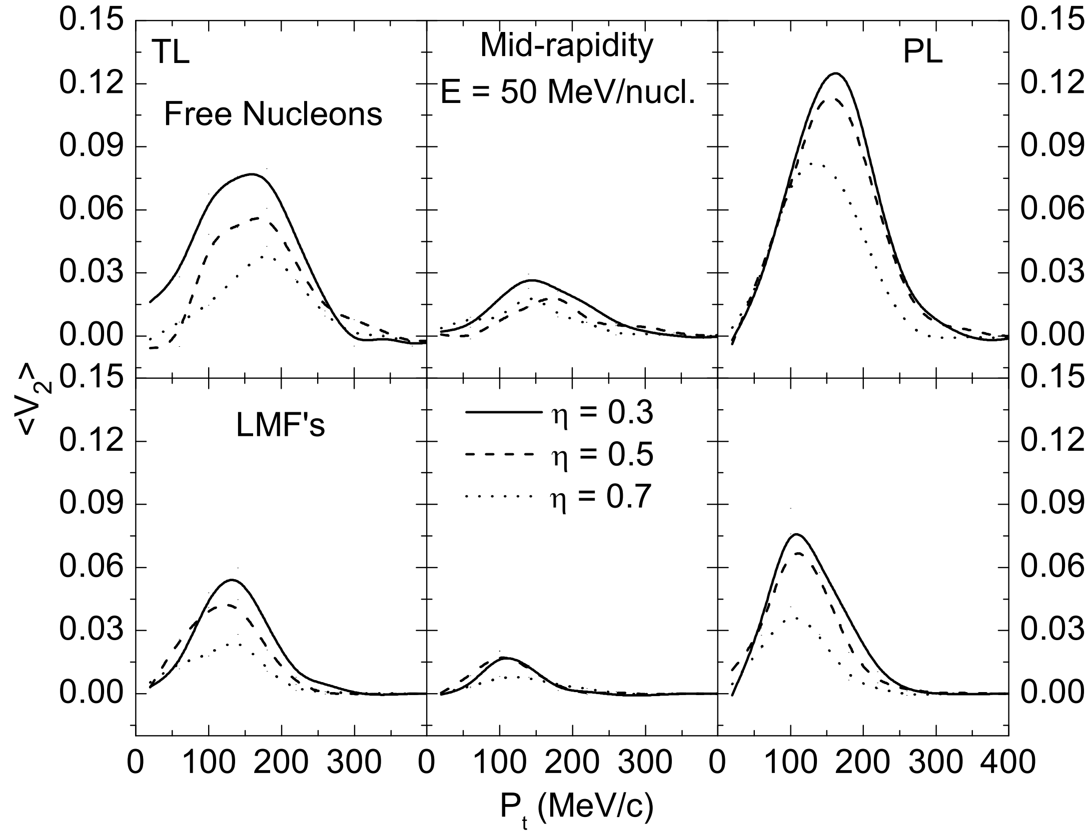

Figure 5.6: The transverse momentum dependence of the elliptical flow at E = 50 MeV/nucl. for different mass asymmetries divided into contributions from target-like, mid-rapidity and projectile-like matter, respectively; the upper and lower panels have same meaning as in Fig. 5.5.

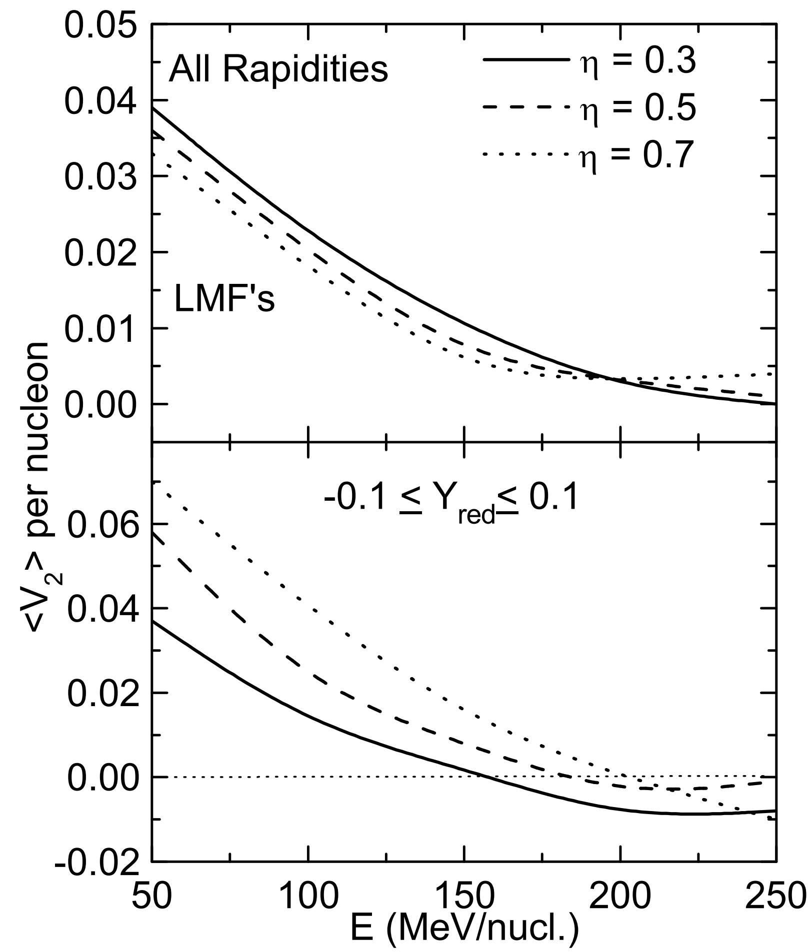

Figure 5.7: The variation of elliptical flow with incident beam energy for different mass asymmetries. The displayed results are at $\hat{b} = 0.3$. Upper panel is integrated over entire rapidity region while lower panel shows results for selected bins only.

process (based on the nucleon-nucleon binary scattering) starts to be predominant [156]. The competition between the mean-field and nucleon-nucleon collisions should strongly depend on the effective interactions, which leads to the divergence of the transition energies calculated by varying the mass asymmetry of a reaction. In other words, participant zone is primarily responsible for the transition from in-plane to out-of-plane. The energy at which this transition is observed is dubbed as the transition energy E_{trans}. That is why, LMF's, which originate from the participant zone, show a clear and systematic transition with the beam energy as well as with the mass asymmetry of a reaction. One should note that transition energy increases with the mass asymmetry of the reaction.

Comparison with Experimental data

To further strengthen our interpretation of the results of elliptical flow $< V_2 >$, we display in Fig. 5.8, the reactions of $_{54}Xe^{129} +_{50} Sn^{124}$ and $_{54}Xe^{129} +_{79} Au^{197}$ ($\eta = 0.2$) using the same conditions. The upper panel shows the variation of elliptical flow per nucleon $< V_2 >$ for the reaction of $_{54}Xe^{129} +_{50} Sn^{124}$ (Z = 2 particles) with incident beam energy, while the impact parameter dependence of elliptical flow for $_{54}Xe^{129} +_{79} Au^{197}$ system is shown in the lower panel. The rapidity cut is in accordance with the experimental findings. The theoretical results are compared with the experimental data extracted by INDRA@(GSI+GANIL) and MSU collaborations, respectively [76]. We find that:

(i) The variation of the elliptical flow with incident energy shows transition from positive to negative values. This change can be centered with properties of hot and dense nuclear matter, indicating a phase transition. Moreover, the mean field, which contributes to the formation of a rotating compound system, becomes less important, and the collective expansion process based on the nucleon-nucleon scattering starts to dominate. This competition between the mean-field and NN collisions depends strongly on the effective interactions leading to different transition energies for different mass asymmetries. This trend is in agreement with experimental findings and

(ii) The variation of elliptical flow with scaled impact parameter ($\hat{b}$) for the reactions of $_{54}Xe^{131} +_{79} Au^{197}$ at E = 50 MeV/nucl. shows that the value of elliptical flow $< V_2 >$ turns more positive with impact parameter. This happens due to the fact that while going

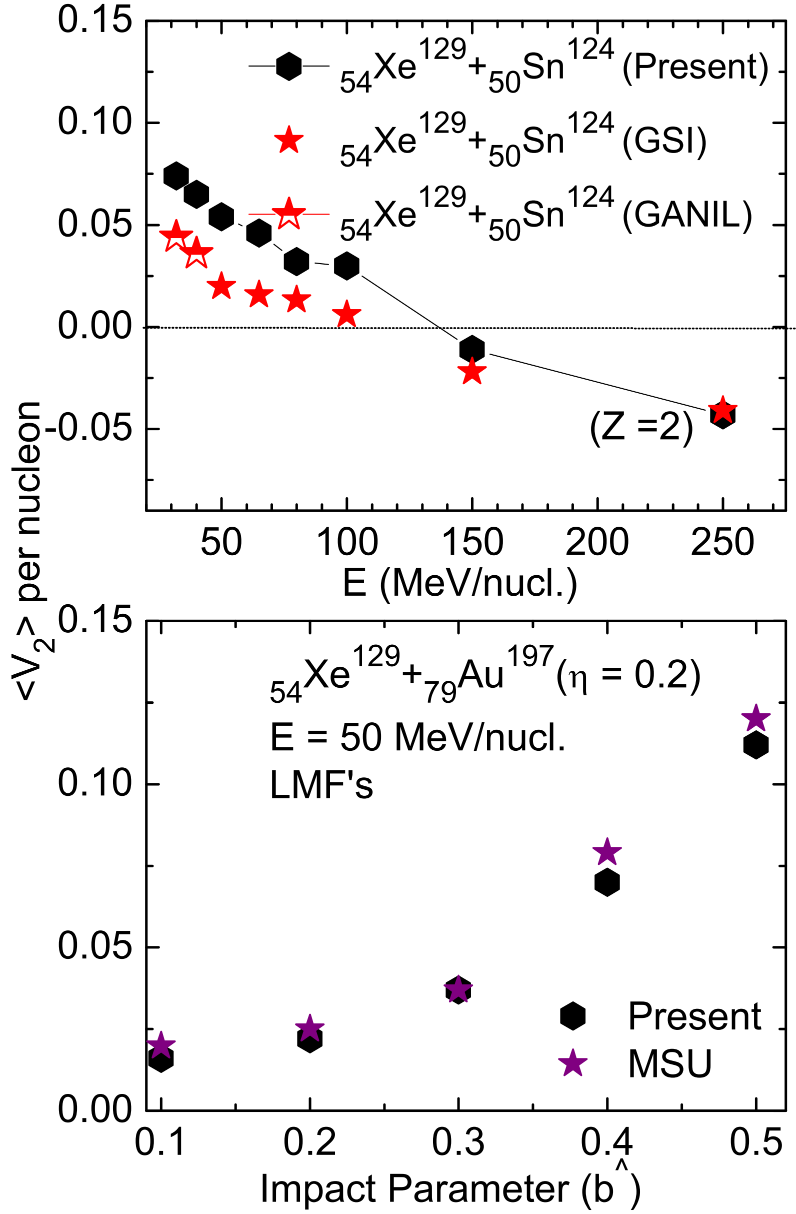

Figure 5.8: (Color online) The energy dependence of elliptical flow for the reaction of $_{54}Xe^{129} +_{50} Sn^{124}$ (upper panel) at $\hat{b} = 0.5$ and impact parameter dependence of elliptical flow for the reaction of $_{54}Xe^{129} +_{79} Au^{197}$ at 50 MeV/nucl. for LMF's (lower panel). Here, experimental findings of INDRA@(GSI+GANIL) and MSU collaborations are taken from ref. [76].

from the central to peripheral geometry, lesser nucleons participate in the collision process leading to enhanced elliptical flow. Also the azimuthal anisotropy becomes larger with the impact parameter and leads to further enhancement of elliptical flow. These observations are consistent with the experimental findings and with other theoretical work [64, 76]. A close agreement with data is obtained at all the scaled impact parameters varying from 0.1 to 0.5 [76].

5.3 Summary

We presented the systematic theoretical results on elliptical flow by analyzing nearly symmetric and asymmetric reactions at different incident energies. In the case of nearly symmetric reactions, general features of elliptical flow are investigated with the help of theoretical simulations, particularly, the transverse momentum, impact parameter, system size dependence and incident energy dependence. Special emphasis was put on the energy dependence of the elliptical flow. We also compared our theoretical calculations with 4π Array data. This comparison, performed for the reaction of ${}_{18}Ar^{40} +_{21} Sc^{45}$ shows that the hard NEOS explains the data nicely. In general, a good agreement is obtained between the data and calculations. We also predict that elliptical flow for different kind of fragments follows power law dependence α C$(A_{tot})^{\tau}$.

Moreover, in case of asymmetric reactions, elliptical flow is analyzed by varying the mass asymmetry of colliding nuclei while total mass is kept fixed. The mass asymmetry dependence of elliptical flow (in terms of transverse momentum dependence) for free nucleons and LMF's shows a weaker squeeze-out flow compared for larger asymmetric reactions. Moreover, the elliptical flow is found to show a transition from in-plane to out-of-plane in the mid rapidity region with incident energy, while no such transition is observed when integrated over the entire rapidity region. The transition energy, at which the elliptical flow $< V_2 >$ changes sign from positive to negative values, is different for different mass asymmetries, and is found to increase with the mass asymmetry for lighter fragments. The comparison with experimental data of INDRA@(GSI+GANIL) and MSU collaborations supports our findings.

Chapter 6

Nuclear Stopping in asymmetric collisions

6.1 Introduction

Nuclear stopping is one of the essential observables which is necessary to understand the basic reaction dynamics including the themalization/equilibrium reached in the reaction. This will also shed light on the production of entropy in a reaction. It is closely related to the question, whether the thermalization (equilibrium) can be reached or not for a colliding system in order to obtain the information about reaction dynamics. This problem has been studied extensively both theoretically and experimentally [30]. Its correlation with light charged particles is also explored. In many cases, nuclear stopping has been studied by baryon rapidity distributions at various beam energies [30]. However, for a meaningful investigation, we study the variation of nuclear stopping by taking into account the mass asymmetry of the colliding pairs (defined in the previous chapters). Following the establishment of radioactive beam facilities in many laboratories, it became possible to study the neutron-rich (or proton-rich) nuclear collisions at intermediate energies. Beside the many existing radioactive beam facilities, many more are being constructed or under planning, including the Cooling Storage Ring (CSR) facility at HIRFL in China, the Radioactive ion beam factory (RIBF) at RIKEN in Japan, the FAIR at GSI in Germany, SPIRAL2/GANIL in France, and Facility for Rare Isotope Beam (FRIB) in the USA [168]. These facilities offer possibility to study the various phenomena. The idea of studying nuclear stopping phenomena was introduced by Bass *et al.*, [169] via the "isospin-mixing" method. In 1988, Bauer [170], pointed out that the nuclear stopping at intermediate energies is determined by the mean-field as well as by the in-medium NN cross sections. In 1998, Li *et al.*, [15] found that the degree of isospin equilibrium depends sensitively on both the in-medium NN cross section and equation of state of asymmetric nuclear matter. Another study in 2001 [171], explored the possibility of using nuclear stopping to probe the isospin dependence of in-medium NN cross-section. In 2002 [18, 172], authors studied the behavior of excitation function $Q_{zz}/nucleon$ and concluded that $Q_{zz}/nucleon$ can provide information about the isospin dependence in terms of binary cross-sections. The recent work of many authors suggested [15, 171, 172] that the degree of approaching isospin equilibration helps in probing the nuclear stopping in HIC. In 2004, M. Di Toro *et al.*, [173] analyzed the stopping and isospin equilibration in relativistic collisions in terms of the imbalance ratio of different particle types in projectile/target rapidity regions in mixed collisions. In 2006, one of us and co-workers [137] correlated the multi-fragmentation with global nuclear stopping. Their study revealed that the light charged particles (LCP's) act in a similar manner as the anisotropy ratio. They, however, excluded the isospin content of the colliding nuclei. In a recent communication, one of us and co-workers [64] tried to study the effect of symmetry energy and isospin-dependent cross-section on nuclear stopping. Our findings revealed that the degree of stopping depends weakly on the symmetry energy and strongly on the isospin-dependent cross-section. Most of the above mentioned theoretical and experimental studies concentrated on the dynamics for symmetric reacting partners only. It is worth mentioning that the FOPI collaboration [147] observed that mass asymmetry of colliding pairs can play a decisive role in the reaction dynamics [141].

Here we plan to study how stopping (and/or thermalization/equilibrium) is affected when the mass asymmetry of the reacting partners is altered. Our present aim, therefore, is atleast two fold:

1. To study the relation between light mass fragments (LMF's) and equilibration of the reaction by taking mass asymmetry into account.
2. To confront our model with the experimental data of INDRA collaboration.

6.2 Global Stopping

The global stopping is defined as the randomization of one-body momentum space or memory loss of the incoming momentum. More the initial memory of nucleons is erased, better it is stopped and better one has average mixing of projectile and target momentum. The degree of stopping however, may vary drastically with incident energies, mass of colliding nuclei and colliding geometry. The colliding nuclei not only compress each other, they also heat the matter. In addition, the destruction of initial correlations, makes the matter homogeneous and one can have global stopping. A complete knowledge about the degree of stopping is very important since it can be connected to the different properties of the system, nuclear equations of state (NEOS) and in-medium properties of the nucleon-nucleon cross-section. Theoretically, these happenings are followed by a variety of models. Some models assume a priori equilibrium (at least at local level) whereas others hunt for the degree of thermalization in a reaction. Several models which depend on the assumption of equilibrium, have been applied successfully to study the physics at low and intermediate energies [83].

On the other hand, light mass fragments are the particles having the range ($2 \leq \mathrm{A} \leq 4$). The detailed analysis of production of different kind of fragments is studied in literature by taking into account different parameters as well as different methods of analysis [109, 111]. Any type of the fragment can be considered for the correlation with the nuclear stopping, provided both the quantities must have similar properties. Out of the different kind of fragments, light charged particles are expected to be an indicator for nuclear stopping because of their origin from the participant zone.

If two nuclei collide, three different scenarios are possible. These different scenarios are shown in Fig.6.1:

1. The nuclei are repelled by each other like in the collision of two hard spheres. (shown by in Fig. 6.1[b]).

2. The nuclei are compressed and mix-up like in the collisions of two (compressible) droplets (shown in Fig. 6.1[c]).

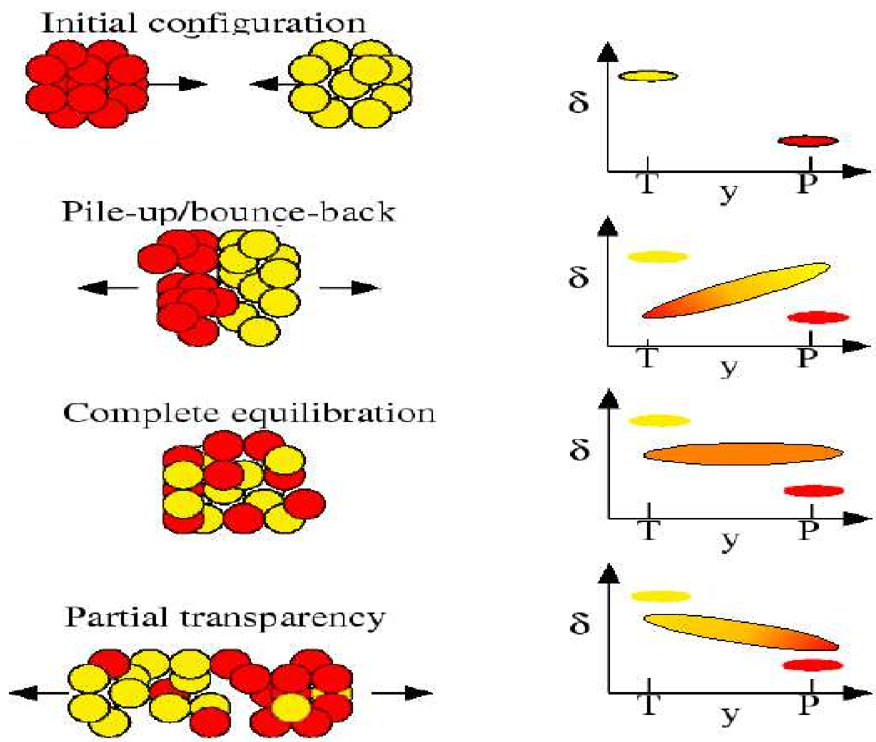

Figure 6.1: Schematic movement of the projectile and target nucleons. The figure is representing (a) initial configuration (b) pile-up/bounce-back (c) complete equilibration (d) partial transparency.

3. The nuclei are passing each other without much interactions like two large crowds of bees (shown in Fig.6.1[d]).

The different scenario would cause different longitudinal momentum distributions for the projectile and target particles. The scenario shown in Fig. 6.1[b] is the one which happens in intermediate energy heavy-ion collisions. The global stopping in heavy-ion collisions has been studied with the help of many different parameters.

6.3 Parameters for describing Nuclear Stopping

6.3.1 Rapidity Distribution

In earlier studies, one used to relate the rapidity distribution with global stopping. The rapidity distribution is defined by Eqn. 4.12. [137]. For a complete stopping, one expects a single Gaussian shape. Obviously, narrow Gaussian indicate better thermalization compared to broader Gaussian.

6.3.2 Anisotropy Ratio

The second possibility to probe the degree of stopping is the anisotropy ratio (R) [171]:

$$R = \frac{2}{\pi} \frac{\left(\sum_i |p_\perp(i)|\right)}{\left(\sum_i |p_\parallel(i)|\right)}, \tag{6.1}$$

where, summation runs over all nucleons. The transverse and longitudinal momenta are $p_\perp(i) = \sqrt{p_x^2(i) + p_y^2(i)}$ and $p_\parallel(i) = p_z(i)$, respectively. Naturally, for a complete stopping, R should be close to unity.

6.3.3 Quadrupole Moment

Another quantity, which is an indicator of nuclear stopping and has been used recently, is the quadrupole moment Q_{zz}, defined as [171]:

$$Q_{zz} = \sum_i \left(2p_z^2(i) - p_x^2(i) - p_y^2(i)\right). \tag{6.2}$$

Naturally, for a complete stopping, Q_{zz} should be close to 0.

In this chapter, we will study the relation between LMF's and stopping (and/or equilibrium) by taking mass asymmetry of the reacting partners into account. Further the theoretical results are compared with the experimental data of INDRA collaboration.

6.4 Results and Discussion

In the present study, projectile mass is varied between 16 and 56 units and targets are chosen as different isotopes of Xe, Sn, Ru in such a manner that total mass of the reaction remains fixed (= 152) for all channels. The reactions under consideration are like this: $_{26}Fe^{56}+_{44}Ru^{96}$ ($\eta = 0.2$), $_{24}Cr^{50} +_{44} Ru^{102}$ ($\eta = 0.3$), $_{20}Ca^{40} +_{50} Sn^{112}$ ($\eta = 0.4$), $_{16}S^{32} +_{50} Sn^{120}$ ($\eta = 0.5$), $_{14}Si^{28} +_{54} Xe^{124}$ ($\eta = 0.6$), $_{8}O^{16} +_{54} Xe^{136}$ ($\eta = 0.7$). Although, total mass remains constant, mass asymmetry keeps varying between 0.2 and 0.7. As stated above, we plan to study the degree of nuclear stopping and emission of fragments by taking mass asymmetry into account. We shall also correlate the degree of nuclear stopping with the emission of light mass fragments. The fragments are constructed within minimum spanning tree (MST) method [27], which binds nucleons if they are within a distance of 4 fm. Finally, the theoretical results are compared with the experimental data extracted by INDRA collaboration.

6.4.1 Snap-shots of Phase space

In Figs. 6.2 and 6.3 we display the final phase space of nucleons for X-Z and P_X-P_Z plane for the reactions of $_{26}Fe^{56} +_{44} Ru^{96}$ having $\eta = 0.2$ (left panel) and $_{8}O^{16} +_{54} Xe^{136}$ having $\eta = 0.7$ (right panel) for a single event at incident energy of 250 MeV/nucl. The top, middle and bottom panels are at $\hat{b} = 0$, 0.3 and 0.6, respectively. Here phase space of light mass fragments (LMF's) [2≤A≤4] and intermediate mass fragments(IMF's)[$(5 \leq A \leq A_{tot}/6)$] is displayed. The phase space is affected with the change of mass asymmetry from $\eta = 0.2$ (nearly symmetric) to 0.7 (highly asymmetric). We note that central collisions lead to complete spherical distribution of particles, indicating, spreading of the nucleons in all directions. It means that breaking of initial correlations among nucleons is maximal in this

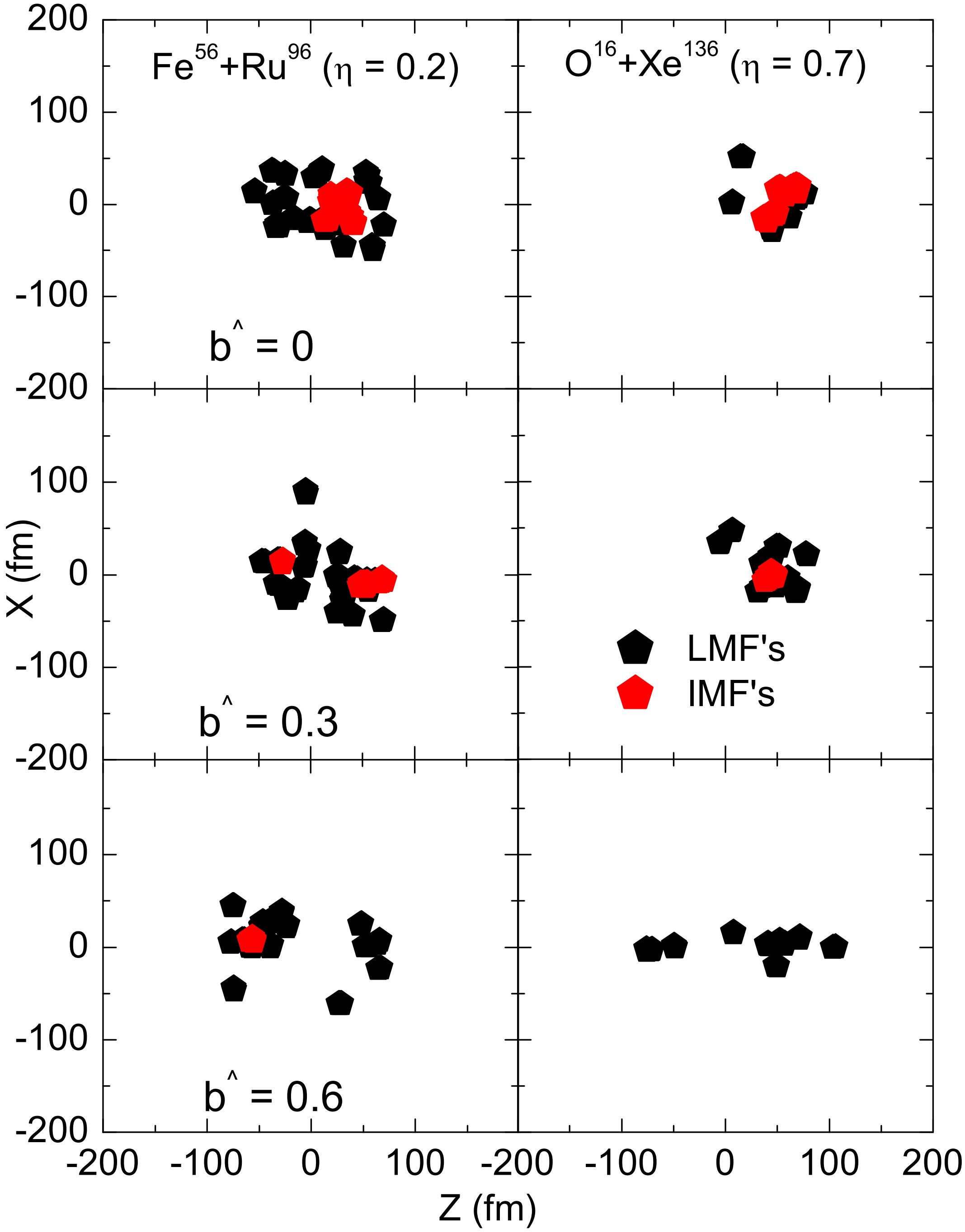

Figure 6.2: The final phase space of a single event for the reaction of ${}_{26}Fe^{56} +_{44} Ru^{96}$ having $\eta = 0.2$ and ${}_{8}O^{16} +_{54} Xe^{136}$ having $\eta = 0.7$ in X-Z plane. The top(a), middle(b) and bottom(c) panels are, respectively, for scaled impact parameters $\hat{b}$ = 0, 0.3, 0.6. Different symbols are for LMF's and IMF's.

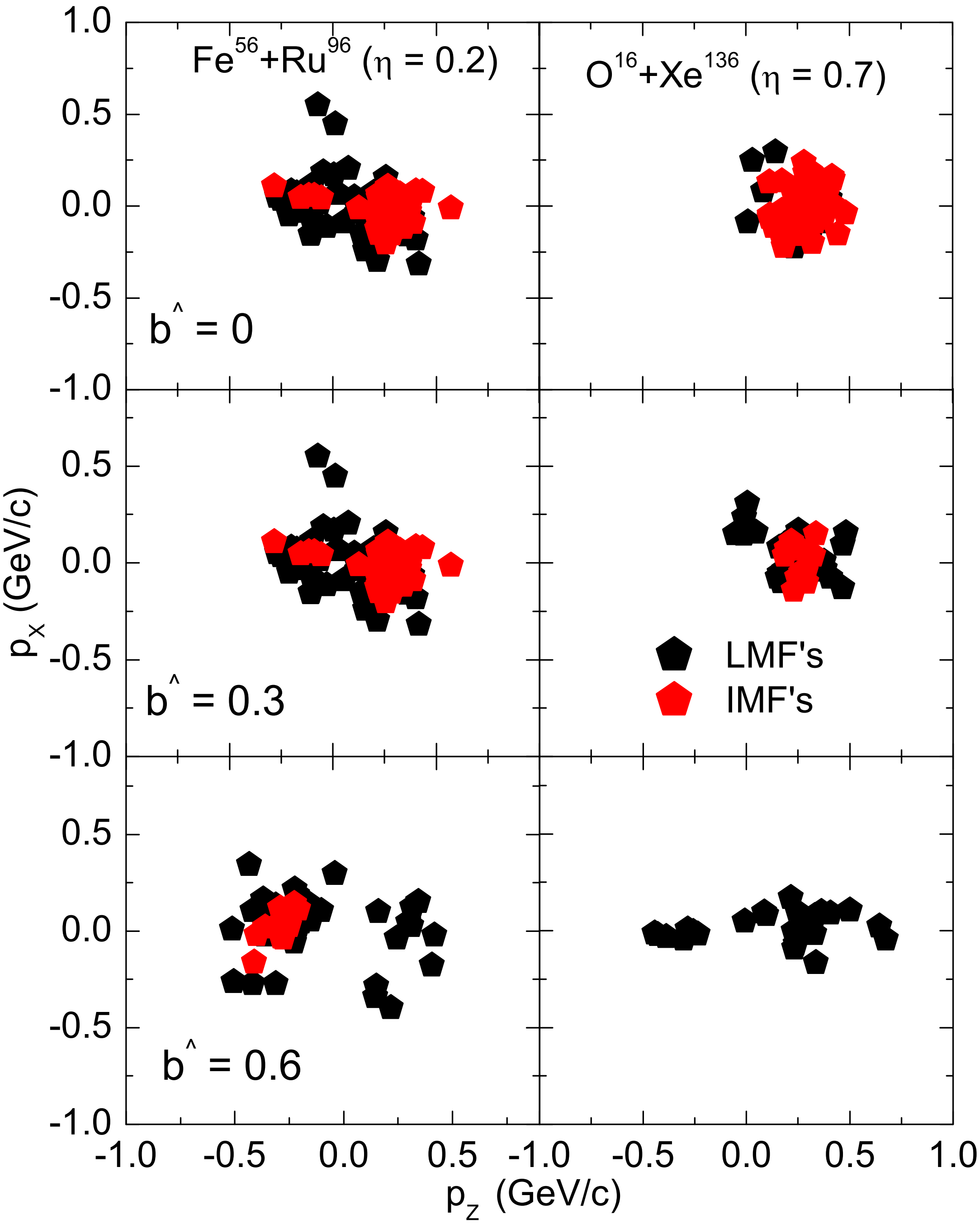

Figure 6.3: Same as Fig.6.2, but for the P_X-P_Z plane.

region and, as a result, more randomization and stopping in the hot and compressed nuclear matter occurs. This effect seems to decrease with impact parameter. Interestingly, we see that there are very few IMF's at $\hat{b} = 0.6$ for $\eta = 0.2$, while no more IMF's for $\eta = 0.7$. Since LMF's originate from the mid-rapidity region, they are better suited for studying the degree of stopping reached in a heavy-ion collision. On the other hand, IMF's seems to originate either from the target or from the projectile region, therefore, are the remnant/residue of the spectator matter.

6.4.2 Rapidity distribution

Fig. 6.4 shows the rapidity distribution $\frac{dN}{dY}$ for the emission of free nucleons (A = 1) as well as light mass fragments (LMF's) $[(2 \leq A \leq 4)]$, and intermediate mass fragments (IMF's) $[(5 \leq A \leq A_{tot}/6)]$ at incident energy E = 250 MeV/nucl. for semi -central collisions. Note that the mass asymmetry varies between 0.2 and 0.7. The $Y_{C.M.}/Y_{beam} = 0$ corresponds to mid-rapidity (participant) zone and hence is responsible for the hot and compressed zone. On the other hand, $Y_{C.M.}/Y_{beam} \neq 0$ corresponds to spectator zone ($Y_{C.M.}/Y_{beam} < -1$ corresponds to target like (TL) and $Y_{C.M.}/Y_{beam} > 1$ corresponds to projectile like (PL) distributions). Free particles and LMF's are produced from the participant zone, thus one can see broader Gaussian, but peaked around the target rapidity as the major contribution is coming from target in all cases. The peak shift toward the mid-rapidity with decrease of mass asymmetry. Therefore, more thermalization is observed in case of nearly symmetric collision compared to asymmetric collision. But, in case of IMF, one can see the peak around the target rapidity because they are produced from the spectator part.

6.4.3 Impact parameter dependence and nuclear stopping

In Fig. 6.5, we display the scaled impact parameter dependence of stopping variables (R and Q_{zz}) along with the multiplicity of LMF's. The results are displayed at E = 250 MeV/nucl. Different curves in each panel corresponds to different mass asymmetries. We observe that $< R >$ and $< 1/Q_{zz} >$ behave in a similar fashion (note that R and Q_{zz} will behave in just opposite fashion). The amount of stopping/equilibrium decreases with the impact parameter due to decrease in the participant zone. On the other hand, stopping decreases

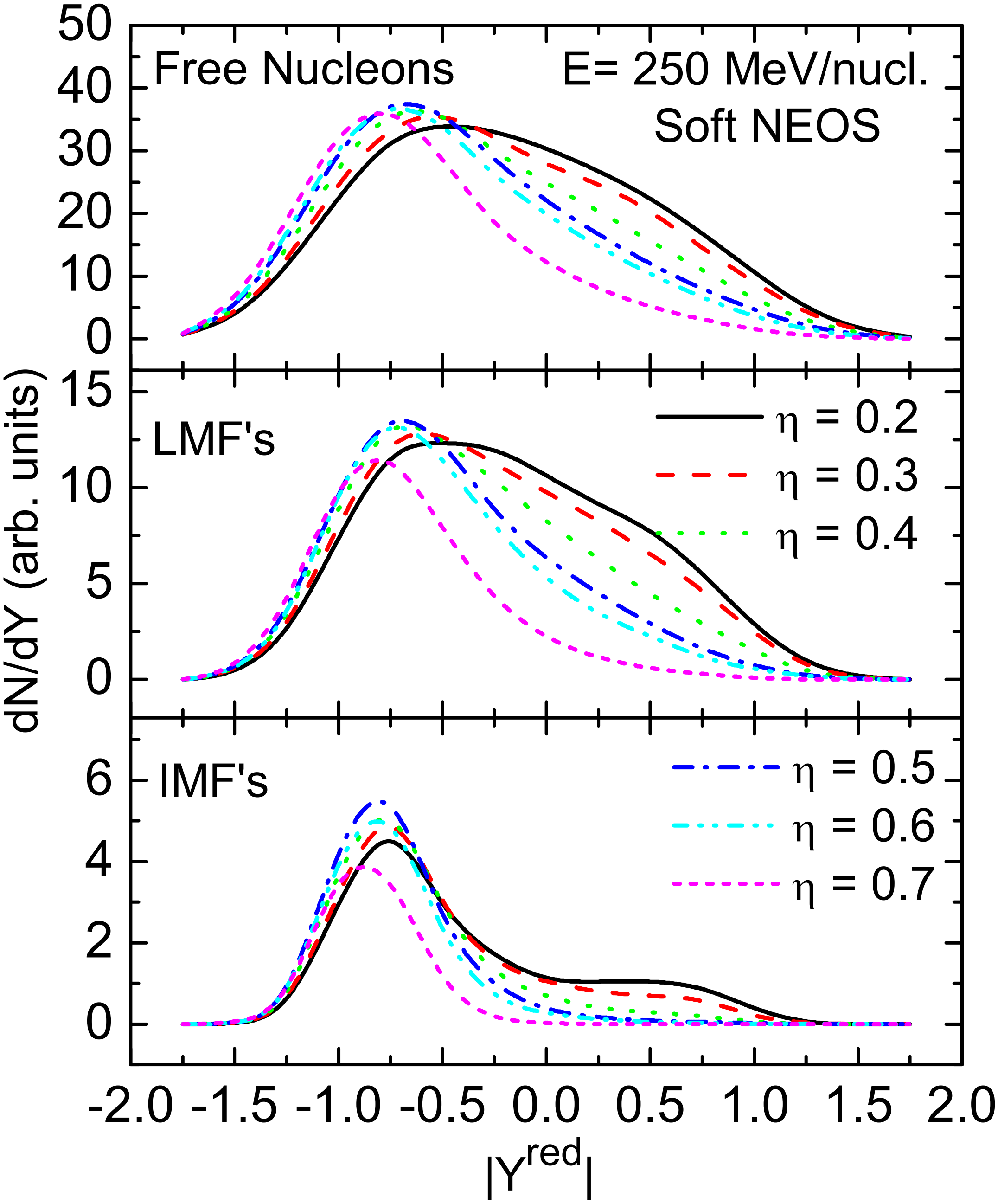

Figure 6.4: The rapidity distribution dN/dY as a function of reduced rapidity for free nucleons, LMF's and IMF's respectively at energy E = 250 MeV/nucl. Different curves correspond to different asymmetries varying from 0.2 to 0.7 for semi-central impact parameter.

with increase in the mass asymmetry of the reaction. As we know, major contribution for the stopping of nuclear matter comes from the hot and compressed matter, which is more in the case of $\eta = 0.2$ and hence the nuclear stopping is more. To correlate the degree of stopping with the multiplicity of light mass fragments, we show in the last panel the impact parameter dependence of the multiplicity of LMF's. The behavior of LMF's with impact parameter is similar to that of anisotropic ratio and inverse of quadrupole moment. The decrease in the multiplicity of LMF's complements with corresponding increase in the heavy fragments. These fragments are the remnant of the spectator matter. Therefore, a decrease in the multiplicity of LMF's with impact parameter measures directly the decrease in the degree of equilibrium and hence nuclear stopping. This implies that the LMF's production can act as an indicator for nuclear stopping. This happens due to the fact that participant zone increases when one moves towards nearly symmetric reactions. Therefore, more LMF's are produced for $\eta = 0.2$ compared to $\eta = 0.7$. It is worth mentioning that in the case of multiplicity of LMF's, we talk about the number of particles while in the case of stopping, it is the momentum phase space (x, y and z components of momentum) that is responsible for the growth.

6.4.4 Mass asymmetry dependence of stopping parameters

The stopping at any time during the collision can be divided into the contributions emerging from the protons and neutrons. We decompose the stopping into the contributions due to protons and neutrons. Here, at each time step during the collision, stopping due to neutrons and protons is analyzed separately.

Fig. 6.6(a) shows the final state quadrupole moment $< 1/Q_{zz} >$ decomposed into the contributions due to neutrons and protons as a function of mass asymmetry η which decreases with the mass asymmetry of reaction. Fig. 6.6(b) shows the final state anisotropy ratio $< R >$ as a function of the mass asymmetry of the system. We see no difference between the contributions due to neutrons and protons. This is due to the fact that $< R >$ is the ratio of the mean transverse momentum $p_{\perp}(i)$ to the mean longitudinal momentum $p_{\parallel}(i) = p_z(i)$. To see the clear contribution of neutrons and protons, one has to look into the contributions of transverse and longitudinal momenta as shown in Fig.6.6(c) and Fig.6.6(d), respectively.

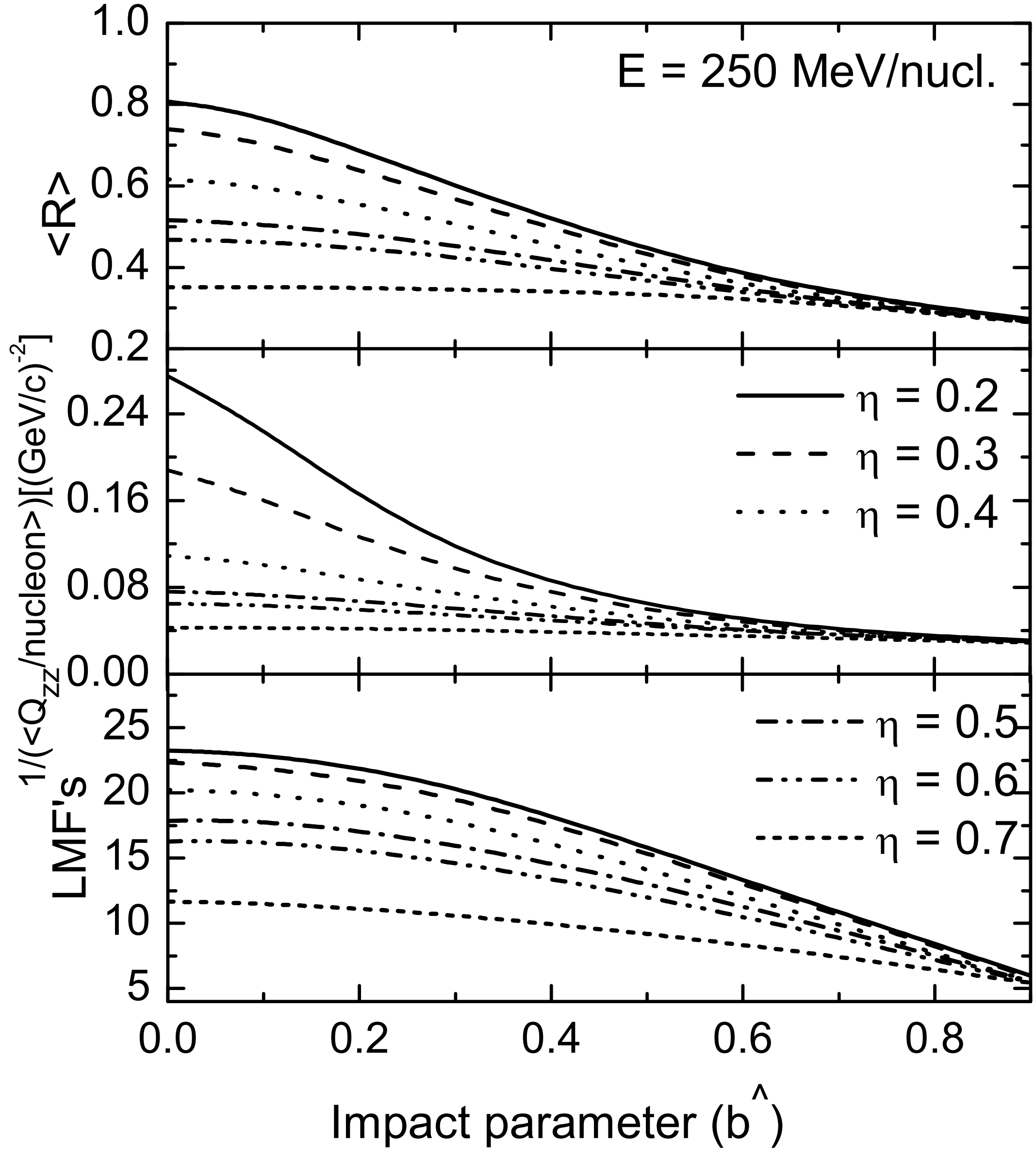

Figure 6.5: The anisotropy ratio $< R >$, quadrupole moment $< 1/Q_{zz} >$ and multiplicity of LMF's as a function of impact parameters. Different curves correspond to different asymmetries varying from 0.2 to 0.7 for semi-central impact parameters.

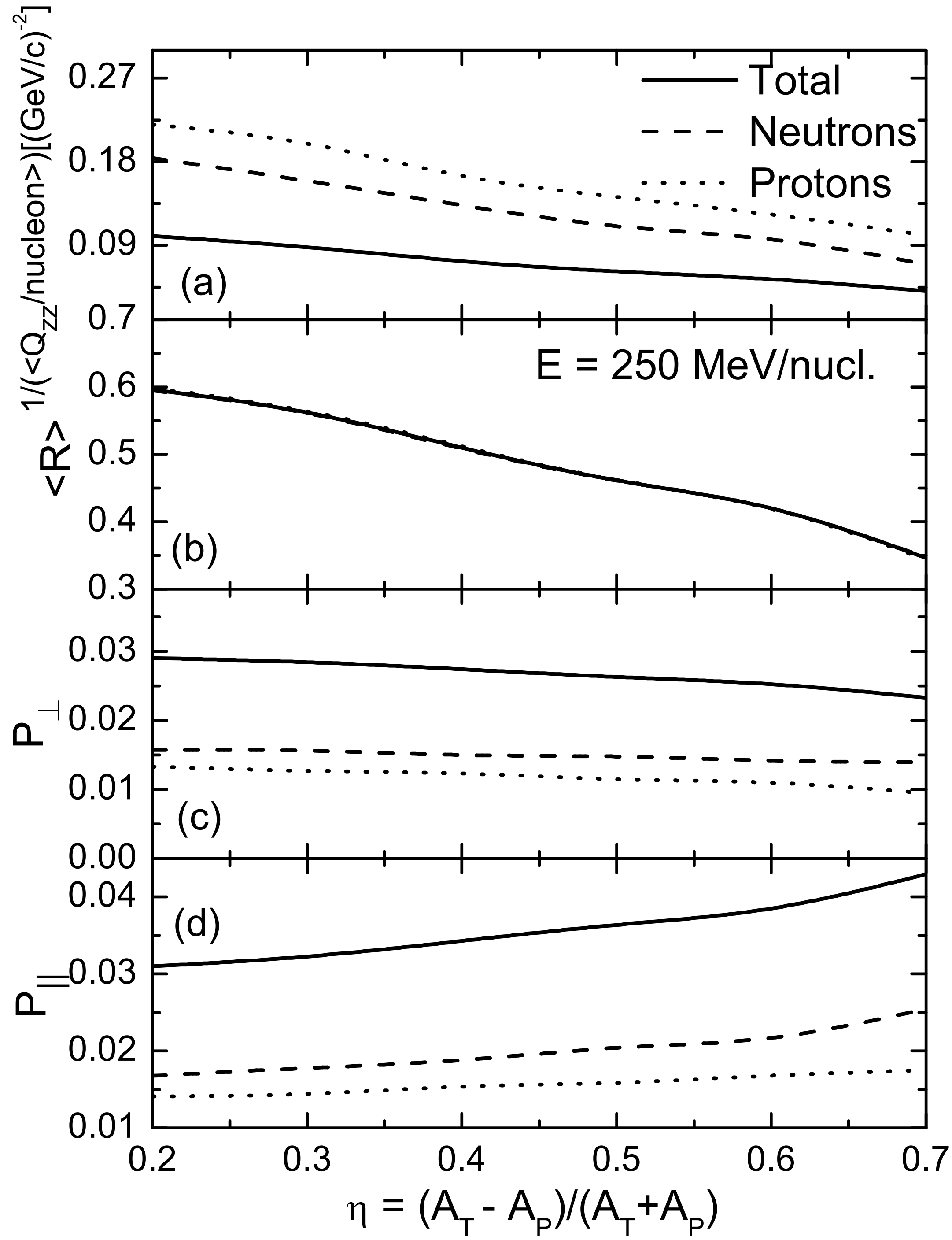

Figure 6.6: The quadrupole moment $< 1/Q_{zz} >$ and anisotropy ratio $< R >$ as a function of mass asymmetry η at energy E = 250 MeV/nucl. The third and fourth panels show the variation of transverse and longitudinal momentum with mass asymmetry, respectively. Different curves correspond to the contribution of neutrons and protons along with total contribution.

Further the contribution of neutrons exceeds the corresponding contributions due to protons.

It will be of further interest to see whether the above findings depend on the isospin asymmetry (N/Z dependence) or not. For this, we display in Fig. 6.7, the anisotropy ratio $< R >$, inverse of quadrupole moment $< Qzz >$ and multiplicity of LMF's as a function of neutron to proton ratio (N/Z) at different impact parameters ranging from central to peripheral one. An increase in the number of neutrons correspond to an increase in mass asymmetry parameter η and hence the absolute value of $< R >$, $< 1/Q_{zz} >$ will decrease with N/Z ratio. Our exclusive findings are: (1) maximum stopping is obtained for the systems with lesser neutron content. This is true at all colliding geometries. This dependence diminishes as one moves from central to peripheral geometry. It is due to the fact that nuclear stopping is governed by the participant zone only. Moreover, in the systems with more neutron content, the role of symmetry energy could be larger, whereas effects due to isospin-dependent cross-section could play a dominant role in systems with less neutron content (proton content). Therefore, there is a possibility that the combined effect of symmetry energy and cross-section could approximately be the same for all systems with different neutron and proton contents [174]. Also neutron-neutron or proton-proton cross-section is a factor of 3 lower than the neutron-proton cross-section. (2) On the other hand, the multiplicity of LMF's follows the similar trend for all asymmetries. This is due to the fact that in case of N/Z = 1.1 ($\eta = 0.2$), participant zone is more compared to N/Z = 1.4 ($\eta = 0.7$). Therefore, more LMF's are produced for N/Z = 1.1 as compared to N/Z = 1.4 and hence LMF's act as an indicator for nuclear stopping.

6.4.5 A comparison with experimental findings

To further strengthen our interpretation of the results, we display in Fig.6.8, the comparison of theoretical results of anisotropy ratio with the experimental data of INDRA collaboration [82]. Here the simulations are performed as per experimental selection. Fig.6.8 (upper panel) shows the reactions of $_{54}Xe^{129} +_{50} Sn^{118}$ and $_{16}S^{32} +_{50} Sn^{120}$ both having N/Z = 1.3. The anisotropy ratio decreases with increase in the incident energy. This happens because transverse component associated with nucleon decreases as incident energy increases. At

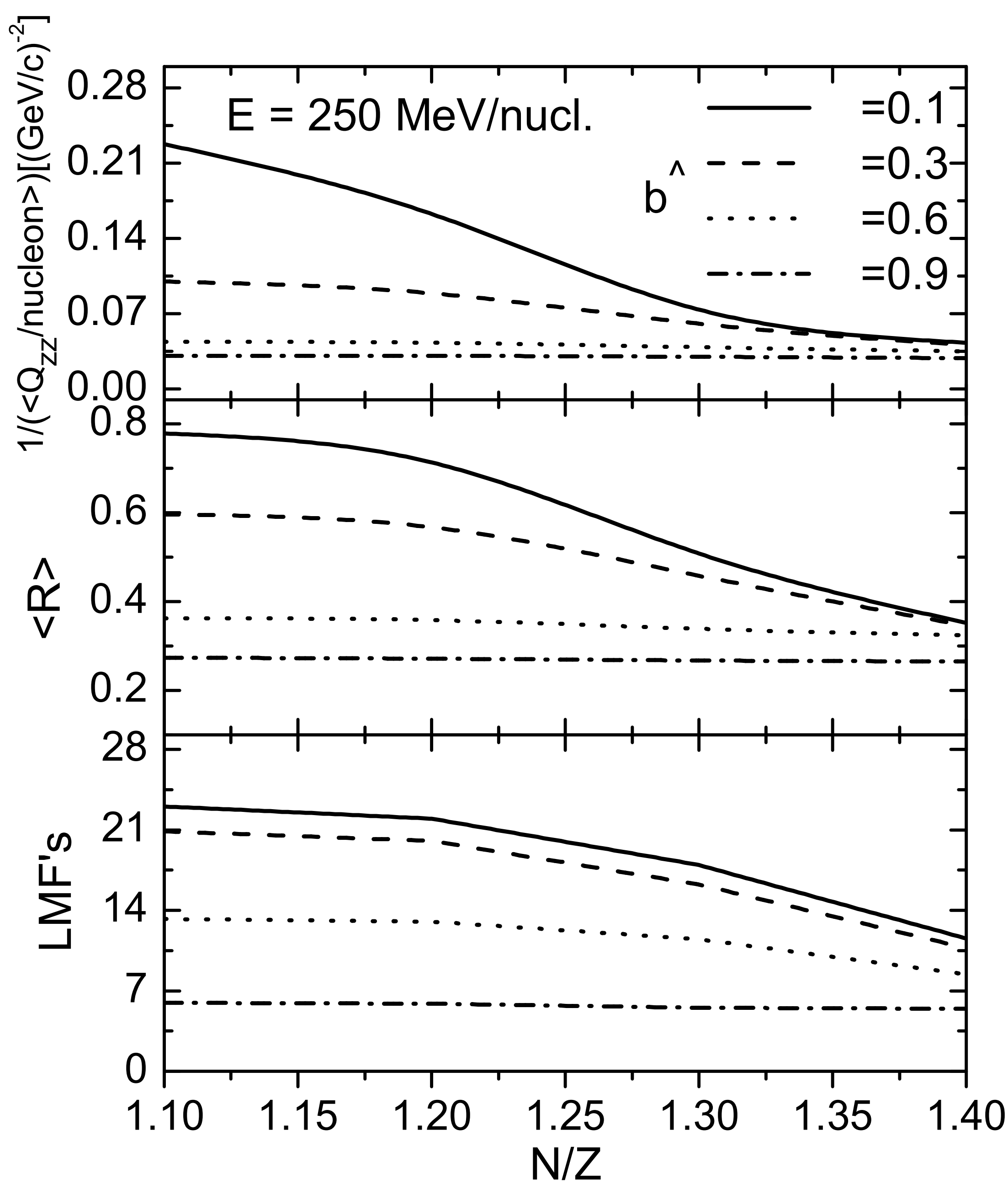

Figure 6.7: Same as Fig.6.5, but as a function of N/Z ratio. Different curves correspond to different impact parameters ranging between central to peripheral one.

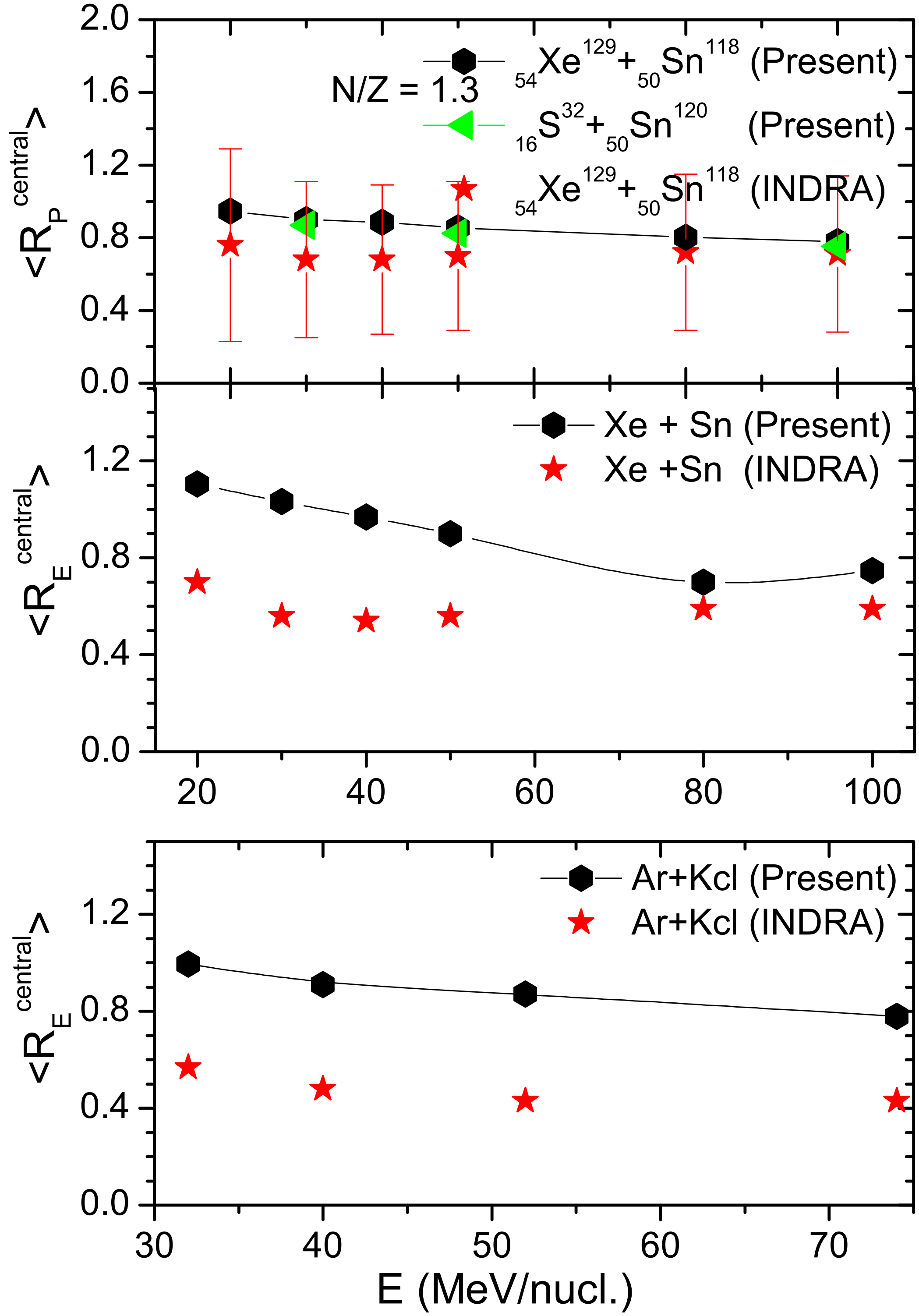

Figure 6.8: Upper panel shows the anisotropy ratio $< R_P >$ as a function of beam energy for the reactions of $_{54}Xe^{129} +_{50} Sn^{118}$ and $_{16}S^{32} +_{50} Sn^{120}$ both having N/Z = 1.3. Middle and bottom panels show the energy dependent anisotropy ratio R_E for the Xe+Sn and Ar+Kcl systems, respectively. Here comparison is shown with experimental results of INDRA collaboration [82].

low incident energies, the nuclei appear to fuse. As incident energy increases, stronger and stronger transparency sets in. These findings are in agreement with many studies available in the literature [171].

Fig.6.8 (middle panel) and Fig. 6.8 (lower panel) show the energy based anisotropy ratio R_E [82] defined as

$$R_E = \frac{1}{2}\frac{[\sum_i E_\perp(i)]}{[\sum_i E_\parallel(i)]}. \tag{6.3}$$

Here the reactions of Xe+Sn and Ar+Kcl are chosen in accordance with the experimental data. Heavier is the system, larger is the value of $< R_E >$. All cases sees values less than unity. However, it should be realized that such low value cannot be reached even for b=0 fm collisions due to geometrical (corona) effects [175]. Due to lack of access to filters, no direct comparison with data could be made. This comparison indicates that the trend of theoretical calculations follows the experimental results.

6.5 Summary

Using the isospin-dependent quantum molecular dynamics (IQMD), we have studied the nuclear stopping in asymmetric colliding channels by keeping total mass fixed. The calculations were carried out by varying the mass asymmetry of the colliding pairs with different neutron-proton ratios at incident beam energy 250 MeV/nucl. The contribution of the neutrons and protons is checked in terms of anisotropy ratio $< R >$ and quadrupole moment $< Q_{zz} >$. The maximum stopping is obtained for nearly symmetric systems. Also a reasonable agreement is observed between theoretical results of anisotropy ratio $< R >$ and energy dependent anisotropy ratio $< R_E >$ with the experimental data of INDRA collaboration.

Chapter 7

Summary and Outlook

"If you think you can, you are right. Just be passionate about it. And if you lack passion, then develop it because success never comes till you are passionate about it."

7.1 Summary

This thesis contains a theoretical study of multi-fragmentation and its related phenomena's like directed transverse flow, rapidity distribution, elliptical flow and nuclear stopping in intermediate energy heavy-ion collisions for asymmetric colliding nuclei. The isospin-dependent quantum molecular dynamics (IQMD) model was used to generate the phase-space of nucleons. The phase space was, then, analyzed using the minimum spanning tree clusterization algorithm to get the useful information about different phenomena's mentioned above.

After an introduction to the field of heavy-ion physics and various phenomena's like multi-fragmentation, collective flow, nuclear stopping and isospin physics, we discussed in **Chapter 1**, the various experimental and theoretical attempts to study these phenomena's. The detail of various theoretical models was discussed in **Chapter 2**. We discussed, in particular, the QMD and IQMD model in detail, which are used for the present study.

In **Chapter 3**, we presented a complete systematic theoretical study of multi-fragmentation for free nucleons and various fragments by simulating different asymmetric reactions at incident beam energies between 50 and 600 MeV/nucl. at semi-central impact parameter using soft and hard nuclear equations of state (NEOS). While the total mass of the system remains constant, mass asymmetry varies between 0.2 and 0.7. In case of nearly symmetric reaction, spectator parts will come from both projectile and target, whereas in the case of highly asymmetric reaction, no spectator part will come from projectile i.e. only target will contribute to the spectators. Although nearly symmetric nuclei depict a well-known trend of rising and falling with peak around E= 100 MeV/nucl., this trend, however, is completely missing for large asymmetric nuclei. The measured distributions are also given as a function of the total charge of all projectile fragments, Z_{bound}. The highly asymmetric system produces largest Z_{bound}, while, maximum number of intermediate mass fragments (IMF's) are produced at $Z_{bound} = 20$. This observation may throw light on the formation mechanisms behind multi-fragmentation. Moreover, the brief study of directed transverse flow shows that the balance energy is affected by the Coulomb interactions as well as different NEOS. This balance energy is further parametrized in terms of mass power law.

In **Chapter 4**, within the semi-classical transport simulations of energetic semi-central collisions of the $_{79}Au^{197} + _{79}Au^{197}$ reaction, we have carried out a new investigation of the interplay between the participant and spectator regions in terms of rapidity distributions. The maxima and minima in the incident energy dependence of elliptical flow are produced by different contributions of the passing time of the spectator and the expansion time of the participant. The shadowing of the spectator matter plays an important role up to later times due to the comparable magnitude of the passing and expansion times up to energies of 400 MeV/nucl. However, at high energies the shadowing effect is dominant only at earlier times due to the fact that the passing time is shorter than the expansion time. The transition from in-plane to out-of-plane emission is observed only when the mid-rapidity region is included into the rapidity bin. Otherwise, no transition is observed. The transition energy is found to be strongly dependent on the size of the rapidity bin, while only weakly dependent on the type of the rapidity distributions. The transition energy is parameterized by a straight-line interpolation. A comparison with experimental bins reveals that a competition is observed between the rapidity bins of $|Y^{red}| \leq 0.1$ and $|Y^{red}| \leq 0.3$. To remove this discrepancy in the middle region for LCP's, one has to reduce the strength of nucleon–nucleon cross-section.

In **Chapter 5**, we presented the systematic theoretical results on the elliptical flow by analyzing nearly symmetric and asymmetric reactions at different incident energies. In the case of nearly symmetric reactions, the general features of the elliptical flow are investigated with the help of theoretical simulations, particularly, the transverse momentum, impact parameter, system size dependence and incident energy dependence. Special emphasis was put on the energy dependence of the elliptical flow. We also compared our theoretical calculations with 4π Array data. This comparison, performed for the reaction of $_{18}Ar^{40} +_{21} Sc^{45}$ shows that the hard NEOS explains the data nicely. In general, a good agreement is obtained between the data and calculations. We also predicted that elliptical flow for different kind of fragments follows power law dependence α C$(A_{tot})^{\tau}$.
Moreover, in the case of asymmetric reactions, elliptical flow is analyzed by varying the mass asymmetry of colliding nuclei while total mass is kept fixed. The mass asymmetry dependence of elliptical flow (in terms of transverse momentum dependence) for free nucleons and LMF's shows a weaker squeeze-out flow compared for larger asymmetric reactions. Moreover, the elliptical flow is found to show a transition from in-plane to out-of-plane in the mid rapidity region with incident energy, while no such transition is observed when integrated over the entire rapidity region. The transition energy, at which elliptical flow $< V_2 >$ changes sign from positive to negative values, is different for different asymmetries, and is found to increase with the mass asymmetry for lighter fragments. The comparison with experimental data of INDRA@(GSI+GANIL) and MSU collaborations supports our findings.

In **Chapter 6**, we have studied the nuclear stopping in asymmetric colliding channels by keeping total mass fixed. The calculations were carried out by varying the mass asymmetry of the colliding pairs with different neutron-proton ratios at incident beam energy 250 MeV/nucl. The contribution of the neutrons and protons is checked in terms of anisotropy ratio $< R >$ and quadrupole moment $< Q_{zz} >$. The maximum stopping is obtained for nearly symmetric systems. Also a good agreement is observed between theoretical results of anisotropy ratio $< R >$ and energy dependent anisotropy ratio $< R_E >$ with the experimental data of INDRA collaboration.

Summarizing, we have attempted to understand the multi-fragmentation and its related phenomena's like directed transverse flow, rapidity distribution, elliptical flow and nuclear stopping in intermediate energy heavy-ion collisions by taking various mass asymmetries into account. The role of Coulomb interactions on the production of various fragments has been investigated in detail. An attempt has been made to understand the interplay between the participant and spectator regions in terms of rapidity distributions. The disappearance of directed transverse flow and elliptical flow and hence balance energy and transition energy respectively is studied in detail. The comparison with different experimental findings is performed, where the data was available in literature.

7.2 Outlook

In the present thesis, author has attempted to pin down the role of mass asymmetry on fragmentation, collective flow and nuclear stopping. The study presented in this thesis is of great importance for experimentalists. Experimental groups can plan the experiments for such studies. Influence of density dependent symmetry energy for asymmetric collisions can be of great interest for theoreticians. The shift in the peak of intermediate mass fragments production has opened up new topic, that one can concentrate upon. By using the reduced NN cross-section with density dependent symmetry energy, one can acheive a good agreement with data. Variable energy cyclotron center (VECC) is going to explore the nuclear dynamics in the energy domain (10 MeV/nucleon $\leq$ E $\leq$ 80 MeV/nucleon). Moreover, by colliding lighter projectiles on heavier targets, radioisotopes can be created which can be useful in medical science.

Bibliography

[1] B. A. Li, L. W. Chen and C. M. Ko, Phys. Rep. **464**, 113 (2008).

[2] L. W. Chen, C. M. Ko, B. A. Li and G. C. Yong, Fron. Phys. China **2**, 327 (2007); J. Carriere, C. J. Horowitz and J. Piekarewicz, Astrophys. J. **593**, 463 (2003).

[3] H. Muller and B. D. Serot, Phys. Rev. C **52**, 2072 (1995).

[4] A. Bonasera, Phys. Rev. C **60**, 065212 (1999); S. Terranova and A. Bonasera, Phys. Rev. C **70**, 024906 (2004).

[5] P. Wang, V. E. Lyubovitskij, T. Gutsche and A. Faessler, Phys. Rev. C **67**, 015210 (2003); F. Giacosa, T. Gutsche, and A. Faessler, Phys. Rev. C **71**, 025202 (2005).

[6] S. E. Jiri *et al.,* Nucl. Phys. B **119**, 538 (2003); F. Csikor *et al.,* Strong and Electroweak Matter 2002 **1**, hep-lat/0301027 (2003); P. Braun-Munzinger and J. Stachel, Nucl. Phys. A **606**, 320 (1996).

[7] J. R. Birkelund, J. R. Huizenga, J. N. De, and D. Sperber, Phys. Rev. Lett. **40**, 1123 (1978); J. N. De and W. Stocker, Phys. Rev. C **42**, R819 (1990); K. P. Singh, D. C. tayal, G. Singh and H. S. hans, Phys. Rev. C **31**, 1726 (1985); K. P. Singh *et al.,* Acta. Phys. Slov. **37**, 316 (1987).

[8] S. V. S. Sastry, S. Kailas, A. K. Mohanty, and A. Saxena, Pramana J. of Physics **64**, 47 (2005); M. Sinha *et al.,* Phys. Rev. C **78**, 027601 (2008); A. Mukherjee *et al.,* phys. Lett. B **636**, 91 (2006).

[9] P. B. Price *et al.,* Phys. Rev. C **46**, 1939 (1992); Z. Ren, C. Xu, and Z. Wang, Phys. Rev. C **70**, 034304 (2004).

[10] Z. H. Liu, X. Z. Zhang, and H. Q. Zhang, Phys. Rev. C **68**, 024305 (2003); C. Yan-huang, A. Smerzi, and M. D. Toro, Phys. Rev. C **50**, 2809 (1994); C. Beck, N. Keeley, and A. Diaz-Torres, Phys. Rev. C **75**, 054605 (2007).

[11] W. Scheid, H. Muller and W. Greiner, Phys. Rev. Lett. **32**, 741 (1974); K. G. R. Doss *et al.*, Phys. Rev. Lett. **57**, 302 (1986); W. Reisdorf *et al.*, Annu. Rev. Nucl. Part. Sci. **47**, 663 (1997).

[12] Y. J. Kim, Ph.D Thesis, Korea University, 2004.

[13] B. K. Agrawal, R. Kumar, and S. K. Dhiman, Phys. Rev. D **77**, 087301 (2008).

[14] D. V. Shetty and S. J. Yennello, Pramana J. Phys. **75**, 259 (2010).

[15] B. A. Li, C. M. Ko, and W. Bauer, Int. J. of Mod. Phys. E **7**, 147 (1998).

[16] A. Bohr and B. R. Mottelson, Nuclear Structure **1**, (Benjamin, New York) (1969).

[17] C. F. Weizsacker, Z. Physik **96**, 431 (1935); H. A. Bethe and R. F. Bacher, Rev. Mod. Phys. **8**, 82 (1936).

[18] B. A. Li and S. J. Yennello, Phys. Rev. C **52**, R1746 (1995).

[19] H. Stocker and W. Greiner, Phys. Rep. **137**, 277 (1986).

[20] C. Hartnack *et al.*, Eur. Phys. J. A **1**, 151 (1998).

[21] R. Donangelo and S. R. Souza, Phys. Rev. C **52**, 326 (1995).

[22] V. Kaur and S. Kumar, Phys. Rev. C **81**, 064610 (2010);

[23] D. J. Magestro, Ph. D. Thesis, Michigan State University (2000).

[24] S. Voloshin and Y. Zhang, Z. Phys. C **70**, 665 (1996).

[25] S. Kumar, V. Kaur, and S. Kumar, Cent. Eur. J. Phys. 9(4), 986 (2011).

[26] V. Kaur, S. Kumar, and R. K. Puri, Phys. Lett. B **697**, 512 (2011).

[27] J. Aichelin, Phys. Rep. **202**, 233 (1991).

[28] G. Peilert, H. Stocker, W. Greiner, A. Rosenhauer, A. Bohnet, and J. Aichelin, Phys. Rev. C **39**, 1402 (1989); A. Bohnet, N. Ohtsuka, J. Aichelin, R. Linden, and A. Faessler, Nucl. Phys. A **494**, 349 (1989); L. Neise, M. Berenguer, C. Hartnack, G. Peilert, H. Stocker and W. Greiner, Nucl. Phys. A **519**, 375 (1990); M. Berenguer, C. Hartnack, G. Peilert, H. Stocker, W. Greiner, J. Aichelin and A. Rosenhauer, J. Phys. G **18**, 655 (1992).

[29] P. B. Gassiaux and J. Aichelin, Phys. Rev. C **56**, 2109 (1997).

[30] J. Cugnon, T. Mizutani and J. Vandermeulen, Nucl. Phys. A **359**, 345 (1981); J. Randrup *et al.*, Nucl. Phys. A **314**, 429 (1979); Z. X. Li *et al.*, Nucl. Phys. A **559**, 603 (1993).

[31] V. Kaur, S. Kumar and R. K. Puri, Nucl. Phys. A **861**, 37 (2011).

[32] M. B. Gottleib, Phys. Rev. **82**, 349 (1951).

[33] B. Jakobsson *et al.,* Z. Phys. A **307**, 293 (1982).

[34] L. G. Moretto, D. N. Delis, and G. J. Wozniak, Phys. Rev. Lett. **71**, 3935 (1993); L. Phair *et al.,* Phys. Rev. Lett. **75**, 213 (1995); L. Phair *et al.,* Phys. Rev. Lett. **77**, 822 (1996); T. C. Sangster *et al.,* Phys. Rev. C **46**, 1404 (1992); D. R. Bowman *et al.,* Nucl. Phys. A **523**, 386 (1991);

[35] N. T. Porlie, Nucl. Phys. A **681**, 253 (2001); B. K. Srivastava *et al.,* Phys. Rev. C **65**, 054617 (2002); J. B. Elliott, L.G Moretto and L. Phair, Phys. Rev. C **71**, 024607 (2005); L. G. Moretto, C. O. Dorso, J. B. Elliott, and L. Phair, Phys. Rev. C **77**, 037603 (2008).

[36] A. Insolia *et al.,* Phys. Rev. C **61**, 044902 (2000).

[37] R. T. de Souza *et al.,* Phys. Lett. B **268**, 6 (1991); T. Li *et al.,* Phys. Rev. Lett. **70**, 1924 (1993); L. Phair *et al.,* Phys. Lett. B **285**, 10 (1992); T. Li *et al.,* Phys. Rev. C **49**, 1630 (1994); C. Williams *et al.,* Phys. Rev. C **55**, R2132 (1997).

[38] W. J. Llope *et al.,* Phys. Rev. C **51**, 1325 (1995); N. T. B. Stone, W. J. Llope, and G. D. Westfall, Phys. Rev. C **51**, 3157 (1995); D. Sisan *et al.,* Phys. Rev. C **63**, 027602 (2001).

[39] M. B. Tsang *et al.,* Phys. Rev. Lett. **92**, 062701 (2004).

[40] Y. Zhang, P. Danielewicz, M. Famaino, Z. Li, W. G. Lynch, and M. B. Tsang, Phys. Lett. B **664**, 145 (2008).

[41] M. B. Tsang *et al.,* Phys. Rev. C **76**, 041302(R) (2007); M. Mocko *et al.,* Eur. Phys. Lett. **79**, 12001 (2007).

[42] T. X. Liu *et al.,* Phys. Rev. C **76**, 034603 (2007).

[43] M. B. Tsang *et al.,* Phys. Rev. Lett. **102**, 122701 (2009).

[44] S. Piantelli *et al.,* Phys. Rev. C **74**, 034609 (2006); S. Piantelli *et al.,* Phys. Rev. C **78**, 064605 (2008).

[45] R. Planeta *et al.,* Phys. Rev. C **77**, 014610 (2008).

[46] see http://www-aladin.gsi.de.

[47] C. A. Ogilvie *et al.,* Phys. Rev. Lett. **67**, 1214 (1991); J. Hubele *et al.,* Phys. Rev. C **46**, R1577 (1992); M. Begemann-Blaich *et al.,* Phys. Rev. C **48**, 610 (1993); A. S. Botvina *et al.,* Nucl. Phys. A **584**, 737 (1995); N. T. B. Stone *et al.,* Phys. Rev. Lett. **78**, 2084 (1997).

[48] B. de Schauenburg, *et al.,* GSI Scientific Rep. **98-1**, p. 56 (1997); W. Reisdorf, Nucl. Phys. A **630**, 15c (1998); W. Reisdorf, *et al., ibid.* **2000-1**, p. 45 (1999); W. Reisdorf, Hirschegg, p. **82** (1999); B. Hong *et al.,* Phys. Rev. C **66**, 034901 (2002).

[49] G. Poggi *et al.,* Nucl. Phys. A **586**, 755 (1995); J. Konopka, *et al.,* GSI Rep. **96-1**, p. 65 (1995); J. P. Alard, *et al., ibid.* **97-1**, p. 54 (1996); N. Bastid, *et al., ibid.* **98-1**, p. 54 (1997); A. Andronic, *et al., ibid.* **98-1**, p. 55 (1997).

[50] see hppp:// www-fopi.gsi.de.

[51] N. Marie *et al.,* Phys. Rev. C **58**, 256 (1998); W. Loveland *et al.,* Phys. Rev. C **59**, 1472 (1999); J. D. Frankland *et al.,* Nucl. Phys. A **689**, 940 (2001); S. Hudan *et al.,* Phys. Rev. C **67**, 064613 (2003); J. D. Frankland *et al.,* Phys. Rev. C **71**, 034607 (2005).

[52] J. Colin *et al.,* Phys. Rev. C **67**, 064603 (2003).

[53] J. Lukasik *et al.,* Phys. Rev. C **66**, 064606 (2002).

[54] L. Manduci *et al.,* Nucl. Phys. A **811**, 93 (2008).

[55] E. Bohnet *et al.,* Phys. Rev. Lett. **103**, 072701 (2009).

[56] E. Galichet, M. Colonna, B. Borderie and M. F. Rivet, Phys. Rev. C **79**, 064615 (2009); E. Galichet *et al.,* Phys. Rev. C **79**, 064614 (2009).

[57] D. V. Shetty *et al.,* Phys. Rev. C **68**, 054605 (2003); D. V. Shetty, S. J. Yennello and G. A. Souliotis, Phys. Rev. C **75**, 034602 (2007).

[58] D. V. Shetty *et al.,* J. Phys. G: Nucl Part. Phys. **36** , 075103 (2009).

[59] D. V. Shetty, G. A. Souliotis, S. Galanopoulos, and S. J. Yennello, Phys. Rev. C **79**, 034603 (2009).

[60] G. D. Westfall *et al.*, Phys. Rev. Lett.**71**, 1986 (1993); M. B. Tsang *et al.*, Phys. Rev. C **53**, 1959 (1996); Y. M. Zheng, C. M. Ko, B. A. Li, and B. Zhang, Phys. Rev. Lett. **83**, 2534 (1999); A. B. Larionov, W. Cassing, C. Greiner, and U. Mosel, Phys. Rev. C **62**, 064611 (2000); B. A. Li, A. T. Sustich, and B. Zhang, *ibid.* **64**, 054604 (2001); C. Alt *et al.*, *ibid.* **68**, 034903 (2003).

[61] J. Lukasik, G. Auger, and M. L. Begemann-Blaich *et al.*, Phys. Lett. B **608**, 223 (2005).

[62] A. Andronic *et al.*, Nucl. Phys. A **679**, 765 (2001); *ibid.* Phys. Lett. B **612**, 173 (2005).

[63] J. Lukasik, *et.al.,* INDRA Collaborations, Int. Workshop on Multifragmentation and related topics (IWM 2003) Caen, France (2003).

[64] S. Kumar, M. K. Sharma, R. K. Puri, K. P. Singh, and I. M. Govil, Phys. Rev. C **58**, 3494 (1998); A. D. Sood, R. K. Puri, and J. Aichelin, Phys. Lett. B **594**, 260 (2004); S. Kumar and R. K. Puri, Phys. Rev. C **60**, 054607 (1999); S. Kumar and R. K. Puri, Phys. Rev. C **58**, 320 (1998); J. Singh and R. K. Puri, *ibid.* **62**, 054602 (2000); S. Kumar, S. Kumar, and R. K. Puri, *ibid.* **81**, 014611 (2010); S. Gautam *et al.*, J. Phys. G **37**, 085102 (2010); S. Kumar, R. K. Puri, and J. Aichelin *ibid.* **58**, 1618 (1998).

[65] A. D. Sood and R. K. Puri, Phys. Rev. C **69**, 054612 (2004); *ibid.* **73**, 067602 (2006); *ibid.* **70**, 034611 (2004); R. Chugh and R. K. Puri, *ibid.* **82**, 014603 (2010).

[66] L. W. Chen and C. M. Ko, Phys. Lett. B **634**, 205 (2006); Phys. Rev. C **73**, 014906 (2006).

[67] H. Stocker *et al.,* Phys. Rev. C **25**, 1873 (1982); A. R. Raduta and F. Gulminelli, *ibid.* **75**, 024605 (2007).

[68] M. Gyulassy, K. A. Frankel, and H. Stöcker, Phys. Lett. B **110**, 185 (1982); P. Danielewicz and M. Gyulassy, Phys. Lett. B **129**, 283 (1983); C. M. Ko and G. Q. Li, J. Phys. G: Nucl. and Part. **22**, 1673 (1996); G. Q. Li, C. M. Ko, and B. A. Li, Phys. Rev. Lett. **74**, 235 (1995); G. Q. Li and C. M. Ko, Nucl. Phys. A **594**, 460 (1995); B. A. Li and C. M. Ko, Phys. Rev. C **52**, 2037 (1995); *ibid.* Phys. Rev. C **58**, R1382 (1998).

[69] T. Gaitanos, H. H. Wolter, C. Fuchs, Phys. Lett. B **478**, 79 (2000); J. Gosset *et al.*, Phys. Rev. Lett. **62**, 1251 (1989); J. Pluta *et al.*, Nucl. Phys. A **562**, 365 (1993); J. Gosset, H. H. Gotbrod, W. G. Meyer, A. M. Poskanzer, A. Sandoval, R. Stock, and G. D. Westfall, Phys. Rev. C **16**, 629 (1977).

[70] H. H. Gutbrod *et al.,* Phys. Lett. B **216**, 267 (1989).

[71] H. H. Gutbrod *et al.,* Phys. Rev. C **42**, 640 (1990).

[72] R. Popescu *et al.,* Phys. Lett. B **331**, 285 (1994).

[73] P. Danielewicz *et al.,* Phys. Rev. Lett. **81**, 2438 (1998).

[74] C. Pinkenburg *et al.,* Phys. Rev. Lett. **83**, 1295 (1999); A. Andronic *et al.,* Eur. Phys. J. A **30**, 31 (2006).

[75] K. H. Ackermann *et al.,* Phys. Rev. Lett. **86**, 402 (2001); C. Adler *et al., ibid.* **87**, 182301 (2001); C. Adler *et al.,* Phys. Rev. C **66**, 034904 (2002); J. Adams *et al., ibid.* **72**, 014904 (2005).

[76] N. Herrmann, J. P. Wessels and T. Wienold, Annu. Rev. Nucl. Part. Sci **49**, 581 (1999); J. Lukasik *et al.,* Proc. of INPC **2**, 513 (2007); J. Lukasik and W. Trautmann (INDRA and ALADIN collaboration), arxiv:0708.2821v1 [nucl-ex],2007; J.Lukasik *et al.*, International workshop on multi-fragmentation and related topics, 4-7 Nov, IWM2007.

[77] P. Crochet *et al.,* Nucl. Phys. A **624**, 755 (1997).

[78] W. Reisdorf *et al.,* Phys. Rev. Lett. **92**, 232301 (2004).

[79] W. Reisdorf *et al.,* Phys. Lett. B **595**, 118 (2004).

[80] W. Trautmann *et al.,* Int. J. Mod. Phys. E **19**, 1653 (2010).

[81] J. Y. Ollitrault, A. M. Poskanzer, and S. A. Voloshin, Phys. Rev. C **80**, 014904 (2009).

[82] G. Lehaut *et al.*, Phys. Rev. Lett. **104**, 232701 (2010).

[83] J. P. Bondorf *et al.*, Nucl. Phys. A **443**, 321 (1985); *ibid* **444**, 460 (1985); *ibid* **448**, 753 (1986); A. S. Botvina *et al.*, Z. Phys. A **345**, 297 (1993); G. A. Souliotis *et al.,* Phys. Rev. C **75**, 011601 (2007).

[84] B. A. Li and D. H. E. Gross, Nucl. Phys. A **554**, 257 (1993); H. M. Xu, C. A. Gagliardi, R. E. Tribble and C. Y. Wong, *ibid.* **569**, 575 (1994); F. Daffin, K. Haglin and W. Bauer, Phys. Rev. C **54**, 1375 (1996); V. de la Mota, F. Sebille, M. Farine, B. Remaud and P. Schuck, *ibid.* **46**, 677 (1992).

[85] C. Fuchs, E. Lehmann, R. K. Puri, L. Sehn, A. Faessler, and H. H. Wolter, J. Phys. G: Nucl. Part. Phys. **22**, 131 (1996); Y. K. Vermani and R. K. Puri, *ibid.* **36**, 105103 (2009); R. K. Puri, N. Ohtsuka, E. Lehmann, A. Faessler, M. A. Matin, D. T. Khoa, G. Batko, and S. W. Huang, Nucl. Phys. A **575**, 733 (1994).

[86] J. P. Bondorf, A.S. Botvina, A.S. Iljinov, I.N. Mishustin, and K. Sneppen, Phys. Rep. **257**, 133 (1995).

[87] D. H. E. Gross, Rep. Prog. Phys. **53**, 605 (1990).

[88] W. Bauer, D. R. Dean, U. Mosel, and U. Post, Phys. Lett. B **150**, 53 (1985); W. Bauer, U. Post, D. R. Dean, and U. Mosel, Nucl. Phys. A **452**, 699 (1986).

[89] J. Pan, S. Das Gupta, Phys. Lett. B **344**, 29 (1995); J. Pan, S. D. Gupta, Phys. Rev. C **51**, 1384 (1995); S. D. Gupta and J. Pan, Phys. Rev. C **53**, 1319 (1996).

[90] W.A. Friedman, Phys. Rev. C **42**, 667 (1990).

[91] E. Schiller, H. Muther, P. Czerski, Phys. Rev. C **59**, 2934 (1999).

[92] A. K. Kerman and S. E. Koonin, Ann. of Phys. **100**, 332 (1976); P. Bonche, S. Koonin and J. W. Negele, Phys. Rev. C **13**, 1226 (1976); K. T. R. Davies and S. E. Koonin, Phys. Rev. C **23**, 2042 (1981); M. D. Toro, G. Russo, and F. Duggan, Phys. Rev. C **21**, 2054 (1980).

[93] G. F. Bertsch, H. Kruse and S. D. Gupta, Phys. Rev. C **29**, R673 (1984); J. J. Molitoris, H. Stocker, and B. L. Winer, Phys. Rev. C **36**, 220 (1987); C. Gale *et al.,* Phys. Rev. C **41**, 1545 (1990).

[94] H. Kruse, B. V. Jacak, and H. Stocker, Phys. Rev. Lett. **54**, 289 (1985); J. J. Molitoris, A. Bonasera, B. L. Winer, and H. Stocker, Phys. Rev. C **37**, 1020 (1988); J. J Molitoris and H. Stocker, Phys. Rev C **32**, R346 (1985).

[95] E. Suraud, C. Gregoire, and B. Tamain, Prog. Part. Nucl. Phys. **23**, 357 (1989).

[96] L. Wilets, Y. Yariv, and R. Chestnut, Nucl. Phys. A **301**, 359 (1978); A. R. Bodmer, C. N. Panos, and A. D. MacKellar, Phys. Rev. C **22**, 1025 (1980); A. Vicentini, G. Jacucci and V. R. Pandharipande, Phys. Rev. C **31**, 1783 (1985).

[97] J. Aichelin and H. Stocker, Phys. Lett. B **176**, 14 (1986).

[98] M. Colonna *et al.,* Phys. Rev. C **57**, 1410 (1998).

[99] C. Hartnack Ph.D thesis, GSI- Report **93-5** (1993); C. Hartnack, L. Zhuxia, L. Neise, G. Peilert, A. Rosenhauer, H. Sorge, J. Aichelin, H. Stocker, and W. Greiner, Nucl. Phys. A **495**, 303 (1989); C. Hartnack, J. Aichelin, H. Stocker, and W. Greiner, Mod. Phys. Lett. A **9**, 1151 (1994); *ibid* Phys. Lett. B **336**, 131 (1994); S. A. Bass M. Hofmann Ch. Hartnack, H. Stöcker, and W. Greiner Phys. Lett. B **335**, 289 (1994); S. Soff, S. A. Bass, C. Hartnack, H. Stocker, and W. Greiner, Phys. Rev. C **51**, 3320 (1995).

[100] B. A. Li, Phys. Rev. Lett. **88**, 192701 (2002) and refs. therein

[101] C. Hartnack, H. Oeschler, and J. Aichelin, Phys. Rev. Lett. **90**, 102302 (2003); J. Phys. G: Nucl. and Part. Phys. **35**, 044021 (2008).

[102] L. Jianye and Z. S. Guang, Z. Phys. A **348**, 31 (1994).

[103] G. Peilert *et al.,* Phys. Lett. B **260**, 271 (1991); G. Peilert *et al.,* Phys. Rev. C **46**, 1457 (1992).

[104] E. Lehmann *et al.,* Phys. Rev. C **51**, 2113 (1995); H. Sorge, Phys. Rev. C **52**, 3291 (1995).

[105] N. Wang, Z. Li, X. Wu, J. Tian, Y. Zhang and M. Liu, Phys. Rev. C **69**, 034608 (2004).

[106] M. Belkacem *et al.,* Phys. Rev. C **58**, 1727 (1998); A. Dumitru *et al.,* Phys. Rev. C **57**, 3271 (1998).

[107] M. Trefz, A. Faessler, and W. H. Dickhoff, Nucl. Phys. A **443**, 499 (1985); A. Faessler, W. H. Dickhoff and M. Trefz, Nucl. Phys. A **428**, 271c (1981); N. Ohtusuka, R. Linden, A. Faessler, and F. B. Malik, Nucl. Phys. A **465**, 550 (1987) and references therein.

[108] K. A. Waged, Phys. Rev. C **63**, 024618 (2001); *ibid.* J. of Phys. G **28**, 2951 (2002).

[109] J. Singh, S. Kumar, and R. K. Puri, Phys. Rev. C **62**, 044617 (2000); *ibid.,* **65**, 024602 (2002).

[110] Suneel Kumar, Ph.D Thesis 1999, Punjab University, Chandigarh (India).

[111] R. K. Puri, C. Hartnack, and J. Aichelin, Phys. Rev. C **54**, R28 (1996); P. B. Gossiaux, R. K. Puri, C. Hartnack, and J. Aichelin, Nucl. Phys. A **619**, 379 (1997); Y. K. Vermani and R. K. Puri, Eur. Phys. Lett. **85**, 62001 (2009); S. Kumar and S. Kumar, Pramana J. of Phys. **74**, 731 (2010); *ibid.* **58**, 2858 (1998); R. K. Puri and J. Aichelin, J. Comp. Phys. **162**, 245 (2000).

[112] W. Botermanns and R. Malfliedt, Phys. Lett. B **215**, 617 (1988); Phys. Rep. **198**, 115 (1990); W. Cassing and U. Mosel, Prog. Nucl. Part, Phys. **25**, 1 (1990).

[113] P. Ring and P. Schuk, The nuclear many-body problem, (Springer-Verlog, 1980); C. Gregoire, B. Remaud, F. Sebille, L. Vincet, and Y. Raffay, Nucl. Phys. A **465**, 317 (1987); W. Bauer, Prog. Part. Nucl. Phys. **30**, 45 (1993); T. Reposeur, V. de la Mota, F. Sebille, and C. O. Dorso, Z. Phys A **357**, 79 (1997).

[114] P.B. Gossiaux, D. Keane, S. Wang, and J. Aichelin, Phys. Rev. C **51**, 3357 (1995).

[115] C. Gale, G. F. Bertsch, and S. D. Gupta, Phys. Rev. C **35**, 1666 (1987); Q. Pan and P. Danielewicz, Phys. Rev. Lett. **70**, 2062 (1993); J. Zhang, S. D. Gupta, and C. Gale, Phys. Rev. C **50**, 1617, (1994); V. Greco, A. Guarnera, M. Colonna, and M. D. Toro, Phys. Rev. C **59**, 810 (1999).

[116] B. A. Li *et al.,* Phys. Rev. Lett. **76**, 4492 (1996).

[117] H. Feldmeier and Jurgen Schnack, Review of Modern Physics, **72**, 655 (2000).

[118] D. T. Khoa *et al.,* Nucl. Phys. A **542**, 671 (1992); D. T. Khoa *et al.,* Nucl. Phys. A **529**, 363 (1991); G. Q. Li *et al.,* Nucl. Phys. A **534**, 697 (1991); G. Peilert *et al.,* Mod. Phys. Lett. A **3**, 459 (1988).

[119] H. Feldmeier and J. Schnack, Prog. Part. Nucl. Phys. **39**, 393 (1997); H. Feldmeier, Nucl. Phys. A **515**, 147 (1990).

[120] A. Ono, H. Horiuchi, T. Maruyama, and A. Ohnishi, Phys. Rev. Lett. **68**, 2898 (1992); A. Ono and H. Horiuchi, Phys. Rev. C **51**, 299 (1995).

[121] J. Molitoris, J. B. Hoffer, H. Kruse, and H. Stocker, Phys.Rev. Lett. **53**, 899 (1984); S. M. Kiselew and Y. E. Polrowskil, Sov. Journ, Nucl. Phys. **38**, 46 (1983).

[122] G. Batko, J. Randrup, and T. Vetter, Nucl. Phys. A **536**, 786 (1992); G. Batko, J. Randrup, and T. Vetter, Nucl. Phys. A **546**, 761 (1992).

[123] J. Cugnon, T. Mizutani, and J. Vandermeulen, Nucl. Phys. A **352**, 505 (1981).

[124] A. Ono and H. Horiuchi, Phys. Rev. C **53**, 2958 (1996).

[125] N. Itagaki *et al.,* Phys. Rev. C **70**, 054307 (2004).

[126] M. Papa, T. Maruyama, and A. Bonasera, Phys. Rev. C **64**, 024612 (2001).

[127] M. Hoffmann *et al.,* Phys. Lett. B **478**, 161 (2000); Y. Akimura *et al.,* Eur. Phys. J. A **25**, 405 (2005).

[128] R. K. Puri, E. Lehmann, A. Faessler, and S. W. Huang, J. Phys. G **21**, 583 (1995); H. Sorge, H. Stocker, and W. Greiner, Ann. Phys. **192**, 266 (1989).

[129] T. Maruyama, S. W. Huang, N. Ohtsuka, G. Q. Li, A. Faessler, and J. Aichelin, Nucl. Phys. A **534**, 720 (1991); T. Maruyama, G. Q. Li, and A. Faessler, Phys. Lett. B **268**, 160 (1991); S. W. Huang, A. Faessler, G. Q. Li, R. K. Puri, E. Lehmann, D. T. Khoa, and M. A. Matin, Phys. Lett. B **298**, 41 (1993).

[130] A. Lang, Blättel, W. Cassing, V. Koch, U. Mosel, and K. Weber, Z. Phys. A **340**, 287 (1991); B. Blättel, V. Koch, W. Cassing, and U. Mosel, Phys. Rev. C **38**, 1767 (1988).

[131] C. Hartnack and J. Aichelin, J. Phys. G: Nucl. and Part. Phys. **28**, 1649 (2002); *ibid.* **30**, s531 (2004).

[132] Y. Yariv and Z. Frankel, Phys. Rev. C **20**, 2227 (1979); J. Cugnon. Phys. Rev. C **22**, 1885 (1980).

[133] S. A. Bass, C. Hartnack, H. Stocker, and W. Greiner, Phys. Rev. C **51**, 3343 (1995).

[134] P. Danielewicz and G. F. Bertsch, Nucl. Phys. A **533**, 712 (1991).

[135] J. Huber and J. Aichelin, Nucl. Phys. A **573**, 587 (1994).

[136] W. Cassing, W. Metag, U. Mosel and K. Nitta, Phys. Rep. **188**, 363 (1990); G. F. Bertsch and S. Das. Gupta, Phys. Rep. **160**, 189 (1988); J. Schnack, Ph. D. Thesis,

GSI report, Darmstadt (1996); A. Ono, H. Horiuchi, T. Maruyama, Phys. Rev. C **48**, 2946 (1993); *ibid.* **47**, 2652 (1993); B. J. VerWest and R. A. Arndt, Phys. Rev. C **25**, 1979 (1982); B. Jakobsson *et al.*, Nucl. Phys. A **509**, 195 (1990); H. W. Barz *et al.*, *ibid.* **548**, 427 (1992).

[137] J. K. Dhawan and R. K. Puri, Phys. Rev. C **75**, 057601 (2007); *ibid.* 057901 (2007).

[138] A. Schuttauf *et al.* Nucl. Phys. A **607** 457 (1996).

[139] J. Y. Liu, Y. F. Yang, W. Zho, S. W. Wang, Q. Zhao, W. J. Guo, and B. Chen, Phys. Rev. C **63**, 054612 (2001); J. Y. Liu, Y. Z. Xing, and W. J. Guo, Chin. Phys. Lett. **20**, 643 (2003).

[140] M. B. Tsang *et al.*, Phys. Rev. Lett. **71**, 1502 (1993).

[141] R. K. Puri and N. Dhiman, Eur. Phys. J. A **23**, 429 (2005); R. Arora, R. K. Puri, and R. K Gupta, *ibid.* **8**, 103 (2000); R. K. Puri, M. K. Sharma, and R. K. Gupta, *ibid.* **3**, 277 (1998); R. K. Puri and R. K. Gupta, Phys. Rev. C **51**, 1568 (1995); R. K. Puri, P. Chattopadhyay, and R. K. Gupta *ibid.* **45**, 1837 (1992); *ibid.* **43**, 315 (1991); R. K. Puri and R. K. Gupta, J. Phys. G: Nucl. Part. Phys. **18**, 903 (1992).

[142] R. K. Gupta, S. Singh, R. K. Puri, and W. Scheid, Phys. Rev. C **47**, 561 (1993); R. K. Gupta, S. Singh, R. K. Puri, A. Sandulescu, W. Greiner and W. Scheid, J. Phys. G **18**, 1533 (1992); S. S Malik, S. Singh, R. K. Puri, S. Kumar and R. K. Gupta, Pramana J. Phys. **32**, 419 (1989); R. K. Puri, S. S. Malik, and R. K. Gupta, Europhys. Lett. **9**, 767 (1989).

[143] R. R. Betts, Proc. Conf. on Resonances in Heavy Ion Reactions (Lecture Notes in Physics 156, 1981) *ed.* K. A. Eberhardt (Berlin: Springer) p 185.

[144] S. Kumar, S. Kumar, and R. K. Puri, Phys. Rev. C **78**, 064602 (2008); NCETEM2007, Thapar University, Patiala (Punjab), **p33**, Feb 1-3, (2007); INPC2007, Tokyo, Japan, **QW-236**, June 3-8, (2007); CITICOMS2007, CIT, Coimbatore, Vol.1, 30, Aug. 27-29 (2007). Y. K. Vermani, S. Goyal and, R. K. Puri, Phys. Rev. C **79**, 064613 (2009).

[145] R. K. Puri and S. Kumar, Phys. Rev. C **57**, 2744 (1998); S. Kumar and R. K. Puri, *ibid.* **58**, 2858 (1998); S. Kumar, S. Kumar, and R. K. Puri, Phys. Rev. C **81**, 014601 (2010).

[146] D. R. Bowman *et al.*, Phys. Rev. C **46**, 1834 (1992); A. Le Fevre *et al.*, Nucl. Phys. A **735**, 219 (2004); J. Lukasik, *et al.*, Phys. Lett. B **566**, 76 (2003); K. Turzo *et al.*, Eur. Phys. J. A **21**, 293 (2004); C. Volant *et al.*, Nucl. Phys. A **734**, 545 (2004).

[147] X. Lopez *et al.*, Phys. Rev. C **76**, 052203R (2007); H. H. Gutbrod *et al.*, Z. Phys. A **337**, 57 (1990).

[148] C. Roy *et al.*, Z. Phys. A **358**, 73 (1997).

[149] Y. M. Zheng *et al.* Phys. Lett. B **194**, 183 (1987). Y. M. Zheng *et al.* J. Phys. G: Nucl. Part. Phys. **22**, 505 (1996).

[150] E. Lehmann, A. Faessler, J. Zipprich, R. K. Puri and S. W. Huang. Z. Phys. A **355**, 55 (1996).

[151] D. Krofcheck *et al.*, Phys. Rev. Lett. **63**, 2028 (1989).

[152] S. J. Lee *et al.*, Phys. Rev. C **68**, 014608 (2003); M. Colonna *et al.*, Phys. Rev. Lett. **88**, 122701 (2002).

[153] J. Y. Liu *et al.*, Phys. Rev. C **70**, 034610 (2004); J. Y. Liu *et al.*, Chin. Phys. Lett. **21**, 1914 (2004).

[154] R. Pak *et al.*, Phys. Rev. C **54**, 2457 (1996); *ibid.* **53**, R1469 (1996).

[155] A. Le Fevre and J. Aichelin, Phys. Rev. Lett. **100**, 042701 (2008); A. Le Fevre *et al.*, Phys. Rev. C **80**, 044615 (2009); Y. K. Vermani, J. K. Dhawan, S. Goyal, R. K. Puri and J. Aichelin, J. Phys. G: Nucl. Part. Phys. **37**, 015105 (2010).

[156] Y. Zhang and Z. Li, Phys. Rev. C **74**, 014602 (2006).

[157] G. Batko *et al.,* J. Phys. G: Nucl. Part. Phys. **20**, 461 (1994).

[158] P. Danielewicz, Nucl. Phys. A **673**, 375 (2000); T. Z. Yan *et al.,* Chin. Phys. lett. **26**, 112501 (2009).

[159] C. Adler *et al.,* Phys. Rev. Lett. **90**, 032301 (2003).

[160] A. D. Sood and R. K. Puri, Phys. Rev. C **79**, 064618 (2009).

[161] H. Sorge, Phys. Rev. Lett. **78**, 2309 (1997).

[162] D. J. Magestro, Ph. D thesis, NSCL, MSU, USA (2000); D. J. Magestro, W. Bauer, and G. D. Westfall, Phys. Rev. C **62**, 041603(R) (2000).

[163] J. D. Bowman, W. J. Swiatecki and C. F. Tsang, Lawrence Berkeley Laboratory Report No. LBL-**2908**, 1973 (unpublished).

[164] G. Westfall *et al.,* Phys. Rev. Lett. **18**, 1202 (1976).

[165] S. Wang *et al.,* Phys. Rev. Lett. **76**, 3911 (1996); D. Brill *et al.,* Z. Phys. A **355**, 61 (1996); N. Bastid *et al.,* Nucl. Phys. A **622**, 573 (1997); G. Stoicea *et al.,* Phys. Rev. Lett. **92**, 072303 (2004).

[166] M. Colona, M. D. Toro, G. Ferini, and V. Greco, *Catania workshop on nucleon and neutrino astrophysics*, 15-16 Feb., (2007); M. Di Toro, S. J. Yennello, and B. A. Li, Eur. Phys. J. A **30**, 153 (2006).

[167] T. Z. Yan *et al.,* Chin. Phys. **16**, 2676 (2007).

[168] W. Zhan *et al.,* Int. J. Mod. Phys. E **15**, 1941 (2006); Y. Yano, Nucl. Inst. Meth. B **261**, 1009 (2007); http://www.gsi.de/fair/index_e.html; http://www.ganinfo.in2p3.fr/research/developments/spiral2; Whitepapers of the 2007 NSAC Long Range Plan Town Meeting, Jan., 2007, Chicago, http://dnp.aps.org.

[169] S. A. Bass, *et al.*, GSI Scientific Report **94** GSI (Germany) 66 (1995).

[170] W. Bauer, Phys. Rev. Lett. **61**, 2534 (1988); B. A. Li and C. M. Ko, Nucl, Phys. A **601** 457 (1996).

[171] J. Y. Liu *et al.*, Phys. Rev. Lett. **86**, 975 (2001); P. Danielwicz, B. Barker and L. Shi, arxiv: 0903.2560v1 [nucl-th] 2009.

[172] L. Q. Feng and L. Z. Xia, Chin. Phys. Lett. **19** 321 (2002); S. J. Yennello *et al.*, Phys. Lett. B **321**, 15 (1994).

[173] T. Gaitanos, M. Colonna, M. Di Toro, and H. H. Wolter, Phys. Lett. B **595**, 209 (2004); A. H. Raduta, M. Colonna and M. Di Toro, Phys. Rev. C **76**, 024602 (2007); M. Di Toro, V. Baran, M. Colonna, G. Ferini, T. Gaitanos, V. Greco, J. Rizzo, and H. H. Wolter, Nucl. Phys. A **787**, 585 (2007).

[174] S. Gautam and A. D. Sood, Phys. Rev C **82**, 014604 (2010).

[175] W. Reisdorf *et al.*, Nucl. Phys. A **612**, 493 (1997).